THE THEORY AND DESIGN OF SWITCHED-MODE POWER TRANSFORMERS FOR MINIMUM CONDUCTOR LOSS

by

Stephen D. Goad

Dissertation submitted to the Faculty of the
Virginia Polytechnic Institute and State University
in partial fulfillment of the requirements for the degree of

DOCTOR OF PHILOSOPHY

in

Electrical Engineering

APPROVED:

Warren L. Stutzman, Chairman

Ioannis M. Besieris

David A. deWolf

Werner E. Kohler

Fred C. Lee

Daniel B. Hodge

December, 1985

Blacksburg, Virginia

THE THEORY AND DESIGN OF SWITCHED-MODE POWER TRANSFORMERS FOR MINIMUM CONDUCTOR LOSS

by

Stephen D. Goad

Committee Chairman: Warren L. Stutzman

Electrical Engineering

(ABSTRACT)

A comprehensive and general analysis of the electromagnetic fields, power dissipation, and energy storage within transformer windings is presented. Emphasis is placed on applications in switched-mode power conversion. One-dimensional radial variation of the field quantities is assumed.

The first phase of the investigation is for sinusoidal excitation; solutions for the current density and magnetic field intensity are derived and studied in order to develop a fundamental understanding of the basic phenomena. Expressions for the power dissipation and energy storage in both single- and multi-layer windings are then derived which, upon investigation, yield a technique for minimizing the power dissipation by choosing an optimum conductor

thickness. Several levels of accuracy, ranging from exact solutions to very simple and physically meaningful series approximations, are defined and examined to determine their usefulness and range of validity.

The time-harmonic treatment is generalized to arbitrary periodic excitation by means of Fourier analysis, resulting in a powerful extension of its applicability to any possible converter topology. Results for several representative waveshapes are presented from which a fundamental dependence on the waveform bandwidth is discovered.

Practical application of the theoretical analysis is considered by developing models for several common winding types: single and multi-filar round wire, litz wire, and sheet conductors. Experimental results are presented and compared with the theoretical results for each of these cases. Finally, a design procedure is outlined for switched-mode power transformers which is based on this work.

TO MY MOTHER

ACKNOWLEDGEMENTS

It is almost always true that major individual efforts benefit from the contributions of others throughout their development. This dissertation is no exception. Usually, these people and their contributions tend to be inadvertently overshadowed and forgotten as time passes. My intention here is to express heartfelt gratitude to these people in hopes that they will be remembered henceforth by both myself and those who may read and use this work.

First and foremost is the institution which has been responsible for the majority of my education. Virginia Tech. I am truly grateful. My only disappointment is that I cannot seem to assemble words which adequately describe my feelings in this regard.

Along with a quality institution come quality people. I have been very fortunate in this respect also. I first thank Dr. Warren L. Stutzman for serving as my committee chairman, for being extremely helpful and effective as my major advisor, and also for being a good friend. I express similar appreciation to Dr. Gary A. Thiele who acted in the same capacity while I was attending Ohio State University. I also express special gratitude to both Dr. Daniel B. Hodge and Dr. Ioannis M. Besieris. I have known Dr. Hodge at both

Ohio State and Virginia Tech. He has been particularly accommodating to me, and I have enjoyed and learned much from our numerous conversations. Dr. Besieris has been very influencial to me throughout my electrical engineering education. My respect for him is unequaled in many ways. I also sincerely appreciate the helpful suggestions from the remainder of my advisory committee: Dr. Fred C. Lee, Dr. David A. deWolf, and Dr. Werner E. Kohler. And finally, a special thanks to the electrical engineering department at Virginia Tech. I truly believe that it offers excellence in education and I hope to be worthy of it.

I am very thankful for the support of my employer, , throughout the past fifteen months. As a participant in their doctoral study program I have been able to pursue my degree requirements while performing research in an exciting and increasingly important area. I believe there is much to be said for this type of mutually beneficial relationship. I wish to express my appreciation to the following key people at who have been instrumental in arranging this relationship: , President and General Manager; , retired Director of Employee Relations; , V.P. Operations; and , Director of Engineering. I especially thank for initially allowing me the time to investigate the problems which

eventually led to the topic of this dissertation. I also extend special thanks to , magnetics designer, who performed the experimental measurements which appear in Chapter 8. I have learned a great deal from who has helped to keep practical reins on my sometimes wandering theoretical tendencies.

Last, but certainly not least, there is my family. I don't know what to say other than I love them and thank them for everything they have done. Without the help and understanding of my wife , this past year would have been very difficult, if not impossible. And my daughter has been a true inspiration through it all.

TABLE OF CONTENTS

CHAPTER 1

INTRODUCTION

A fundamental design goal of all power conversion processes is the maximization of the conversion efficiency. Ideally, there should be no losses experienced during the conversion process. This goal must usually be pursued in the presence of many other system requirements and constraints; consequently, it is common for design scenarios to involve tradeoffs between the efficiency and these other factors. Virtually all usable power in the world today is converted and processed into a form for a specific purpose. Therefore, any increase in conversion efficiency which can be accomplished without negative repercussions is potentially of great benefit to society.

The stringent requirements of the space program in the United States spurred new emphasis on the desire to increase the efficiency and to reduce the size and weight of electrical power conversion systems. The development of switched-mode power conversion techniques is one of the most important results of this renewed interest. Switched-mode power conversion involves the controlled systematic switching of electrical energy from which the desired conversion process is accomplished by means of an

appropriate circuit topology. Regulation of the conversion process is generally implemented through control of the switching device(s). In addition to solid-state switching devices, transformers and energy storage reactive elements typically perform important functions in these processes. Recent technological advances in these devices, especially switching devices, have resulted in higher efficiencies than were previously attainable using conventional power conversion techniques. A further development made possible by recent advances is the capability of switching at higher rates. The benefits of increased switching frequencies manifest themselves in the form of reduced size and weight as a direct result of frequency scaling reactive components and transformers.

State-of-the-art switched mode power conversion technology continues to be driven by the space program and also by the military. For example, one of the most formidable tasks associated with the newly proposed strategic defense initiative is the efficient generation, conversion, and processing of the vast amounts of required power. As the components of these systems become more producible and cost effective, newer technology gradually finds its niche in an increasing number of applications in the private sector. Today, the switched-mode power conversion industry is in the midst of rapid technological

change and expansion into the private sector. In many instances, the private sector is beginning to participate in much of the basic research, providing yet another source for the advancement of the technology.

Within the switched-mode power conversion industry, there is a continuing effort to increase switching rates. The advantages of increasing operating frequencies are well-known and have already been mentioned. The primary advantage is a reduction in the size and weight of the reactive components and transformers which comprise a large percentage of most converters. In addition, higher operating frequencies can also lead to faster dynamic response if properly implemented. There are, however, several factors which inhibit the progress toward higher frequencies. One major factor of practical importance is the development and availability of cost effective components which will effectively and reliably perform their indicated functions at high frequencies. Other important factors include the technical level of understanding and the ability to design in an increasingly hostile environment of what used to be second order, but are now dominant, parasitic effects associated with high frequency operation. Both of these examples are to a large degree the result of being a relatively new technology. As the technology matures they should begin to play a lesser role.

Furthermore, the progress toward higher operating frequencies has a more fundamental limitation. Namely, as one increases the operating frequency for the purpose of reducing size and weight, there usually results a requirement for a corresponding increase in efficiency. This is easily understood from basic thermal considerations. Two naturally occurring processes for removing heat from a material body which is dissipating power are free air convection and radiation. Under these conditions, the temperature rise of a body above the ambient temperature of the surrounding medium is directly proportional to the power dissipated within the body and inversely proportional to the surface area of the body. Consequently, to operate a component at a given temperature as its size decreases, there must be a corresponding reduction in the power dissipation within the component. This in turn implies a higher system efficiency. Although other methods of heat removal are possible, they are limited in value. For example, heat may be removed via conduction through heat sinks, or by forced air convection with fans. However, both of these methods increase the size of the system, therefore cancelling size reductions obtained by increasing the operating frequency. Another alternative is to develop components which will operate at higher levels of temperature stress. This is possible to a certain degree

but limitations are frequently reached due to technological obstacles, increased cost, and reliability problems.

The importance of increasing system efficiencies through the reduction of internal losses is emphasized by the preceding discussion. There are certainly limitations (100% efficiency is neither possible nor practical) to this approach also; however, it is the most promising at present. There are many opportunities for improving the performance of components used in this relatively new technology. Two very important components, solid-state power switching devices and power transformers, are good candidates for improvements in efficiency since they contribute a major portion of the losses in a switched-mode power converter. Much emphasis has been placed on power switching devices which have recently undergone orders of magnitude in improvement leading to increased switching rates, efficiency, and power handling capability. Recent developments in metal oxide field effect transistors (MOSFET's) are a good example of this.

Corresponding advances in the design of power transformers have not occurred on the same scale. Although new materials and techniques are being introduced, they are not widely understood and often misapplied. Few techniques based on minimizing losses and size are available, and they are usually based on oversimplifications. A major objective

of the work in this dissertation is to help alleviate these deficiencies. A more detailed description of this work will follow after a brief introductory discussion of power transformers within the context of switched-mode power conversion.

Two important functions of power transformers in switched-mode power conversion are electrical isolation and the transformation of voltage and current levels. Although they are not necessarily required in all applications, they are typically found in a large majority of them. Losses in power transformers occur in both the core material and the conductors which make up the windings. Ferromagnetic oxides, or ferrites, are the predominant materials used in cores. There are three basic contributions to the losses in ferrites: hysteresis, eddy currents, and residual losses. Even though core losses are important, the treatment in this dissertation is limited to losses which are generated within winding conductors. The designer usually has a large degree of flexibility and control over the arrangement and choice of conductors used in transformer windings. It will be seen that this can lead to optimization techniques which minimize the power dissipation in the conductors.

Power dissipation in a conducting medium may be divided into two subsets. The first is normally referred to as the DC power dissipation or loss. It is generated by steady

currents which flow uniformly through the cross section of a conductor. DC losses are a function of the conductivity, the cross-sectional area, and the length of the conductor. The second type of power dissipation is sometimes referred to as AC loss, and is due to eddy currents. Eddy currents are defined as those currents which are produced as a result of voltages induced by time-varying magnetic fields.

Eddy currents may be further classified into those due to the skin effect and those due to the proximity effect. Skin effect is the phenomenon of non-uniform current distribution over a conductor cross section caused by the time variation of the magnetic fields within the conductor itself. According to Maxwell's equations, these magnetic fields coexist with longitudinal currents that tend to add vectorially near the surface and cancel in the center of the conductor. Proximity effect is similar, except that the non-uniform current distribution is induced by the time variation of externally produced magnetic fields such as those from another conductor in close proximity. Actually, the classification of eddy currents into those caused by the skin and proximity effects is one of convenience which is helpful in visualizing the complexity of the phenomenon. In reality, Maxwell's equations apply to an overall system of conductors, so that all mutual interactions are accounted for. When this is done, there results a unique current

density distribution in each conductor. There are many ways of separating these distributions into various components which aid in developing a better physical understanding of the phenomena. The aforementioned separation is probably one of the most popular.

A non-uniform current distribution follows by definition from the presence of eddy currents. This necessarily results in greater loss than the ideal case of uniform current distribution. The extent of the increased loss is related to the degree of nonuniformity which is in turn related to the frequency of variation of the magnetic fields. As the frequency increases, the eddy currents become more localized. The unit of measure for this localization is the skin depth. In light of the earlier discussions concerning the recent trends toward higher frequencies, and the relationship between frequency and efficiency; the importance of accurately determining current distributions and their associated losses becomes clear. This need is further accentuated by the usual requirement of tight coupling between windings in a transformer which leads to an exaggerated proximity effect.

The purpose of this dissertation is first to accurately model and analyze the aforementioned phenomena in power transformer windings with emphasis on applications in switch-mode power conversion. Results from this analysis

are then studied in order to develop a fundamental understanding of these phenomena. Based on this understanding, techniques for improving and optimizing the design for minimum conductor loss are derived. An additional benefit of the analysis is the capability of determining the energy stored in the magnetic fields within the windings. These fields are usually referred to as leakage fields, and the energy stored in them can be used to determine the leakage inductance. The leakage inductance is a parasitic element which accounts for components of magnetic flux which do not link both the primary and secondary. It appears in the equivalent circuit model of a transformer, and is a very important element in numerous types of switched-mode power converters.

CHAPTER 2

HISTORICAL PERSPECTIVE

Very little work has been done toward accurately determining and minimizing the power dissipation in transformer windings with emphasis on applications in switched-mode power conversion. This chapter is therefore devoted to chronologically presenting some of the major contributions which are related and have led to this topic. It begins with some of the first work involved with the discovery of the skin effect in long cylindrical wires. It then highlights the major developments up to some of the more recent work which is more directly applicable to the subject matter of this dissertation. For convenience, the references are also listed chronologically. An attempt is made in this chapter to put the contributions of this dissertation research into perspective. Thus, original contributions contained herein are mentioned where they relate to earlier work. For these reasons it may be more meaningful to read this chapter again after completing the rest of the material.

2.1 THE EARLY YEARS

It was Maxwell [1] who first considered the effect of introducing time-varying quantities on the current distribution in a long cylindrical wire of circular cross section. He showed that the current density and other field quantities were in general a function of the radial distance from the center of the conductor. He derived expressions for the effective resistance and inductance by first expanding the field quantities into a power series in the radial coordinate and allowing the coefficients to be a function of time. The resulting series contained time derivatives of the current; hence, the solution was very general. Although this work established the important concept that the distribution of current is modified by introducing time variations, it is believed that Maxwell did not pursue this subject to the point of developing an understanding of the skin effect as it exists today.

Maxwell's work prompted several prominent scientists such as Rayleigh, Kelvin, and Heaviside to continue research efforts in this area in the years to follow. Lord Rayleigh [2, 3, 4] first considered the time-harmonic case by introducing quantities that varied sinusoidally in time. Using the results of Maxwell, he derived series expressions in the radial coordinate for the effective resistance and inductance of a long cylindrical wire. Even though his

series converged slowly and only for low frequencies, Lord Rayleigh was able to draw some very important fundamental conclusions. For low frequencies, he found that the current density approaches a uniform distribution which leads to minimum resistance and maximum self inductance. At high frequencies, he also concluded that the current density becomes highly nonuniform and concentrates near the surface. Consequently, he reasoned that the effective resistance increases without limit, and also that the self inductance approaches a minimum value as the frequency increases.

Prof. D.E. Hughes [5] performed some key experiments during the same time period which helped to demonstrate and confirm these phenomena. Some important new conclusions were also reached during these experiments, such as the advantages of using stranded conductors to reduce eddy currents.

Kelvin and Heaviside provided more important theoretical and experimental results during the ensuing years which continued and expanded on Rayleigh's work. Kelvin, in his inaugural address to the IEE [6], spoke at length about the far-reaching implications of the frequency dependence of current distributions. He presented an enlightening analogy with the motion of a viscous fluid in a longitudinally vibrating tube. In those days, mechanical analogies such as this were very helpful in visualizing the more abstract concepts of electricity and magnetism.

Although unable to locate the specific references, the author has also encountered descriptions of contributions made by M. Wien [7] and A. Sommerfeld in 1904 [8]. They both considered the effect on the current distribution when a conductor is wound into a solenoidal coil. Wien derived series solutions for the effective resistance and inductance which were valid only for low frequencies, and whose terms were difficult and laborious to calculate. Sommerfeld was able to find solutions which were valid over the entire frequency range.

2.2 APPLICATIONS IN POWER GENERATION AND TRANSMISSION

In 1905, A.B. Field [9] first considered the effects of eddy currents in slot-wound conductors such as those found in the armatures of direct current machines or the stators of induction motors and alternators. The conductors in these machines were typically located in slots surrounded on three sides by a high permeability material such as iron. The magnetic field intensity was assumed to vary as a function of the slot depth only and to be directed transversely across the slot. This geometry is very similar to the one used in this dissertation for the transformer, except for the fact that no radius of curvature is accounted for. Consequently, Field's results are analogous to the thin-layer approximation derived in Chapter 4. He found

that the current concentrates in the upper portion (open end) of the slot and showed that many of the existing designs at that time produced excessive losses. He suggested several techniques for reducing the losses, such as using stranded conductors and interleaving layers of conductors in configurations which would encourage a more uniform flux distribution. Although Field's results and conclusions are important and informative, they are not suitable for use here for several reasons. First of all, the notation is somewhat outdated and designed specifically for application to slot-wound conductors. Secondly, there is no provision for including the radius of curvature in transformer windings. And lastly, Field does not take advantage of the simplified mathematics of time-harmonic analysis. His solutions are therefore very cumbersome by present day standards.

M.B. Field, A.B. Field's brother, continued and extended the work of his brother in 1906 [10]. He introduced the term *idle currents* to denote currents which consume energy but do not perform any useful work. This terminology was subsequently criticized by several people and has since been discarded. M.B. Field made several new contributions. Probably the most important was the discovery of the existence of critical conductor depths which resulted in minimum losses. He also mentioned the possibility of using

Fourier analysis to handle the near square-wave currents in the conductors of direct current machines. This was not pursued, however, presumably because the series converged rather slowly and also because the prospect of performing the necessary calculations without a computer was too overwhelming.

In the years that followed, many others made contributions toward improving the theory and developing a wide variety of techniques to reduce losses in slot-wound conductors. W.V. Lyon [16, 22, 23] simplified the mathematics considerably by introducing hyperbolic functions with complex arguments. He also considered stranded conductors and several methods of interleaving conductors to reduce losses. Similar contributions were made by H.W. Taylor [18], R.E. Gilman [19, 27], and I.H. Summers [30].

In 1907, L. Cohen [11] extended the earlier work on solenoidal coils by Wien and Sommerfeld in 1904. He was discouraged by the previous lack of agreement with experimental measurements, and therefore set out to improve the theory by allowing longitudinal variation in the fields and currents. This treatment is analogous to the two-dimensional tranformer problem which is defined, but not solved, in Section 3.3. Cohen considers a long single-layer coil in air for which he derives expressions for the power dissipation, effective resistance, and effective inductance.

Although his results show marked improvement in accuracy, their application is limited to long single layer coils which are carrying a sinusoidal current. Furthermore, he does not consider techniques for minimizing the conductor losses. Several years later, S. Butterworth [21, 28] also considered eddy current losses in solenoidal coils. His approach, quite different than Cohen's, was applicable to short coils with relatively wide wire spacings. He also considered the effects of stranded wire and multi-layer coils, and briefly addressed the issue of minimizing the power dissipation.

During the time period from 1909 to 1940, there was much research activity in the investigation of the high-frequency effects of eddy currents for various conductor shapes and configurations. Most of these contributions are not directly applicable or easily adaptable to the solenoidal transformer geometry used here. However, many of the results are fundamental in nature and therefore useful in achieving a thorough understanding of the phenomena associated with eddy currents. Several of the major contributors along with their publications are summarized in the following areas: solid wires, tubular conductors, and coaxial cables - A. Russell [12], H.B. Dwight [15, 24, 25, 26], H.L. Curtis [20], A.H.M. Arnold [33, 34]; stranded conductors - G.W.O. Howe [14]; rectangular conductors - J.D. Cockroft [31], W.

Jackson [32], A.H.M. Arnold [35]; and general works involving several geometries - G.W.O. Howe [17], C. Snow [29]. One of the most important and comprehensive experimental researches conducted on skin effect during this time period was by Kennelly, Laws, and Pierce [13]. Most of the aforementioned theoretical analyses are compared with these experimental results to examine their validity.

2.3 RECENT CONTRIBUTIONS

There were at least two significant contributions in the 1940's for which the primary intended application was transformers. The first was by E. Bennett and S.C. Larson [36]. In it they presented a comprehensive and straightforward analysis for the effective resistance of multi-layer coils in transformers carrying sinusoidal currents. Although this analysis resembled earlier treatments on slot-wound conductors, the authors were unaware of that work when they submitted their manuscript. They subsequently demonstrated the similarities between the two applications. The rectangular coordinate system was used; consequently, there was no way to determine the effect of the radius of curvature in a cylindrical winding. Their results are therefore equivalent to the thin-layer approximation derived in this dissertation. Bennett and Larson presented several curves for the current density and

magnetic field intensity within the conductors. They also plotted the relative power dissipation in the conductors versus the conductor thickness expressed in skin depths. From this they discovered the existence of an optimum conductor thickness which yielded minimum power dissipation at a given frequency. When the appropriate parameters are properly related, the thin-layer approximation contained herein for the case of sinusoidal excitation is in agreement with the results of Bennett and Larson.

Five years later, with no apparent knowledge of the work of Bennett and Larson, T.H. Long [37] presented a similar analysis for the effective resistance of multi-layer windings. Although not as comprehensive in coverage, many of the same conclusions were drawn. However, Long did make two new contributions. He found the optimum conductor thickness for a multi-layer winding with identical layers and he derived an approximation to include end effects.

No further work of significance appeared until 1966 when P.L. Dowell [39] expanded the earlier analysis so that it could be conveniently applied to modern transformers. In the process he derived expressions for the leakage inductance as well as the effective resistance. A further important attribute of his work is its ability to handle sectionalized windings. Dowell does not, however, give any consideration to methods for minimizing the losses.

There was also a renewed interest in the 1960's on applications involving slot-wound conductors in rotating machinery, primarily by P. Silvester [40-45]. Most of the techniques used by Silvester involve numerical methods which became possible with the advent of more powerful computers. Although these techniques are very general and capable of analyzing complex geometries, their usefulness in the transformer application does not presently appear to justify their added complexity. Moreover, these techniques tend to be less revealing on the fundamental nature of the solutions.

Two books written in the 1960's are also useful as general references. *Eddy Currents* by Lammeraner and Stafl [38] is a valuble treatise on methods and applications for eddy currents. *Soft Ferrites: Properties and Applications* by E.C. Snelling [46] provides an equally useful reference on ferrites and their applications. Of particular interest for the work here are his discussions on power transformers and the properties of windings in Chapters 9 and 11, respectively.

The next important contribution was by M.P. Perry in 1979 [47], and later in 1981 [49] in an extension of the former. Like Dowell, his work served mainly to modernize the theory and its applicability. But unlike Dowell, he stressed the concept of designing windings for mimimum

losses. Perry's model was still one-dimensional and only for sinusoidally time-varying currents. Although the rectangular coordinate system was the primary setting for his analysis and results, Perry did introduce the notion of using the cylindrical coordinate system to take into account the effect of the radius of curvature. But he did not carry this treatment through to any extent. Also in 1979, T.H. Putman [48] considered eddy-current losses in large electrical reactors. The theoretical content of this paper was very limited and primitive. His major contribution involved devising a thermodynamic based method for experimentally measuring the losses in large reactors.

As far as the author has been able to determine, the first and only treatment of transformers for switched-mode power conversion was by P.S. Venkatraman in 1984 [50]. His most important contribution was to directly apply the work of Dowell [39] to extend the application to rectangular wave currents by using Fourier analysis. He derived expressions and plotted curves for both the effective resistance and leakage inductance of a transformer winding carrying rectangular wave currents.

Venkatraman's work is a valuable contribution to modern switched-mode power conversion. It clearly establishes the influence of the current waveshape on determining losses in transformer windings. There are many limitations to its application, however, and there is much room for improvement

and extension. First of all, only rectangular wave currents were considered. A wide variety of current waveforms are encountered in modern switched-mode power conversion, and it appears that the number will continue to grow as more and more circuit topologies are discovered. Certainly, techniques employing Fourier analysis are capable of providing a means for handling arbitrary waveforms. Venkatraman also does not consider the very important concept of minimizing the winding conductor losses. Presumably, since an arbitrary waveform can be expressed as a sum of sinusoids, the minimization problem should be solvable just as it is for the case of a pure sinusoid. The resulting solution should be expected to be a complicated function of the harmonic content of the waveform. A challenging task would therefore be to cast the solution into a form which relates to fundamental characteristics of the waveform. The accomplishment of this task would be of considerable value in leading to a better understanding of the phenomena. Two other limitations of Venkatraman's work which could be addressed are: the exact solution of the one-dimensional problem in the cylindrical coordinate system in order to include the effects of the radius of curvature; and the generalization of the notation so that individual layers and sectionalized windings within complicated transformers can be conveniently analyzed.

2.4 CONTRIBUTIONS OF THIS EFFORT

The primary objective of this dissertation is to provide a comprehensive, general treatment of the theory and design of switched-mode power transformers for minimum conductor loss. The author's philosophical approach to accomplishing this goal follows. First, the most general mathematical model is defined and discussed (Chapter 3). This model is then specialized to facilitate a methodical development and complete study of the time-harmonic sinusoidal analysis (Chapters 3, 4, 5, and 6). An attempt is made to encompass all of the previous work in a generalized treatment which also serves to introduce new and expanded solutions. The flow of the analysis begins with exact solutions and proceeds with several successively less accurate approximations. Each approximation is studied in detail to determine the conditions under which it is valid. The sinusoidal analysis is then generalized to arbitrary periodic waveforms through the use of Fourier techniques (Chapter 7). All of the same approximations are then reconsidered, the last of which leads to an interesting and enlightening physical interpretation. Finally, the analysis is applied to several popular conductor arrangements and some experimental measurements are presented and compared with the theoretical predictions (Chapter 8). Based on both the experimental and theoretical results, conclusions are

drawn and a design procedure for minimizing the power dissipation in transformer windings is outlined (Chapter 9). In addition, several possibilities for future work are discussed which could lead to increased accuracy or broader application.

CHAPTER 3

FORMULATION

Any engineering effort should be well-defined whether it involves research, design, or experimental work. The intent of this chapter is to provide a complete and clearly stated formulation of the problem considered here. This includes discussions of the problem constraints, its range of application, and the preliminary assumptions of the analysis. In the process of achieving this goal, most of the introductory theoretical analysis is also presented.

First, the physical geometry is considered. The cylindrical coordinate system is chosen as the setting for the mathematical description, and physical quantities are introduced within this context. Possible limitations which may arise as a result of the chosen geometry are discussed. Next, the electromagnetic field equations which mathematically model the problem are presented. General equations are introduced first, and are then methodically specialized for the work here. A general two-dimensional model is initially described. Conditions are then specified which allow simplification to a one-dimensional model. All subsequent work in this dissertation uses the one-dimensional model.

3.1 GEOMETRY

A perspective sketch of a typical high frequency power transformer for a modern switched-mode power converter is shown in Figure 3.1.1. The core geometry in this particular example is known as a PQ-core. The center leg of the core is circular in cross section as is the bobbin upon which the solenoidal-shaped windings are wound. Thus, except for the outer portion of the core and possible winding imperfections, the geometry of the transformer is axially symmetric. For these reasons, the cylindrical coordinate system is the natural choice for describing and analyzing these transformers. Many other core geometries and corresponding bobbins are available. The majority of them are very similar and can also be adequately represented in this manner. For example, EE-cores have center legs with a square cross section. This does not present a significant problem in practice, since after the first few layers, the windings begin to take on a circular shape. The current trend, however, is away from this type of core and toward those with circular cross section. The only major core geometry which is not represented well in the cylindrical coordinate system is the toroid. But even for this shape, if the radius is large enough, it may be treated as if it were cut and straightened into a long solenoid.

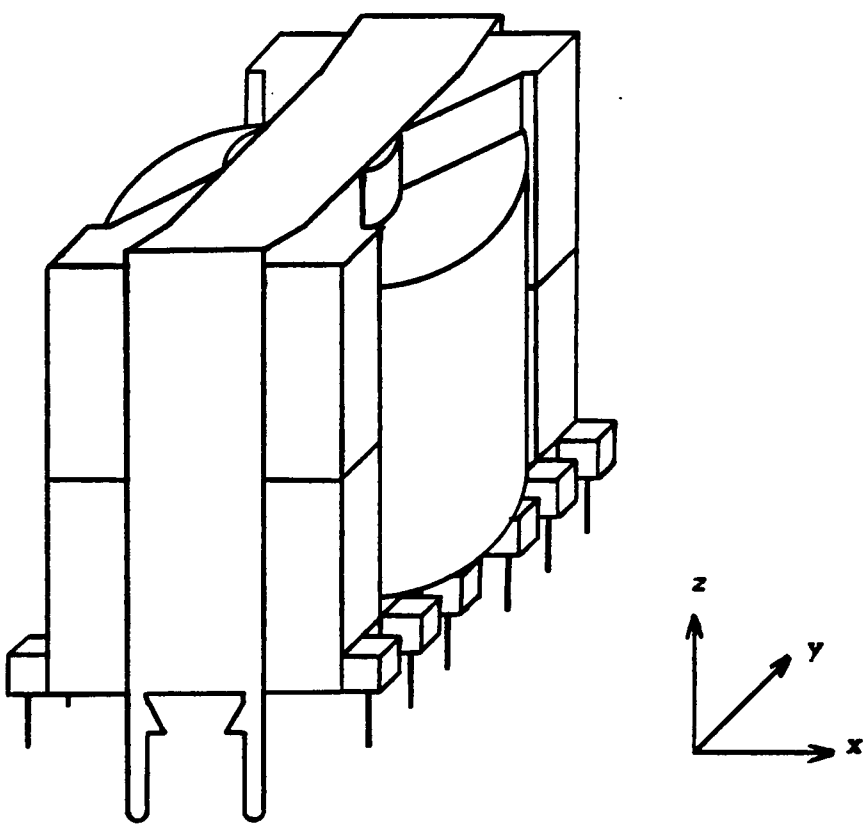

Figure 3.1.1. Perspective sketch of a typical high frequency power transformer (PQ-core) for a modern switched-mode power converter.

Figure 3.1.2 shows the cross section of a typical transformer. This illustration is designed to represent the most important aspects of transformer construction for the analysis here and to introduce some of the quantities and symbols to be used. It is not intended to be dimensionally accurate. The main features of this geometry along with some assumptions which are based on them are listed below. Some of these have already been mentioned, but are repeated here for completeness:

- The cylindrical coordinate system is used for the mathematical representation. Its orientation with respect to the transformer is indicated in both Figures 3.1.1 and 3.1.2.
- Axial symmetry about the z-axis is assumed; consequently, no quantities can exhibit ϕ-dependence. Because of this symmetry, only half of the cross-sectional view is shown in Figure 3.1.2.
- A core of ferrite material surrounds the winding portion of the transformer.
- The length of the winding area in the axial direction is denoted as l.
- A general transformer winding contains N alternating layers of conductor and insulator.

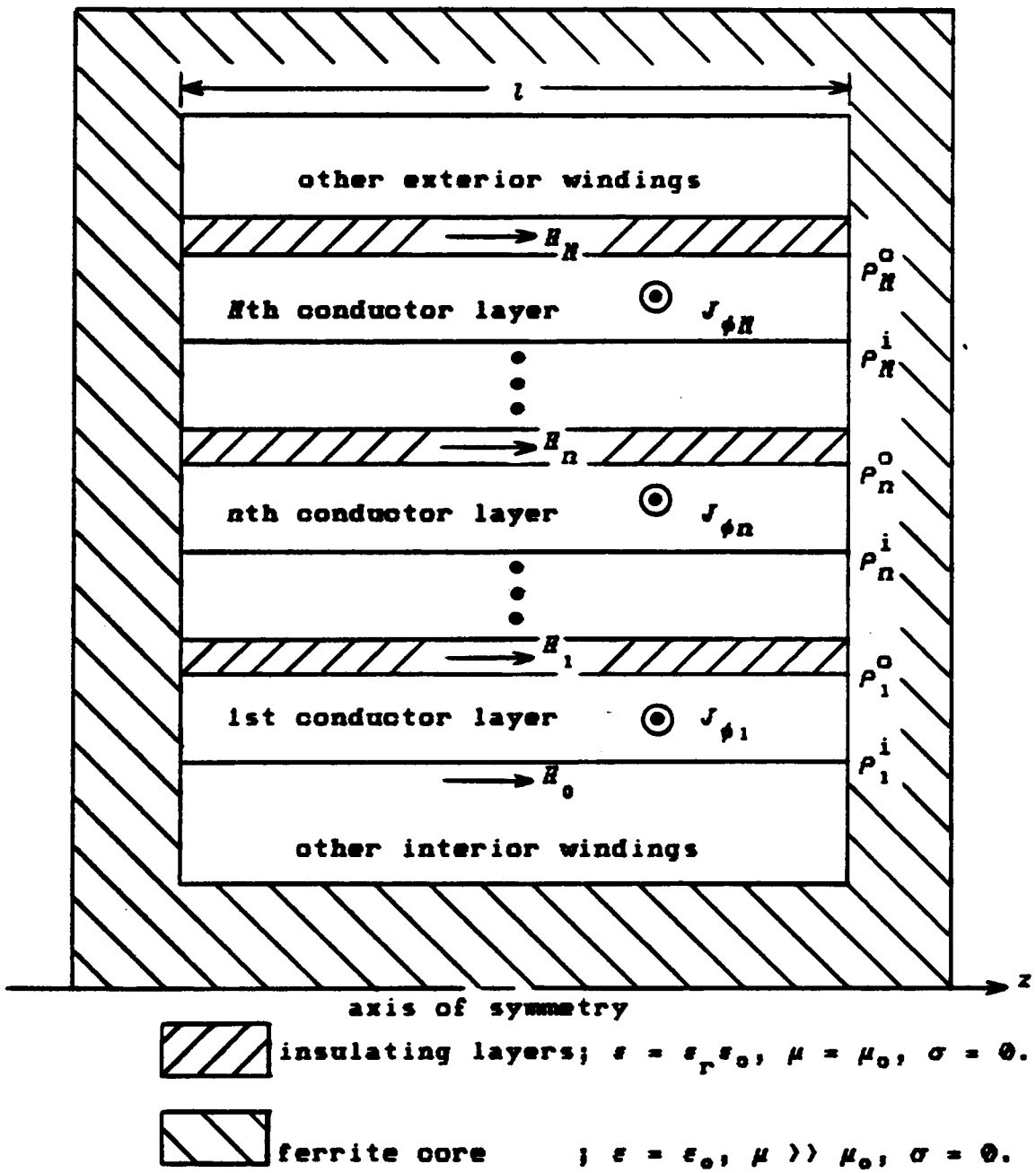

Figure 3.1.2. Cross-sectional view of a typical high frequency power transformer for a modern switched-mode power converter.

- The nth conductor layer is bounded by the inner and outer radii, ρ_n^i and ρ_n^o, respectively. The arrangement of conductors within the conducting layers is not defined at this point.
- The layers of insulating material are automatically defined to be bounded by the adjacent conductor layers.
- Other windings to the interior and exterior may be present and are modelled in a similar manner.

The macroscopic electrical properties of the materials in the transformer are described by their constitutive parameters. These parameters are shown in Figure 3.1.2 and summarized here for convenience:

- The ferrite core material is assumed to be lossless with real permeability $\mu \gg \mu_o$, free-space permittivity ε_o, and zero conductivity σ.
- The insulating material is assumed to be a lossless, non-magnetic dielectric with real relative permittivity ε_r, free-space permeability μ_o, and zero conductivity σ.
- The conducting material is assumed to be a good conductor with high conductivity σ. It has both free-space permittivity ε_o and permeability μ_o.

While the above characteristics describe the conducting material accurately, both the ferrite and insulating material could, in general, be more complex. Since the main interest here is to analyze phenomena within the conducting regions, only those characteristics of the surrounding regions which have a significant influence in accomplishing this are included. Actually, the above model for the insulating material is general enough for any construction that the author is aware of. On the other hand, if one were interested in determining the losses in the ferrite, its model would need to be generalized to include nonlinear hysteresis effects, complex permeability, and finite conductivity. Further discussion of these topics is included in the next section in relation to Maxwell's equations and in the following chapter when determining boundary conditions.

3.2 ELECTROMAGNETIC FIELD EQUATIONS

The scope of the treatment in this dissertation is limited to the winding portion of the transformer. Describing, understanding, and optimizing performance based on phenomena within the winding region involves the determination and manipulation of quantities such as the electromagnetic fields, current density, power dissipation, and stored energy.

Within the winding region, the insulating material has been defined such that it is lossless. In practice, the losses there are so small when compared to those in the conductors that the validity of this assumption is beyond reasonable doubt. Electromagnetic fields will, however, be present in these regions, and they will contribute to the energy stored in the winding. It will be seen later that the insulation layers will also play a role in determining the boundary conditions for the conductor layers. For these reasons, the insulating material is only of secondary importance. Its effects are simple and can be incorporated as needed in the process of analyzing the conductor layers. With this in mind, this effort will now focus on the analysis of the conductor layers.

The conducting regions are assumed to be isotropic, linear, and nonmagnetic; their macroscopic properties are described through the constitutive parameters:

ε_o = free-space permittivity = 8.854×10^{-12} [F/m] (3.2.1a)

μ_o = free-space permeability = $4\pi \times 10^{-7}$ [H/m] (3.2.1b)

σ = conductivity of copper = 5.7×10^{7} [S/m] (3.2.1c)

The conductivity for copper has been chosen because of its universal use in transformers of the type considered here. Other good conductors can be treated by simply substituting the appropriate value for the conductivity. The time-harmonic Maxwell's equations for the conducting regions are given by

$$\nabla \times \mathbf{E} = -j\omega\mathbf{B} \tag{3.2.2a}$$

$$\nabla \times \mathbf{H} = j\omega\mathbf{D} + \mathbf{J}, \tag{3.2.2b}$$

where the $e^{j\omega t}$ convention has been used in defining the phasor field quantities in boldface. The equation of continuity is

$$\nabla \cdot \mathbf{J} = 0 \tag{3.2.3}$$

since there can be no permanent distribution of free charge ($\rho = 0$) in regions with finite conductivity. The divergence relations

$$\nabla \cdot \mathbf{B} = 0 \tag{3.2.4a}$$

$$\nabla \cdot \mathbf{D} = 0 \tag{3.2.4b}$$

are also valid in the conductors. These equations are not independent of the curl and continuity equations, however, since they may be derived from them through the use of vector identities. The macroscopic properties in equations (3.2.1) for the conducting layers give rise to the following constitutive relationships:

$$\mathbf{D} = \varepsilon_o \mathbf{E} \qquad (3.2.5a)$$

$$\mathbf{B} = \mu_o \mathbf{H} \qquad (3.2.5b)$$

$$\mathbf{J} = \sigma \mathbf{E}. \qquad (3.2.5c)$$

Using these relationships, Maxwell's curl equations may be rewritten explicitly in terms of the magnetic field intensity H and current density J,

$$\nabla \times \mathbf{J} = -j\omega\mu_o\sigma\mathbf{H} \qquad (3.2.6a)$$

$$\nabla \times \mathbf{H} = (1 + j\frac{\omega\varepsilon_o}{\sigma})\mathbf{J}. \qquad (3.2.6b)$$

These equations can now be solved for J and H from which E, D, and B can be determined from the simple linear relationships in equations (3.2.5). The corresponding divergence relations become

$$\nabla \cdot \mathbf{H} = 0 \qquad (3.2.7a)$$

$$\nabla \cdot \mathbf{J} = 0. \qquad (3.2.7b)$$

The latter equation gives the same result as the equation of continuity which will therefore not be repeated. Further simplification of Maxwell's equations is still possible. Consider the second term on the right-hand side of equation (3.2.6b). This term is called the displacement current (it is perhaps more recognizable when written in terms of D or E), and it is widely known that it can usually be neglected in conducting regions. Mathematically, this condition is expressed by the requirement that

$$\frac{\omega \varepsilon_o}{\sigma} \ll 1. \qquad (3.2.8)$$

The only unknown quantity in this expression is frequency. So, rearranging and substituting the numerical values for the permittivity and conductivity given in equations (3.2.1a) and (3.2.1c) yields

$$f \ll \frac{\sigma}{2\pi\varepsilon_o} = \frac{5.7 \times 10^{7}}{2\pi \times 8.854 \times 10^{-12}} \approx 1 \times 10^{18} \text{ Hz.} \qquad (3.2.9)$$

This frequency lies in the lower portion of the X-ray band and corresponds to a wavelength of 3×10^{-10} m or 3 Å. Presently, the range of fundamental frequencies used in switched-mode power conversion technology ranges from the upper end of the audio band, about 20 kHz, to a few Mhz. While the current trend is toward higher switching frequencies, values approaching X-ray frequencies would not occur for years and would require a completely new technology. Obviously, transformers like those described here would be useless. Thus, it is seen that neglecting the displacement current is certainly valid for any application which could possibly use one of these transformers. Maxwell's curl and divergence equations have now been simplified as far as possible for the conducting regions under consideration and are summarized for convenience:

$$\nabla \times \mathbf{J} = -j\omega\mu_0\sigma\mathbf{H} \qquad (3.2.10a)$$

$$\nabla \times \mathbf{H} = \mathbf{J} \qquad (3.2.10b)$$

$$\nabla \cdot \mathbf{H} = 0 \qquad (3.2.10c)$$

$$\nabla \cdot \mathbf{J} = 0. \qquad (3.2.10d)$$

It is instructive for two reasons to pause at this point and derive the conservation of power equation, or Poynting's theorem. The first reason is because it takes on a somewhat unfamiliar and specfic form in a source-free conducting region. Secondly, several quantities which will be used extensively can be introduced in the process. Following the usual technique, scalar multiply equation (3.2.10a) by $\mathbf{H}^*$ and the conjugate of equation (3.2.10b) by J, and subtract these results to give

$$\nabla \cdot \frac{1}{2\sigma}(\mathbf{J} \times \mathbf{H}^*) + j2\omega\frac{1}{4}\mu_o |\mathbf{H}|^2 + \frac{1}{2\sigma}|\mathbf{J}|^2 = 0. \quad (3.2.11)$$

This is the point form of the conservation of power equation. The first term is the divergence of the complex Poynting vector

$$\mathbf{S} \doteq \frac{1}{2\sigma}(\mathbf{J} \times \mathbf{H}^*) \qquad [W/m^2] \qquad (3.2.12a)$$

which represents the volume density of complex power leaving a point. This quantity is more commonly expressed in terms of E rather than J since that is its more general definition. The second term is $j2\omega$ times the time-averaged magnetic energy density

$$w_m \doteq \frac{1}{4}\mu_o |\mathbf{H}|^2 \qquad [J/m^3] \qquad (3.2.12b)$$

which in the time domain corresponds to the time rate of change of the magnetic energy density. Notice that the similar term involving the electric energy density is absent from the equation, a result of neglecting the displacement current. The last term is directly recognizable as the time-averaged power dissipation density

$$p_d \doteq \frac{1}{2\sigma}|J|^2 \qquad [W/m^3]. \qquad (3.2.12c)$$

Substituting the definitions in equations (3.2.12) into Poynting's theorem results in the more concise form

$$\nabla \cdot S + j2\omega w_m + p_d = 0. \qquad (3.2.13)$$

The regional form of Poynting's theorem for a volume v bounded by a closed surface s is obtained by integrating equation (3.2.13) over the volume v and applying the divergence theorem to the first term. The result is

$$\iint_s S \cdot ds + j2\omega W_m + P_d = 0, \qquad (3.2.14)$$

where the first term is the complex power flowing out through the closed surface s,

$$W_m \doteq \frac{1}{2}\iiint_v \frac{1}{2}\mu_o |H|^2 dv \qquad [J] \qquad (3.2.15a)$$

is the time-averaged stored magnetic energy within the volume v, and

$$P_d = \frac{1}{2}\iiint_v \frac{1}{\sigma}|J|^2 dv \quad [W] \qquad (3.2.15b)$$

is the time-averaged power dissipated within the volume v.

As the final step in manipulating Maxwell's equations, it would be desirable to uncouple them such that each involves only a single quantity. Returning to equations (3.2.10), take the curl of equation (3.2.10b) and substitute equation (3.2.10a) into the right-hand side to obtain

$$\nabla \times \nabla \times \mathbf{H} = -j\omega\mu_o\sigma\mathbf{H}. \qquad (3.2.16a)$$

Reversing the roles of the same two equations and following the same process yields

$$\nabla \times \nabla \times \mathbf{J} = -j\omega\mu_o\sigma\mathbf{J}. \qquad (3.2.16b)$$

Thus, both the magnetic field intensity and the current density (D, E, and B also) satisfy the same vector equation. Only the boundary conditions will make each solution unique. Equations similar to those above are also derivable for non-conducting matter, and they are referred to as vector wave equations or vector Helmholtz equations. These

equations are of the same form except for one fundamental difference: here, the right-hand side contains only a single power of the frequency whereas the vector wave equation contains the square of the frequency. Thus, only the first derivative with respect to time appears in the equivalent time-domain equation while the second derivative appears in the corresponding vector wave equation. The terminology *vector diffusion equation* is therefore more appropriate and is adopted here in reference to equations (3.2.16). The methods of solution for these two classes of equations are identical for the time-harmonic case since they differ only by a complex constant. This difference, however, results in a radically different behavior in the solutions. The solutions of the vector diffusion equations (3.2.16) cannot be wave-type solutions.

Anticipating clearer interpretations of the solutions to follow, the usual high conductivity approximation for skin depth is introduced at this point,

$$\delta \doteq \sqrt{\frac{2}{\omega \mu_o \sigma}} \,. \qquad (3.2.17)$$

The vector diffusion equations can now be rewritten to include this parameter, yielding

$$\nabla \times \nabla \times \mathbf{H} = -j\frac{2}{\delta^2}\mathbf{H} \qquad (3.2.18a)$$

$$\nabla \times \nabla \times \mathbf{J} = -j\frac{2}{\delta^2}\mathbf{J}. \qquad (3.2.18b)$$

Although the analogy is not exact, the skin depth appears in the same place in the diffusion equation as the wavelength does in the wave equation, and it may be loosely interpreted in the same manner. Instead of being the length of the period of a traveling wave, the skin depth provides a measure of the rate of decay of the exponential type solutions of the diffusion equation.

The diffusion equations, along with their appropriate boundary conditions, ultimately govern the remainder of the analysis to be performed. Once solved, their solutions shall be studied and used to determine important characteristics such as power dissipation and stored energy in various types of transformer windings. Searches can then be conducted for techniques to optimize the design with respect to these characteristics. Expressions for other useful quantities, such as effective resistance and leakage inductance, will also be derived which will add to the understanding of the results and simplify experimental verification.

3.3 GENERAL TWO-DIMENSIONAL PROBLEM

The divergence and curl vector differential operators expressed in cylindrical coordinates for a general vector field $\mathbf{A}$ are

$$\nabla \cdot \mathbf{A} = \frac{1}{\rho}\frac{\partial(\rho A_\rho)}{\partial \rho} + \frac{1}{\rho}\frac{\partial A_\phi}{\partial \phi} + \frac{\partial A_z}{\partial z} \qquad (3.3.1a)$$

and

$$\nabla \times \mathbf{A} = \left[\frac{1}{\rho}\frac{\partial A_z}{\partial \phi} - \frac{\partial A_\phi}{\partial z}\right]\hat{\rho} + \left[\frac{\partial A_\rho}{\partial z} - \frac{\partial A_z}{\partial \rho}\right]\hat{\phi} + \frac{1}{\rho}\left[\frac{\partial(\rho A_\phi)}{\partial \rho} - \frac{\partial A_\rho}{\partial \phi}\right]\hat{z}. \qquad (3.3.1b)$$

In the previous section, the geometrical assumption of axial symmetry was made. There can therefore be no ϕ-dependence and the above vector differential operators simplify to

$$\nabla \cdot \mathbf{A}(\rho, z) = \frac{1}{\rho}\frac{\partial(\rho A_\rho)}{\partial \rho} + \frac{\partial A_z}{\partial z} \qquad (3.3.2a)$$

$$\nabla \times \mathbf{A}(\rho, z) = -\frac{\partial A_\phi}{\partial z}\hat{\rho} + \left[\frac{\partial A_\rho}{\partial z} - \frac{\partial A_z}{\partial \rho}\right]\hat{\phi} + \frac{1}{\rho}\frac{\partial(\rho A_\phi)}{\partial \rho}\hat{z}. \qquad (3.3.2b)$$

This assumption is the basis for the terminology *two-dimensional* since all quantities are, in general, a function of the two coordinates ρ and z.

Also a result of axial symmetry (see Figure 3.1.2), note that the conductor layers are solenoidally wound which implies only a $\hat{\phi}$-component for the current density; hence,

$$\mathbf{J} = J_{\phi}(\rho,z)\hat{\phi}. \tag{3.3.3}$$

Using this in equations (3.3.2) gives the following form of the vector differential operators for the current density:

$$\nabla \cdot \mathbf{J} = \nabla \cdot J_{\phi}(\rho,z)\hat{\phi} = 0 \tag{3.3.4a}$$

$$\nabla \times \mathbf{J} = \nabla \times J_{\phi}(\rho,z)\hat{\phi}$$

$$= -\frac{\partial}{\partial z}\left[J_{\phi}(\rho,z)\right]\hat{\rho} + \frac{1}{\rho}\frac{\partial}{\partial \rho}\left[\rho J_{\phi}(\rho,z)\right]\hat{z}. \tag{3.3.4b}$$

These results can now be compared to Maxwell's equations (3.2.10). The first result shows that the current density satisfies the divergence equation solely as a result of the geometrical assumptions, certainly an acceptable result. The second result implies that the magnetic field intensity has both radial and longitudinal components (from 3.2.10a),

$$\mathbf{H} = H_{\rho}(\rho,z)\hat{\rho} + H_{z}(\rho,z)\hat{z}. \tag{3.3.5}$$

The vector components and their functional dependence for the current density and magnetic field intensity have

now been determined for the general two-dimensional problem and are given in equations (3.3.3) and (3.3.5). Substituting these into equations (3.2.10) yields Maxwell's equations specialized to the two-dimensional case:

$$-\frac{\partial}{\partial z}\left[J_\phi(\rho,z)\right]\hat{\rho} + \frac{1}{\rho}\frac{\partial}{\partial\rho}\left[\rho J_\phi(\rho,z)\right]\hat{z}$$

$$= -j\frac{2}{\delta^2}H_\rho(\rho,z)\hat{\rho} - j\frac{2}{\delta^2}H_z(\rho,z)\hat{z} \qquad (3.3.6a)$$

$$\frac{\partial}{\partial z}\left[H_\rho(\rho,z)\right]\hat{\phi} - \frac{\partial}{\partial\rho}\left[H_z(\rho,z)\right]\hat{\phi} = J_\phi(\rho,z)\hat{\phi} \qquad (3.3.6b)$$

$$\frac{1}{\rho}\frac{\partial}{\partial\rho}\left[\rho H_\rho(\rho,z)\right] + \frac{\partial}{\partial z}\left[H_z(\rho,z)\right] = 0 \qquad (3.3.6c)$$

$$\frac{1}{\rho}\frac{\partial}{\partial\phi}\left[J_\phi(\rho,z)\right] = 0. \qquad (3.3.6d)$$

The uncoupled vector diffusion equation for the current density may be determined in a similar manner via equation (3.2.18b), yielding

$$\frac{\partial^2 J_\phi}{\partial\rho^2} + \frac{1}{\rho}\frac{\partial J_\phi}{\partial\rho} - \left[j\frac{2}{\delta^2} + \frac{1}{\rho^2}\right]J_\phi + \frac{\partial^2 J_\phi}{\partial z^2} = 0, \qquad (3.3.7)$$

where the notation has been simplified by dropping the independent variable arguments which are now understood from the context of the two-dimentional problem. Similarly, the vector diffusion equation (3.2.18a) for the magnetic field

intensity reduces to two coupled equations for the radial and longitudinal components,

$$\frac{\partial^2 H_\rho}{\partial z^2} - \frac{\partial^2 H_z}{\partial z \partial \rho} - j\frac{2}{\delta^2} H_\rho = 0 \qquad (3.3.8a)$$

$$\frac{\partial^2 H_z}{\partial \rho^2} - \frac{\partial^2 H_\rho}{\partial \rho \partial z} + \frac{1}{\rho}\frac{\partial H_z}{\partial \rho} - \frac{1}{\rho}\frac{\partial H_\rho}{\partial z} - j\frac{2}{\delta^2} H_z = 0. \qquad (3.3.8b)$$

This concludes the general statement of the two-dimensional problem. Given the appropriate boundary conditions, equations (3.3.7) and (3.3.8) can be solved and the analysis can continue. Although not pursued further here, one approach to the solution might proceed as follows. Use the separation of variables method to find the general solution to equation (3.3.7) for the current density. This solution will be in the form of a summation of eigenfunctions which span the two-dimensional space. The corresponding solutions for the radial and longitudinal components of the magnetic field intensity can then be determined from the simple derivatives in equation (3.3.6a). Suitable boundary conditions must then be enforced to solve for the arbitrary weighting constants in the summation and the eigenvalues or separation constants.

The approach outlined above is certainly possible and not overly difficult. The author has found, however, that

simplification to a one-dimensional model provides much more insight while sacrificing little generality and accuracy for the applications interested in here. It is the logical first step in developing a fundamental understanding of the basic phenomena. In addition, the one-dimensional simplification makes the generalization to arbitrary periodic waveforms (to be considered later) much more tractable. Making that generalization in the two-dimensional problem would introduce Fourier analysis into an already complicated and unrevealing solution. Subsequent evaluations would therefore involve endless studies of computer results, and there would be little hope of visualizing and understanding the problem in a fundamental way from simple observation of the solutions.

Before abandoning the two-dimensional model, one further comment is appropriate. It will be seen later that there are indeed limitations of the one-dimensional model which the two-dimensional model could possibly resolve. These limitations are second order effects for most present applications, but that may change in the future. The abandonment is therefore temporary and further work is planned in the future.

The one-dimensional model is introduced in the next section along with the assumptions necessary for its use. The remainder of the work in this dissertation employs this

work exclusively. As will be seen, even the solutions resulting from this model require extensive use of a computer . There are, however, several approximations possible which greatly simplify the solutions and enhance the basic understanding of them.

3.4 ONE-DIMENSIONAL SIMPLIFICATION

The one-dimensional simplification results from longitudinal assumptions in addition to the axial symmetry of the two-dimensional model. In particular, the insulation and conductor layers are assumed to be wound uniformly in the z-direction. Also, the solenoidal coils formed by these layers are assumed to be long enough to ignore end effects. The result of these assumptions is that physical quantities will no longer exhibit longitudinal variation.

Having a physically long winding is not the only condition which contributes to this simplification. The existence of the high permeability ferrite core surrounding the winding enhances its validity also. The reason for this is the tendency for the magnetic fields exterior to the ferrite to be normal to its surface, resulting in a predominantly longitudinally directed magnetic field. From equation (3.3.6a) it is seen that longitudinal variation in the current density cannot be supported without a radially directed magnetic field. This effect is discussed further

in the first section of the next chapter on boundary conditions.

Paralleling the development in the previous section, the divergence and curl vector differential operators for a general vector field $\mathbf{A}$ under the one-dimensional assumptions are given by

$$\nabla \cdot \mathbf{A}(\rho) = \frac{1}{\rho}\frac{\partial(\rho A_\rho)}{\partial \rho} \tag{3.4.1a}$$

$$\nabla \times \mathbf{A}(\rho) = -\frac{\partial A_z}{\partial \rho}\hat{\phi} + \frac{1}{\rho}\frac{\partial(\rho A_\phi)}{\partial \rho}\hat{z}, \tag{3.4.1b}$$

where only the radial dependence remains. The current density and magnetic field intensity are now expressed simply as

$$\mathbf{J} = J_\phi(\rho)\hat{\phi} \tag{3.4.2a}$$

$$\mathbf{H} = H_z(\rho)\hat{z}. \tag{3.4.2b}$$

Note that there is no longer a radial component of the magnetic field intensity. Using these expressions in equations (3.2.10) further simplifies Maxwell's equations to

$$\frac{1}{\rho}\frac{\partial}{\partial \rho}\left[\rho J_\phi(\rho)\right]\hat{z} = -j\frac{2}{\delta^2}H_z(\rho)\hat{z} \tag{3.4.3a}$$

$$-\frac{\partial}{\partial\rho}\left[H_z(\rho)\right]\hat{\phi} = J_\phi(\rho)\hat{\phi} \qquad (3.4.3b)$$

$$\frac{\partial}{\partial z}\left[H_z(\rho)\right] = 0 \qquad (3.4.3c)$$

$$\frac{1}{\rho}\frac{\partial}{\partial\phi}\left[J_\phi(\rho)\right] = 0, \qquad (3.4.3d)$$

where both of the divergence relations are now satisfied as a result of the geometrical assumptions. The vector diffusion equations are found in a similar manner by using the relations in (3.4.2) in equations (3.2.18),

$$\rho^2\frac{\partial^2 H_z}{\partial\rho^2} + \rho\frac{\partial H_z}{\partial\rho} - j2\frac{\rho^2}{\delta^2}H_z = 0 \qquad (3.4.4a)$$

$$\rho^2\frac{\partial^2 J_\phi}{\partial\rho^2} + \rho\frac{\partial J_\phi}{\partial\rho} - \left[j2\frac{\rho^2}{\delta^2} + 1\right]J_\phi = 0. \qquad (3.4.4b)$$

The radial dependence of these quantities is now understood and has been eliminated to simplify the notation. Completely uncoupled one-dimensional second order differential equations have now been derived for the current density and magnetic field intensity. They may both be solved separately, or either one may be solved and equations (3.4.3a) and (3.4.3b) used to find the undetermined quantity.

In order to put equations (3.4.4) into a more recognizable form, the independent variable substitution

$$x \doteq \sqrt{2}\frac{\rho}{\delta} \tag{3.4.5}$$

is introduced, yielding

$$x^2\frac{\partial^2 H_z}{\partial x^2} + x\frac{\partial H_z}{\partial x} - jx^2 H_z = 0 \tag{3.4.6a}$$

$$x^2\frac{\partial^2 J_\phi}{\partial x^2} + x\frac{\partial J_\phi}{\partial x} - \left[jx^2 + 1\right]J_\phi = 0. \tag{3.4.6b}$$

Both of these equations are examples of a special form of Bessel's differential equation due to Lord Kelvin. The general solutions are given by

$$H_z(x) = A_0(\mathrm{ber}_0 x + j\mathrm{bei}_0 x) + B_0(\mathrm{ker}_0 x + j\mathrm{kei}_0 x) \tag{3.4.7a}$$

$$J_\phi(x) = A_1(\mathrm{ber}_1 x + j\mathrm{bei}_1 x) + B_1(\mathrm{ker}_1 x + j\mathrm{kei}_1 x). \tag{3.4.7b}$$

These solutions are collectively referred to as Kelvin functions. More specifically, ber and bei are Kelvin functions of the first kind, and ker and kei are Kelvin functions of the second kind. The subscripts indicate the

order which for here is either zero or one. A_0, B_0, A_1, and B_1 are arbitrary complex coefficients which must be determined from boundary conditions to give the particular solutions. An appendix is provided, Appendix B, which deals exclusively with Kelvin functions. If unfamiliar with them, the reader is strongly urged to review this appendix. Many properties of the Kelvin functions which will be used extensively are included such as recurrence relations, indefinite integrals, and large argument asymptotic approximations.

Before continuing with the determination of the particular solutions of equations (3.4.6), two very useful relationships between the arbitrary complex coefficients of the two general solutions are derived. The procedure involves substituting the general solutions in equations (3.4.7) into equation (3.4.3b), employing the recurrence relations (B.2.3), and reducing the result to

$$A_1 = -\frac{(1-j)}{\delta}A_0 \qquad (3.4.8a)$$

$$B_1 = -\frac{(1-j)}{\delta}B_0. \qquad (3.4.8b)$$

CHAPTER 4

SOLUTION OF THE SINGLE-LAYER PROBLEM

The particular solutions for the current density and magnetic field intensity in a single conductor layer are derived and examined in this chapter. The single-layer problem is the most basic one to be considered, upon which the generalizations to multiple layer windings and arbitrary periodic waveforms will be made.

The first section contains a general discussion of the behavior of magnetic fields at the boundary between a high permeability ferrite and a nonmagnetic medium. Boundary conditions for a single conductor layer are derived and then applied to the general solutions obtained in the previous chapter. The resulting particular solutions are studied in detail, and the effects of varying several different parameters are examined. Two successive approximations are then introduced: the large argument asymptotic approximation and the thin-layer approximation. Both of these approximations are also examined thoroughly, and the conditions under which each is valid are considered.

4.1 BOUNDARY CONDITIONS

Consider the boundary between a high permeability ferrite ($\mu_1 \gg \mu_o$) and a nonmagnetic medium ($\mu_2 = \mu_o$) depicted in Figure 4.1.1. For the purposes of this illustration, the ferrite permeability is assumed to be real and constant, and both media are assumed to have finite conductivities. The subscript 1 denotes the ferrite region for which B_{t1} and H_{t1} are the tangential fields, B_{n1} and H_{n1} the normal fields, B_1 and H_1 the corresponding magnitudes, and α_1 the angle between the fields and a line normal to the boundary. The subscript 2 denotes similarly defined quantities in the nonmagnetic region: B_{t2}, H_{t2}, B_{n2}, H_{n2}, B_2, H_2, and α_2. Boundary conditions for this type of interface require continuity of both the tangential magnetic field intensities and the normal magnetic flux densities, which are mathematically expressed as

$$H_{t1} = H_{t2} \tag{4.1.1a}$$

$$B_{n1} = B_{n2} \tag{4.1.1b}$$

or, equivalently, as

$$H_1 \sin\alpha_1 = H_2 \sin\alpha_2 \tag{4.1.2a}$$

$$B_1 \cos\alpha_1 = B_2 \cos\alpha_2 . \tag{4.1.2b}$$

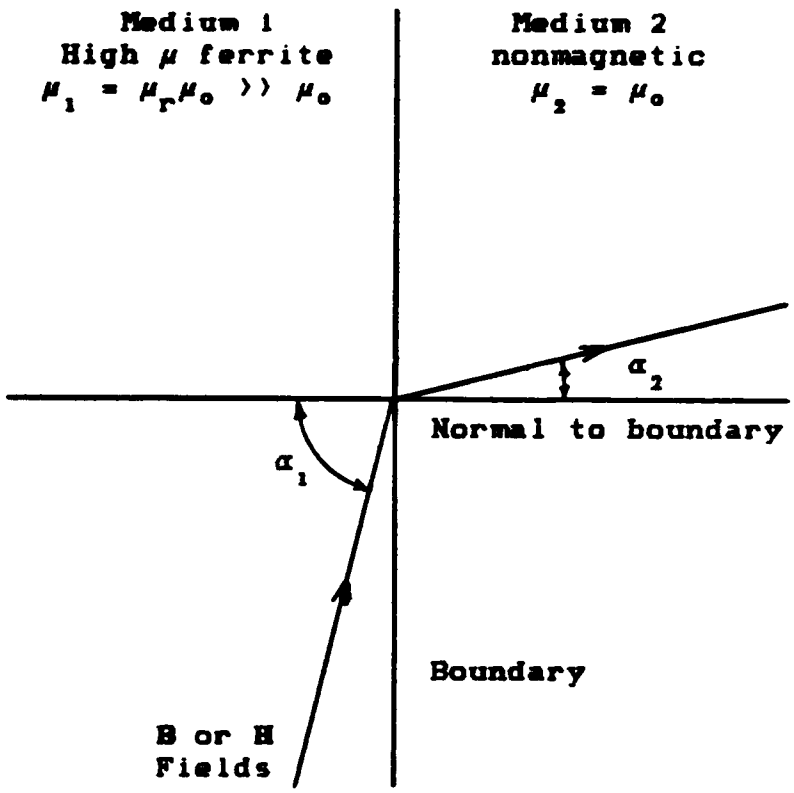

Figure 4.1.1. Boundary between a high permeability ferrite and a nonmagnetic medium.

From these equations and the constitutive relationships

$$B_1 = \mu_1 H_1 = \mu_r \mu_o H_1 \qquad (4.1.3a)$$

$$B_2 = \mu_2 H_2 = \mu_o H_2, \qquad (4.1.3b)$$

the following expression relating the angles of incidence of the fields is easily derived:

$$\tan\alpha_1 = \mu_r \tan\alpha_2. \qquad (4.1.4)$$

μ_r is the relative permeability of the ferrite. A typical value for this quantity for ferrites used in switched-mode power converters is about 3000. Used in the above equation, this large value suggests a tendency for either α_1 to be near $\pi/2$ or α_2 to be near zero, or both. For example, if $\alpha_1 = 89°$, then $\alpha_2 = 1.09°$. Even for an almost grazing incidence in the ferrite of $\alpha_1 = 89.9°$, the fields in the nonmagnetic medium are nearly normal to the boundary with $\alpha_2 = 10.8°$. Another useful relationship may easily be derived from equations (4.1.1), (4.1.2), and (4.1.3) which relates the magnitudes of magnetic field intensity in the two regions:

$$H_2 = H_1\sqrt{1 + (\mu_r^2 - 1)\cos^2\alpha_1} \approx H_1 \mu_r \cos\alpha_1, \qquad (4.1.5)$$

where the latter approximation is valid for $\mu_r \gg 1$. Using the same numbers as in the examples above; $H_2 = 52.4H_1$ when $\alpha_1 = 89°$, and $H_2 = 5.3H_1$ when $\alpha_1 = 89.9°$. So, the general tendency is for the magnetic field intensity to emerge from a high permeability ferrite into a nonmagnetic region normal to the boundary and larger in magnitude. This behavior becomes more pronounced as the permeability of the ferrite increases. The following discussion of boundary conditions for the single-layer case uses the results of this behavior.

Consider now the single-layer problem as shown in Figure 4.1.2. This is a magnified view of the *n*th layer of a winding corresponding to the cross-sectional representation in Figure 3.1.2. In addition to the geometrical assumptions made in the last chapter, the following are also made with respect to the single-layer problem and Figure 4.1.2:

- The magnetic field intensity within the ferrite core is assumed to be uniform with magnitude H_f and oriented as shown in Figure 4.1.2.
- The relative permeability of the ferrite is assumed to be large enough so that the behavior mentioned above is displayed at the ferrite-to-nonmagnetic (both insulating and conducting regions of the winding) boundaries. Namely, it emerges normal to the ferrite and higher in magnitude.

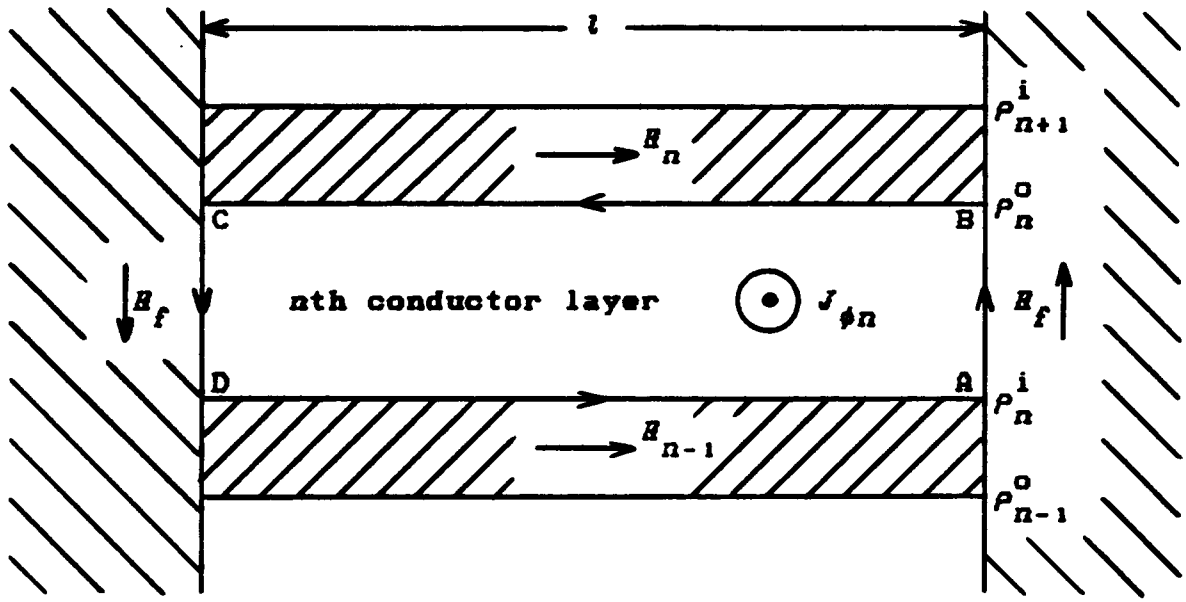

Figure 4.1.2. Magnified view of the nth conductor layer geometry corresponding to the cross-sectional representation of a typical high frequency power transformer shown in Figure 3.1.2.

- The length l of the winding is assumed to be large compared to the radial thickness of the insulating and conducting layers.
- The magnetic field intensity in the insulating layers is assumed to be uniform and referenced as shown in Figure 4.1.2.

It should now be evident why the presence of the ferrite enhances the conditions necessary for the one-dimensional approximation.

Following the notation in Figures 3.1.2 and 4.1.2, the magnetic field intensity at the boundary of the nth conductor layer and within the nth insulation layer is

$$\mathbf{H} = H_n \hat{\mathbf{z}};\ \rho_n^o \le \rho \le \rho_{n+1}^i;\ n = 0,1,2,\ldots,N, \qquad (4.1.6)$$

where H_0 corresponds to the inner boundary of the total winding as well as the first layer. Note that the fields are uniform in the insulation layers. This is the result of assuming that the insulation layers have zero conductivity; consequently, only displacement currents exist which are much smaller in magnitude than the conduction currents in the conductor layers. Also, the wavelength in the insulation layers is many orders of magnitude larger than the radial thickness of the layers.

The boundary conditions may now be related to the total current in the conductor layers through the use of Ampere's law around the closed path ABCDA surrounding the nth layer

$$\oint \mathbf{H} \cdot d\mathbf{l} = I_n, \tag{4.1.7}$$

where I_n is the total positive $\hat{\phi}$-directed current in the nth conductor layer passing through the surface defined by the closed path ABCDA. In terms of the current density, I_n may be expressed by the simple integral

$$I_n = \iint_S \mathbf{J} \cdot d\mathbf{s} = \int_{-l/2}^{+l/2} dz \int_{\rho_n^i}^{\rho_n^o} J_{\phi n}(\rho) d\rho \tag{4.1.8}$$

or, alternatively, as

$$I_n = l \int_{\rho_n^i}^{\rho_n^o} J_{\phi n}(\rho) d\rho \doteq l K_n, \tag{4.1.9}$$

where K_n is defined as current per unit axial length in the nth conductor layer. Turning now to the left side of equation (4.1.7), the closed path integral can be expanded and simplified as follows:

$$\oint \mathbf{H} \cdot d\mathbf{l} = \int_{\rho_n^i}^{\rho_n^o} H_f d\rho + \int_{+l/2}^{-l/2} H_n dz - \int_{\rho_n^o}^{\rho_n^i} H_f d\rho + \int_{-l/2}^{+l/2} H_{n-1} dz$$

$$= 2H_f \tau_n - lH_n + lH_{n-1}$$

$$\approx l(H_{n-1} - H_n) \,, \qquad (4.1.10)$$

where τ_n is defined to be the thickness of the nth conductor layer

$$\tau_n \doteq \rho_n^o - \rho_n^i. \qquad (4.1.11)$$

The terms resulting from the line integrals within the ferrite may be neglected because of the assumption of a long solenoid and the fact that the magnetic field intensity is much larger in the winding region. The latter is especially true for transformers which are nearly ideal since they have a very large magnetizing inductance and correspondingly small magnetizing current relative to the load current. Under these conditions, the fields in the ferrite core are determined by the magnetizing current, and those in the winding regions are determined by the much larger load currents. For an inductor, which can also usually be treated by the analysis here, the situation is somewhat different. The magnetizing and load current are one and the same; consequently, the magnetic field intensity in the

winding region will be of the same order of magnitude as it is in the ferrite. Thus, the assumption of a long solenoid becomes more important in the simplification of equation (4.1.10) for an inductor. It is worth noting that the situation just described for an inductor does not contradict the discussion at the beginning of this section concerning the behavior of the magnetic field intensity at a ferrite-to nonmagnetic boundary. The smaller differences in magnitude can be resolved through appropriate angles of incidence or a lower permeability which is typically the case for inductors.

The simplifications obtained in equations (4.1.9) and (4.1.10) may be substituted back into Ampere's law (4.1.7) to yield

$$H_n - H_{n-1} = -K_n = -\frac{I_n}{l}. \qquad (4.1.12)$$

It is important to remember that the magnetic field intensity is referenced to the positive $\hat{z}$-direction and that the current density is referenced to the positive $\hat{\phi}$-direction. Thus, if the magnetic field intensity at the outer boundary H_n is more positive than that at the inner boundary H_{n-1}, then the net current flow will be in the negative $\hat{\phi}$-direction.

4.2 PARTICULAR SOLUTIONS

First, the particular solution for the magnetic field intensity in the nth conductor layer is considered since the necessary boundary conditions have already been determined. The general solution under the one-dimensional simplification is given in equation (3.4.7a) and is repeated here,

$$H_{zn}(x) = A_{0n}(\mathrm{ber}_0 x + j\,\mathrm{bei}_0 x) + B_{0n}(\mathrm{ker}_0 x + j\,\mathrm{kei}_0 x); \quad (4.2.1)$$

where the subscript n has been added to denote the nth conductor layer, and the independent variable x is defined as in equation (3.4.5)

$$x = \sqrt{2}\frac{\rho}{\delta}, \quad (4.2.2)$$

and the skin depth δ by equation (3.2.17). Note that x is a unitless quantity. Boundary conditions from equations (4.1.6) for the single-layer problem can also be written in this form:

$$H_{zn}(x_n^i) = H_{n-1}; \; n = 1,2,\ldots,N \quad (4.2.3a)$$

$$H_{zn}(x_n^o) = H_n \; ; \; n = 1,2,\ldots,N, \quad (4.2.3b)$$

where the transformed inner and outer boundary radii satisfy equation (4.2.2) also. Applying these boundary conditions to the general solution produces a system of two equations which must be solved for the two arbitrary constants A_{0n} and B_{0n}. The resulting particular solution for the nth conductor layer is

$$E_{zn}(x) = A_{0n}(\mathrm{ber}_0 x + j\,\mathrm{bei}_0 x) + B_{0n}(\mathrm{ker}_0 x + j\,\mathrm{kei}_0 x);$$

$$x_n^i \le x \le x_n^o;\ n = 1,2,\ldots,N, \qquad (4.2.4)$$

where

$$A_{0n} = \frac{H_n(\mathrm{ker}_0 x_n^i + j\,\mathrm{kei}_0 x_n^i) - H_{n-1}(\mathrm{ker}_0 x_n^o + j\,\mathrm{kei}_0 x_n^o)}{\left[(\mathrm{ber}_0 x_n^o + j\,\mathrm{bei}_0 x_n^o)(\mathrm{ker}_0 x_n^i + j\,\mathrm{kei}_0 x_n^i) - (\mathrm{ber}_0 x_n^i + j\,\mathrm{bei}_0 x_n^i)(\mathrm{ker}_0 x_n^o + j\,\mathrm{kei}_0 x_n^o)\right]} \qquad (4.2.5a)$$

$$B_{0n} = \frac{H_{n-1}(\mathrm{ber}_0 x_n^o + j\,\mathrm{bei}_0 x_n^o) - H_n(\mathrm{ber}_0 x_n^i + j\,\mathrm{bei}_0 x_n^i)}{\left[(\mathrm{ber}_0 x_n^o + j\,\mathrm{bei}_0 x_n^o)(\mathrm{ker}_0 x_n^i + j\,\mathrm{kei}_0 x_n^i) - (\mathrm{ber}_0 x_n^i + j\,\mathrm{bei}_0 x_n^i)(\mathrm{ker}_0 x_n^o + j\,\mathrm{kei}_0 x_n^o)\right]}. \qquad (4.2.5b)$$

These solutions are easily verified by checking to see that the boundary conditions are satisfied.

The particular solution for the current density in the nth conductor layer can now be found by employing Maxwell's curl equation (3.4.3b) for the one-dimensional case. This tedious work has already been done, however, and it resulted in the simple relationships between arbitrary constants given in equations (3.4.8). The solution is therefore simply

$$J_{\phi n}(x) = A_{1n}(\mathrm{ber}_1 x + j\,\mathrm{bei}_1 x) + B_{1n}(\mathrm{ker}_1 x + j\,\mathrm{kei}_1 x);$$

$$x_n^i \le x \le x_n^o;\ n = 1,2,\ldots,N, \qquad (4.2.6)$$

where

$$A_{1n} = -\frac{(1-j)}{\delta} A_{0n} \qquad (4.2.7a)$$

$$B_{1n} = -\frac{(1-j)}{\delta} B_{0n}. \qquad (4.2.7b)$$

The particular solutions for the magnetic field intensity and current density in a single layer have now been determined. They are exact within the context of the one-dimensional problem. For reasons that will become more apparent later, it is appropriate to rearrange these solutions slightly in order to introduce normalized, unitless quantities. This will facilitate the presentation of graphical results as well as make the results more

universally applicable. Let $\tilde{\rho}$ denote the unitless radial coordinate normalized to a skin depth:

$$\tilde{\rho} \triangleq \frac{\rho}{\delta}. \qquad (4.2.8)$$

The tilde notation is used throughout this dissertation for normalized, unitless quantities. In all cases when distances are involved, the tilde represents the same quantity except normalized to a skin depth. The previously defined variable x can therefore be written as

$$x = \sqrt{2\tilde{\rho}}. \qquad (4.2.9)$$

Normalization is also convenient for the magnetic field intensity; let

$$H_{zn}(x) \triangleq (H_n - H_{n-1})\tilde{H}_{zn}(x) = -K_n\tilde{H}_{zn}(x). \qquad (4.2.10)$$

The normalized magnetic field intensity $\tilde{H}_{zn}(x)$ is also unitless. It is normalized with respect to the current per unit length (or linear current density) which flows in the conductor layer. The negative sign is a result of the reference directions chosen for the fields and currents. Comparing equation (4.2.10) and equations (4.2.4) and (4.2.5), and introducing the definition for the ratio of boundary conditions

$$\Gamma_n \doteq \frac{H_{n-1}}{H_n}, \qquad (4.2.11)$$

yields the following final form for the normalized magnetic field intensity:

$$\tilde{H}_{zn}(x) = \frac{1}{1-\Gamma_n}\left[\tilde{A}_{0n}(\mathrm{ber}_0 x + j\,\mathrm{bei}_0 x) + \tilde{B}_{0n}(\mathrm{ker}_0 x + j\,\mathrm{kei}_0 x)\right];$$

$$x_n^i \le x \le x_n^o;\ n = 1,2,\ldots,N, \qquad (4.2.12)$$

where

$$\tilde{A}_{0n} = \frac{(\mathrm{ker}_0 x_n^i + j\,\mathrm{kei}_0 x_n^i) - \Gamma_n(\mathrm{ker}_0 x_n^o + j\,\mathrm{kei}_0 x_n^o)}{\left[(\mathrm{ber}_0 x_n^o + j\,\mathrm{bei}_0 x_n^o)(\mathrm{ker}_0 x_n^i + j\,\mathrm{kei}_0 x_n^i) - (\mathrm{ber}_0 x_n^i + j\,\mathrm{bei}_0 x_n^i)(\mathrm{ker}_0 x_n^o + j\,\mathrm{kei}_0 x_n^o)\right]} \qquad (4.2.13a)$$

$$\tilde{B}_{0n} = \frac{\Gamma_n(\mathrm{ber}\ x_n^o + j\,\mathrm{bei}\ x_n^o) - (\mathrm{ber}_0 x_n^i + j\,\mathrm{bei}_0 x_n^i)}{\left[(\mathrm{ber}_0 x_n^o + j\,\mathrm{bei}_0 x_n^o)(\mathrm{ker}_0 x_n^i + j\,\mathrm{kei}_0 x_n^i) - (\mathrm{ber}_0 x_n^i + j\,\mathrm{bei}_0 x_n^i)(\mathrm{ker}_0 x_n^o + j\,\mathrm{kei}_0 x_n^o)\right]} \qquad (4.2.13b)$$

A similar procedure can be followed for the current density. In this case, the normalization is with respect to a uniform current density which is determined as if the radial thickness were one skin depth:

$$J_{\phi n}(x) \doteq \frac{(H_n - H_{n-1})}{\delta} \tilde{J}_{\phi n}(x) = -\frac{K_n}{\delta} \tilde{J}_{\phi n}(x). \qquad (4.2.14)$$

Comparing this with equations (4.2.6) and (4.2.7), and using the results just obtained during the normalization process of the magnetic field intensity yields

$$\tilde{J}_{\phi n}(x) = \frac{1}{1-\Gamma_n}\left[\tilde{A}_{1n}(\mathrm{ber}_1 x + j\,\mathrm{bei}_1 x) + \tilde{B}_{1n}(\mathrm{ker}_1 x + j\,\mathrm{kei}_1 x)\right];$$

$$x_n^i \le x \le x_n^o;\ n = 1,2,\ldots,N, \qquad (4.2.15)$$

where

$$\tilde{A}_{1n} = -(1-j)\tilde{A}_{0n} \qquad (4.2.16a)$$

$$\tilde{B}_{1n} = -(1-j)\tilde{B}_{0n}. \qquad (4.2.16a)$$

A detailed study of the magnetic field intensity and current density is now possible. Formulas from [55] have been employed for the Kelvin functions in a computer program which calculates the normalized quantities defined above. The results will be plotted versus the normalized radial coordinate $\tilde{\rho}$. There are three parameters which may be varied: $\tilde{\rho}_n^i$, $\tilde{\rho}_n^o$, and Γ_n. Remember that the corresponding boundary radii in the expressions appear in terms of x which is related to $\tilde{\rho}$ by the proportionality constant $\sqrt{2}$. For the

purpose of these numerical studies, it is much easier to understand the results if the normalized inner and outer boundary radii $\tilde{\rho}_n^i$ and $\tilde{\rho}_n^o$ are transformed into the equivalent pair

$$\tilde{\rho}_n \doteq \frac{1}{2}(\tilde{\rho}_n^o + \tilde{\rho}_n^i) \qquad (4.2.17a)$$

$$\tilde{\tau}_n \doteq \tilde{\rho}_n^o - \tilde{\rho}_n^i. \qquad (4.2.17b)$$

$\tilde{\rho}_n$ is simply the mean normalized radius of the nth layer, i.e. the radial distance from the z-axis to the center of the layer. τ_n is the normalized radial thickness of the nth conductor layer. Reversing this transformation results in the equivalent relations

$$\tilde{\rho}_n^i = \tilde{\rho}_n - \frac{1}{2}\tilde{\tau}_n \qquad (4.2.18a)$$

$$\tilde{\rho}_n^o = \tilde{\rho}_n + \frac{1}{2}\tilde{\tau}_n. \qquad (4.2.18b)$$

Similar formulas for the actual distances are obtained by simply removing the tildes from the equations above.

Figures 4.2.1 through 4.2.12 present the results of the computations for the current density and magnetic field intensity in the single-layer case. Normalized quantities are used throughout these results. The independent

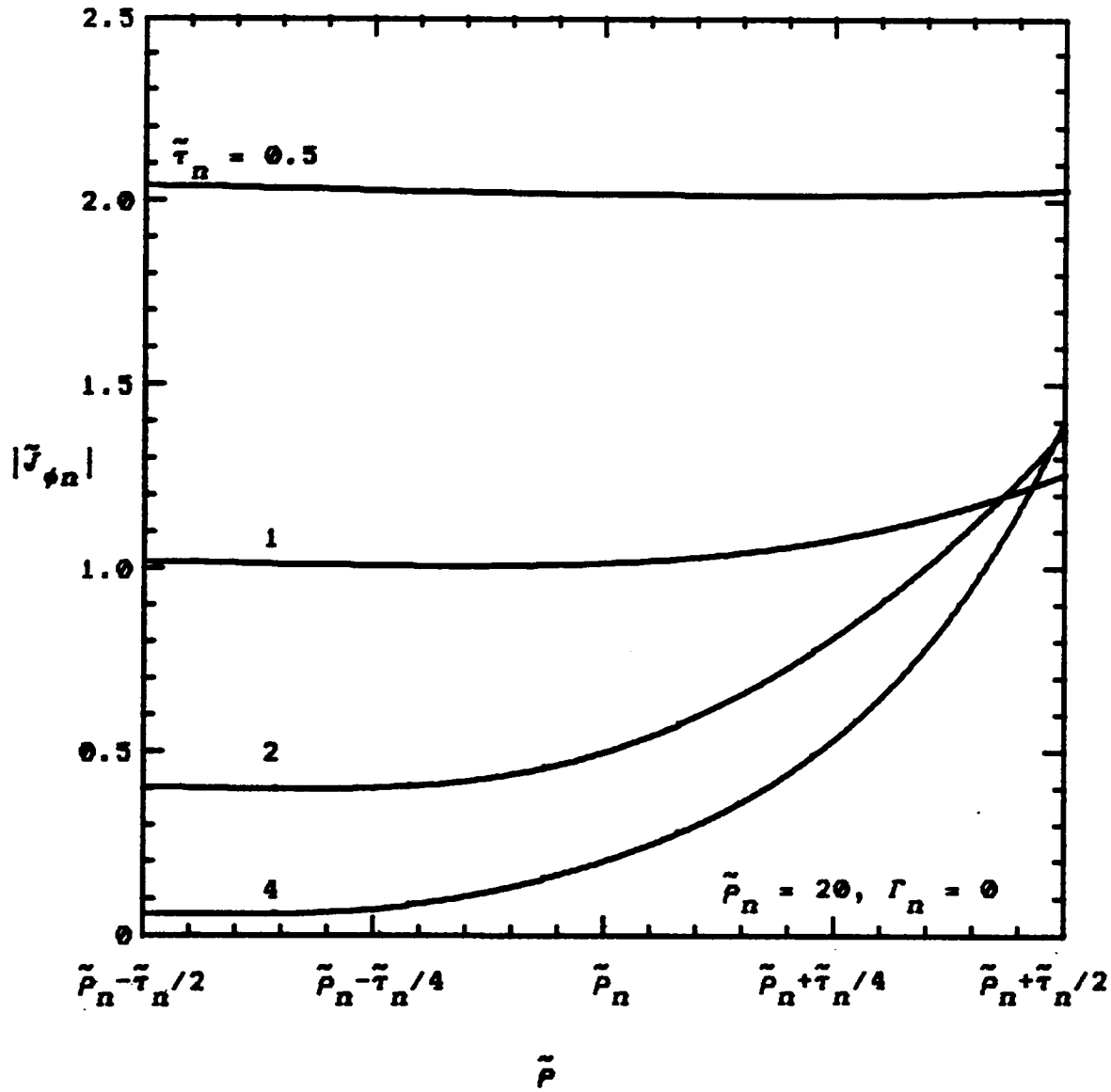

Figure 4.2.1. Magnitude of the normalized current density vs. the normalized radial distance in the nth conductor layer with the normalized conductor thickness varied as a parameter.

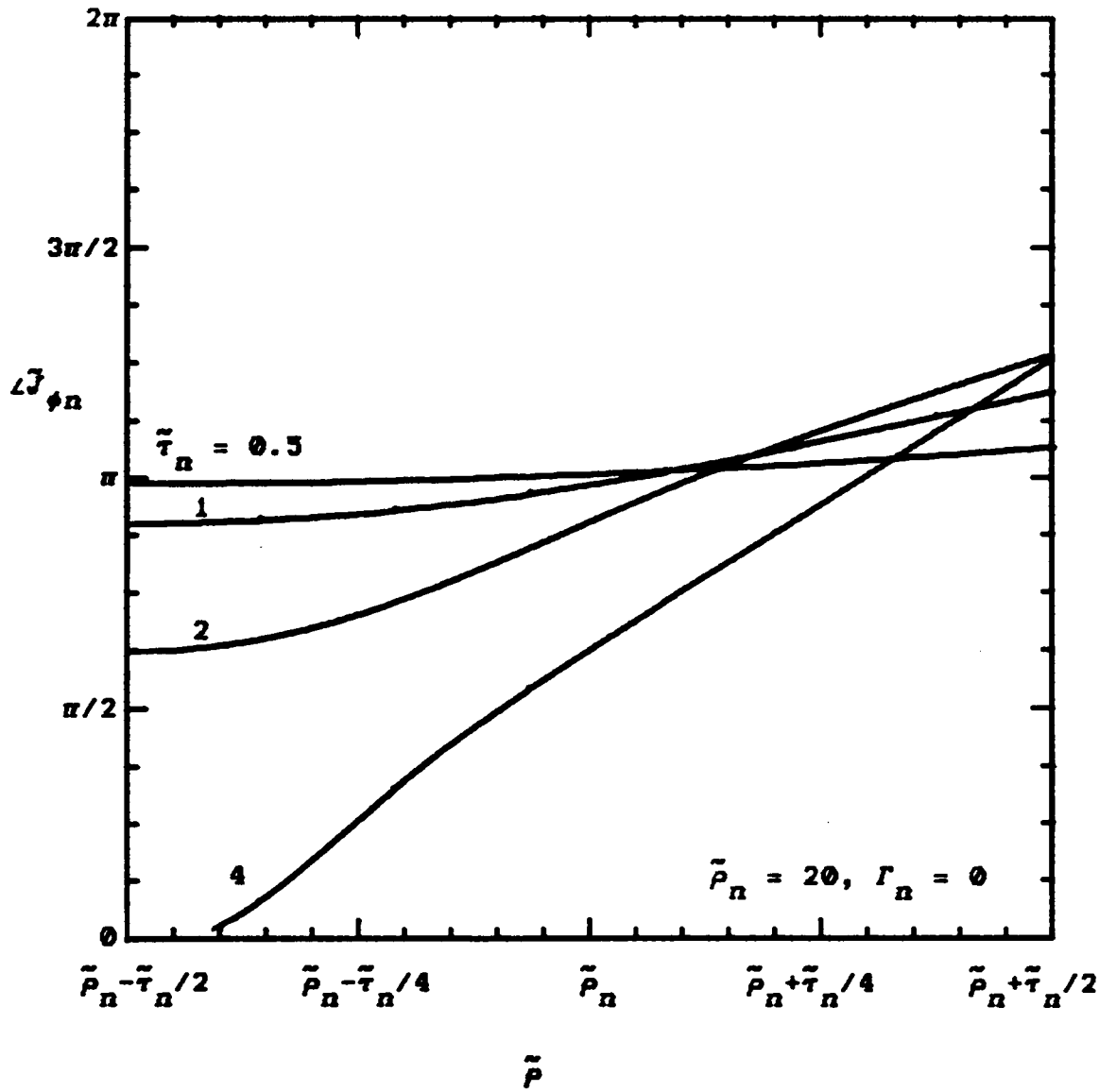

Figure 4.2.2. Phase of the normalized current density vs. the normalized radial distance in the nth conductor layer with the normalized conductor thickness varied as a parameter.

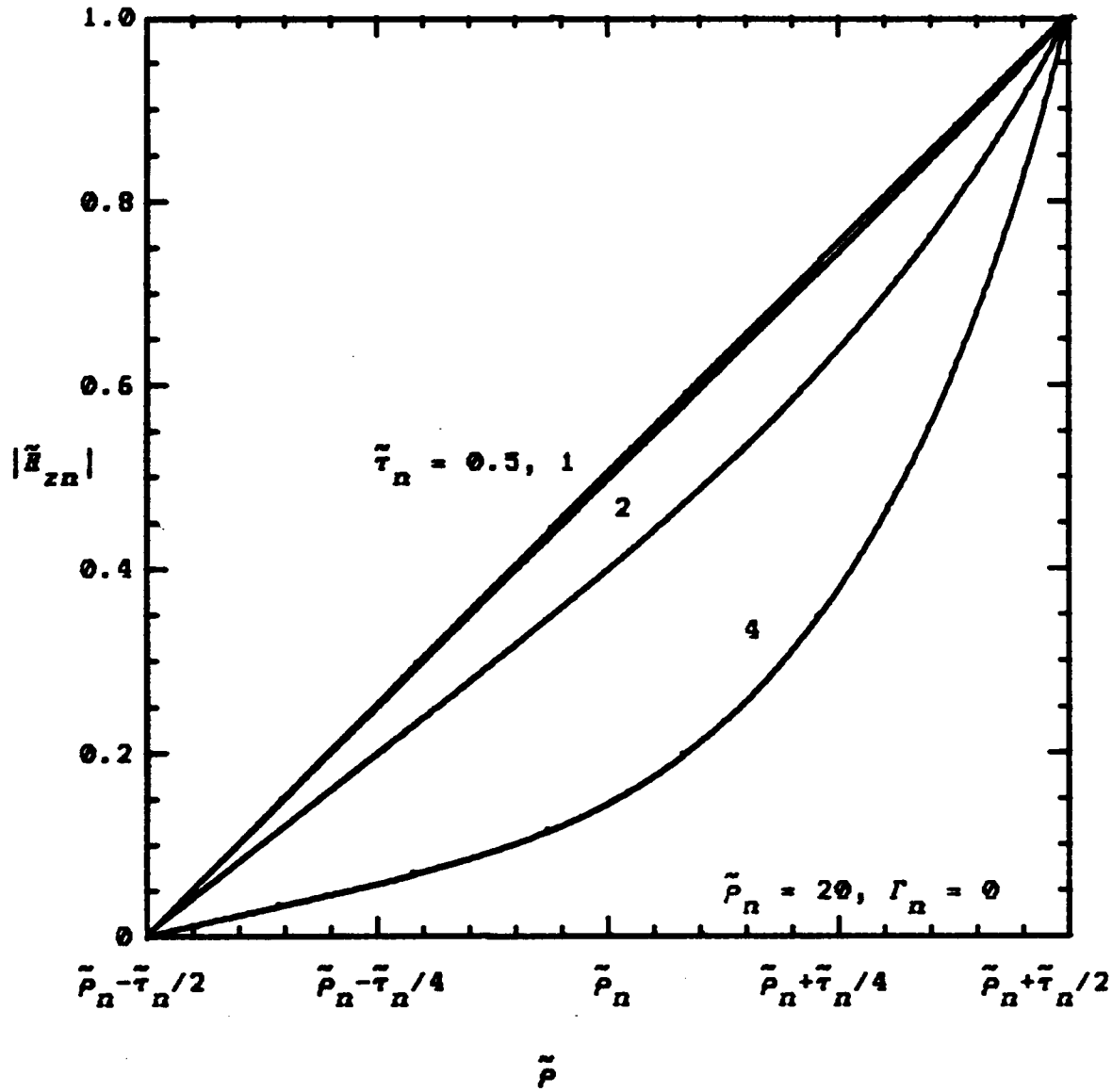

Figure 4.2.3. Magnitude of the normalized magnetic field intensity vs. the normalized radial distance in the nth conductor layer with the normalized conductor thickness varied as a parameter.

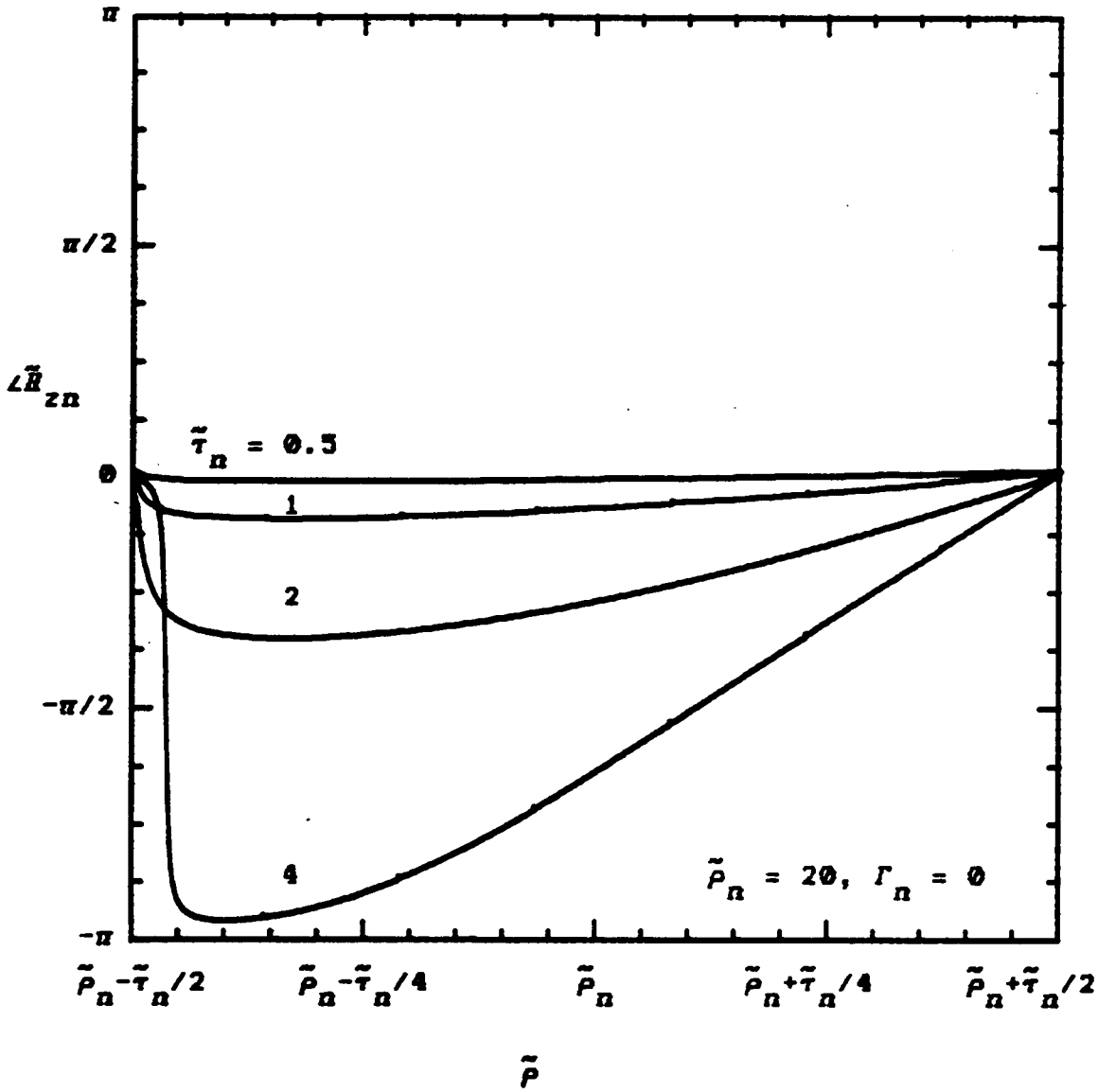

Figure 4.2.4. Phase of the normalized magnetic field intensity vs. the normalized radial distance in the nth conductor layer with the normalized conductor thickness varied as a parameter.

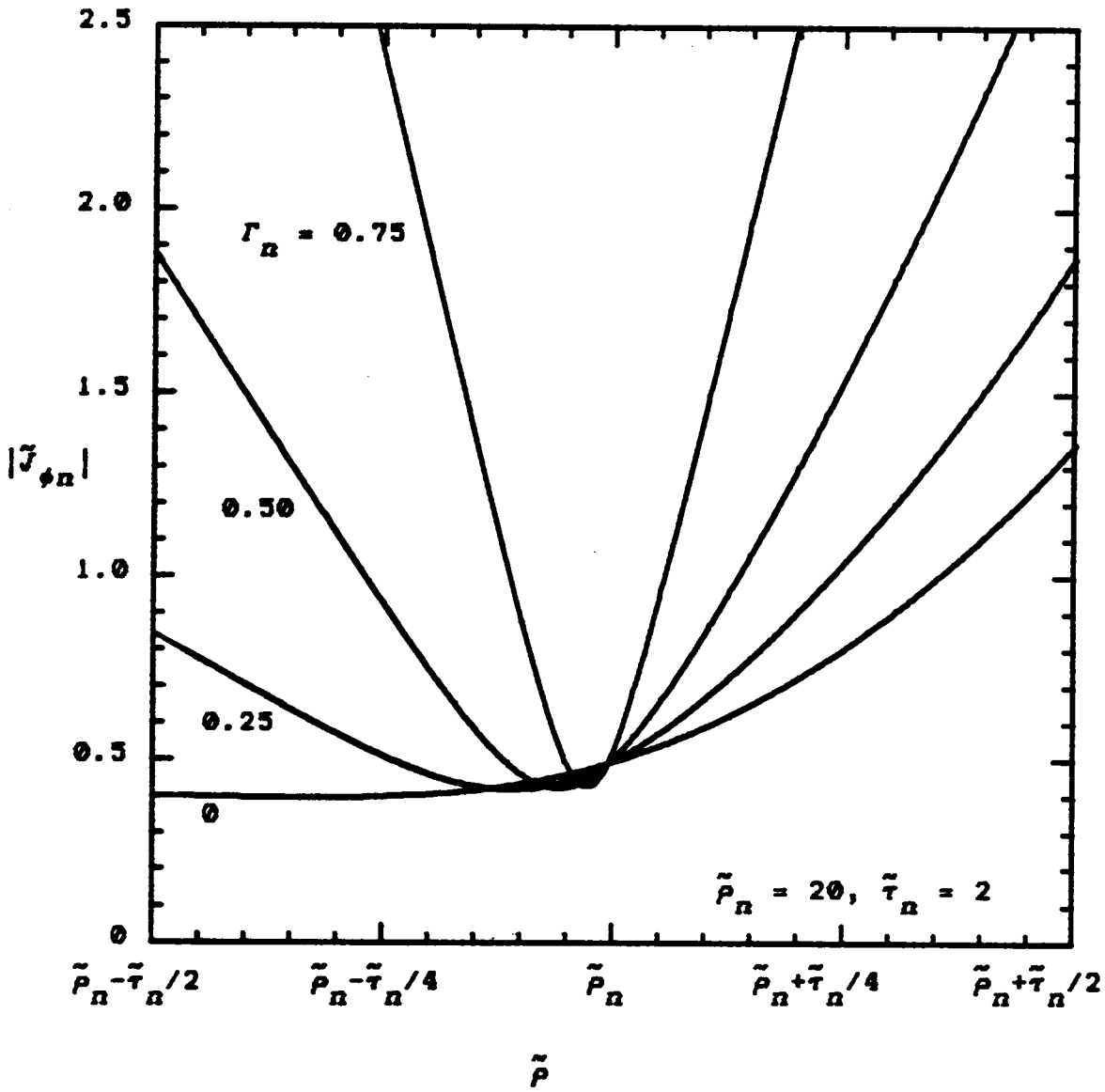

Figure 4.2.5a. Magnitude of the normalized current density vs. the normalized radial distance in the *n*th conductor layer with the boundary condition ratio varied as a parameter for values less than unity.

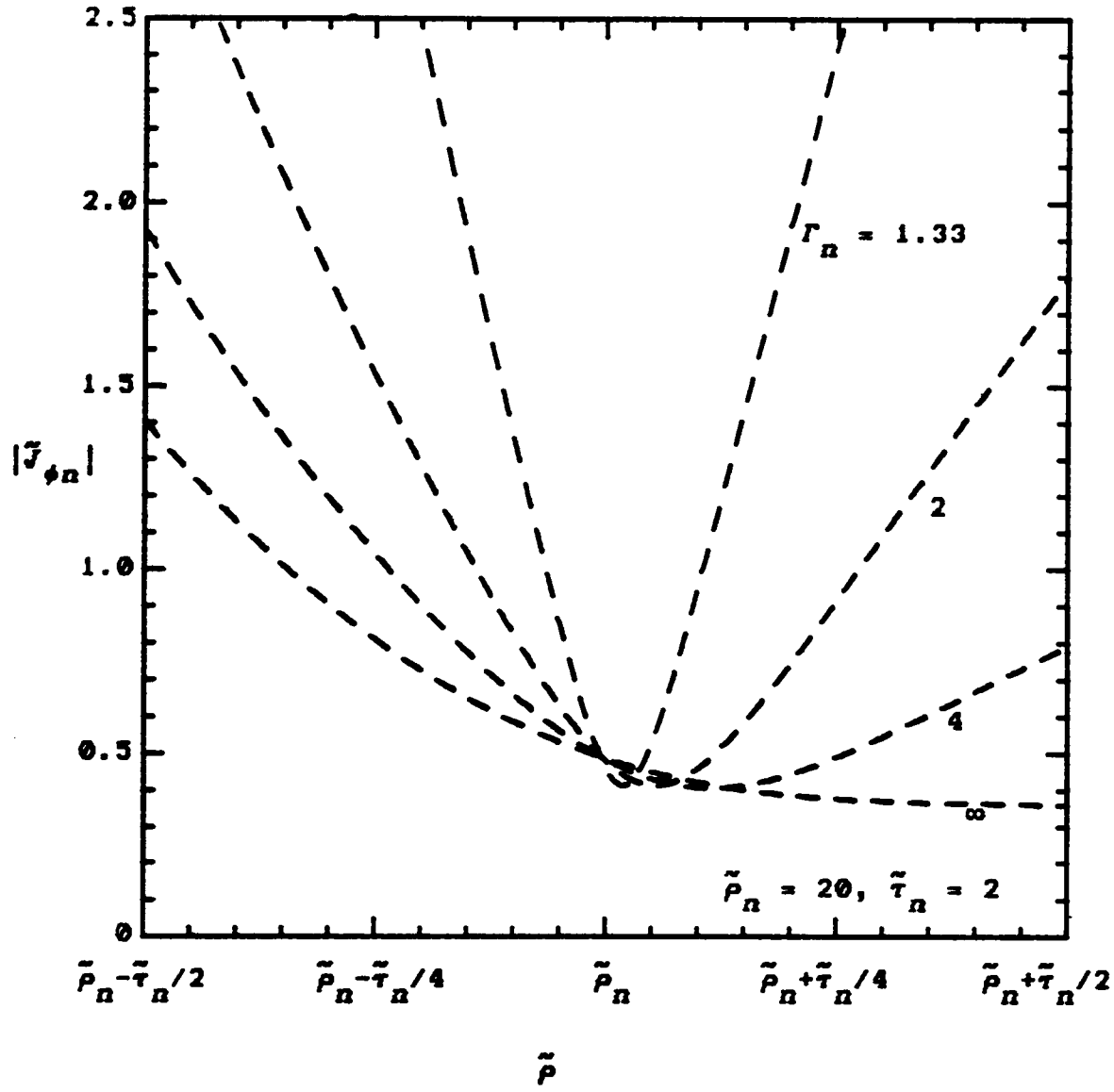

Figure 4.2.5b. Magnitude of the normalized current density vs. the normalized radial distance in the nth conductor layer with the boundary condition ratio varied as a paremeter for values greater than unity.

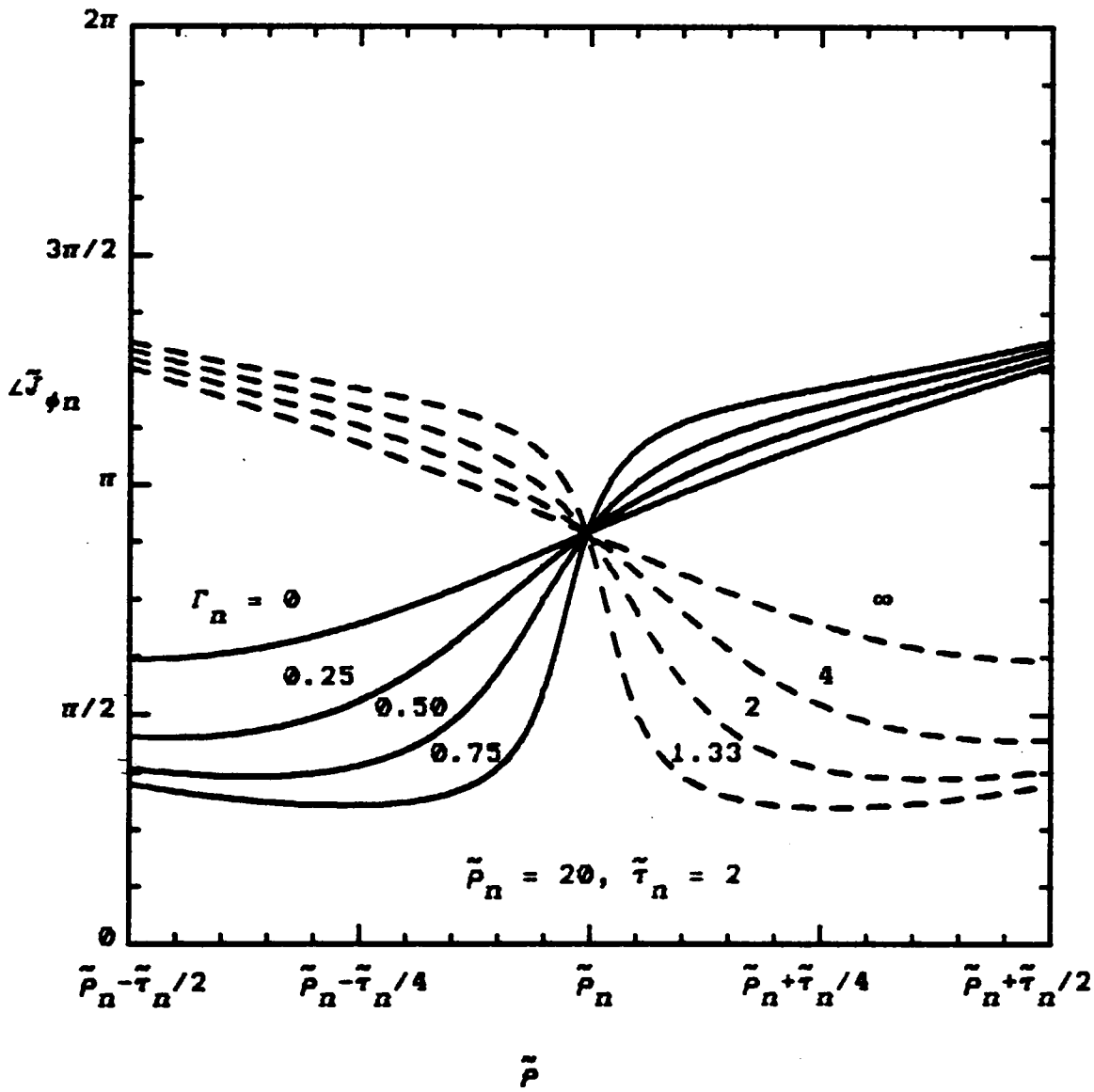

Figure 4.2.6. Phase of the normalized current density vs. the normalized radial distance in the nth conductor layer with the boundary condition ratio varied as a parameter for values less than unity (solid lines) and greater than unity (dashed lines).

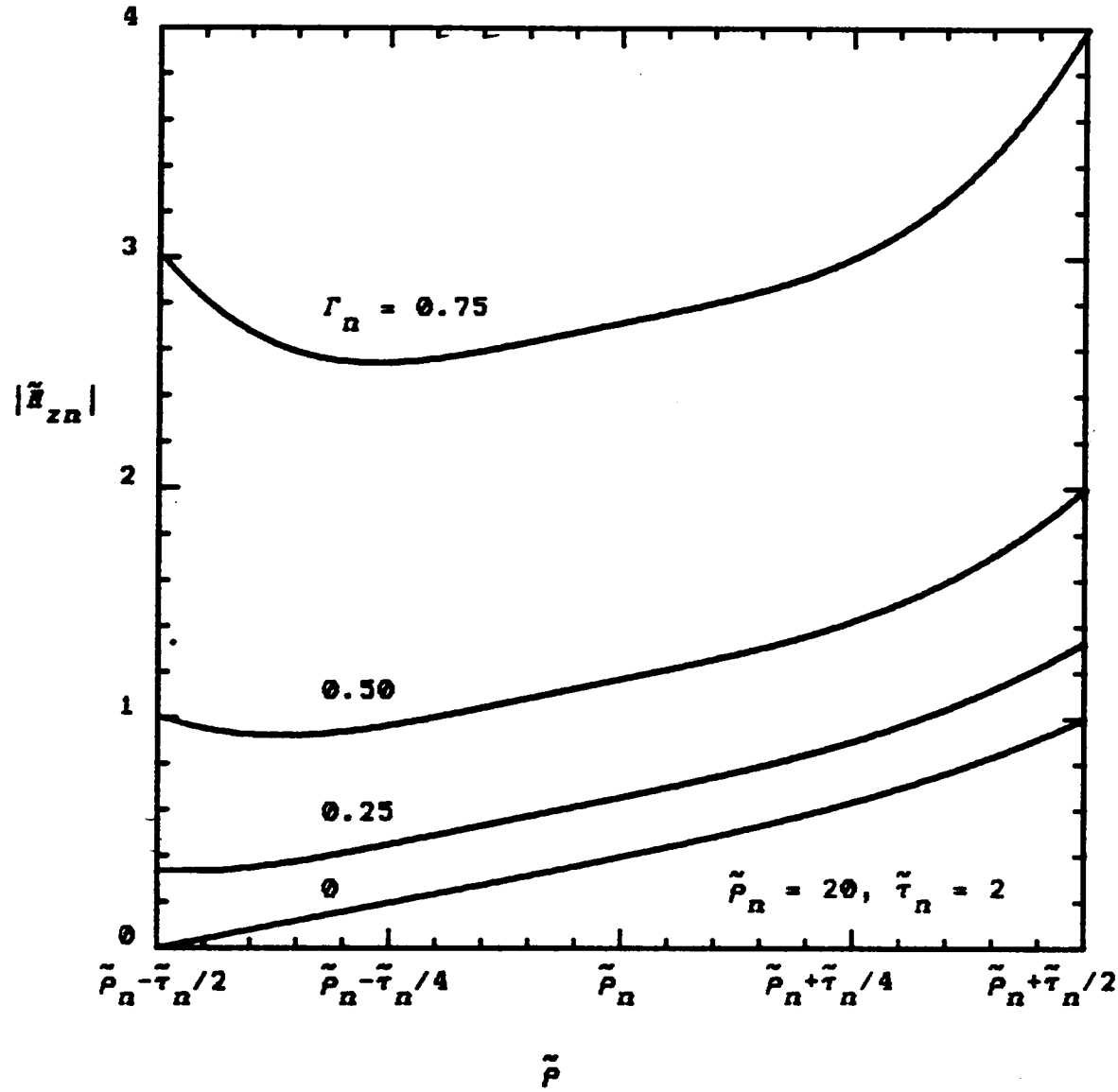

Figure 4.2.7. Magnitude of the normalized magnetic field intensity vs. the normalized radial distance in the *n*th conductor layer with the boundary condition ratio varied as a parameter.

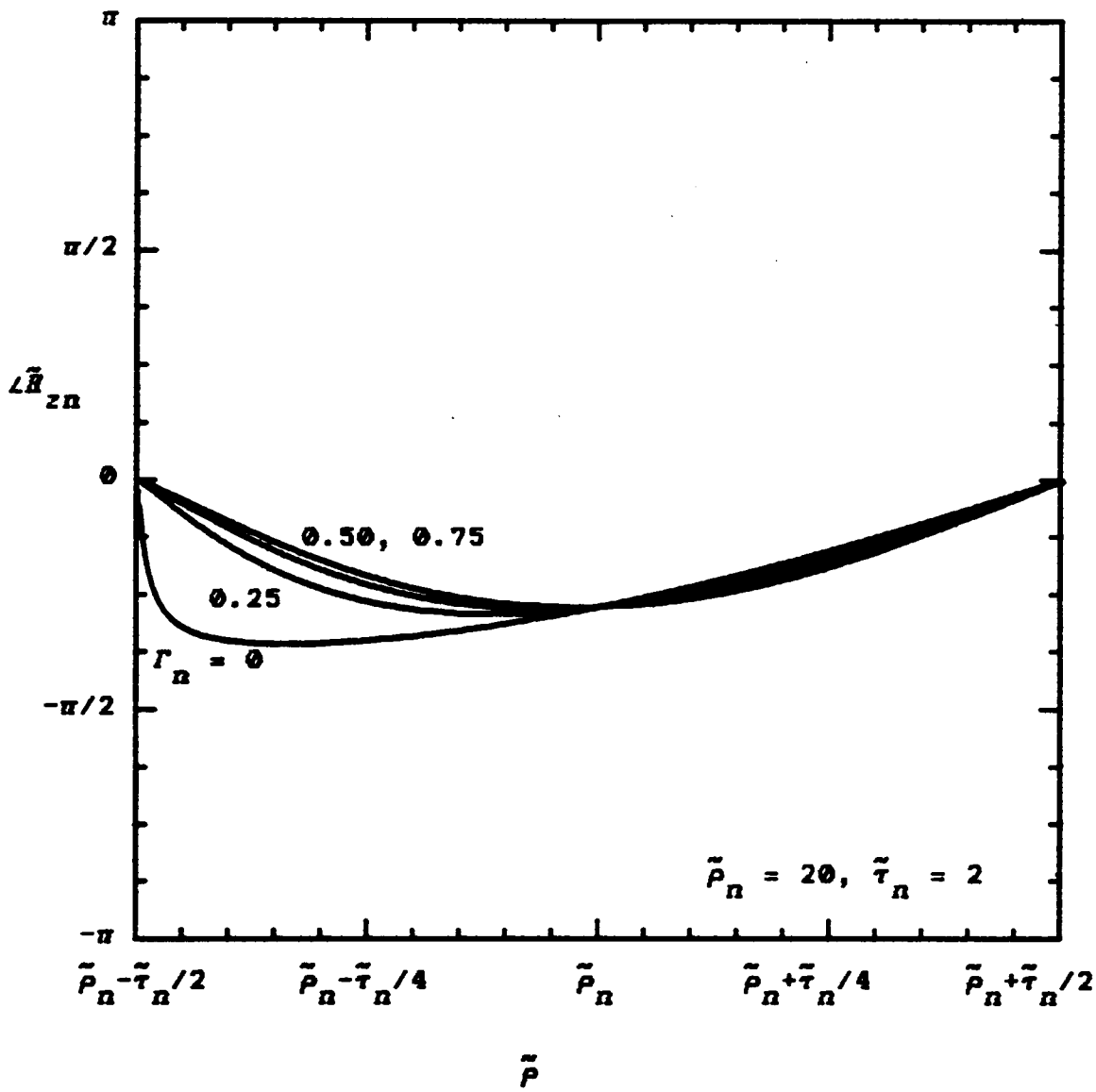

Figure 4.2.8. Phase of the normalized magnetic field intensity vs. the normalized radial distance in the nth conductor layer with the boundary condition ratio varied as a parameter.

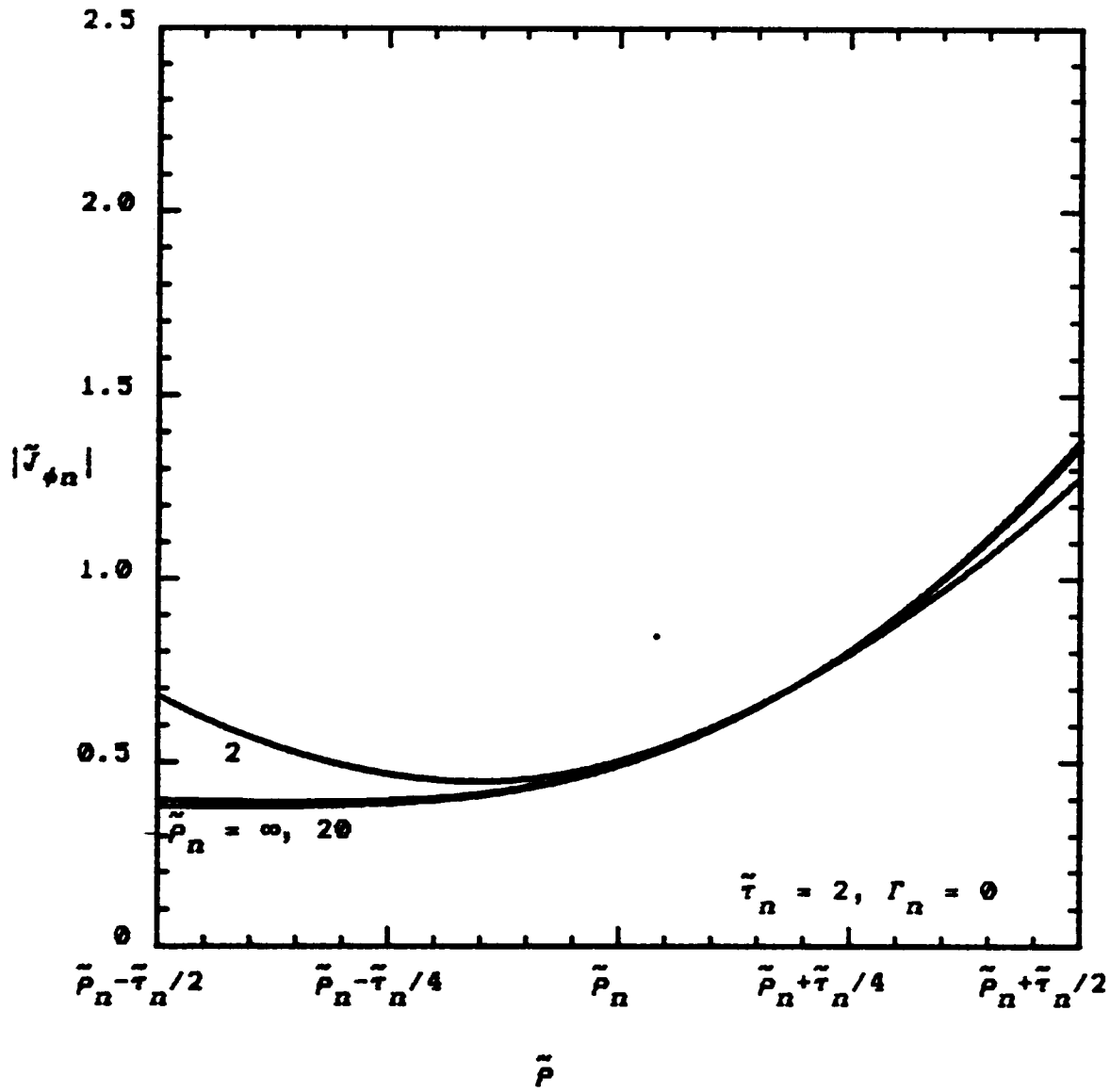

Figure 4.2.9. Magnitude of the normalized current density vs. the normalized radial distance in the nth conductor layer with the normalized conductor mean radius varied as a parameter.

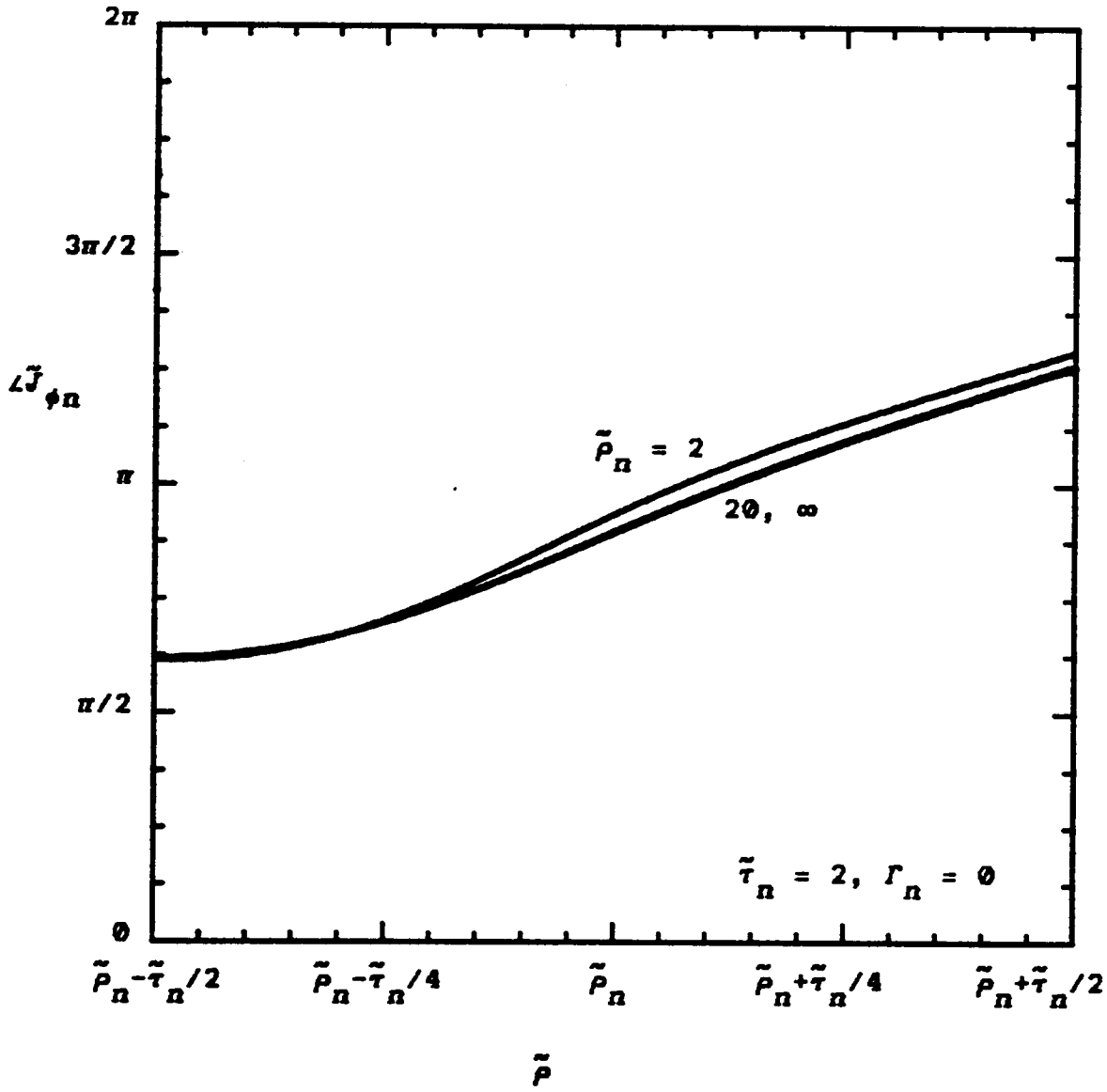

Figure 4.2.10. Phase of the normalized current density vs. the normalized radial distance in the nth conductor layer with the normalized conductor mean radius varied as a parameter.

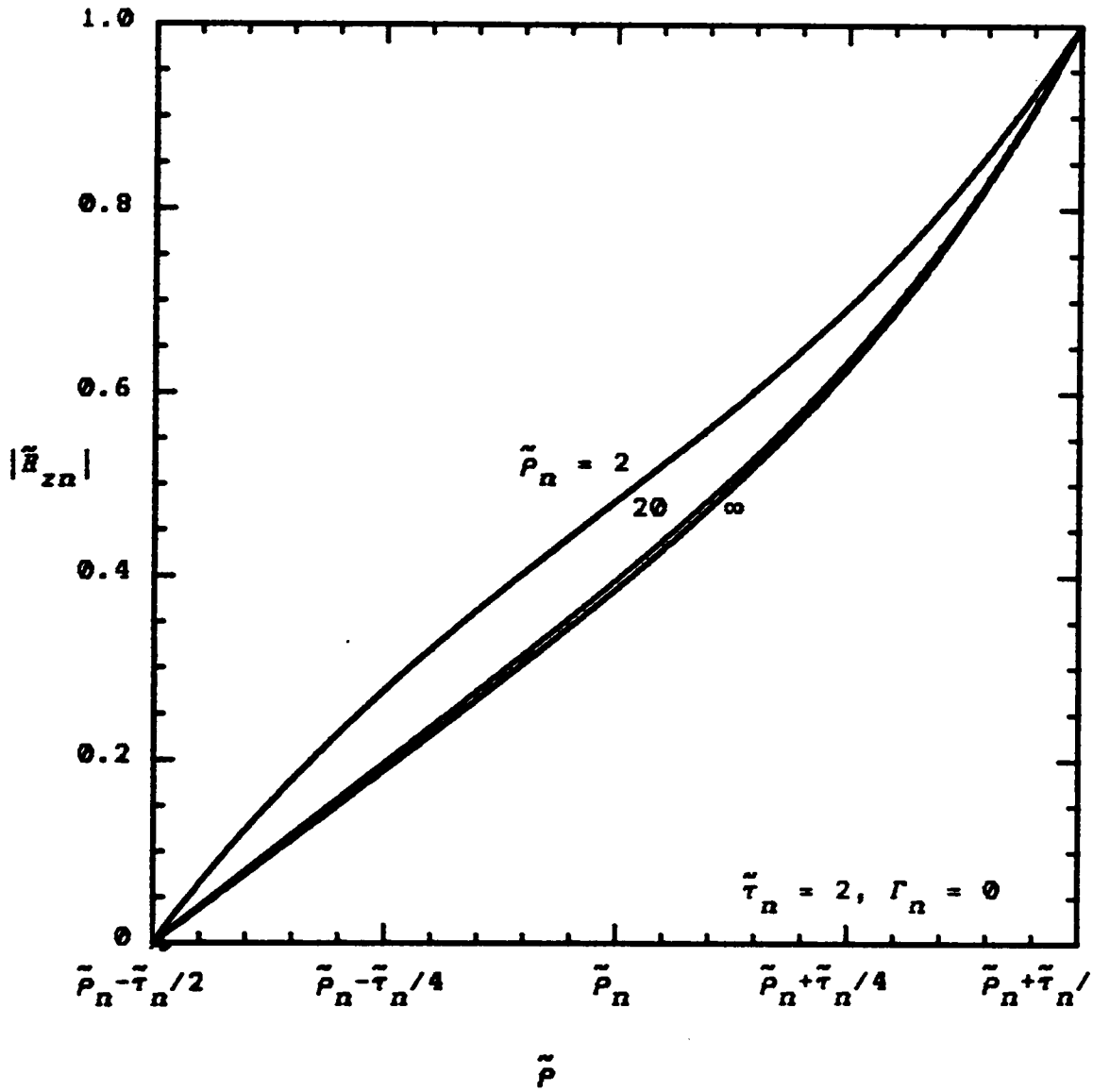

Figure 4.2.11. Magnitude of the normalized magnetic field intensity vs. the normalized radial distance in the nth conductor layer with the normalized conductor mean radius varied as a parameter.

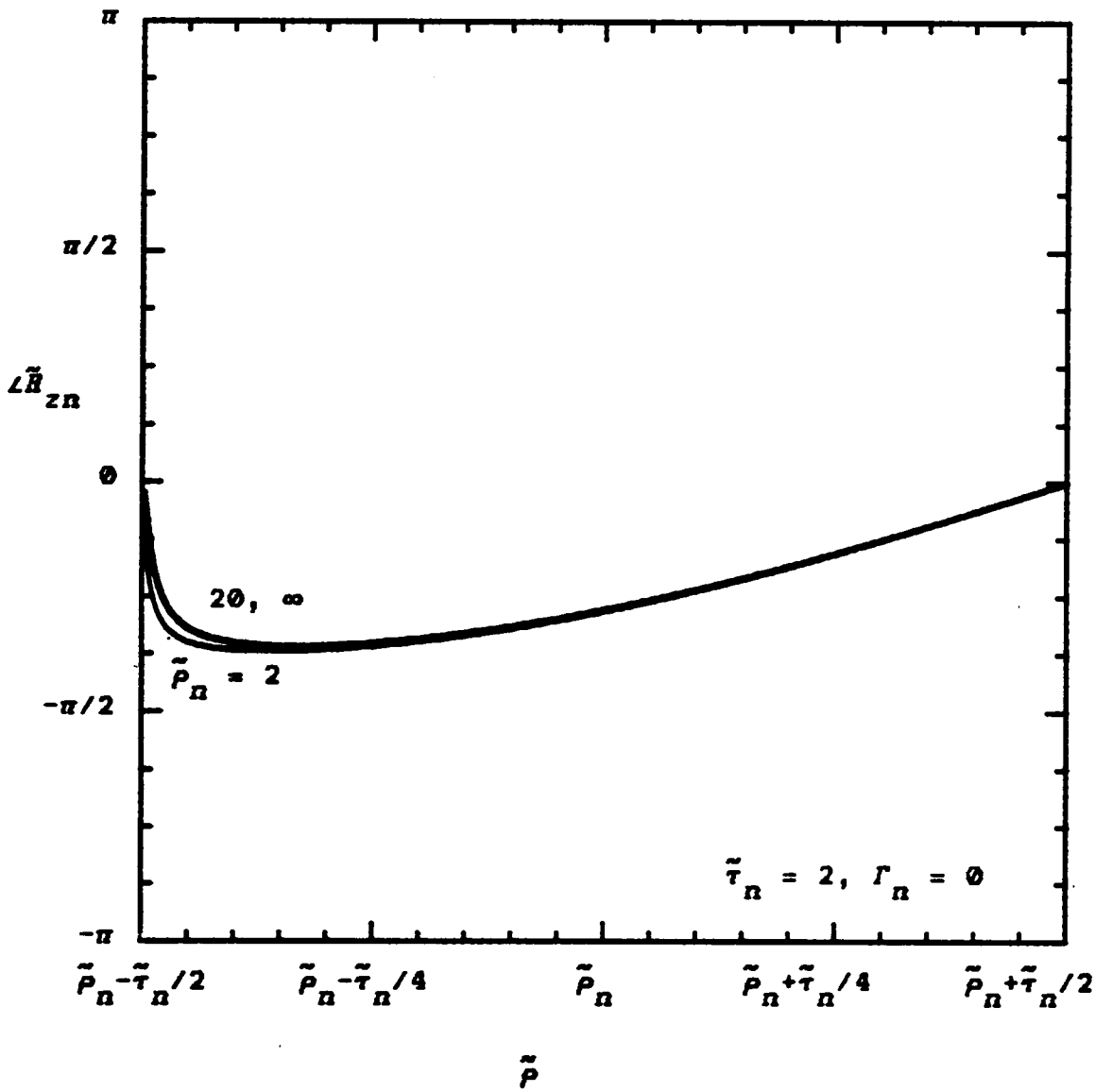

Figure 4.2.12. Phase of the normalized magnetic field intensity vs. the normalized radial distance in the nth conductor layer with the normalized conductor mean radius varied as a parameter.

variable, used for the abscissa in each case, is the normalized radial coordinate $\tilde{\rho}$ which ranges from the inner boundary to the outer boundary of the nth conductor layer. The three parameters $\tilde{\tau}_n$, Γ_n, and $\tilde{\rho}_n$ are in turn varied so that the effects of each on the results can be studied. The parameter $\tilde{\tau}_n$ is varied in Figures 4.2.1 through 4.2.4, Γ_n in Figures 4.2.5 through 4.2.8, and $\tilde{\rho}_n$ in Figures 4.2.9 through 4.2.12. The common set of values from which the parameters are varied is given by: $\tilde{\tau}_n = 2$, $\Gamma_n = 0$, and $\tilde{\rho}_n = 20$. $\tilde{\tau}_n = 2$ represents a conductor thickness of two skin depths. $\Gamma_n = 0$ corresponds to zero magnetic field intensity at the inner boundary. This important case always occurs at the first layer of the first winding in a transformer. It will be seen later that this is a favorable condition for several reasons, and designs should strive to include it in as many layers as possible. Finally, $\tilde{\rho}_n = 20$ is chosen because it represents a practical minimum value for most current applications. It corresponds to a minimum frequency of 20 kHz (frequencies below this generally cause audible noise problems) and a minimum radius of approximately 0.37 in or 9.4 mm.

First, consider the effects of varying the conductor thickness. Figures 4.2.1 and 4.2.2 show the magnitude and phase of the current density, respectively. For small values of $\tilde{\tau}$, the magnitude increases and approaches a

uniform distribution, and the phase is nearly constant. This corresponds to the low frequency or DC case. As the conductor thickness increases, the current begins to crowd near the outer boundary and phase variation appears across the layer indicating a presence of circulating currents. This corresponds to increasing the frequency (for constant thickness), and the well-known skin effect is apparent. In general, the current will tend to migrate to the boundary with the largest magnetic field intensity. This is commonly referred to as the proximity effect since these boundary conditions are determined partially by the presence of currents in nearby layers. The Γ_n parameter study which follows reveals this effect in more detail. Figures 4.2.3 and 4.2.4 show curves for the magnitude and phase of the magnetic field intensity using the same values of normalized conductor thickness. For low values the magnitude varies linearly with radial distance, and the phase is constant. This is in agreement with the corresponding uniform current distribution. As the thickness increases, the high frequency effects are once again noticed. Note that the boundary conditions are satisfied: namely, zero magnitude at the inner boundary and zero phase at both boundaries. The unity magnitude at the outer boundary is the result of the normalization process.

Next, consider the variation of the boundary condition ratio Γ_n displayed in Figures 4.2.5 through 4.2.8. The magnitude of the current density is shown in Figure 4.2.5 which is split into two sets of curves, a and b. For values less than unity in Figure 4.2.5a, the magnetic field intensity is greater at the outer boundary, and the current migrates in that direction. This migration is more pronounced as the ratio approaches zero which corresponds to a greater relative difference in the boundary values. Also, the current crowding is, in general, more pronounced as the ratio approaches unity. This is because the magnetic field intensity in the whole region is effectively biased to values which are increasingly greater than zero. It is helpful to remember that the total current (which is proportional to the difference in the magnetic field intensity boundary values) in the conductor layer is held constant throughout these variations as a result of the normalization process. Thus, the effects of varying Γ_n are the sole result of the location of the nth layer in relation to other layers. This is another example of the proximity effect in which the current crowding and circulating currents increase dramatically when the conductor is located in regions with high external magnetic fields. Figure 4.2.5b shows a similar set of curves for values of Γ_n greater than unity. In particular, the values chosen are

the reciprocals of those in Figure 4.2.5a. The boundary conditions are therefore reversed, and the curves are approximate mirror images of each other about the center of the layer. This would be exactly true if the radius was infinite, in which case the results should approach those of a flat plate. The phase of the current density under the same conditions is shown in Figure 4.2.6. These curves are combined into one plot with dashed lines used to distinguish between the two sets of magnitude plots. The phase variations confirm the presence of higher circulating currents as Γ_n approaches unity. Because of the symmetrical nature of the problem for reciprocal values of the boundary condition ratio, and because this nature is already very much evident at the minimum normalized mean radius of 20; only values between zero and unity will be considered henceforth. The only practical difference between the two cases is the relative direction of the net and circulating currents. The magnitude and phase of the magnetic field intensity using the same values of the boundary condition ratio are presented in Figures 4.2.7 and 4.2.8. The results agree with those for the current density as Maxwell's equations dictate they should. Interpreting the results, however, is somewhat more abstract since it is more common to think in terms of currents in conductors. Note that in Figure 4.2.7 the difference in the boundary conditions

remains constant at unity because the enclosed net current has been factored out during the normalization process. Consequently, higher values of Γ_n correspond to higher external magnetic fields as mentioned earlier. A final curious observation is evident from both the magnitude and phase curves of the magnetic field intensity. Both become more symmetrical as Γ_n increases as should be expected, but the magnitude curves begin to bow downward and the phase variations become slightly less pronounced. Perhaps this can be explained in conjunction with the effects that were noticed on the current density. In particular, the circulating currents nearer the boundaries become much greater relative to the net current flow in the center which suggests a diminishing of the magnetic fields in the center of the layer.

Lastly, consider the effects of varying the normalized radial distance $\tilde{\rho}_n$ to the center of the layer which is summarized in Figures 4.2.9 through 4.2.12. Only three values are needed to demonstrate these effects which turn out to be second order compared to those already considered. The value $\tilde{\rho}_n = 2$ is used as a lower limit, and it corresponds to a solenoid which is approaching a solid cylinder. This is currently of little practical use in light of the minimum value of 20 previously discussed. But it may become more important in future constructions which

take advantage of extremely high frequency operation. The other two values considered are $\tilde{\rho}_n = 20$ and $\tilde{\rho}_n = \infty$ which bound most current applications. As can be seen in all four sets of curves, there is almost no difference in the results for these two cases. This suggests asymptotic behavior for large values of $\tilde{\rho}$ which may lead to possible simplification of the formulas thus far obtained. This is the topic of the next section.

4.3 LARGE ARGUMENT ASYMPTOTIC APPROXIMATION

The expressions derived in the previous section are complicated, offer little insight to the problem, and involve numerous computations of first and second order Kelvin functions. In the process of studying the effects of parameter variations, large argument asymptotic behavior of the solutions was discovered. Indeed, it turns out that there are large argument asymptotic expressions for all of the Kelvin functions which can be used confidently under most conditions. These expressions are summarized in Appendix B which deals exclusively with Kelvin functions. A practical minimum value for $\tilde{\rho}$ for present day applications was found to be 20 which, according to equation (4.2.9), corresponds to a value of $x = 28.3$ for the argument of the Kelvin functions. Figures in Appendix B indicate that the accuracy of the large argument asymptotic approximation is

better than 1% for zero order Kelvin functions and 2% for first order ones. Remembering that these are worst-case conditions, one can proceed to use the asymptotic formulas with reasonable confidence that they will yield practical and usable results. Also, there is the additional incentive that simpler and more revealing expressions may result.

This is indeed the case. Substituting the asymptotic expressions in equations (B.4.2) and (B.4.3) into equations (4.2.12) and (4.2.13) for the normalized nth layer magnetic field intensity gives, after considerable manipulation,

$$\tilde{H}_{zn}(\tilde{\rho}) \sim \frac{1}{1-\Gamma_n}\left[\frac{\tilde{\rho}_n}{\tilde{\rho}}\right]^{\frac{1}{2}} \frac{1}{\sinh[(1+j)\tilde{\tau}_n]}$$

$$\left\{\left[1+\frac{1}{2}\frac{\tilde{\tau}_n}{\tilde{\rho}_n}\right]^{\frac{1}{2}}\sinh(1+j)\left[\tilde{\rho}-\tilde{\rho}_n+\frac{\tilde{\tau}_n}{2}\right] - \Gamma_n\left[1-\frac{1}{2}\frac{\tilde{\tau}_n}{\tilde{\rho}_n}\right]^{\frac{1}{2}}\sinh(1+j)\left[\tilde{\rho}-\tilde{\rho}_n-\frac{\tilde{\tau}_n}{2}\right]\right\};$$

$$\tilde{\rho}_n-\frac{\tilde{\tau}_n}{2} \le \tilde{\rho} \le \tilde{\rho}_n+\frac{\tilde{\tau}_n}{2};\ n = 1,2,\ldots,N. \qquad (4.3.1)$$

The parameters Γ_n, $\tilde{\rho}_n$, and $\tilde{\tau}_n$ materialize naturally in the development of this expression and are incorporated exclusively. This is the major reason for defining these quantities earlier along with the fact that, in hindsight, they are also more appropriate for investigating the results. These three parameters were originally defined in

equations (4.2.11) and (4.2.17). The "asymptotically equal to" symbol ~ is introduced in this expression, and will be used henceforth to indicate large argument asymptotic approximations. This expression is still not a simple one, but in the least its functional character is more recognizable. The complex-valued arguments for the hyperbolic trigonometric functions suggest the presence of exponentially damped sinusoids. Note that these arguments are no longer dominated by the presence of the mean radius which has been assumed to be large. Instead, the mean radius is effectively subtracted out of the argument which is now on the order of the conductor thickness. The effects of the mean radius are therefore minor and limited to the proportionality constants in the magnitude. This agrees with the results of the parameter study at the end of the previous section which led to this approximation in the first place. Finally, it is encouraging to see that the asymptotic expression satisfies the boundary conditions identically. This is easily verified by evaluating it at the inner and outer boundaries, and remembering the defining equation (4.2.10) for the normalized magnetic field intensity.

A similar procedure may be followed for the normalized current density given by equations (4.2.15) and (4.2.16), giving

$$\tilde{J}_{\phi n}(\tilde{\rho}) \sim -(1+j)\frac{1}{1-\Gamma_n}\left[\frac{\tilde{\rho}_n}{\tilde{\rho}}\right]^{\frac{1}{2}}\frac{1}{\sinh[(1+j)\tilde{\tau}_n]}$$

$$\left\{\left[1+\frac{1}{2}\frac{\tilde{\tau}_n}{\tilde{\rho}_n}\right]^{\frac{1}{2}}\cosh(1+j)\left[\tilde{\rho}-\tilde{\rho}_n+\frac{\tilde{\tau}_n}{2}\right] - \Gamma_n\left[1-\frac{1}{2}\frac{\tilde{\tau}_n}{\tilde{\rho}_n}\right]^{\frac{1}{2}}\cosh(1+j)\left[\tilde{\rho}-\tilde{\rho}_n-\frac{\tilde{\tau}_n}{2}\right]\right\};$$

$$\tilde{\rho}_n-\frac{\tilde{\tau}_n}{2} \le \tilde{\rho} \le \tilde{\rho}_n+\frac{\tilde{\tau}_n}{2};\ n = 1,2,\ldots,N. \qquad (4.3.2)$$

This expression is almost identical in appearance to the one obtained for the normalized magnetic field intensity. The only differences are the addition of the complex constant (1+j) and the change from hyperbolic sines to hyperbolic cosines.

To verify the validity of the large argument asymptotic approximations, equations (4.3.1) and (4.3.2) have been programmed and evaluated for some representative examples. The quantity of interest is the normalized mean radius $\tilde{\rho}_n$; consequently, the parameter study in Figures 4.2.9 through 4.2.12 is duplicated in Figures 4.3.1 through 4.3.4 with additional curves for the asymptotic expressions. The exact results using the Kelvin functions are repeated as solid lines, and the new large argument asymptotic approximations are added as the dashed lines. The $\tilde{\rho}_n = \infty$ case is eliminated for clarity since it differs little from the $\tilde{\rho}_n = 20$ case. Also, for $\tilde{\rho}_n = \infty$, the exact and asymptotic solutions will be identical by definition. The figures show

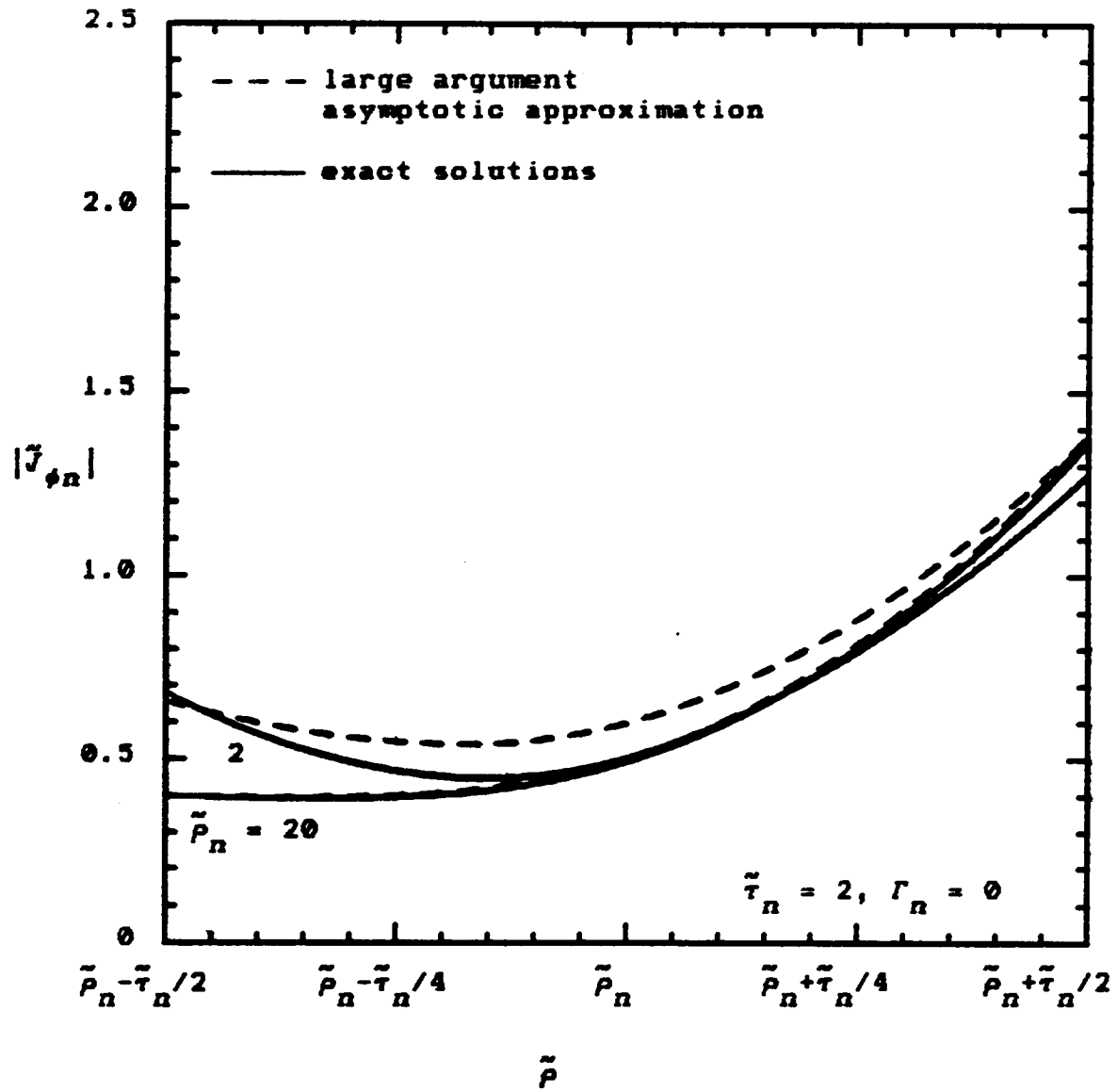

Figure 4.3.1. Magnitude of the normalized current density vs. the normalized radial distance in the nth conductor layer with the normalized conductor mean radius varied as a parameter.

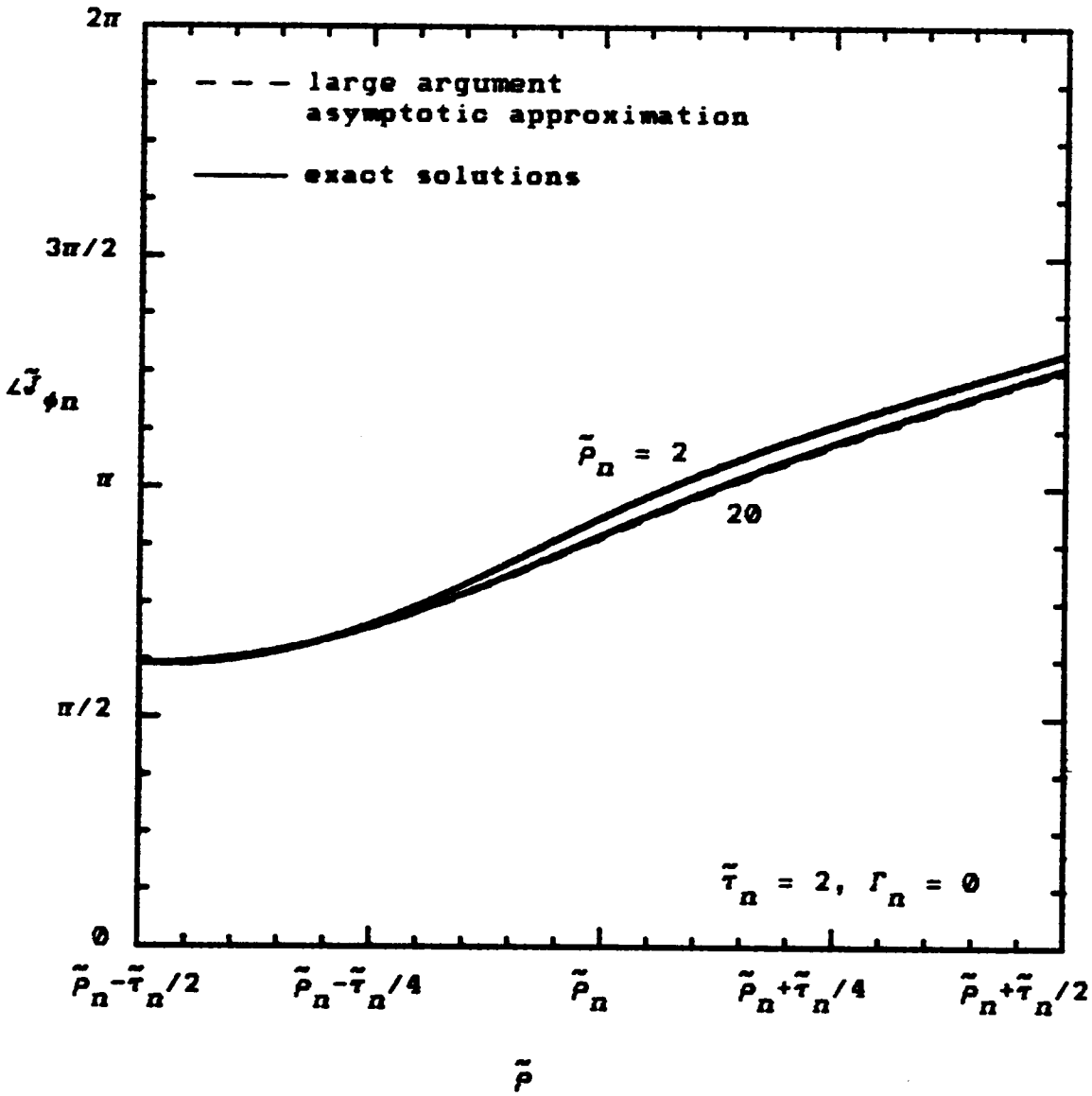

Figure 4.3.2. Phase of the normalized current density vs. the normalized radial distance in the nth conductor layer with the normalized conductor mean radius varied as a parameter.

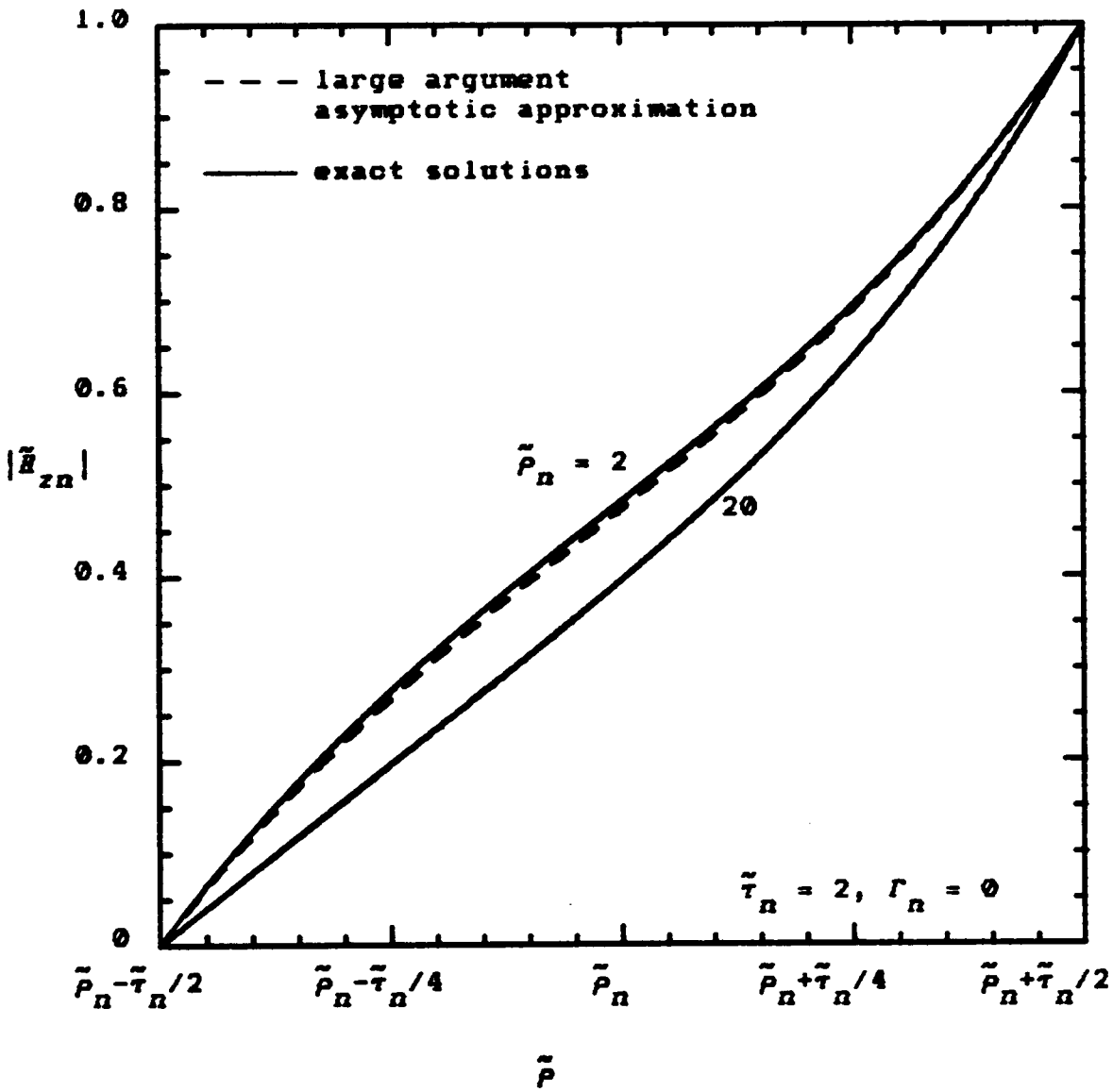

Figure 4.3.3. Magnitude of the normalized magnetic field intensity vs. the normalized radial distance in the nth conductor layer with the normalized conductor mean radius varied as a parameter.

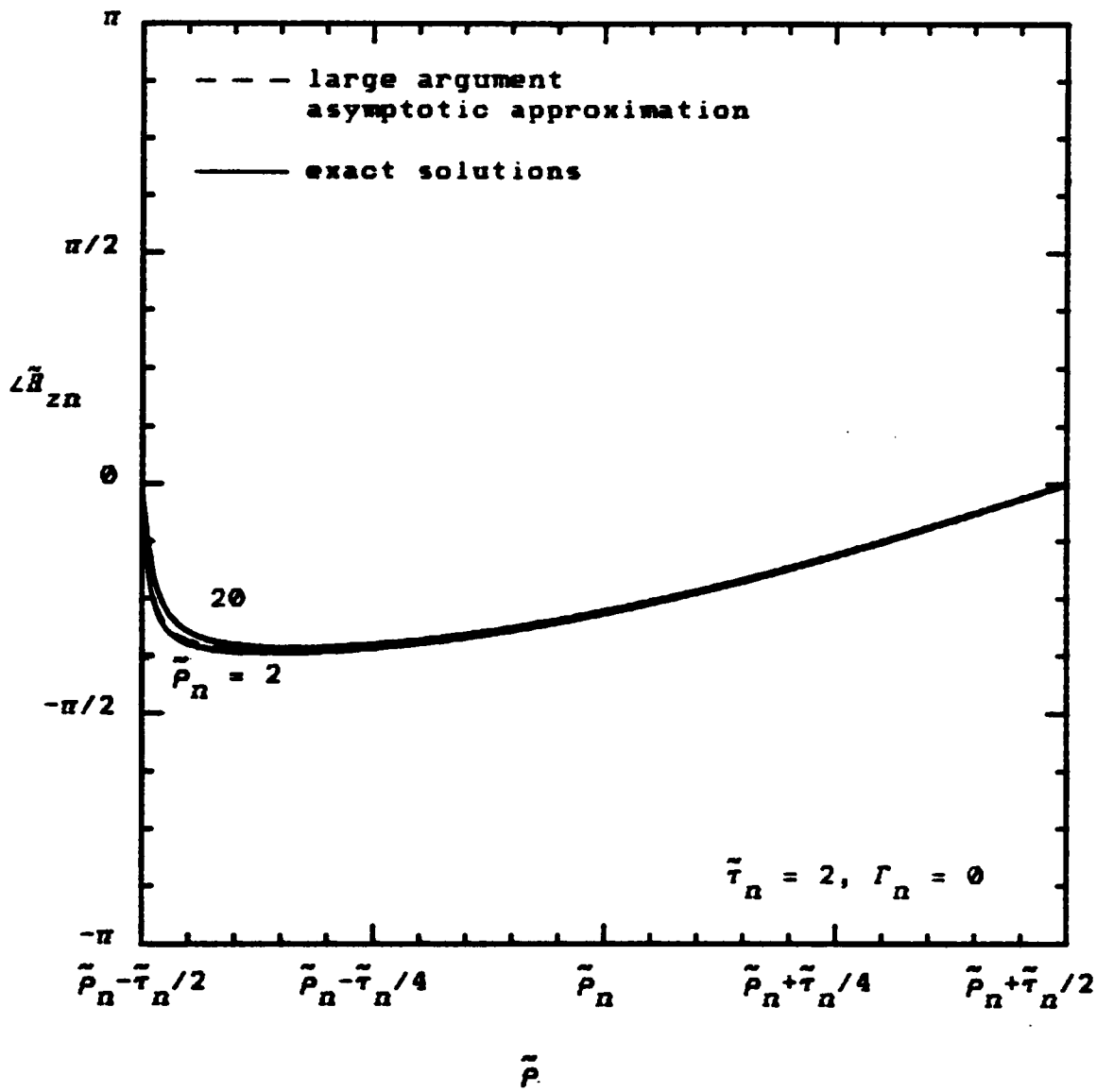

Figure 4.3.4. Phase of the normalized magnetic field intensity vs. the normalized radial distance in the nth conductor layer with the normalized conductor mean radius varied as a parameter.

that, for both quantities, the magnitude and phase of the exact and approximate curves are indistinguishable at $\tilde{\rho}_n = 20$. Thus, as expected, the large argument asymptotic approximation is quite adequate for most present applications. The curves for $\tilde{\rho}_n = 2$ are also shown for possible future need and academic interest. The agreement at such a small value is somewhat surprising, especially for the magnetic field intensity. The approximations for the current density are not quite as good, but still very respectable. This is because the current density involves first order Kelvin functions for which the large argument asymptotic approximations are not as accurate as for the zero order ones.

The impressive results of the large argument asymptotic approximations encourage still further investigation for simplification which follows in the next section.

4.4 THIN-LAYER APPROXIMATION

Thus far, the only approximation made has resulted from the assumption that the mean radius of the conductor layer is large in comparison with the skin depth. That approximation proved to be quite good for a wide range of radial distances. The parameter study of the normalized thickness $\tilde{\tau}_n$ presented in Figures 4.2.1 through 4.2.4 suggests another possible simplification. There, it is

evident that as the conductor layer thickness increases above one skin depth, several undesirable phenomena come into play. Current migrates to the boundaries of the conductor, and phase variation appears across the layer, indicating the presence of circulating currents. The conductor will therefore become inefficiently utilized, and an increase in power dissipation will result. These effects will be examined in detail in the next chapter, and an optimization procedure based on them will be developed.

For now, however, the above discussion along with the previous parameter studies suggest that for a well-designed transformer which makes efficient use of its conductors, the layer thicknesses should not be significantly greater than a skin depth. Coupled with the previous large argument asymptotic approximation, the thin-layer approximation

$$\frac{\tilde{\tau}_n}{\tilde{\rho}_n} \ll 1; \quad n = 1,2,\ldots,N \tag{4.4.1}$$

follows. Thus, thin-layer means thin when compared to the mean radius of the layer, and not when compared to a skin depth. Note that this condition can be expressed in terms of the normalized quantities as shown or, equivalently, in terms of the actual distances. The resulting normalized magnetic field intensity and current density follow almost

trivially by using the above condition to eliminate appropriate terms from equations (4.3.1) and (4.3.2); hence,

$$\tilde{H}_{zn}(\tilde{\rho}) \approx \frac{1}{1-\Gamma_n} \frac{1}{\sinh[(1+j)\tilde{\tau}_n]}$$

$$\left\{\sinh\left[(1+j)(\tilde{\rho}-\tilde{\rho}_n+\frac{\tilde{\tau}_n}{2})\right] - \Gamma_n \sinh\left[(1+j)(\tilde{\rho}-\tilde{\rho}_n-\frac{\tilde{\tau}_n}{2})\right]\right\};$$

$$\tilde{\rho}_n-\frac{\tilde{\tau}_n}{2} \le \tilde{\rho} \le \tilde{\rho}_n+\frac{\tilde{\tau}_n}{2};\ n = 1,2,\ldots,N \qquad (4.4.2)$$

and

$$\tilde{J}_{\phi n}(\tilde{\rho}) \approx -(1+j) \frac{1}{1-\Gamma_n} \frac{1}{\sinh[(1+j)\tilde{\tau}_n]}$$

$$\left\{\cosh\left[(1+j)(\tilde{\rho}-\tilde{\rho}_n+\frac{\tilde{\tau}_n}{2})\right] - \Gamma_n \cosh\left[(1+j)(\tilde{\rho}-\tilde{\rho}_n-\frac{\tilde{\tau}_n}{2})\right]\right\};$$

$$\tilde{\rho}_n-\frac{\tilde{\tau}_n}{2} \le \tilde{\rho} \le \tilde{\rho}_n+\frac{\tilde{\tau}_n}{2};\ n = 1,2,\ldots,N, \qquad (4.4.3)$$

where the "approximately equal to" symbol $\approx$ has been adopted to set apart this result from the asymptotic approximation. It is important to realize that only the magnitude terms have been simplified. It is not valid to ignore the last term in the hyperbolic function arguments. This would result in a large error in the total argument which is on

the order of the layer thickness. The situation here is somewhat analogous to the far-field approximation which is frequently used to simplify the analysis of antenna radiation and electromagnetic propagation problems. To facilitate this understanding, it is perhaps useful to define the displaced radial coordinate

$$\tilde{\rho}' \doteq \tilde{\rho} - \tilde{\rho}_n \tag{4.4.4}$$

so that equations (4.4.2) and (4.4.3) become

$$\tilde{H}_{zn}(\tilde{\rho}') \approx \frac{1}{1-\Gamma_n} \frac{1}{\sinh[(1+j)\tilde{\tau}_n]}$$

$$\left\{\sinh\left[(1+j)(\tilde{\rho}'+\frac{\tilde{\tau}_n}{2})\right] - \Gamma_n \sinh\left[(1+j)(\tilde{\rho}'-\frac{\tilde{\tau}_n}{2})\right]\right\};$$

$$-\frac{\tilde{\tau}_n}{2} \le \tilde{\rho}' \le +\frac{\tilde{\tau}_n}{2};\ n = 1,2,\ldots,N \tag{4.4.5}$$

and

$$\tilde{J}_{\phi n}(\tilde{\rho}') \approx -(1+j) \frac{1}{1-\Gamma_n} \frac{1}{\sinh[(1+j)\tilde{\tau}_n]}$$

$$\left\{\cosh\left[(1+j)(\tilde{\rho}'+\frac{\tilde{\tau}_n}{2})\right] - \Gamma_n \cosh\left[(1+j)(\tilde{\rho}'-\frac{\tilde{\tau}_n}{2})\right]\right\};$$

$$-\frac{\tilde{\tau}_n}{2} \le \tilde{\rho}' \le +\frac{\tilde{\tau}_n}{2};\ n = 1,2,\ldots,N. \qquad (4.4.6)$$

It is immediately apparent from these expressions why the arguments cannot be simplified.

The next step is to perform some calculations to determine the range of validity of the thin-layer approximation. Actually, this has already been done. Curves for $\tilde{\rho}_n = \infty$ appear in the parameter study of the normalized mean radius in Figures 4.2.9 through 4.2.12. The thin-layer approximations in equations (4.4.2) and (4.4.3) were actually used to compute these curves. Thus, for conductor thicknesses up to two skin depths, the thin-layer approximation is very good. It will be shown in the next chapter that designs optimized for minimum power dissipation will never result in thicknesses greater than this.

Before proceeding to optimization considerations, it is convenient to pause now and examine the behavior of the solutions in some limiting cases. This will help to provide an intuitive understanding and also some confidence in the validity of the solutions. The thin-layer approximation furnishes a simplified framework for these investigations. First, consider the low-frequency case. As the frequency approaches zero (DC), the skin depth increases without bound and the normalized distance quantities will therefore also

approach zero. Under these conditions, equations (4.4.5) and (4.4.6) become

$$\tilde{H}_{zn}(\tilde{\rho}') \underset{f\to 0}{\approx} \frac{1}{2}\frac{1+\Gamma_n}{1-\Gamma_n} + \frac{\tilde{\rho}'}{\tilde{\tau}_n} \qquad (4.4.7a)$$

$$\tilde{J}_{\phi n}(\tilde{\rho}') \underset{f\to 0}{\approx} -\frac{1}{\tilde{\tau}_n} \qquad (4.4.7b)$$

or, in terms of the actual unnormalized quantities,

$$H_{zn}(\rho') \underset{f\to 0}{\approx} \frac{1}{2}(H_n+H_{n-1}) + (H_n-H_{n-1})\frac{\rho'}{\tau_n} \qquad (4.4.8a)$$

$$J_{\phi n}(\rho') \underset{f\to 0}{\approx} -(H_n-H_{n-1})\frac{1}{\tau_n} = \frac{K_n}{\tau_n}. \qquad (4.4.8b)$$

The current density is uniform, and the corresponding magnetic field intensity varies linearly from the inner boundary value to the outer boundary value. These are the expected DC results. For high frequencies, the same quantities take on the form

$$\tilde{H}_{zn}(\tilde{\rho}') \underset{f\to\infty}{\approx} \frac{1}{1-\Gamma_n} e^{-(1+j)\tilde{\tau}_n/2}\left[e^{+(1+j)\tilde{\rho}'} + \Gamma_n e^{-(1+j)\tilde{\rho}'}\right] \qquad (4.4.9a)$$

$$\tilde{J}_{\phi n}(\tilde{\rho}') \underset{f\to\infty}{\approx} -\frac{1+j}{1-\Gamma_n} e^{-(1+j)\tilde{\tau}_n/2}\left[e^{+(1+j)\tilde{\rho}'} - \Gamma_n e^{-(1+j)\tilde{\rho}'}\right] \qquad (4.4.9b)$$

or

$$H_{zn}(\tilde{\rho}') \underset{f\to\infty}{\approx} e^{-(1+j)\tilde{\tau}_n/2}\left[H_n e^{+(1+j)\tilde{\rho}'} + H_{n-1} e^{-(1+j)\tilde{\rho}'}\right] \quad (4.4.8a)$$

$$J_{\phi n}(\tilde{\rho}') \underset{f\to\infty}{\approx} -\frac{1+j}{\delta} e^{-(1+j)\tilde{\tau}_n/2}$$

$$\left[H_n e^{+(1+j)\tilde{\rho}'} - H_{n-1} e^{-(1+j)\tilde{\rho}'}\right]. \quad (4.4.10b)$$

Examination of these expressions reveals the crowding tendencies near the boundaries and the proportionality of them to the boundary conditions. Also evident is the fact that the fields and currents vanish in the limit at the center of the layer.

As a final confidence builder for the thin-layer approximations, it is encouraging to find that they satisfy both Maxwell's equations and the boundary conditions.

CHAPTER 5

OPTIMIZATION OF THE SINGLE-LAYER WINDING

In the last chapter the particular solutions for the magnetic field intensity and current density were determined for the single-layer problem. These solutions were studied in detail, and approximations were introduced to simplify the expressions and provide insight to the problem. During this process some interesting properties of the solutions were discovered which lead into the topic for this chapter, optimization. Before any optimization can take place, an appropriate quantity or quantities must be selected for optimization. Again, the results of the last chapter suggest a starting point. The power dissipation in the *n*th conductor layer is considered first. Next, the energy stored in the magnetic field within the *n*th conductor layer is determined. Both of these are studied at the three previously defined levels of accuracy: exact, large argument asymptotic approximation, and thin-layer approximation. As a consequence of these studies, an optimization technique based on them is developed at each of these three levels. Finally, a fourth and final level, the two-term series approximation, is introduced which provides a particularly simple and useful result in closed form.

5.1 POWER DISSIPATION

The time-averaged power dissipated in the nth conductor layer is determined in a straightforward manner by performing the integration in equation (3.2.15b) over the conducting region. First, the exact one-dimensional solutions for the current density are substituted. This will, of course, yield an exact expression for the power dissipation which can then be used to determine the validity of the various approximations. Employing the definitions in equations (4.2.8), (4.2.14), and (4.2.17); the integration initially proceeds as follows:

$$P_n = \frac{1}{2}\iiint_V \frac{1}{\sigma}|J|^2 dv$$

$$= \frac{1}{2\sigma}\int_0^{2\pi} d\phi \int_{-l/2}^{+l/2} dz \int_{\rho_n^i}^{\rho_n^o} |J_{\phi n}(\rho)|^2 \rho d\rho$$

$$= \frac{\pi l}{\sigma}|K_n|^2 \int_{\tilde{\rho}_n^i}^{\tilde{\rho}_n^o} |\tilde{J}_{\phi n}(\tilde{\rho})|^2 \tilde{\rho} d\tilde{\rho} = \frac{\pi l \tilde{\rho}_n}{\sigma}|K_n|^2 \tilde{P}_n;$$

$$n = 1,2,\ldots,N, \qquad (5.1.1)$$

where $\tilde{P}_n$ is defined as the normalized power dissipated in the nth conductor layer and is given by

$$\tilde{P}_n = \frac{1}{\tilde{\rho}_n} \int_{\tilde{\rho}_n^i}^{\tilde{\rho}_n^o} |\tilde{J}_{\phi n}(\tilde{\rho})|^2 \tilde{\rho} d\tilde{\rho}; \quad n = 1,2,\ldots,N. \qquad (5.1.2)$$

The subscript d has been dropped (dissipation now understood from context) in these expressions and replaced by the subscript n to indicate the nth layer. The normalization is such that the new quantity $\tilde{P}_n$ is unitless. The factored out portion $\frac{\pi l \tilde{\rho}_n}{\sigma} |K_n|^2$ represents the power dissipated in a one skin depth thick conductor layer carrying a uniform current density. As before, the reason for this normalization choice will become more apparent later when the approximate expressions are derived.

Substituting the exact solution from equations (4.2.15) and (4.2.16) into equation (5.1.2) above, and changing the variable of integration to x gives

$$\tilde{P}_n = \frac{1}{x_n \sqrt{2}} \int_{x_n^i}^{x_n^o} |\tilde{J}_{\phi n}(x)|^2 x dx$$

$$= \frac{\sqrt{2}}{x_n} \left| \frac{1}{1-\tilde{\Gamma}_n} \right|^2 \left\{ |\tilde{A}_{0n}|^2 \int_{x_n^i}^{x_n^o} (\mathrm{ber}_1^2 x + \mathrm{bei}_1^2 x) x dx \right.$$

$$\left. + 2\mathrm{Re}\left[\tilde{A}_{0n} \tilde{B}_{0n}^* \right] \int_{x_n^i}^{x_n^o} (\mathrm{ber}_1 x \mathrm{ker}_1 x + \mathrm{bei}_1 x \mathrm{kei}_1 x) x dx \right.$$

$$- 2\mathrm{Im}\left[\tilde{A}_{0n}\tilde{B}^{*}_{0n}\right]\int_{x_n^i}^{x_n^o}(\mathrm{bei}_1 x\,\mathrm{ker}_1 x - \mathrm{ber}_1 x\,\mathrm{kei}_1 x)x\,dx$$

$$+ |\tilde{B}_{0n}|^2\int_{x_n^i}^{x_n^o}(\mathrm{ker}_1^2 x + \mathrm{kei}_1^2 x)x\,dx\Big\};\ n = 1,2,\ldots,N \quad (5.1.3)$$

where the arbitrary complex constants $\tilde{A}_{0n}$ and $\tilde{B}_{0n}$ are given by equations (4.2.13). The four intergrals above involving first order Kelvin functions have been evaluated and are summarized in equations (B.3.2) and (B.3.3) of Appendix B. Performing the integrations and substituting for the constants yields the exact solution which turns out to be very lengthy and tedious. It is included here for completeness and future reference:

$$\tilde{P}_n = \frac{\sqrt{2}}{x_n}\left|\frac{1}{1-\Gamma_n}\right|^2\left[T_{1n} + T_{2n} + T_{3n} + T_{4n}\right];\ n = 1,2,\ldots,N, \quad (5.1.4)$$

where the four new terms are defined as

$$T_{1n} \doteq \frac{1}{|\tilde{D}_{0n}|^2}$$

$$\Big\{\left[\mathrm{ker}_0^2 x_n^i + \mathrm{kei}_0^2 x_n^i\right] - 2\mathrm{Re}(\Gamma_n)\left[\mathrm{ker}_0 x_n^i \mathrm{ker}_0 x_n^o + \mathrm{kei}_0 x_n^i \mathrm{kei}_0 x_n^o\right]$$

$$- 2\mathrm{Im}(\Gamma_n)\left[\mathrm{kei}_0 x_n^i \mathrm{ker}_0 x_n^o - \mathrm{ker}_0 x_n^i \mathrm{kei}_0 x_n^o\right] + |\Gamma_n|^2\left[\mathrm{ker}_0^2 x_n^o + \mathrm{kei}_0^2 x_n^o\right]\Big\}$$

$$\left\{\frac{x_n^o}{\sqrt{2}}\left[\mathrm{ber}_1 x_n^o \mathrm{ber}_0 x_n^o - \mathrm{ber}_1 x_n^o \mathrm{bei}_0 x_n^o + \mathrm{bei}_1 x_n^o \mathrm{ber}_0 x_n^o + \mathrm{bei}_1 x_n^o \mathrm{bei}_0 x_n^o\right]\right.$$
$$\left. - \frac{x_n^i}{\sqrt{2}}\left[\mathrm{ber}_1 x_n^i \mathrm{ber}_0 x_n^i - \mathrm{ber}_1 x_n^i \mathrm{bei}_0 x_n^i + \mathrm{bei}_1 x_n^i \mathrm{ber}_0 x_n^i + \mathrm{bei}_1 x_n^i \mathrm{bei}_0 x_n^i\right]\right\}$$

(5.1.4a)

$$T_{2n} \doteq -\frac{1}{|\tilde{D}_{0n}|^2}$$
$$\left\{\left[\mathrm{ber}_0 x_n^i \mathrm{ker}_0 x_n^i + \mathrm{bei}_0 x_n^i \mathrm{kei}_0 x_n^i\right] - \mathrm{Re}(\Gamma_n)\left[\mathrm{ber}_0 x_n^o \mathrm{ker}_0 x_n^i\right.\right.$$
$$\left. + \mathrm{bei}_0 x_n^o \mathrm{kei}_0 x_n^i + \mathrm{ber}_0 x_n^i \mathrm{ker}_0 x_n^o + \mathrm{bei}_0 x_n^i \mathrm{kei}_0 x_n^o\right] - \mathrm{Im}(\Gamma_n)$$
$$\left[\mathrm{ber}_0 x_n^o \mathrm{kei}_0 x_n^i - \mathrm{bei}_0 x_n^o \mathrm{ker}_0 x_n^i + \mathrm{bei}_0 x_n^i \mathrm{ker}_0 x_n^o - \mathrm{ber}_0 x_n^i \mathrm{kei}_0 x_n^o\right]$$
$$\left. + |\Gamma_n|^2\left[\mathrm{ber}_0 x_n^o \mathrm{ker}_0 x_n^o + \mathrm{bei}_0 x_n^o \mathrm{kei}_0 x_n^o\right]\right\}$$
$$\left\{\frac{x_n^o}{\sqrt{2}}\left[\mathrm{bei}_1 x_n^o \mathrm{ker}_0 x_n^o + \mathrm{bei}_1 x_n^o \mathrm{kei}_0 x_n^o - \mathrm{ker}_1 x_n^o \mathrm{bei}_0 x_n^o + \mathrm{ker}_1 x_n^o \mathrm{ber}_0 x_n^o\right.\right.$$
$$\left. - \mathrm{ber}_1 x_n^o \mathrm{kei}_0 x_n^o + \mathrm{ber}_1 x_n^o \mathrm{ker}_0 x_n^o + \mathrm{kei}_1 x_n^o \mathrm{ber}_0 x_n^o + \mathrm{kei}_1 x_n^o \mathrm{bei}_0 x_n^o\right]$$
$$\left. - \frac{x_n^i}{\sqrt{2}}\left[\mathrm{bei}_1 x_n^i \mathrm{ker}_0 x_n^i + \mathrm{bei}_1 x_n^i \mathrm{kei}_0 x_n^i - \mathrm{ker}_1 x_n^i \mathrm{bei}_0 x_n^i + \mathrm{ker}_1 x_n^i \mathrm{ber}_0 x_n^i\right.\right.$$
$$\left.\left. - \mathrm{ber}_1 x_n^i \mathrm{kei}_0 x_n^i + \mathrm{ber}_1 x_n^i \mathrm{ker}_0 x_n^i + \mathrm{kei}_1 x_n^i \mathrm{ber}_0 x_n^i + \mathrm{kei}_1 x_n^i \mathrm{bei}_0 x_n^i\right]\right\}$$

(5.1.4b)

$$T_{3n} \doteq \frac{1}{|\tilde{D}_{0n}|^2}$$
$$\left\{\left[\mathrm{ber}_0 x_n^i \mathrm{kei}_0 x_n^i - \mathrm{bei}_0 x_n^i \mathrm{ker}_0 x_n^i\right] - \mathrm{Re}(\Gamma_n)\left[\mathrm{ber}_0 x_n^o \mathrm{kei}_0 x_n^i\right.\right.$$

$$-\mathrm{bei}_0 x_n^o \mathrm{ker}_0 x_n^i + \mathrm{ber}_0 x_n^i \mathrm{kei}_0 x_n^o - \mathrm{bei}_0 x_n^i \mathrm{ker}_0 x_n^o \Big] - \mathrm{Im}(\Gamma_n)$$

$$\Big[-\mathrm{ber}_0 x_n^o \mathrm{ker}_0 x_n^i - \mathrm{bei}_0 x_n^o \mathrm{kei}_0 x_n^i + \mathrm{bei}_0 x_n^i \mathrm{kei}_0 x_n^o + \mathrm{ber}_0 x_n^i \mathrm{ker}_0 x_n^o \Big]$$

$$+ |\Gamma_n|^2 \Big[\mathrm{ber}_0 x_n^o \mathrm{kei}_0 x_n^o - \mathrm{bei}_0 x_n^o \mathrm{ker}_0 x_n^o \Big] \Big\}$$

$$\Big\{ \frac{x_n^o}{\sqrt{2}} \Big[\mathrm{ker}_1 x_n^o \mathrm{ber}_0 x_n^o + \mathrm{ker}_1 x_n^o \mathrm{bei}_0 x_n^o - \mathrm{ber}_1 x_n^o \mathrm{ker}_0 x_n^o - \mathrm{ber}_1 x_n^o \mathrm{kei}_0 x_n^o$$

$$+ \mathrm{kei}_1 x_n^o \mathrm{bei}_0 x_n^o - \mathrm{kei}_1 x_n^o \mathrm{ber}_0 x_n^o - \mathrm{bei}_1 x_n^o \mathrm{kei}_0 x_n^o + \mathrm{bei}_1 x_n^o \mathrm{ker}_0 x_n^o \Big]$$

$$- \frac{x_n^i}{\sqrt{2}} \Big[\mathrm{ker}_1 x_n^i \mathrm{ber}_0 x_n^i + \mathrm{ker}_1 x_n^i \mathrm{bei}_0 x_n^i - \mathrm{ber}_1 x_n^i \mathrm{ker}_0 x_n^i - \mathrm{ber}_1 x_n^i \mathrm{kei}_0 x_n^i$$

$$+ \mathrm{kei}_1 x_n^i \mathrm{bei}_0 x_n^i - \mathrm{kei}_1 x_n^i \mathrm{ber}_0 x_n^i - \mathrm{bei}_1 x_n^i \mathrm{kei}_0 x_n^i + \mathrm{bei}_1 x_n^i \mathrm{ker}_0 x_n^i \Big] \Big\}$$

(5.1.4c)

$$\Gamma_{4n} \doteq \frac{1}{|\tilde{D}_{0n}|^2}$$

$$\Big\{ \Big[\mathrm{ber}_0^2 x_n^i + \mathrm{bei}_0^2 x_n^i \Big] - 2\mathrm{Re}(\Gamma_n) \Big[\mathrm{ber}_0 x_n^i \mathrm{ber}_0 x_n^o + \mathrm{bei}_0 x_n^i \mathrm{bei}_0 x_n^o \Big]$$

$$- 2\mathrm{Im}(\Gamma_n) \Big[\mathrm{bei}_0 x_n^i \mathrm{ber}_0 x_n^o - \mathrm{ber}_0 x_n^i \mathrm{bei}_0 x_n^o \Big] + |\Gamma_n|^2 \Big[\mathrm{ber}_0^2 x_n^o + \mathrm{bei}_0^2 x_n^o \Big] \Big\}$$

$$\Big\{ \frac{x_n^o}{\sqrt{2}} \Big[\mathrm{ker}_1 x_n^o \mathrm{ker}_0 x_n^o - \mathrm{ker}_1 x_n^o \mathrm{kei}_0 x_n^o + \mathrm{kei}_1 x_n^o \mathrm{ker}_0 x_n^o + \mathrm{kei}_1 x_n^o \mathrm{kei}_0 x_n^o \Big]$$

$$- \frac{x_n^i}{\sqrt{2}} \Big[\mathrm{ker}_1 x_n^i \mathrm{ker}_0 x_n^i - \mathrm{ker}_1 x_n^i \mathrm{kei}_0 x_n^i + \mathrm{kei}_1 x_n^i \mathrm{ker}_0 x_n^i + \mathrm{kei}_1 x_n^i \mathrm{kei}_0 x_n^i \Big] \Big\},$$

(5.1.4d)

and $\tilde{D}_{0n}$ is defined to be the denominator of the arbitrary constants in equations (4.2.13), namely,

$$\mathcal{D}_{0n} = (\mathrm{ber}_0 x_n^o + j\mathrm{bei}_0 x_n^o)(\mathrm{ker}_0 x_n^i + j\mathrm{kei}_0 x_n^i)$$

$$- (\mathrm{ber}_0 x_n^i + j\mathrm{bei}_0 x_n^i)(\mathrm{ker}_0 x_n^o + j\mathrm{kei}_0 x_n^o). \qquad (5.1.5)$$

Note that Γ_n has been treated as a complex quantity in general. In practice, this rarely occurs. This quantity was defined in equation (4.2.11) as the ratio of the magnetic field intensity at the inner boundary to that at the outer boundary. While the boundary values themselves are complex in general, the ratio of them will usually be real because currents in adjacent layers are assumed to be in phase. Remember that the boundary conditions are determined successively from the enclosed current in each layer (see equation (4.1.12)). Thus, the boundary condition ratio will always be real within a single winding which by definition carries the same current, and the only condition under which it will become complex is at the interface between two windings carrying currents which are out of phase. Since the main interest at this point is restricted to a single layer, and then to a multi-layer winding; examples will include only real values for Γ_n. Most of the equations resulting from the analysis will be kept general, however, so that later more global problems can be considered such as how to order several different windings.

The evaluation of equation (5.1.4) is a formidable task to say the least. But it is one about which a computer will

offer no complaints (not necessarily the case for the programmer, though). From this equation, it is evident that the normalized power dissipated in the nth layer is a function of three independent variables: x_n^i, x_n^o, and Γ_n or equivalently: $\tilde{\tau}_n$, $\tilde{\rho}_n$, and Γ_n. For the following graphical results, the normalized conductor thickness $\tilde{\tau}_n$ is chosen as the abscissa. The normalized mean radius $\tilde{\rho}_n$ and the boundary condition ratio Γ_n will be varied as parameters.

Figure 5.1.1 shows the normalized power dissipated vs. the conductor thickness for several values of the boundary condition ratio between zero and unity. Values greater than unity are not shown since they produce essentially the same results as their reciprocal values. The normalized conductor mean radius is held constant at 20. The behavior of these curves is quite interesting. The power dissipation actually passes through a minimum with respect to the conductor layer thickness. For small values of the normalized conductor thickness, the current density is nearly uniform, and the solutions exhibit typical DC behavior. This was first noticed in the previous chapter (see Figures 4.2.1 through 4.2.4). The dissipated power is therefore inversely proportional to the conductor thickness because as the thickness increases the current density decreases causing a corresponding decrease in the power dissipation. As the thickness approaches one skin depth,

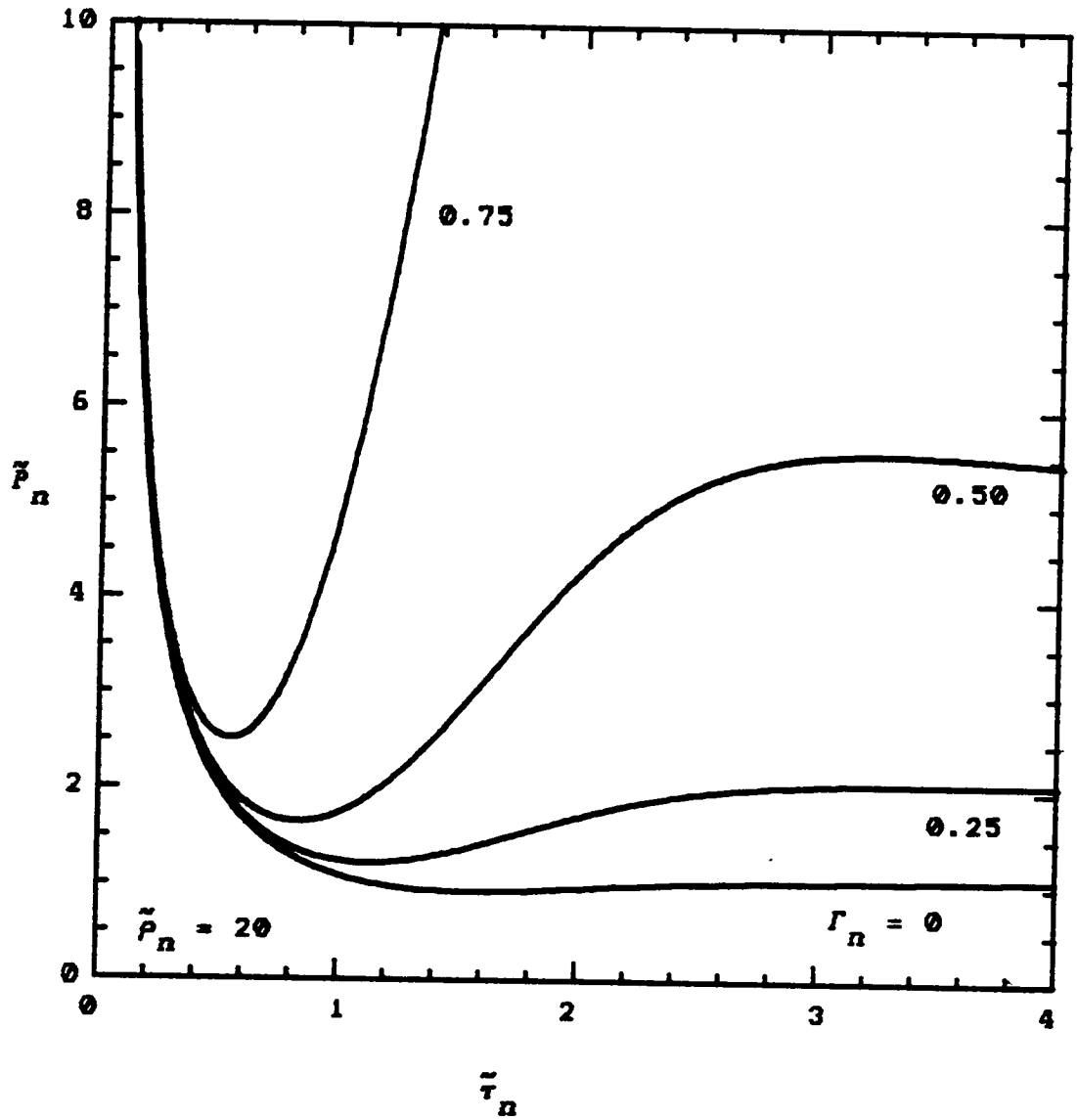

Figure 5.1.1. Normalized power dissipation in the nth layer vs. normalized conductor thickness with the boundary condition ratio varied as a parameter.

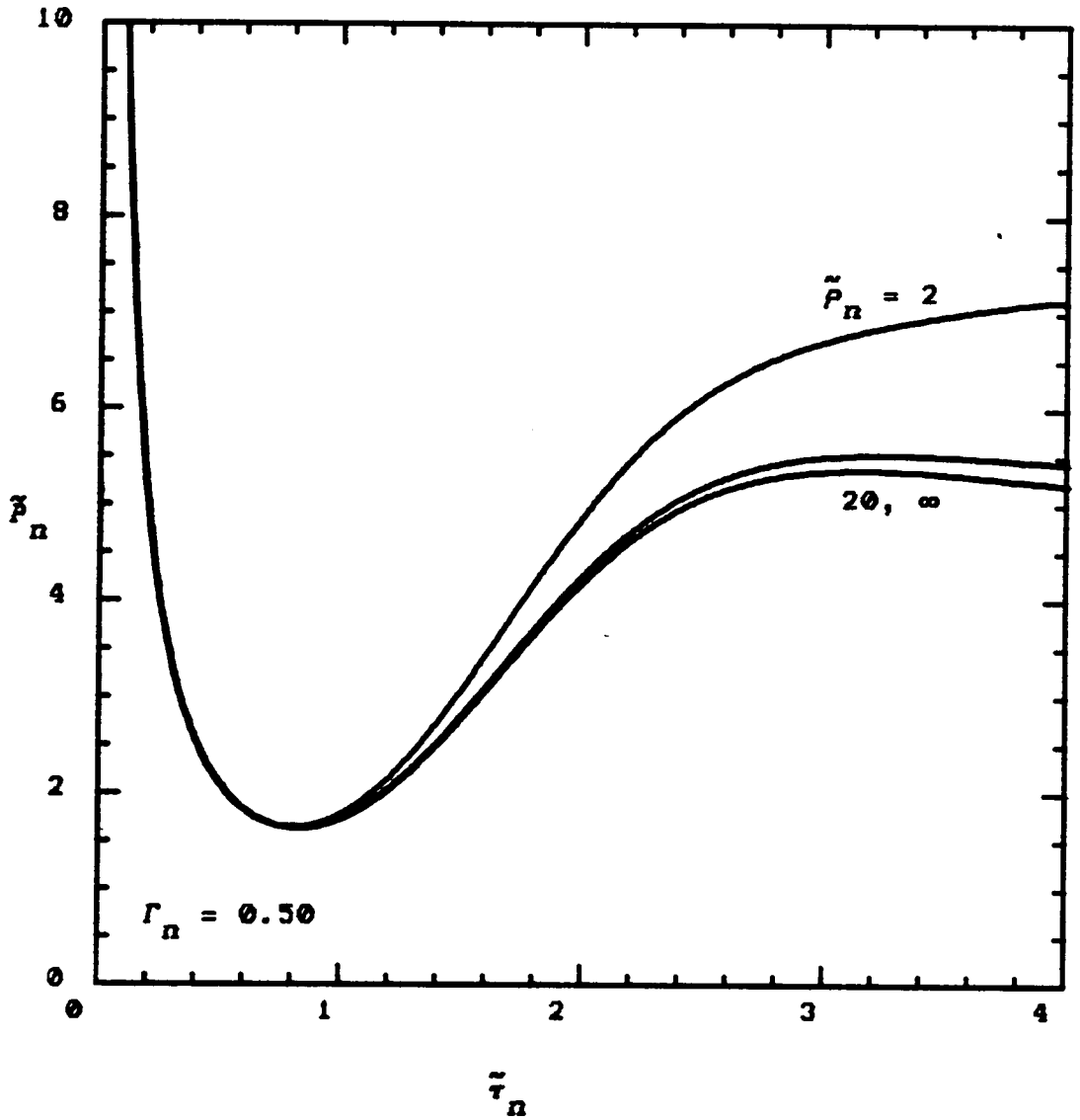

Figure 5.1.2. Normalized power dissipation in the *n*th layer vs. normalized conductor thickness with the normalized conductor mean radius varied as a parameter.

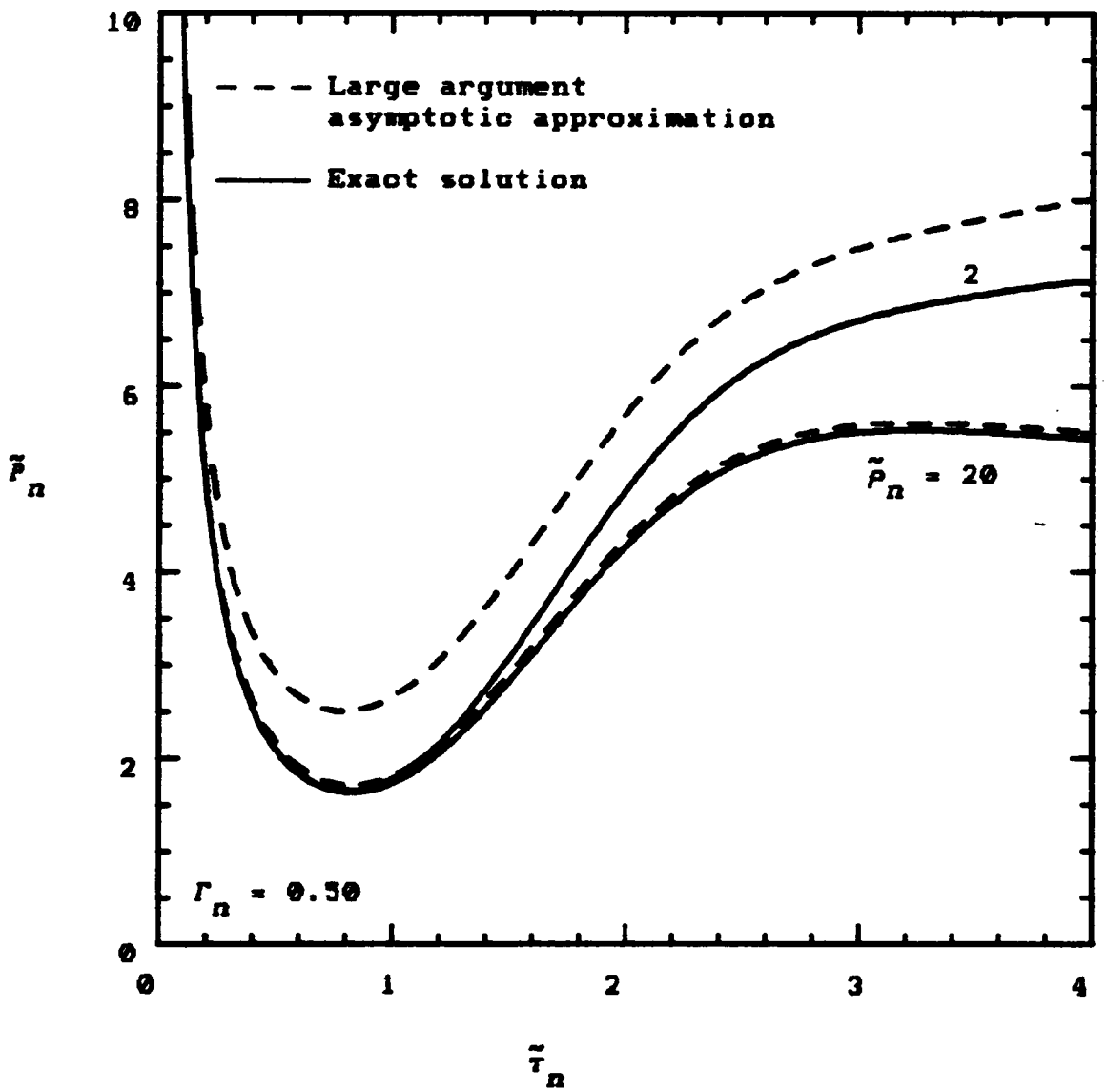

Figure 5.1.3. Normalized power dissipation in the *n*th layer vs. normalized conductor thickness with the normalized conductor mean radius varied as a parameter.

proximity effects begin to come into play. It was seen in the previous chapter that this causes current crowding and circulating currents. One would therefore expect the power dissipation to increase as a result. Thus, instead of continuing to asymptotically approach zero, the curves pass through a minimum and begin to increase again. The location and the sharpness of this minimum vary dramatically as a function of the boundary condition ratio Γ_n. This results because of the presence of external magnetic fields which influence the behavior within the conductor layer (the proximity effect). This behavior was demonstrated quite well in Figures 4.2.5 through 4.2.8, where it was evident that a boundary condition ratio approaching unity was equivalent to increasing the level of the external fields while keeping the enclosed current constant. Although it is difficult to see from the curve for $\Gamma_n = 0$ in Figure 5.1.1, it does have a broad minimum centered near one and a half skin depths. Finally, after passing through a minimum and then increasing again, the power dissipation begins to level off and asymptotically approaches a constant value for large conductor thicknesses. This is because increasing the conductor thickness beyond a certain point results in increasing only the unused portion of the conductor, since the currents are confined to a region near the boundaries.

Figure 5.1.2 presents another family of curves, where the normalized conductor center radius is varied, and the boundary condition ratio is fixed at $\Gamma_n = 0.5$. As before, there is very little difference in the curves from the practical minimum value of $\tilde{\rho}_n = 20$ all the way to $\tilde{\rho}_n = \infty$. Even for the small value of $\tilde{\rho}_n = 2$, the difference is not great especially in the critical region near the minimum.

So once again there is motivation to pursue a large argument asymptotic approximation. This is particularly true in light of the lengthy expressions in equations (5.1.4). There are two possible paths to follow which could, in general, lead to different results. The first and more exact one is to substitute the large argument asymptotic approximations of the Kelvin functions into equations (5.1.4) and simplify. The second alternative approach is to substitute the large argument asymptotic approximation already obtained for the current density in equation (4.3.2) into equation (5.1.1), and then perform the integration and simplify. The author has followed both paths and found that they lead to the same result:

$$\tilde{P}_n \sim \left|\frac{1}{1-\Gamma_n}\right|^2 \frac{1}{\cosh 2\tilde{\tau}_n - \cos 2\tilde{\tau}_n}$$

$$\left\{\left[\left(1 + \frac{1}{2}\frac{\tilde{\tau}_n}{\tilde{\rho}_n}\right) + \left(1 - \frac{1}{2}\frac{\tilde{\tau}_n}{\tilde{\rho}_n}\right)|\Gamma_n|^2\right]\left[\sinh 2\tilde{\tau}_n + \sin 2\tilde{\tau}_n\right]\right.$$

$$- 4\mathrm{Re}(\Gamma_n)\left[1 - (\frac{1}{2}\frac{\tilde{\tau}_n}{\tilde{\rho}_n})^2\right]^{\frac{1}{2}}\left[\cosh\tilde{\tau}_n\sin\tilde{\tau}_n + \cos\tilde{\tau}_n\sinh\tilde{\tau}_n\right]\Big\};$$

$$n = 1,2,\ldots,N. \qquad (5.1.6)$$

Although both paths are very tedious and lengthy, the second one is easier. Figure 5.1.3 presents a comparison of the large argument asymptotic approximation and the exact solutions for $\Gamma_n = 0.5$. The approximation is very good at $\tilde{\rho} = 20$; and, although not shown, the curves match exactly when $\tilde{\rho}_n \to \infty$ as they must. The agreement is not nearly as good at $\tilde{\rho}_n = 2$, and care should be exercised if future applications approach this range. The normalized conductor thickness which results in minimum power dissipation is approximated well, but the power dissipation itself is significantly higher than it should be.

Continuing on to the thin-layer approximation defined by equation (4.4.1) allows the $\tilde{\tau}_n/\tilde{\rho}_n$ terms to be neglected, yielding

$$\tilde{P}_n \approx |\frac{1}{1-\Gamma_n}|^2 \frac{1}{\cosh 2\tilde{\tau}_n - \cos 2\tilde{\tau}_n}\Big\{\left[1 + |\Gamma_n|^2\right]\left[\sinh 2\tilde{\tau}_n + \sin 2\tilde{\tau}_n\right]$$

$$- 4\mathrm{Re}(\Gamma_n)\left[\cosh\tilde{\tau}_n\sin\tilde{\tau}_n + \cos\tilde{\tau}_n\sinh\tilde{\tau}_n\right]\Big\};$$

$$n = 1,2,\ldots,N. \qquad (5.1.7)$$

The normalized conductor mean radius is now totally eliminated from the expression, which corresponds to letting $\tilde{\rho}_n \to \infty$. This expression for the thin-layer approximation was actually used to compute the $\tilde{\rho}_n = \infty$ curve in Figure 5.1.2. Once again, the practical range [20, ∞] for $\tilde{\rho}_n$ is seen have nearly the same result; and the power dissipation is represented well by the thin-layer approximation.

Before continuing to consider the energy stored, the low and high frequency limiting conditions for the normalized power in equation (5.1.7) are summarized. They are simple and useful formulas which help to confirm the work thus far:

$$\tilde{P}_n \underset{f\to 0}{\approx} \frac{1 - 2\mathrm{Re}(\Gamma_n) + |\Gamma_n|^2}{|1 - \Gamma_n|^2} \frac{1}{\tilde{\tau}_n} \qquad (5.1.8a)$$

$$\tilde{P}_n \underset{f\to \infty}{\approx} \frac{1 + |\Gamma_n|^2}{|1 - \Gamma_n|^2} \qquad (5.1.9a)$$

which, for real Γ_n, become

$$\tilde{P}_n \underset{f\to 0}{\approx} \frac{1}{\tilde{\tau}_n} \qquad (5.1.8b)$$

$$\tilde{P}_n \underset{f\to \infty}{\approx} \frac{1 + \Gamma_n^2}{(1 - \Gamma_n)^2}. \qquad (5.1.9b)$$

Equation (5.1.8b) gives the expected DC result when substituted back into the defining equation (5.1.1). Equation (5.1.9b) gives the constant values which the curves in Figure 5.1.1 asymptotically approach as the conductor thickness increases.

5.2 ENERGY STORAGE

Following exactly the same procedure as in the previous section, the time-averaged energy stored in the nth conductor layer is now derived and studied. Using the definitions in equations (4.2.8), (4.2.10), and (4.2.17) in the integration of equation (3.2.15a) gives

$$W_n \doteq \frac{1}{2}\iiint_V \frac{1}{2}\mu_o |\mathbf{H}|^2 dv$$

$$= \frac{1}{4}\mu_o \int_0^{2\pi} d\phi \int_{-l/2}^{+l/2} dz \int_{\rho_n^i}^{\rho_n^o} |H_{zn}(\rho)|^2 \rho d\rho$$

$$= \frac{\pi\mu_o l\delta^2}{2}|K_n|^2 \int_{\tilde{\rho}_n^i}^{\tilde{\rho}_n^o} |\tilde{H}_{zn}(\tilde{\rho})|^2 \tilde{\rho} d\tilde{\rho} \doteq \frac{\pi\mu_o l\delta^2}{4}\tilde{\rho}_n |K_n|^2 \tilde{W}_n;$$

$$n = 1,2,\ldots,N, \qquad (5.2.1)$$

where $\tilde{W}_n$ is defined as the normalized energy stored in the nth conductor layer and is given by

$$\tilde{U}_n = \frac{2}{\tilde{\rho}_n}\int_{\tilde{\rho}_n^i}^{\tilde{\rho}_n^o} |\tilde{H}_{zn}(\tilde{\rho})|^2 \tilde{\rho} d\tilde{\rho};\ n = 1,2,\ldots,N. \qquad (5.2.2)$$

The subscript m has been dropped (magnetic now understood from context) from these expressions and replaced by the subscript n to indicate the nth layer. The normalization is such that the new quantity $\tilde{U}_n$ is unitless. The factored out portion in equation (5.2.1) is proportional to the energy stored in a one skin depth thick conductor layer carrying a uniform current density.

Substituting the exact solution from equations (4.2.12) and (4.2.13) into equation (5.2.2) above, and changing the variable of integration to x gives

$$\tilde{U}_n = \frac{\sqrt{2}}{x_n}\int_{x_n^i}^{x_n^o} |\tilde{H}_{zn}(x)|^2 x dx$$

$$= \frac{\sqrt{2}}{x_n}\left|\frac{1}{1-\Gamma_n}\right|^2 \left\{ |\tilde{A}_{0n}|^2 \int_{x_n^i}^{x_n^o} (\mathrm{ber}_0^2 x + \mathrm{bei}_0^2 x) x dx \right.$$

$$+ 2\mathrm{Re}\left[\tilde{A}_{0n}\tilde{B}_{0n}^*\right] \int_{x_n^i}^{x_n^o} (\mathrm{ber}_0 x \mathrm{ker}_0 x + \mathrm{bei}_0 x \mathrm{kei}_0 x) x dx$$

$$\left. - 2\mathrm{Im}\left[\tilde{A}_{0n}\tilde{B}_{0n}^*\right] \int_{x_n^i}^{x_n^o} (\mathrm{bei}_0 x \mathrm{ker}_0 x - \mathrm{ber}_0 x \mathrm{kei}_0 x) x dx \right.$$

$$+ |\tilde{B}_{0n}|^2 \int_{x_n^i}^{x_n^o} (\mathrm{ker}_0^2 x + \mathrm{kei}_0^2 x) x dx \Big\}; \quad n = 1,2,\ldots,N. \qquad (5.2.3)$$

The four integrals in this expression are summarized in equations (B.3.2) and (B.3.3) of Appendix B. Using those formulas and substituting equations (4.2.13) for the arbitrary constants $\tilde{A}_{0n}$ and $\tilde{B}_{0n}$ yields the exact solution (which is very similar in form to the corresponding result for the normalized power):

$$\tilde{U}_n = \frac{\sqrt{2}}{x_n} \left| \frac{1}{1-\Gamma_n} \right|^2 \left[T'_{1n} + T'_{2n} + T'_{3n} + T'_{4n} \right]; \quad n = 1,2,\ldots,N, \qquad (5.2.4)$$

where the four new primed terms are defined as

$$T'_{1n} \doteq \frac{1}{|\tilde{D}_{0n}|^2}$$

$$\Big\{ \left[\mathrm{ker}_0^2 x_n^i + \mathrm{kei}_0^2 x_n^i \right] - 2\mathrm{Re}(\Gamma_n) \left[\mathrm{ker}_0 x_n^i \mathrm{ker}_0 x_n^o + \mathrm{kei}_0 x_n^i \mathrm{kei}_0 x_n^o \right]$$

$$- 2\mathrm{Im}(\Gamma_n) \left[\mathrm{kei}_0 x_n^i \mathrm{ker}_0 x_n^o - \mathrm{ker}_0 x_n^i \mathrm{kei}_0 x_n^o \right] + |\Gamma_n|^2 \left[\mathrm{ker}_0^2 x_n^o + \mathrm{kei}_0^2 x_n^o \right] \Big\}$$

$$\Big\{ \frac{x_n^o}{\sqrt{2}} \left[-\mathrm{ber}_0 x_n^o \mathrm{ber}_1 x_n^o + \mathrm{ber}_0 x_n^o \mathrm{bei}_1 x_n^o - \mathrm{bei}_0 x_n^o \mathrm{ber}_1 x_n^o - \mathrm{bei}_0 x_n^o \mathrm{bei}_1 x_n^o \right]$$

$$- \frac{x_n^i}{\sqrt{2}} \left[-\mathrm{ber}_0 x_n^i \mathrm{ber}_1 x_n^i + \mathrm{ber}_0 x_n^i \mathrm{bei}_1 x_n^i - \mathrm{bei}_0 x_n^i \mathrm{ber}_1 x_n^i - \mathrm{bei}_0 x_n^i \mathrm{bei}_1 x_n^i \right] \Big\}$$

(5.2.4a)

$$T'_{2n} \doteq -\frac{1}{|\tilde{D}_{0n}|^2}$$

$$\left\{\left[\mathrm{ber}_0 x_n^i \mathrm{ker}_0 x_n^i + \mathrm{bei}_0 x_n^i \mathrm{kei}_0 x_n^i\right] - \mathrm{Re}(\Gamma_n)\left[\mathrm{ber}_0 x_n^o \mathrm{ker}_0 x_n^i\right.\right.$$

$$\left. + \mathrm{bei}_0 x_n^o \mathrm{kei}_0 x_n^i + \mathrm{ber}_0 x_n^i \mathrm{ker}_0 x_n^o + \mathrm{bei}_0 x_n^i \mathrm{kei}_0 x_n^o\right] - \mathrm{Im}(\Gamma_n)$$

$$\left[\mathrm{ber}_0 x_n^o \mathrm{kei}_0 x_n^i - \mathrm{bei}_0 x_n^o \mathrm{ker}_0 x_n^i + \mathrm{bei}_0 x_n^i \mathrm{ker}_0 x_n^o - \mathrm{ber}_0 x_n^i \mathrm{kei}_0 x_n^o\right]$$

$$\left. + |\Gamma_n|^2\left[\mathrm{ber}_0 x_n^o \mathrm{ker}_0 x_n^o + \mathrm{bei}_0 x_n^o \mathrm{kei}_0 x_n^o\right]\right\}$$

$$\left\{\frac{x_n^o}{\sqrt{2}}\left[-\mathrm{bei}_0 x_n^o \mathrm{ker}_1 x_n^o - \mathrm{bei}_0 x_n^o \mathrm{kei}_1 x_n^o + \mathrm{ker}_0 x_n^o \mathrm{bei}_1 x_n^o - \mathrm{ker}_0 x_n^o \mathrm{ber}_1 x_n^o\right.\right.$$

$$\left. + \mathrm{ber}_0 x_n^o \mathrm{kei}_1 x_n^o - \mathrm{ber}_0 x_n^o \mathrm{ker}_1 x_n^o - \mathrm{kei}_0 x_n^o \mathrm{ber}_1 x_n^o - \mathrm{kei}_0 x_n^o \mathrm{bei}_1 x_n^o\right]$$

$$- \frac{x_n^i}{\sqrt{2}}\left[-\mathrm{bei}_0 x_n^i \mathrm{ker}_1 x_n^i - \mathrm{bei}_0 x_n^i \mathrm{kei}_1 x_n^i + \mathrm{ker}_0 x_n^i \mathrm{bei}_1 x_n^i - \mathrm{ker}_0 x_n^i \mathrm{ber}_1 x_n^i\right.$$

$$\left.\left. + \mathrm{ber}_0 x_n^i \mathrm{kei}_1 x_n^i - \mathrm{ber}_0 x_n^i \mathrm{ker}_1 x_n^i - \mathrm{kei}_0 x_n^i \mathrm{ber}_1 x_n^i - \mathrm{kei}_0 x_n^i \mathrm{bei}_1 x_n^i\right]\right\}$$

(5.2.4b)

$$T'_{3n} \doteq \frac{1}{|\tilde{D}_{0n}|^2}$$

$$\left\{\left[\mathrm{ber}_0 x_n^i \mathrm{kei}_0 x_n^i - \mathrm{bei}_0 x_n^i \mathrm{ker}_0 x_n^i\right] - \mathrm{Re}(\Gamma_n)\left[\mathrm{ber}_0 x_n^o \mathrm{kei}_0 x_n^i\right.\right.$$

$$\left. - \mathrm{bei}_0 x_n^o \mathrm{ker}_0 x_n^i + \mathrm{ber}_0 x_n^i \mathrm{kei}_0 x_n^o - \mathrm{bei}_0 x_n^i \mathrm{ker}_0 x_n^o\right] - \mathrm{Im}(\Gamma_n)$$

$$\left[-\mathrm{ber}_0 x_n^o \mathrm{ker}_0 x_n^i - \mathrm{bei}_0 x_n^o \mathrm{kei}_0 x_n^i + \mathrm{bei}_0 x_n^i \mathrm{kei}_0 x_n^o + \mathrm{ber}_0 x_n^i \mathrm{ker}_0 x_n^o\right]$$

$$\left. + |\Gamma_n|^2\left[\mathrm{ber}_0 x_n^o \mathrm{kei}_0 x_n^o - \mathrm{bei}_0 x_n^o \mathrm{ker}_0 x_n^o\right]\right\}$$

$$\left\{\frac{x_n^o}{\sqrt{2}}\left[-\mathrm{ker}_0 x_n^o \mathrm{ber}_1 x_n^o - \mathrm{ker}_0 x_n^o \mathrm{bei}_1 x_n^o + \mathrm{ber}_0 x_n^o \mathrm{ker}_1 x_n^o + \mathrm{ber}_0 x_n^o \mathrm{kei}_1 x_n^o\right.\right.$$

$$\left. - \mathrm{kei}_0 x_n^o \mathrm{bei}_1 x_n^o + \mathrm{kei}_0 x_n^o \mathrm{ber}_1 x_n^o + \mathrm{bei}_0 x_n^o \mathrm{kei}_1 x_n^o - \mathrm{bei}_0 x_n^o \mathrm{ker}_1 x_n^o\right]$$

$$- \frac{x_n^i}{\sqrt{2}}\Big[-ker_0 x_n^i ber_1 x_n^i - ker_0 x_n^i bei_1 x_n^i + ber_0 x_n^i ker_1 x_n^i + ber_0 x_n^i kei_1 x_n^i$$

$$-kei_0 x_n^i bei_1 x_n^i + kei_0 x_n^i ber_1 x_n^i + bei_0 x_n^i kei_1 x_n^i - bei_0 x_n^i ker_1 x_n^i\Big]\Big\} \tag{5.2.4c}$$

$$\Gamma'_{4n} \doteq \frac{1}{|\tilde{D}_{0n}|^2}$$

$$\Big\{\Big[ber_0^2 x_n^i + bei_0^2 x_n^i\Big] - 2Re(\Gamma_n)\Big[ber_0 x_n^i ber_0 x_n^o + bei_0 x_n^i bei_0 x_n^o\Big]$$

$$- 2Im(\Gamma_n)\Big[bei_0 x_n^i ber_0 x_n^o - ber_0 x_n^i bei_0 x_n^o\Big] + |\Gamma_n|^2\Big[ber_0^2 x_n^o + bei_0^2 x_n^o\Big]\Big\}$$

$$\Big\{\frac{x_n^o}{\sqrt{2}}\Big[-ker_0 x_n^o ker_1 x_n^o + ker_0 x_n^o kei_1 x_n^o - kei_0 x_n^o ker_1 x_n^o - kei_0 x_n^o kei_1 x_n^o\Big]$$

$$- \frac{x_n^i}{\sqrt{2}}\Big[-ker_0 x_n^i ker_1 x_n^i + ker_0 x_n^i kei_1 x_n^i - kei_0 x_n^i ker_1 x_n^i - kei_0 x_n^i kei_1 x_n^i\Big]\Big\}, \tag{5.2.4d}$$

and $\tilde{D}_{0n}$ is given by equation (5.1.5). The corresponding large argument asymptotic approximation is determined as before, yielding

$$\tilde{U}_n \sim \Big|\frac{1}{1-\Gamma_n}\Big|^2 \frac{1}{\cosh 2\tilde{\tau}_n - \cos 2\tilde{\tau}_n}$$

$$\Big\{\Big[\Big(1 + \frac{1}{2}\frac{\tilde{\tau}_n}{\tilde{\rho}_n}\Big) + \Big(1 - \frac{1}{2}\frac{\tilde{\tau}_n}{\tilde{\rho}_n}\Big)|\Gamma_n|^2\Big]\Big[\sinh 2\tilde{\tau}_n - \sin 2\tilde{\tau}_n\Big]$$

$$+ 4Re(\Gamma_n)\Big[1 - \Big(\frac{1}{2}\frac{\tilde{\tau}_n}{\tilde{\rho}_n}\Big)^2\Big]^{\frac{1}{2}}\Big[\cosh\tilde{\tau}_n \sin\tilde{\tau}_n - \cos\tilde{\tau}_n \sinh\tilde{\tau}_n\Big]\Big\};$$

$$n = 1, 2, \ldots, N. \tag{5.2.5}$$

Likewise, the thin-layer approximation is

$$\tilde{U}_n \approx \left|\frac{1}{1-\Gamma_n}\right|^2 \frac{1}{\cosh 2\tilde{\tau}_n - \cos 2\tilde{\tau}_n} \left\{\left[1 + |\Gamma_n|^2\right]\left[\sinh 2\tilde{\tau}_n - \sin 2\tilde{\tau}_n\right]\right.$$

$$\left. + 4\mathrm{Re}(\Gamma_n)\left[\cosh\tilde{\tau}_n \sin\tilde{\tau}_n - \cos\tilde{\tau}_n \sinh\tilde{\tau}_n\right]\right\};$$

$$n = 1,2,\ldots,N. \qquad (5.2.6)$$

Both of these expressions are functionally similar in appearance to their counterparts for the dissipated power. There are key sign changes, however, which result in major differences in the characteristics of the solutions.

Figures 5.2.1 through 5.2.3 present the graphical results for the normalized energy stored in the nth conductor layer. They correspond to the same conditions under which the normalized power dissipation was presented in Figures 5.1.1 through 5.1.3. All of the curves for the stored energy begin at zero for zero conductor thickness and increase almost linearly for small thicknesses. This behavior continues until the thickness reaches approximately two skin depths, at which time it passes through a slight maximum and then approaches a constant value for large values of thickness. The curves shift upward dramatically as the boundary condition ratio increases. This is easily understood since it corresponds to increasing the level of the magnetic field intensity via the boundary conditions

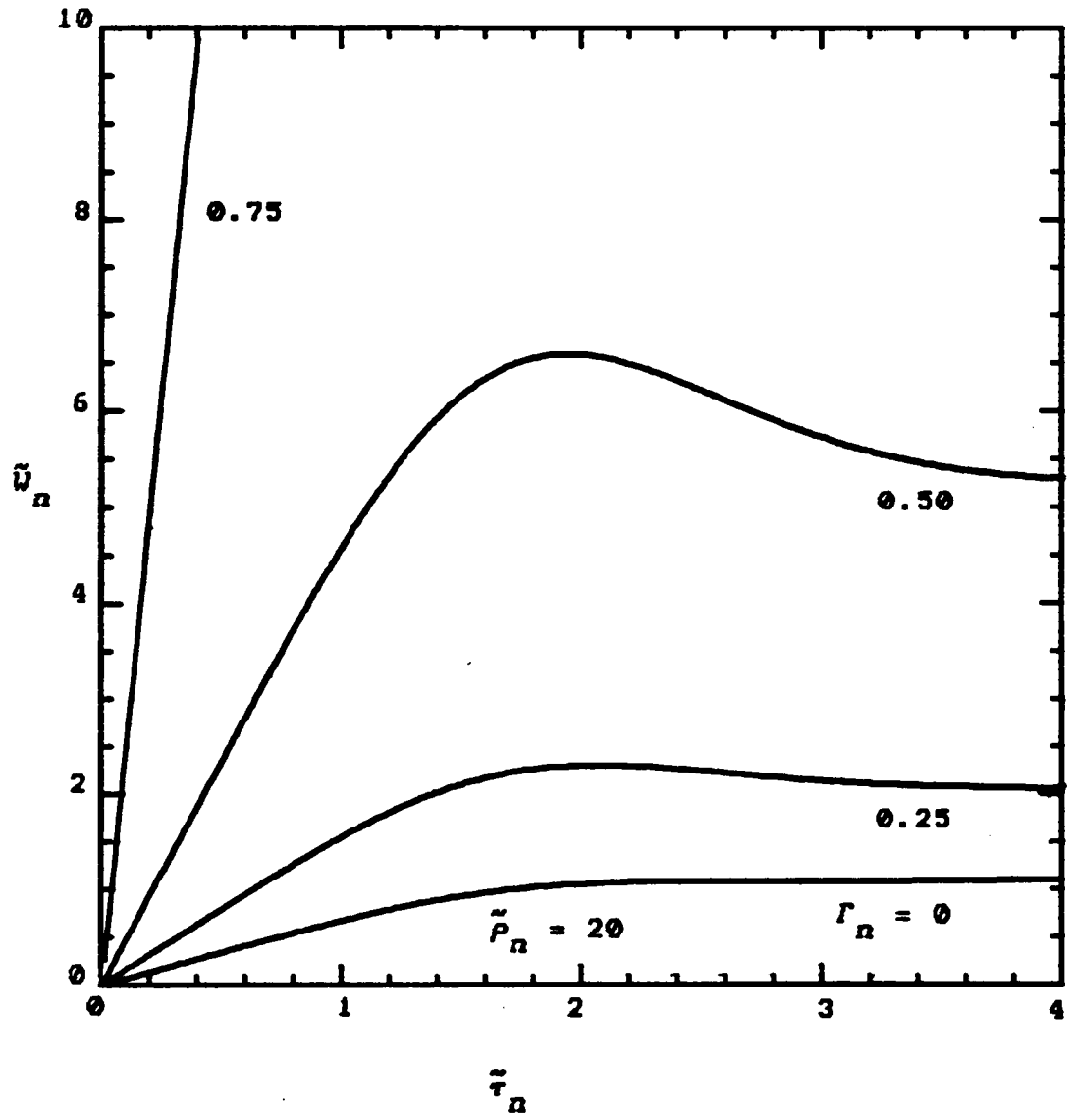

Figure 5.2.1. Normalized energy stored in the nth layer vs. normalized conductor thickness with the boundary condition ratio varied as a parameter.

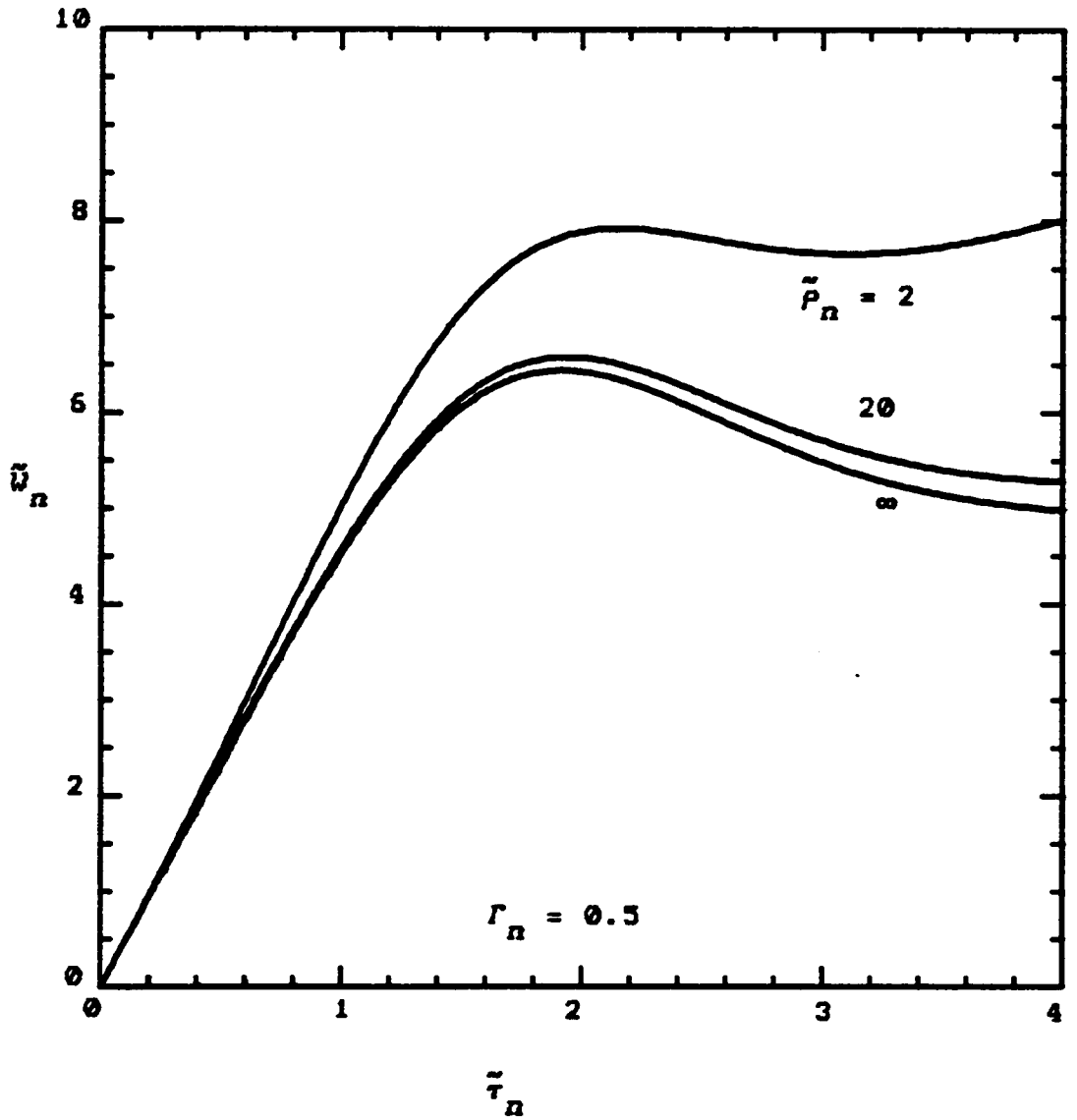

Figure 5.2.2. Normalized energy stored in the nth layer vs. normalized conductor thickness with the normalized conductor mean radius varied as a parameter.

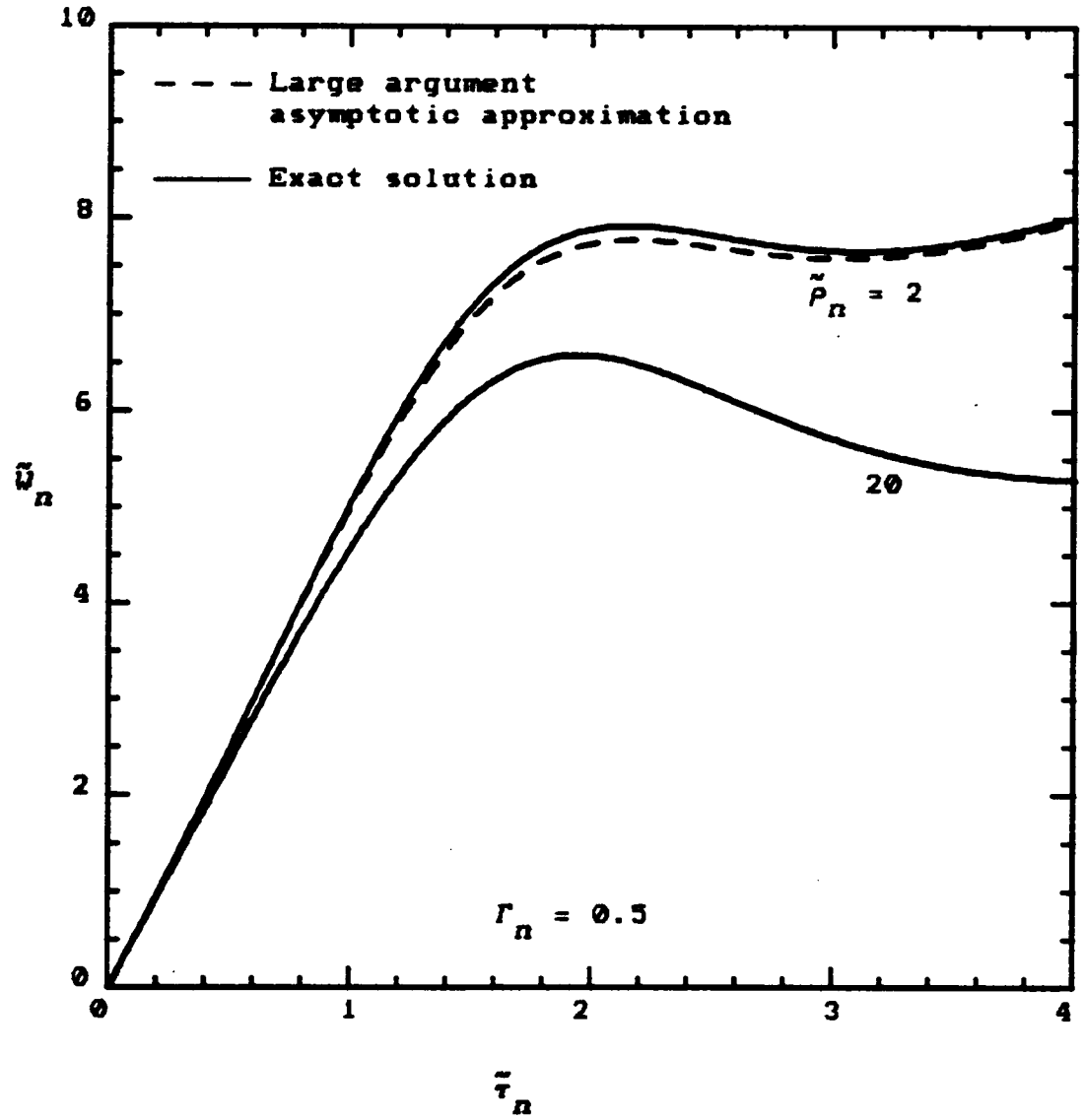

Figure 5.2.3. Normalized energy stored in the *n*th layer vs. normalized conductor thickness with the normalized conductor mean radius varied as a parameter.

which are influenced by external conductors (see Figure 4.2.7). The effect of the normalized mean radius is once again seen to be minor in the range [20, ∞]. As $\tilde{\rho}_n$ decreases below this range, the curve shifts upward especially for large thicknesses. It is interesting to note that the minima of the normalized power curves occur roughly in the middle of the linear region of the stored energy curves. As before, both the large argument asymptotic and the thin-layer approximations are very good for conditions of current practical interest. In fact, the approximations here are somewhat better than those for the normalized power dissipation. This goes back to the difference in the accuracy of large argument asymptotic approximations of zero order Kelvin functions as compared to first order ones.

Finally, the low and high frequency limiting forms for the thin-layer approximation of equation (5.2.6) are derived and summarized:

$$\tilde{W}_n \underset{f\to 0}{\approx} \frac{1 + \mathrm{Re}(\Gamma_n) + |\Gamma_n|^2}{|1 - \Gamma_n|^2} \frac{2\tilde{\tau}_n}{3} \qquad (5.2.7a)$$

$$\tilde{W}_n \underset{f\to \infty}{\approx} \frac{1 + |\Gamma_n|^2}{|1 - \Gamma_n|^2} \qquad (5.2.8a)$$

which, for real Γ_n, become

$$\tilde{w}_n \underset{f\to 0}{\approx} \frac{1 + \Gamma_n + \Gamma_n^2}{(1 - \Gamma_n)^2} \frac{2\tilde{\tau}_n}{3} \qquad (5.2.7b)$$

$$\tilde{w}_n \underset{f\to \infty}{\approx} \frac{1 + \Gamma_n^2}{(1 - \Gamma_n)^2}. \qquad (5.2.8b)$$

Equations (5.2.7) verify the linear dependence and reduce to the correct DC result when substituted into the defining equation (5.2.1). Equations (5.2.8) give simple expressions for the constant values which the curves in Figure 5.2.1 asymptotically approach as the conductor thickness increases.

5.3 MINIMUM POWER OPTIMIZATION

Both the power dissipated and energy stored in the *n*th layer of a winding have now been determined. How can performance be optimized based on these quantities? Obviously, it is desirable to minimize the power dissipation since this will result in a higher overall converter efficiency. It also lowers the operating temperature of the transformer, which results in either reduced stress or a possible size reduction. The stored energy represents energy stored in the leakage fields of the transformer which

gives rise to what is commonly referred to as the leakage inductance. In most applications the leakage inductance is a parasitic element that one would like to eliminate. In a few limited applications it can be used in a beneficial way. But even for these cases it is not necessarily desirable to increase or decrease the leakage inductance but to simply know what it is. So, in summary, it is generally desirable to minimize both the power dissipation and the energy storage with emphasis on the the former.

The exact solutions and their large argument asymptotic approximations are functions of three independent variables: the normalized mean radius $\tilde{\rho}_n$, the normalized conductor thickness $\tilde{\tau}_n$, and the boundary condition ratio r_n.

The effect of the mean radius thus far has been minor especially in the practical range [20, ∞]. Below this range both the normalized power dissipation and energy storage increase only slightly. Optimization with respect to the mean radius is therefore not very useful. In fact, most designs do not offer much flexibility in this respect since the frequency and throughput power roughly determine the overall transformer size. There are two possible options available to the designer with respect to the mean radius which may reduce the power dissipation and energy stored in the leakage fields. The first is to keep the absolute mean radius as small as possible (see equations (5.1.1) and

(5.2.1)). Secondly, it may be desirable to keep the normalized mean radius large (see Figures 5.1.2 and 5.2.2). Both of these can be accomplished simultaneously if the operating frequency is increased enough.

A similar situation exists for the boundary condition ratio. It is evident from Figures 5.1.1 and 5.2.1 that this ratio should be kept as small as possible. The boundary conditions of any given conductor layer are determined by its position relative to the other layers in the transformer, and also by the currents in those layers. It is therefore desirable to arrange the windings in such a way to minimize the boundary condition ratio for as many layers as possible. Thus, optimization with respect to the boundary condition ratio is a global consideration which cannot be exploited within the single-layer problem. Global topics will be considered in more detail later. For now, the boundary condition ratio is considered to be a given quantity which cannot be changed.

The third and final parameter available in the single-layer problem is the normalized conductor thickness $\tilde{\tau}_n$. Fortunately, this parameter provides an excellent basis for optimization. This is immediately evident from the normalized power dissipation curves in Figures 5.1.1 through 5.1.3. All of these curves exhibit a unique minimum at a certain normalized conductor thickness. These points will

be designated as the normalized optimum thicknesses $\tilde{\tau}_n^{opt}$ and the corresponding normalized power dissipation minima $\tilde{P}_n^{min}$. A similar examination of Figures 5.2.1 through 5.2.3 does not reveal any optimization possibilities with respect to the stored energy other than the obvious one of reducing the thickness to zero which is certainly not practical. It is encouraging to note that the minima of the normalized power curves occur at thicknesses which result in stored energies that are somewhat below their maxima. The single-layer optimization is therefore chosen to be based on minimizing the power dissipation, with the possibility of adjusting the stored energy if the application demands it.

Minimizing the power dissipation with respect to the conductor thickness is a straightforward procedure and involves solving the equation

$$\frac{\partial \tilde{P}_n}{\partial \tilde{\tau}_n} = 0 \qquad (5.3.1)$$

for the optimum thickness $\tilde{\tau}_n^{opt}$ and checking to see that the resulting power is the desired minimum $\tilde{P}_n^{min}$. Even though the procedure is straightfoward, the possibility of applying it to the exact solution in equations (5.1.4) is somewhat intimidating. The author has pursued this exercise to the point where it was realized that analytical

simplification was no longer apparent. The obvious alternative is to use a computer. An algorithm based on a discrete form of Newton's method is employed to find the minimum of the normalized power dissipation. Convergence to an acceptable accuracy is obtained after only two to five iterations depending on parameter values and the accuracy of the initial guess. Results are presented in Figures 5.3.1 through 5.3.3. The optimized quantities $\tilde{\tau}_n^{opt}$ and $\tilde{P}_n^{min}$ are both functions of two parameters. The first and most important is the boundary condition ratio Γ_n which is chosen as the abscissa. The second is the normalized mean radius $\tilde{\rho}_n$ which only slightly affects the results. Figure 5.3.1 gives the results for the optimum conductor layer thickness. Notice that the optimum thickness lies in the approximate range 0 to 1.57 skin depths. This is an important result, one which provides a very useful and handy rule of thumb. Note also that the optimum thickness decreases as the boundary condition ratio increases toward unity, a result that was also evident in the previously obtained curves for the normalized power dissipation. Figure 5.3.2 shows the corresponding minimum values of the normalized power dissipation. Even under optimum conditions the power dissipation increases, first slowly, then more rapidly as the boundary condition ratio approaches unity. Similar and even more exaggerated behavior is exhibited by

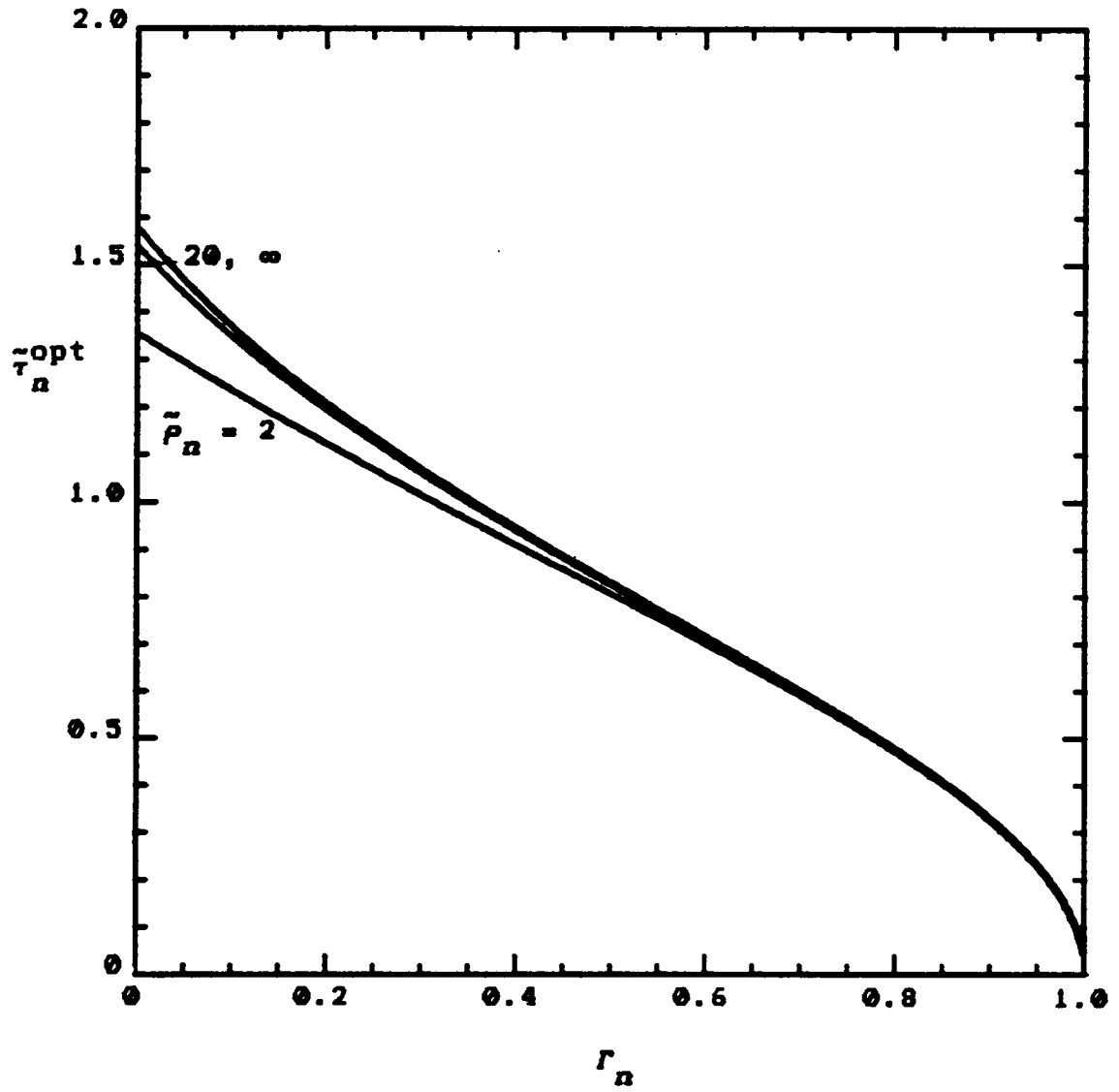

Figure 5.3.1. Normalized optimum conductor thickness of the *n*th layer vs. boundary condition ratio with the normalized conductor mean radius varied as a parameter.

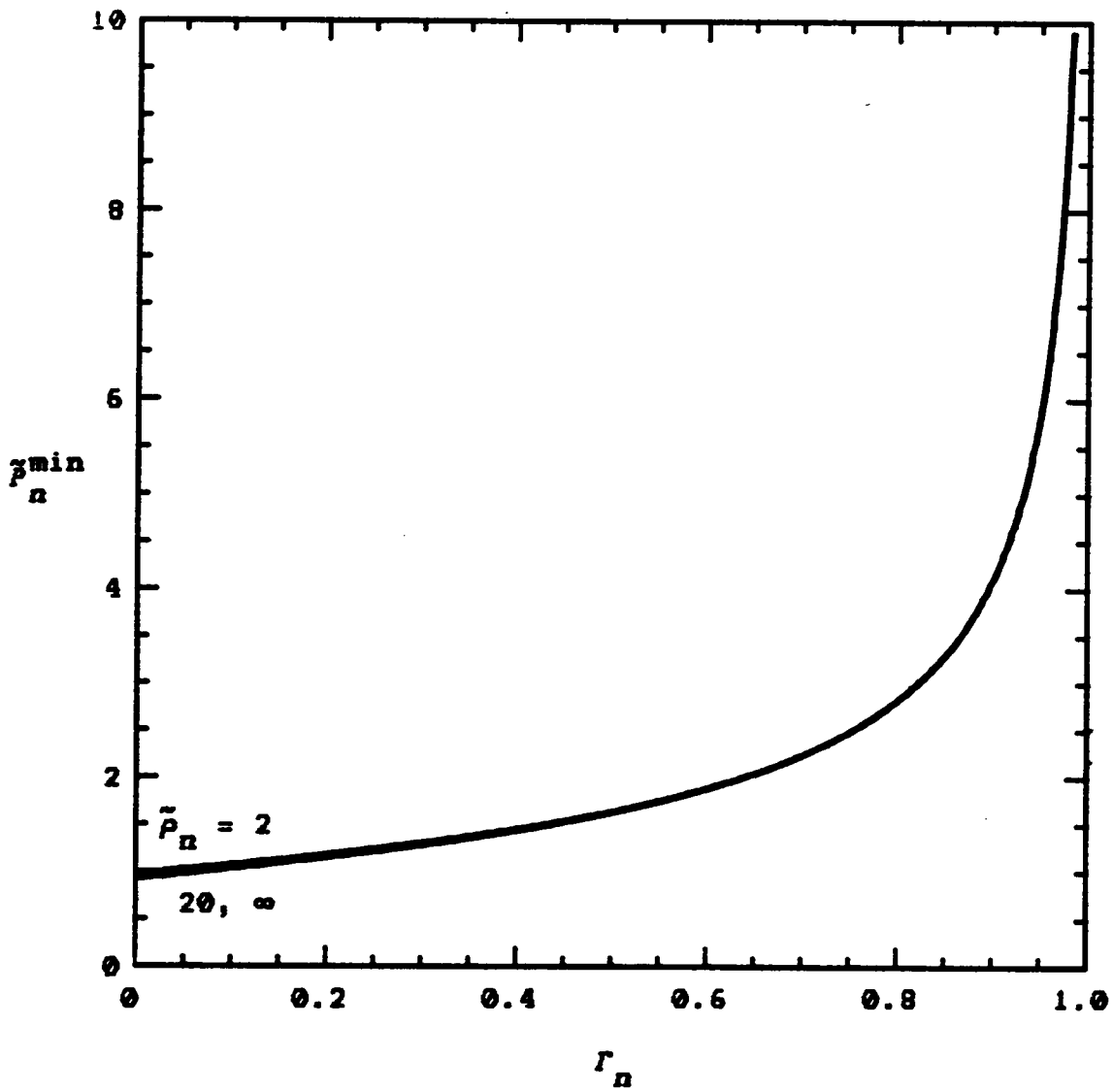

Figure 5.3.2. Minimum normalized power dissipation (at optimum conductor thickness) in the nth layer vs. boundary condition ratio with the normalized conductor mean radius varied as a parameter.

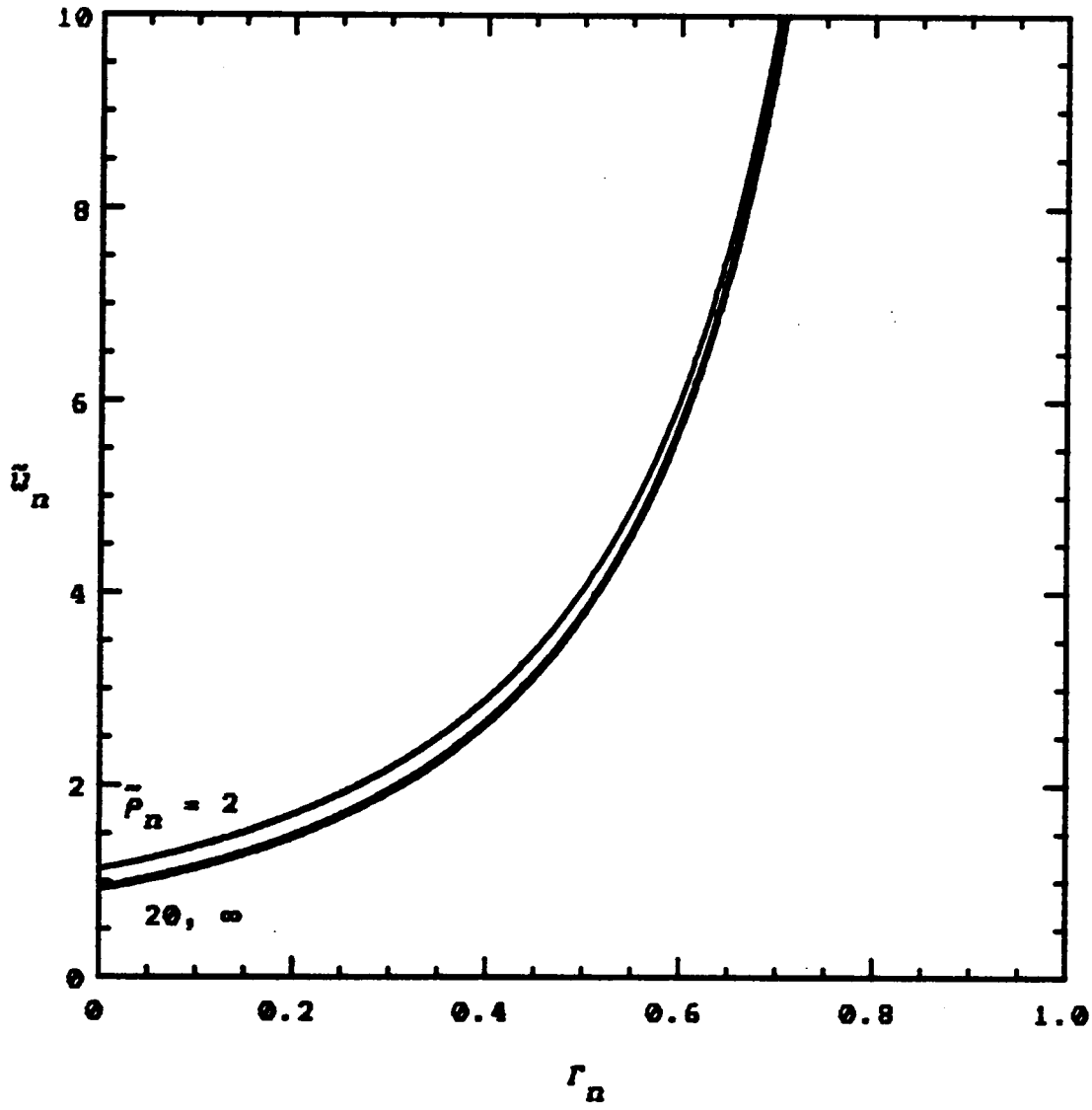

Figure 5.3.3. Normalized energy stored (at optimum conductor thickness) in the *n*th layer vs. boundary condition ratio with the normalized conductor mean radius varied as a parameter.

the stored energy in Figure 5.3.3. In conclusion, it is interesting to note that the optimized solutions seem to exhibit less dependency on the conductor mean radius than the solutions in general. This is because major differences which occur for very small mean radii do not appear until above the optimum thickness (see Figures 5.1.2 and 5.2.2).

In keeping with previous work, the logical next step is to perform the minimization on the large argument asymptotic approximation in equation (5.1.6). This is much more tractable than using the exact solutions, and results in the transcendental equation

$$(1 + |\Gamma_n|^2)\cosh\tilde{\tau}_n\cos\tilde{\tau}_n\left\{1 + \frac{1}{2}\frac{\tilde{\tau}_n}{\tilde{\rho}_n}\frac{1 - |\Gamma_n|^2}{1 + |\Gamma_n|^2}\left[1 - \frac{(\sinh 2\tilde{\tau}_n + \sin 2\tilde{\tau}_n)(\cosh 2\tilde{\tau}_n - \cos 2\tilde{\tau}_n)}{4\tilde{\tau}_n \sinh 2\tilde{\tau}_n \sin 2\tilde{\tau}_n}\right]\right\} =$$

$$\mathrm{Re}(\Gamma_n)\left[1-\left(\frac{1}{2}\frac{\tilde{\tau}_n}{\tilde{\rho}_n}\right)^2\right]^{\frac{1}{2}}(\cosh^2\tilde{\tau}_n + \cos^2\tilde{\tau}_n)\left\{1 + \left[1-\left(\frac{1}{2}\frac{\tilde{\tau}_n}{\tilde{\rho}_n}\right)^2\right]^{-1}\left(\frac{1}{2}\frac{\tilde{\tau}_n}{\tilde{\rho}_n}\right)^2\left[\frac{(\cosh\tilde{\tau}_n\sin\tilde{\tau}_n + \cos\tilde{\tau}_n\sinh\tilde{\tau}_n)(\cosh 2\tilde{\tau}_n - \cos 2\tilde{\tau}_n)}{4\tilde{\tau}_n\sinh\tilde{\tau}_n\sin\tilde{\tau}_n(\cosh^2\tilde{\tau}_n + \cos^2\tilde{\tau}_n)}\right]\right\}. \quad (5.3.2)$$

Further simplification of this expression does not seem possible, and again one must turn to the resources of a

computer. There are two main choices, the first of which is to solve the above equation numerically. The second one is to employ the same algorithm that was used on the exact solutions, the only change being that the large argumemt asymptotic approximation from equation (5.1.6) replaces the exact solution. The latter alternative is chosen since the algorithm has already been developed. Actually, the two methods are essentially equivalent; the only difference being that the derivative is computed numerically by the computer in the latter. Optimization results for the large argument asymptotic approximation are very close to the exact results. So close, in fact, that the curves nearly match and plotting them would only clutter the existing graphs. Referring back to the comparisons in Figures 5.1.3 and 5.2.3 shows that the large argument asymptotic approximation is extremely good for normalized mean radii greater than 20. Even for a small value of two the optimum thickness is predicted well, and the only appreciable error is in the power dissipation itself which is overestimated. In light of these facts, results for the large argument asymptotic approximation will not be graphically presented here or in the remainder of the dissertation. Its main purpose will be to provide an intermediate result in the determination of the thin-layer approximation. The necessary software for this approximation has been developed, however, if needed for a particular application.

Continuing on to the thin-layer approximation, there are again two possible routes to follow. The first is to begin with the thin-layer approximation for the normalized power dissipation, take the derivative with respect to the normalized conductor thickness, and set the result equal to zero. The second approach takes advantage of the fact that this process has already been performed on the large argument asymptotic approximation, and it resulted in equation (5.3.2). The thin-layer approximation as defined by equation (4.4.1) can therefore be directly applied to this expression, resulting in considerable simplification:

$$(1 + |\Gamma_n|^2)\cosh\tilde{\tau}_n\cos\tilde{\tau}_n \approx \mathrm{Re}(\Gamma_n)(\cosh^2\tilde{\tau}_n + \cos^2\tilde{\tau}_n) \qquad (5.3.3a)$$

which, for real Γ_n, becomes

$$\frac{\cosh\tilde{\tau}_n}{\cos\tilde{\tau}_n} + \frac{\cos\tilde{\tau}_n}{\cosh\tilde{\tau}_n} \approx \frac{1}{\Gamma_n} + \Gamma_n. \qquad (5.3.3b)$$

It should be mentioned that exactly the same result is reached if the first approach described above is followed. Careful manipulation of this expression results in the following alternative representation for equation (5.3.3b):

$$\frac{\cos\tilde{\tau}_n}{\cosh\tilde{\tau}_n} \approx \begin{cases} \Gamma_n & ; \ 0 \le \Gamma_n \le 1 \\ 1/\Gamma_n & ; \ 1 \le \Gamma_n \le \infty \end{cases}, \qquad (5.3.4)$$

where the symbol x has been carried through to indicate that this result arises from the thin-layer approximation. The equivalence of the solutions for reciprocal values of the boundary condition ratio is immediately evident from this representation. The left side of equation (5.3.4) is equal to one at $\tilde{\tau}_n = 0$. As $\tilde{\tau}_n$ increases the numerator decreases and the denominator increases, so that the ratio of the two decreases. This continues until the the ratio becomes zero at $\tilde{\tau}_n = \pi/2$. It is clear from this discussion that the range $[0, \pi/2]$ for the normalized conductor thickness provides the physically meaningful solutions to the optimization problem. This range spans all possible boundary condition ratios and confirms earlier interpretations of the graphical results.

The transcendental equation (5.3.4) is easy to solve on a computer. The results correspond to the $\tilde{\rho}_n = \infty$ curves presented along with the exact solutions in Figures 5.3.1 through 5.3.3. The accuracy of this approximation is once again seen to be very good and almost indistinguishable from the $\tilde{\rho}_n = 20$ results.

5.4 TWO-TERM SERIES APPROXIMATION

The third and final level of approximation will now be considered. Motivation is again provided by the encouraging results obtained thus far, and also by the desire to find closed form solutions for the optimization problem. Although the thin-layer approximation is fairly simple, a solution in closed form might provide more insight. Also, further simplification will prove to be very useful later in the generalizations to multi-layer windings and arbitrary periodic current waveforms.

The most important observation made so far, which leads into the possibility for further simplification, is the fact that the optimization process has led to normalized conductor thicknesses that are restricted to the range $[0, \pi/2]$. This suggests a series expansion about zero which would be valid for small values of $\tilde{\tau}_n$. Beginning with the thin-layer approximation for the normalized power dissipation given in equation (5.1.7), and substituting the first few terms of the Maclaurin series for each trigonometric and hyperbolic function yields, after considerable manipulation, the very simple result

$$\tilde{P}_n \approx \frac{1}{\tilde{\tau}_n}\left\{1 + \frac{\tilde{\tau}_n^4}{45}\left[\frac{4(1+|\Gamma_n|^2) + 7\mathrm{Re}(\Gamma_n)}{|1 - \Gamma_n|^2}\right]\right\} \qquad (5.4.1a)$$

which, for real Γ_n, becomes

$$\tilde{p}_n \approx \frac{1}{\tilde{\tau}_n}\left\{1 + \frac{\tilde{\tau}_n^4}{45}\left[\frac{4(1+\Gamma_n^2) + 7\Gamma_n}{(1 - \Gamma_n)^2}\right]\right\}. \qquad (5.4.1b)$$

Enough terms (three to be specific) have been included for each function to give the first two terms in the overall expression. These are actually the first two terms in the Laurent expansion (hence the terminology *two-term series approximation*) of the normalized power dissipation in the nth conductor layer. The first term represents the well known DC result and contains the singularity at zero thickness. The second term provides the first correction to the DC results and will hopefully provide good accuracy throughout the optimization region. Figure 5.4.1 shows the resulting curves for this two-term series approximation and compares them with the thin-layer approximation for two different boundary condition ratios. The agreement is indeed quite good throughout the minimum region but begins to diverge for larger thicknesses. Incidently, progress is being made toward obtaining the third term in the Laurent expansion which is proportional to $\tilde{\tau}_n^8$. It is not really needed here in the sinusoidal analysis, but it may prove useful in the extension to arbitrary periodic waveforms (see Chapter 7).

The same procedure can be followed for the normalized energy stored in the nth conductor layer given in equation (5.2.6), yielding

$$\tilde{W}_n \approx \frac{2\tilde{\tau}_n}{3} \frac{1 + |\Gamma_n|^2 + \mathrm{Re}(\Gamma_n)}{|1 - \Gamma_n|^2}$$

$$\left\{1 - \frac{\tilde{\tau}_n^4}{630}\left[\frac{16(1+|\Gamma_n|^2) + 31\mathrm{Re}(\Gamma_n)}{1 + |\Gamma_n|^2 + \mathrm{Re}(\Gamma_n)}\right]\right\} \qquad (5.4.2a)$$

which, for real Γ_n, becomes

$$\tilde{W}_n \approx \frac{2\tilde{\tau}_n}{3} \frac{1 + \Gamma_n^2 + \Gamma_n}{(1 - \Gamma_n)^2}\left\{1 - \frac{\tilde{\tau}_n^4}{630}\left[\frac{16(1 + \Gamma_n^2) + 31\Gamma_n}{1 + \Gamma_n^2 + \Gamma_n}\right]\right\}. \qquad (5.4.2b)$$

The first term again represents the DC result, and the second term provides a correction. Figure 5.4.2 presents the corresponding graphical results along with the thin-layer approximation. The accuracy here is also very good throughout the region $[0, \pi/2]$.

The two-term series approximations derived above provide extremely simple expressions for use in the optimization process. Performing the differentiation according to equation (5.3.1) on equation (5.4.1a) yields a solution in closed form, namely,

$$\tilde{\tau}_n^{opt} \approx \left\{15\left[\frac{|1 - \Gamma_n|^2}{4(1+|\Gamma_n|^2) + 7Re(\Gamma_n)}\right]\right\}^{\frac{1}{4}}. \qquad (5.4.3)$$

And substituting this result back into equation (5.4.1b) gives the corresponding minimum power dissipation

$$\tilde{P}_n^{min} \approx \frac{4}{3}\frac{1}{\tilde{\tau}_n^{opt}} = \frac{4}{3}\left\{\frac{1}{15}\left[\frac{4(1+|\Gamma_n|^2) + 7Re(\Gamma_n)}{|1 - \Gamma_n|^2}\right]\right\}^{\frac{1}{4}}. \qquad (5.4.4)$$

These two equations are plotted in Figures 5.4.3 and 5.4.4 along with the results arrived at earlier for the thin-layer approximation. Specifically, equation (5.3.4) is solved numerically for $\tilde{\tau}_n^{opt}$ which is in turn substituted into equation (5.1.7) to calculate $\tilde{P}_n^{min}$. The agreement is impressive especially for the minimum power dissipation. Some error in the optimum conductor thickness does arise for small boundary condition ratios. It was pointed out earlier that small boundary condition ratios are desirable. The worst-case error occurs for $\Gamma_n = 0$, where the two-term series approximation gives $\tilde{\tau}_n^{opt} \approx 1.39$ which is about 11.4% below the thin-layer approximation result of $\pi/2$. The error in the corresponding minimum power is less than 4.5%. Finally, the optimum thickness can also be substituted into equation (5.4.2b) to evaluate the two-term series approximation of the stored energy under optimum conditions.

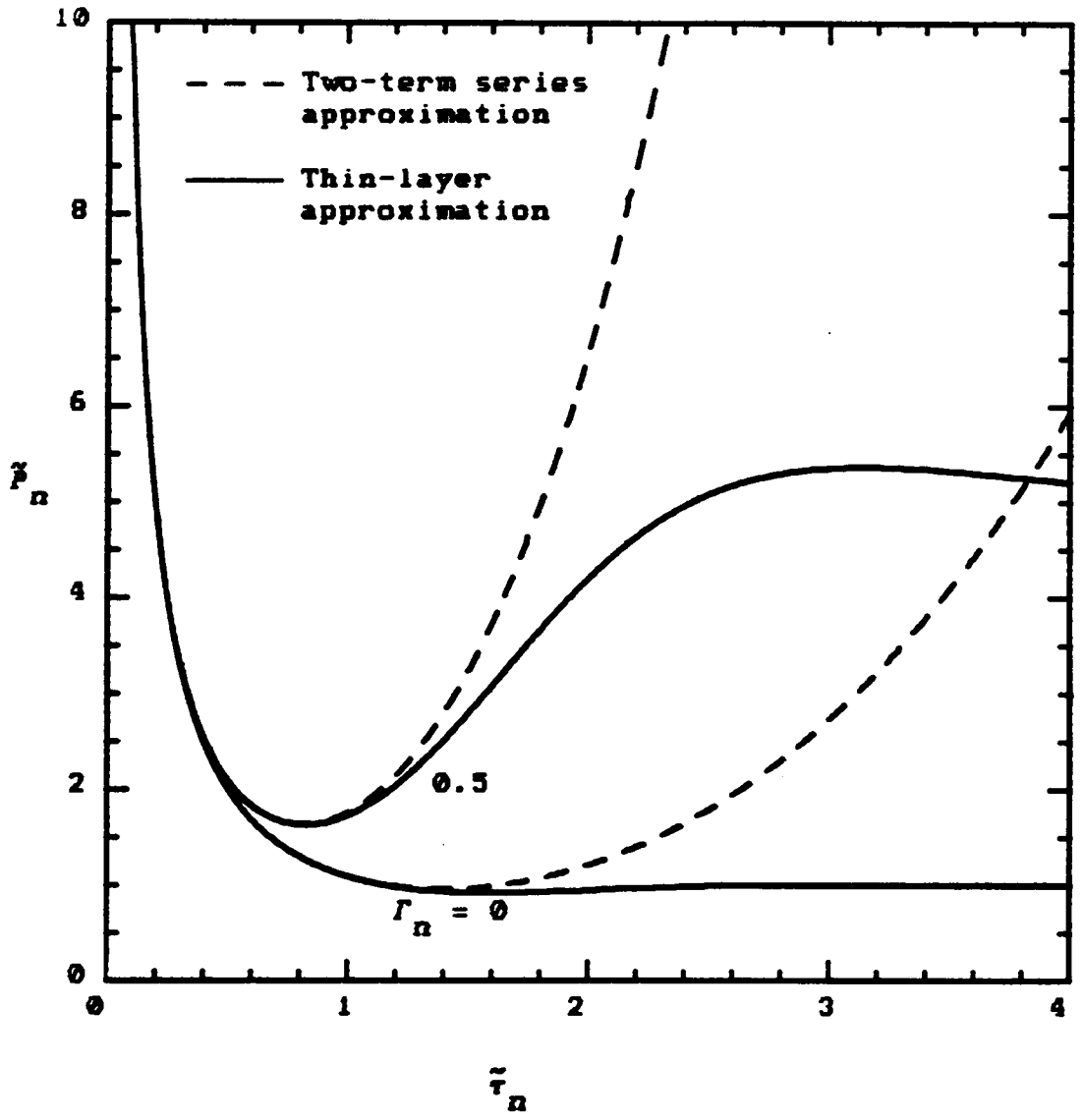

Figure 5.4.1. Normalized power dissipation in the *n*th layer vs. normalized conductor thickness with the boundary condition ratio varied as a parameter.

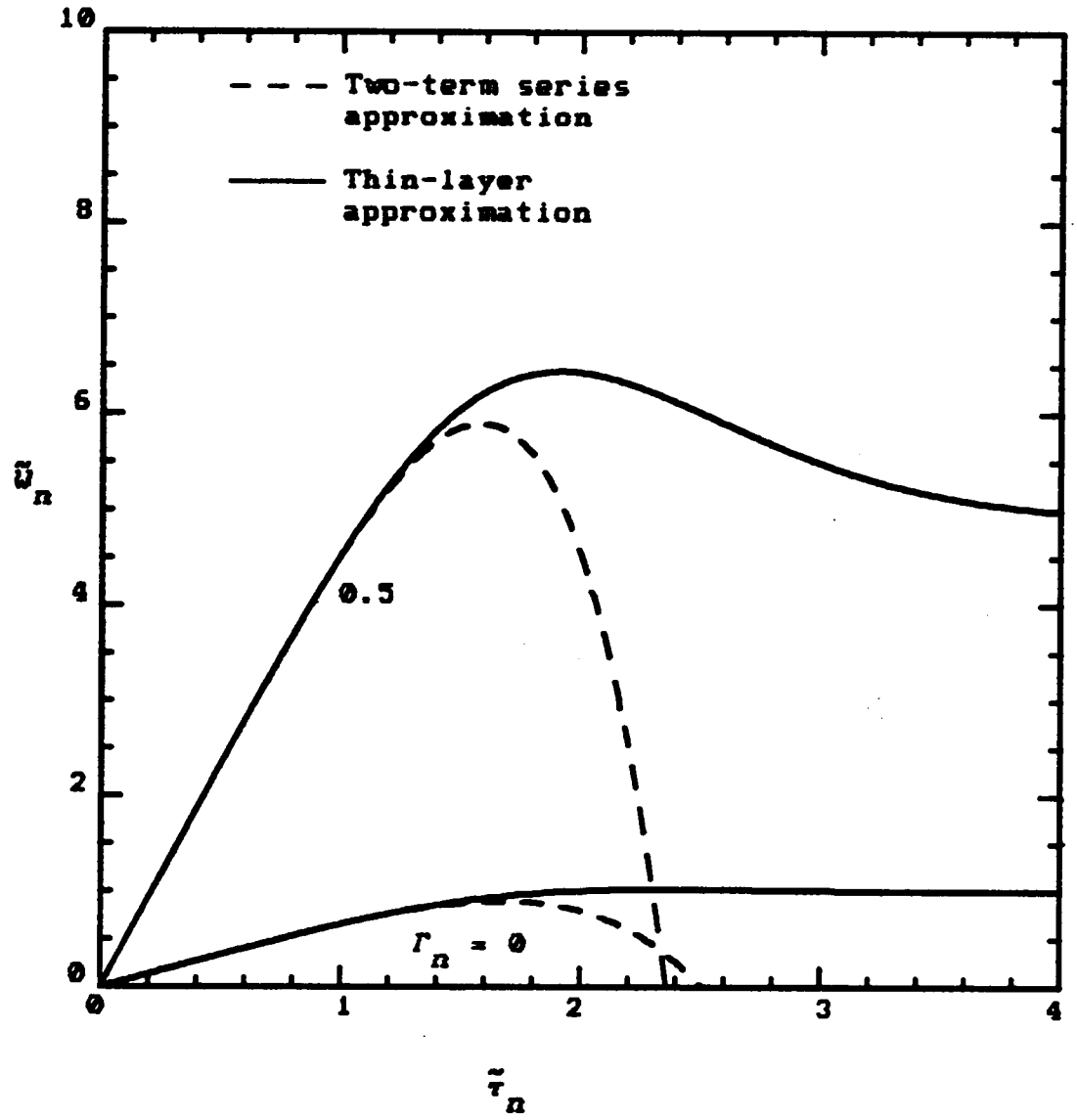

Figure 5.4.2. Normalized energy stored in the nth layer vs. normalized conductor thickness with the boundary condition ratio varied as a parameter.

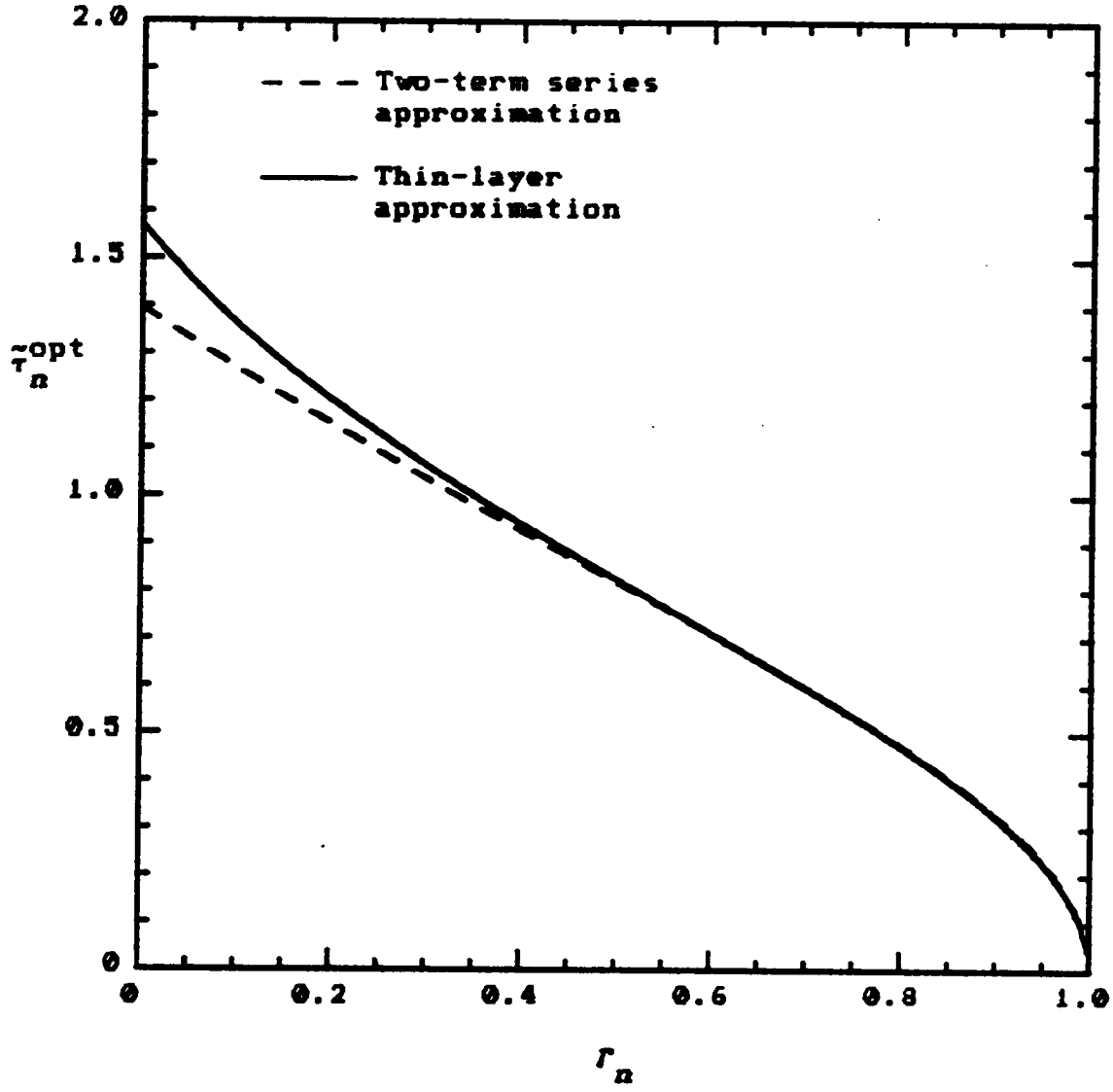

Figure 5.4.3. Optimum normalized conductor thickness (for minimum power dissipation) of the nth layer vs. boundary condition ratio.

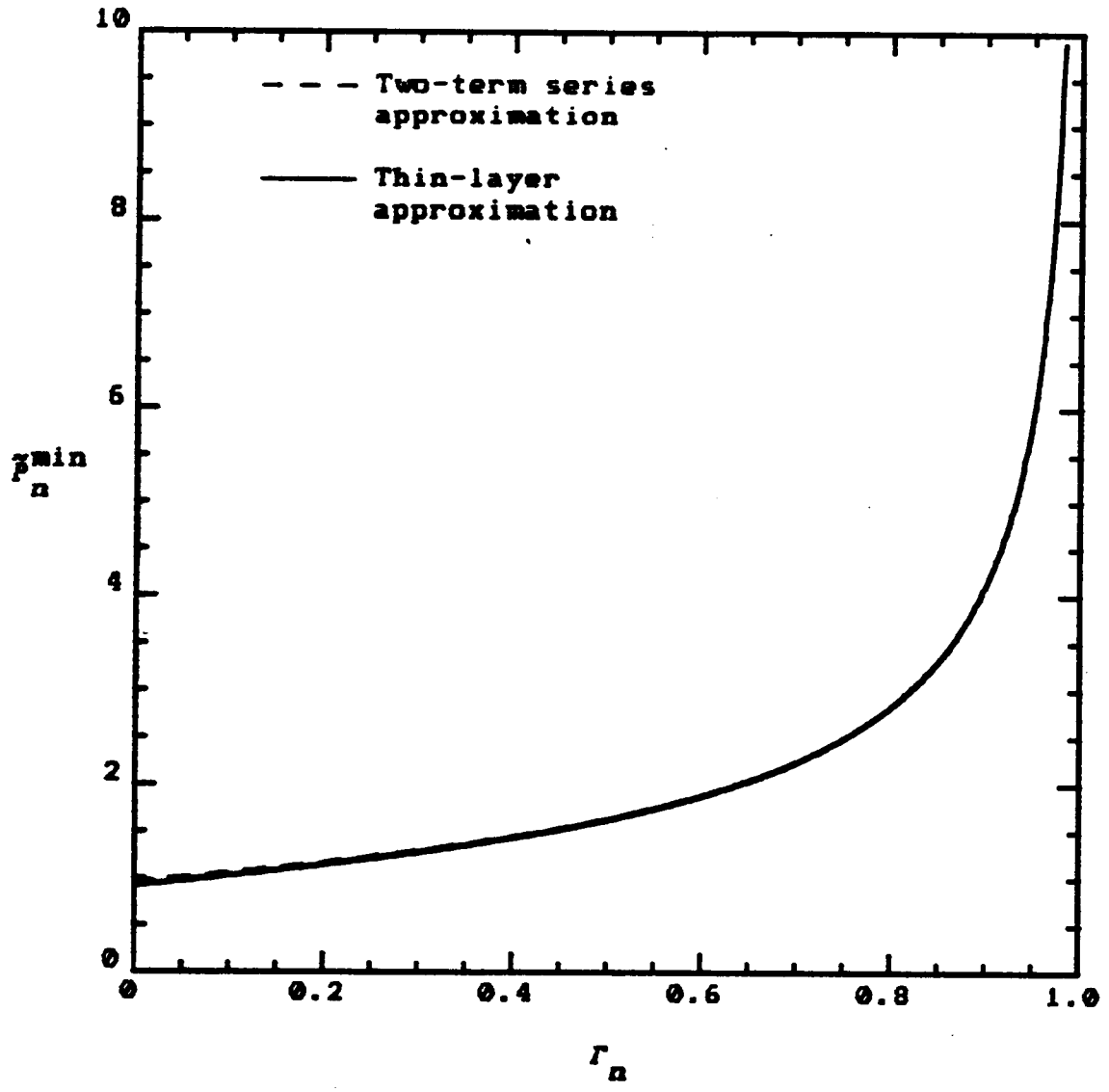

Figure 3.4.4. Minimum normalized power dissipation (at optimum conductor thickness) in the nth layer vs. boundary condition ratio.

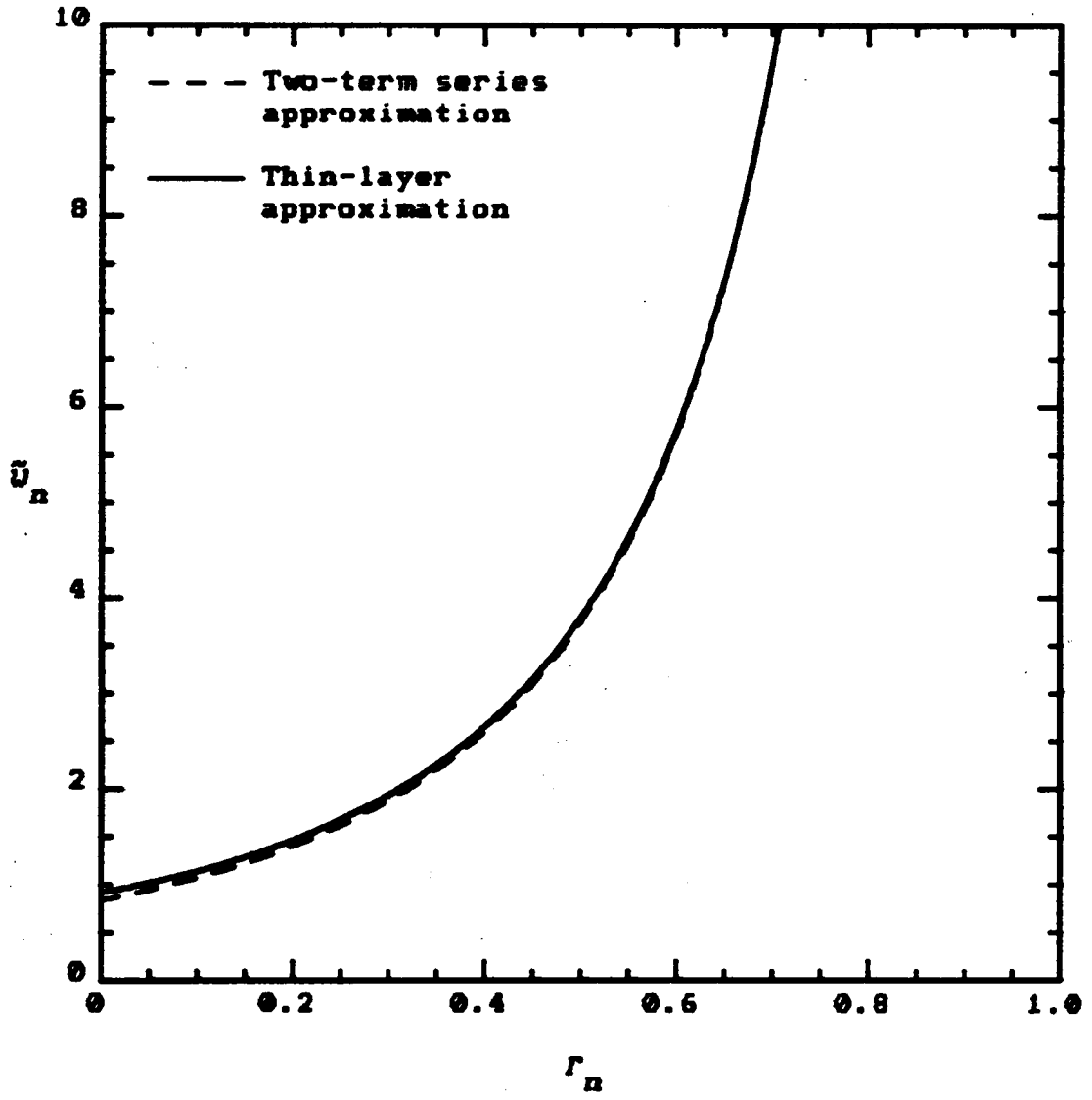

Figure 5.4.5. Normalized energy stored (at the optimum conductor thickness) in the nth layer vs. boundary condition ratio.

The results are plotted in Figure 5.4.5 along with the corresponding thin-layer approximation. The accuracy is seen to be comparable to that for the power dissipation.

Before continuing to the multi-layer winding, it is perhaps worthwhile to summarize the approximations that have been defined and their associated limitations. The exact solutions for the one-dimensional problem have been determined and, of course, can be used if needed. They are complex expressions which involve Kelvin functions, require extensive use of a computer, and offer little insight into the problem. The computational results of the exact solutions prompted the large argument asymptotic approximation which resulted in considerable simplification of the exact expressions. The accuracy was very good except for very small arguments. But these small values were shown to lie outside the range of most practical designs. A simple extension of the large argument asymptotic approximation evolved from the additional requirement that the conductor thickness be much smaller than the conductor mean radius. The new expressions were called the thin-layer approximations, and they were also found to be very accurate under most practical conditions. In fact, if one adheres to optimized designs for minimum power dissipation, the resulting optimum normalized conductor thicknesses are restricted to the range $[0, \pi/2]$ which guarentees that the

thin-layer approximation will be reasonably good at the very least. Finally, the two-term series approximation has just been introduced, and it is also quite accurate for this range. It is very attractive because it produces closed form solutions to the optimization problem. It is very important, however, to limit its use to this range. This cannot be overemphasized. Blind application of the two-term series approximation to determine power dissipation and stored energy could result in very large errors (see Figures 5.4.1 and 5.4.2).

CHAPTER 6

MULTI-LAYER WINDINGS

The solution to the single-layer winding was presented in Chapter 5. In that derivation all results were expressed in terms of the general *n*th layer within a winding. At the time that was unnecessary, but the reasons for doing so will become clear in this chapter which is concerned with extending these solutions to the case of an *M*-layer winding. A large part of this effort will involve summing several single-layer solutions, a process which will take advantage of the general notation just discussed.

First, some new definitions are introduced, and some practical assumptions are made associated with the multi-layer winding. The power dissipation and energy stored are then determined. The total power dissipation in the winding can be minimized using the same techniques as those for the single-layer problem. All previously defined levels of approximations are derived, and several graphical results are presented. Finally, two additional techniques for reducing the power dissipation in a multi-layer winding are presented via illustrative examples. One involves individual-layer optimization, and the other splitting the winding into sections.

6.1 PRACTICAL MULTI-LAYER ASSUMPTIONS

The most important assumptions to be made result from realizing that individual layers within most windings are identical in several ways. Figures 3.1.2 and 4.1.2 may be useful supplements to this discussion. First, the thicknesses of the individual conductor layers are assumed to be equal:

$$\tilde{\tau}_n = \tilde{\tau} \; ; \quad n = 1,2,\ldots,N. \tag{6.1.1}$$

This equation also holds for the unnormalized thicknesses. Similarly, the total current and therefore the current per unit axial length for each layer is assumed to be identical:

$$K_n = K \; ; \quad n = 1,2,\ldots,N. \tag{6.1.2}$$

Since the radial distances must now be described for a total winding, some definitions need to be introduced to account for the insulation layers. Each conductor layer is assumed to have associated with it an insulation layer located radially adjacent to it and to the exterior. The thickness of this nth insulation layer is defined as

$$d_n \doteq \rho_{n+1}^{i} - \rho_n^{o} \; ; \; n = 1,2,\ldots,N \tag{6.1.3a}$$

or, in normalized quantities,

$$\tilde{d}_n = \tilde{\rho}^{i}_{n+1} - \tilde{\rho}^{o}_{n} \; ; \; n = 1,2,\ldots,N. \qquad (6.1.3b)$$

For a practical multi-layer winding, the insulation thicknesses are also assumed to be identical:

$$\tilde{d}_n = \tilde{d} \; ; \quad n = 1,2,\ldots,N. \qquad (6.1.4)$$

Using all of the above definitions and assumptions along with the established ones for the conductor layers allows the following simple formulas for the boundary radii to be derived:

$$\tilde{\rho}^{i}_{n} = \tilde{\rho}^{i}_{1} + (n-1)\tilde{d} + (n-1)\tilde{\tau} \; ; \quad n = 1,2,\ldots,N \qquad (6.1.5a)$$

$$\tilde{\rho}^{o}_{n} = \tilde{\rho}^{i}_{1} + (n-1)\tilde{d} + n\tilde{\tau} \; ; \quad n = 1,2,\ldots,N. \qquad (6.1.5b)$$

The mean radius of the nth conductor layer is therefore simply

$$\tilde{\rho}_{n} = \tilde{\rho}^{i}_{1} + (n-1)\tilde{d} + (n-\tfrac{1}{2})\tilde{\tau} \; ; \quad n = 1,2,\ldots,N \qquad (6.1.6)$$

by equation (4.2.17a). Again, note that these expressions can also be written in terms of the unnormalized quantities.

It is now possible to determine the magnetic field intensity boundary conditions for the entire winding. Using the assumption of identical currents per unit axial length from equation (6.1.2) and successively applying equation (4.1.12) which relates these currents to the boundary conditions results in the relation

$$H_n = H_0 - nK \; ; \quad n = 1,2,\ldots,N, \tag{6.1.7}$$

where H_0 is defined to be the magnetic field intensity at the inner boundary of the total winding and must be determined from the currents in other windings to the interior. Remember that the currents are referenced in the positive $\hat{\phi}$-direction so that a negative value for K produces a positively increasing magnetic field (referenced in the $\hat{z}$-direction) as one travels radially outward. In addition to acting as the boundary conditions for the individual conductor layers, the values defined above are assumed to exist throughout the insulation layers. Let the overall boundary condition ratio of the winding be defined as

$$\Gamma \doteq \frac{H_0}{H_N} = \frac{H_0}{H_0 - NK}, \tag{6.1.8}$$

where the last step follows directly from equation (6.1.7).

The boundary condition ratio for each individual layer was defined in equation (4.2.11), and can also be written as

$$\Gamma_n \triangleq \frac{H_{n-1}}{H_n} = \frac{H_0 - (n-1)K}{H_0 - nK}. \qquad (6.1.9)$$

These two boundary condition ratios can be related by solving equation (6.1.8) for either H_0 or K, substituting the result into equation (6.1.9), and simplifying. The resulting relationship is

$$\Gamma_n = \frac{\Gamma(N-n+1) + (n-1)}{\Gamma(N-n) + n}. \qquad (6.1.10)$$

This important result shows that the boundary condition ratio for each individual conductor layer within a winding can be determined solely in terms of the ratio for the total winding. This is a direct consequence of assuming equal currents in each layer.

The assumptions made in this section are practical in the sense that most transformer windings are wound as an entity, using the same conductor and insulation throughout. One possible condition that is not covered is when only a fraction of the final layer is used. Fractional layers can be handled in a straightforward manner based on the existing work. They are not included here because it results in cluttered notation without introducing anything conceptually new.

6.2 POWER DISSIPATION

The total power dissipated in an N-layer winding is simply the sum of the powers dissipated in the individual layers:

$$P = \sum_{n=1}^{N} P_n = \frac{\pi l}{\sigma}|K|^2 \sum_{n=1}^{N} \tilde{\rho}_n \tilde{P}_n. \qquad (6.2.1)$$

This result has been written in terms of the normalized nth layer power dissipation $\tilde{P}_n$ which was defined in equations (5.1.1) and (5.1.2). The assumption of identical currents from equation (6.1.1) has also been used in this result. It is now appropriate to introduce a new quantity, the winding mean radius, which will prove to be useful in the ensuing manipulations. The winding mean radius is defined as the average of the mean radii of the individual conductor layers:

$$\rho_w = \frac{1}{N} \sum_{n=1}^{N} \rho_n = \rho_1^i + \left(\frac{N-1}{2}\right) d + \left(\frac{N}{2}\right) \tau \qquad (6.2.2a)$$

or, in normalized form,

$$\tilde{\rho}_w = \frac{1}{N} \sum_{n=1}^{N} \tilde{\rho}_n = \tilde{\rho}_1^i + \left(\frac{N-1}{2}\right) \tilde{d} + \left(\frac{N}{2}\right) \tilde{\tau}, \qquad (6.2.2b)$$

where equation (6.1.6) has been substituted and the summation performed to obtain the final expressions. Equations (6.1.6) and (6.2.2b) can be combined to eliminate the winding inner radius $\tilde{\rho}_1^i$, so that

$$\tilde{\rho}_n = \tilde{\rho}_w + \left[n - \frac{N+1}{2}\right](\tilde{\tau} + \tilde{d}). \qquad (6.2.3)$$

This is an important expression because it relates the quantities which are most useful for evaluating the expressions and understanding the results of the multi-layer problem. Equation (6.2.1) is now rearranged into the form

$$P = \frac{\pi l}{\sigma}|K|^2 \sum_{n=1}^{N} \tilde{\rho}_n \tilde{P}_n = \frac{\pi l}{\sigma}|K|^2 N \tilde{\rho}_w \tilde{P}, \qquad (6.2.4a)$$

where

$$\tilde{P} = \frac{1}{N} \sum_{n=1}^{N} \frac{\tilde{\rho}_n}{\tilde{\rho}_w} \tilde{P}_n. \qquad (6.2.4b)$$

$\tilde{P}$ represents the normalized power dissipation per layer in an N-layer winding. It has been defined in this way so that the results are more directly comparable to the single-layer case. In other words, $\tilde{P}$ is a measure of the power dissipation in an individual layer (in an averaged sense)

within an N-layer winding, while $\tilde{P}_n$ is a measure of the power dissipation in a single-layer by itself. Obviously the two should agree for $N = 1$, and this is indeed the case as evidenced from equations (6.2.3), (6.2.4b), and (5.1.1). This special case will also provide a useful and convenient check for the numerical results.

The procedure for determining the normalized power dissipation per layer in an N-layer winding is straightforward. The results from the single-layer problem are simply substituted into equation (6.2.4b), and the practical multi-layer assumptions from equations (6.1.1) and (6.1.3b) are invoked. There were a total of four levels of results obtained in the previous chapter for the normalized power dissipated in the nth conductor layer: exact, large argument asymptotic approximation, thin-layer approximation, and the two-term series approximation. The corresponding mathematical expressions are given in equations (5.1.4), (5.1.6), (5.1.7), and (5.4.1), respectively.

The exact solution of the multi-layer winding does not offer analytical simplification, so it will not be repeated. One must simply make the indicated substitutions, evaluate the expressions, and sum the results. This systematic process is easily incorporated into the computer programs for the single-layer case, thereby extending their applicability to the multi-layer case.

Some simplification does result in the large argument asymptotic approximation by substituting equation (5.1.6) into (6.2.4b), mostly in the form of factoring certain parts of the expression outside the summation. The result, after incorporating the practical multi-layer assumptions discussed in Section 6.1, is

$$\tilde{P} \sim \frac{1}{N}\left\{\left[\frac{\sinh 2\tilde{\tau} + \sin 2\tilde{\tau}}{\cosh 2\tilde{\tau} - \cos 2\tilde{\tau}}\right]\sum_{n=1}^{N}\frac{\tilde{\rho}_n}{\tilde{\rho}_w}\left[\frac{1 + |\Gamma_n|^2}{|1 - \Gamma_n|^2} + \frac{1}{2}\frac{\tilde{\tau}}{\tilde{\rho}_n}\frac{1 - |\Gamma_n|^2}{|1 - \Gamma_n|^2}\right]\right.$$

$$\left. - 4\left[\frac{\cosh\tilde{\tau}\sin\tilde{\tau} + \cos\tilde{\tau}\sinh\tilde{\tau}}{\cosh 2\tilde{\tau} - \cos 2\tilde{\tau}}\right]\sum_{n=1}^{N}\frac{\tilde{\rho}_n}{\tilde{\rho}_w}\left[1 - \left(\frac{1}{2}\frac{\tilde{\tau}}{\tilde{\rho}_n}\right)^2\right]^{\frac{1}{2}}\frac{\mathrm{Re}(\Gamma_n)}{|1 - \Gamma_n|^2}\right\}. \quad (6.2.5)$$

Evaluation of the two summations in this expression is very involved when one considers that equations (6.1.10) and (6.2.3) must be used to replace Γ_n and $\tilde{\rho}_n$, respectively. It is possible to analytically perform the first summation, but the process is very lengthy and the result is not particularly useful. It is not useful because the second summation cannot be simplified in a similar way due to the presence of the square root. The form given above in equation (6.2.5) is therefore the most consistent and convenient form for programming.

The thin-layer approximation is defined by the condition in equation (4.4.1) which, for equal conductor thicknesses, becomes

$$\frac{\tilde{\tau}}{\tilde{\rho}_n} \ll 1 \; ; \quad n = 1,2,\ldots,N. \tag{6.2.6}$$

Thus, the conductor thickness is assumed to be much smaller than the mean radius of any layer. If, in addition, it is assumed that the insulation thickness is much smaller than the mean radii:

$$\frac{\tilde{d}}{\tilde{\rho}_n} \ll 1 \; ; \quad n = 1,2,\ldots,N; \tag{6.2.7}$$

then one might conclude from equation (6.2.3) that

$$\tilde{\rho}_n \approx \tilde{\rho}_w \; ; \quad n = 1,2,\ldots,N. \tag{6.2.8}$$

This is true only if the number of layers is not great enough to make the total thickness of the winding on the order of the winding mean radius. What has really happened here is that the thin-layer approximation has been extended to imply a thin-winding approximation, which can be stated mathematically as

$$N \frac{\tilde{\tau} + \tilde{d}}{\tilde{\rho}_w} \ll 1. \tag{6.2.9}$$

For the sake of avoiding a new name, the terminology thin-layer approximation will continue to be used in the multi-layer case, with the understanding that thin means thin enough that condition (6.2.9) is satisfied. The derivation of the thin-layer approximation of the normalized power dissipated per layer begins by substituting equation (5.1.7) into equation (6.2.4b). The same result is reached if the thin-layer approximation conditions from (6.2.6) and (6.2.8) above are used to simplify the large argument approximation in equation (6.2.5), namely,

$$\tilde{P} \approx \frac{1}{N}\left\{\left[\frac{\sinh 2\tilde{\tau} + \sin 2\tilde{\tau}}{\cosh 2\tilde{\tau} - \cos 2\tilde{\tau}}\right]\sum_{n=1}^{N}\left[\frac{1 + |\Gamma_n|^2}{|1 - \Gamma_n|^2}\right]\right.$$

$$\left. - 4\left[\frac{\cosh\tilde{\tau}\sin\tilde{\tau} + \cos\tilde{\tau}\sinh\tilde{\tau}}{\cosh 2\tilde{\tau} - \cos 2\tilde{\tau}}\right]\sum_{n=1}^{N}\left[\frac{\mathrm{Re}(\Gamma_n)}{|1 - \Gamma_n|^2}\right]\right\}. \quad (6.2.10)$$

Both summations in this expression can now be evaluated when equation (6.1.10) is used to replace Γ_n. After considerable algebraic manipulation, the result is

$$\tilde{P} \approx \frac{2}{3}\left|\frac{1}{1-\Gamma}\right|^2\left\{\left[\frac{\sinh 2\tilde{\tau} + \sin 2\tilde{\tau}}{\cosh 2\tilde{\tau} - \cos 2\tilde{\tau}}\right]\left[(N^2+\tfrac{1}{2})(1+|\Gamma|^2) + (N^2-1)\mathrm{Re}(\Gamma)\right]\right.$$

$$\left. - 2\left[\frac{\cosh\tilde{\tau}\sin\tilde{\tau} + \cos\tilde{\tau}\sinh\tilde{\tau}}{\cosh 2\tilde{\tau} - \cos 2\tilde{\tau}}\right]\left[(N^2-1)(1+|\Gamma|^2) + (N^2+2)\mathrm{Re}(\Gamma)\right]\right\}. \quad (6.2.11)$$

This result can be compared with the corresponding single-layer expression in equation (5.1.7). They are similar except for the additional appearance of N in the above expression. As a matter of fact, for large N the expression as a whole becomes proportional to N^2. A dramatic increase in the power dissipation should therefore be expected as the number of layers is increased. Remember that one factor of N has already been factored out, so that this is a per layer result.

Before presenting the graphical results of the thin-layer approximation, the two-term series approximation is derived. Again, there are two approaches which lead to the same result. The first is to substitute the single-layer two-term approximation from equation (5.4.1a) into equation (6.2.4b), and simplify. Alternatively, the series approximations for the transcendental functions could be introduced into the thin-layer approximation in equation (6.2.11) above. The result is

$$\tilde{P} \approx \frac{1}{\tilde{\tau}} \left\{ 1 + \frac{\tilde{\tau}^4}{45} \left[\frac{(5N^2-1)(1+|\Gamma|^2) + (5N^2+2)\mathrm{Re}(\Gamma)}{|1-\Gamma|^2} \right] \right\}, \quad (6.2.12)$$

where the presence of the N^2 factor is again noticed. But it appears only in the second term of the series, suggesting that it will not come into play until after the low frequency region of the curves.

It is worthwhile to pause here and note that the three approximations derived here for the multi-layer winding (equations (6.2.5), (6.2.11), and (6.2.12)) all reduce to their single-layer counterparts (equations (5.1.6), (5.1.7), and (5.4.1)) when $N = 1$.

The single-layer graphical results revealed that the additional accuracy afforded by the exact solutions and the large argument approximations was unnecessary for values of the normalized mean radii greater than 20 (see Figures 5.1.2 and 5.1.3). One would expect similar behavior in the multi-layer solutions since they are essentially summations of single-layer solutions. This is indeed the case, and for that reason they will not be graphically presented here. If smaller radii are encountered, the author has developed the necessary software to handle it. Focusing then on the thin-layer and two-term series approximations, Figures 6.2.1 and 6.2.2 show a comparison of these for several values N. As expected, the two-term series approximation is accurate up through the minimum region but then begins to diverge rapidly. All of these curves are for a winding boundary condition ratio of zero. As the number of layers increases, the curves shift upward and their minima become much sharper. It is interesting to note that this is similar to the behavior of the single-layer solutions as Γ_n approaches one. This is because, in the multi-layer case, the boundary

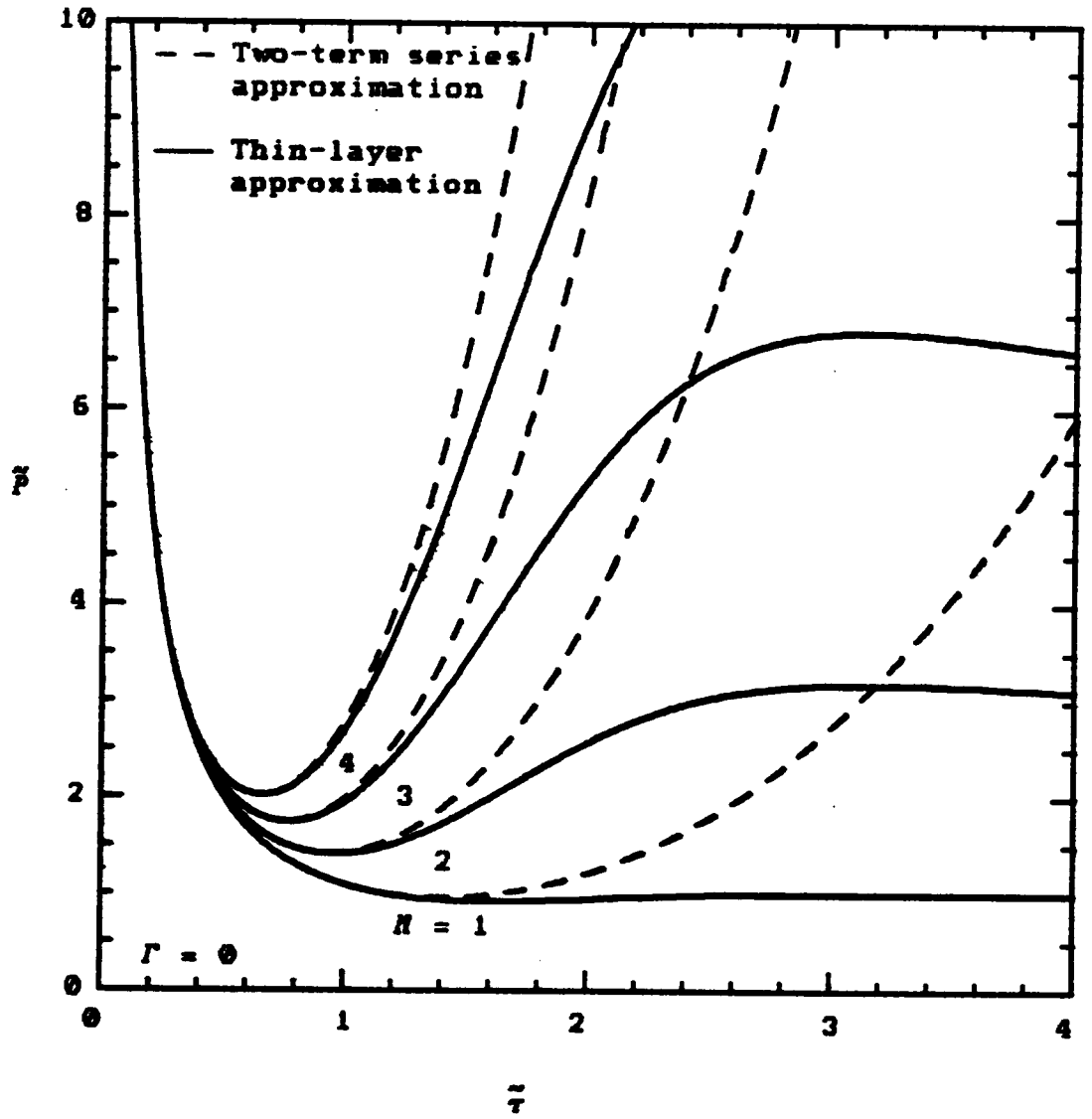

Figure 6.2.1. Normalized power dissipation per layer in an N-layer winding vs. normalized conductor thickness with the number of layers varied as a parameter for some low values.

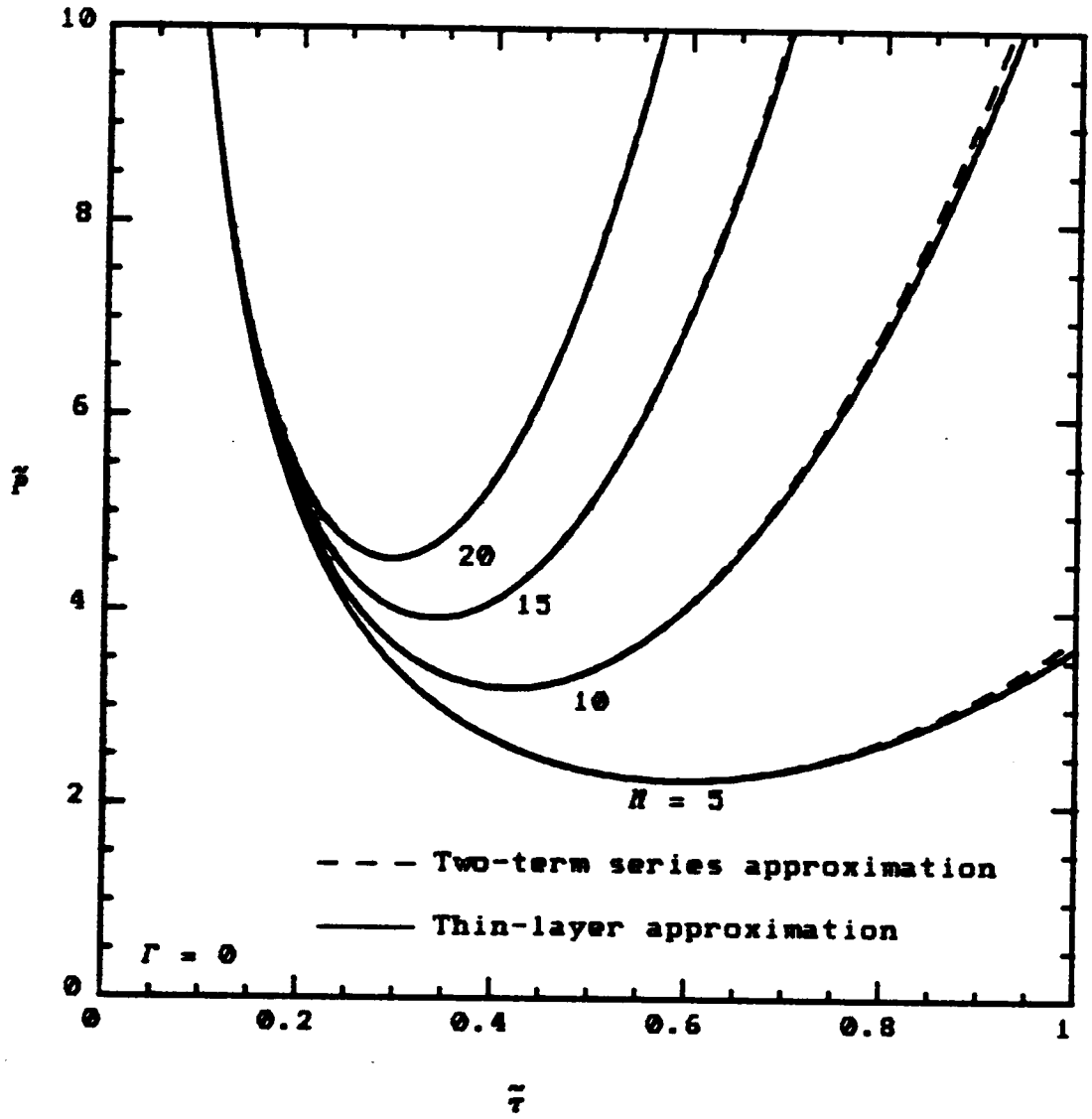

Figure 6.2.2. Normalized power dissipation per layer in an N-layer winding vs. normalized conductor thickness with the number of layers varied as a parameter for some higher values.

condition ratio of the individual layers approach unity with increasing radius (see equation (6.1.10)). For these same reasons, the curves for the multi-layer winding will exhibit even more exaggerated behavior in this respect as the overall winding boundary condition ratio approaches unity. This is an undesirable situation which can usually be avoided by judiciously choosing the winding order or by splitting the windings. The latter is the topic of the last section in this chapter.

6.3 ENERGY STORAGE

The derivation of the energy stored in a multi-layer winding is similar to the derivation of the power dissipation for the single-layer problem except for one very important difference. The insulation layers are ignored (other than accounting for their thickness when determining boundary radii) when deriving the power dissipation because they are assumed to be a dielectric with zero conductivity. There can therefore be no losses in the insulation layers. The insulation layers cannot be neglected, however, in the determination of the energy storage. The magnetic field intensity has been assumed to be constant within the individual insulation layers. Consequently, they will contribute significantly to the total energy stored in a winding as will be shown shortly.

Each conductor layer has an insulation layer associated with it which is radially adjacent and to the exterior. See Figure 3.1.2. The magnetic field intensities in the insulation layers are given generally in equation (4.1.6), and then specifically under the practical multi-layer assumptions in equation (6.1.7). In order to derive the energy stored in the nth insulation layer, these values must be substituted into equation (3.2.15a), and the integration performed over the insulation layer volume. The notation W_n^i is introduced, where the superscript i distinguishes it as being associated with an insulation layer. The integration proceeds as follows:

$$W_n^i = \frac{1}{2}\iiint_V \frac{1}{2}\mu_o |\mathbf{H}|^2 dv$$

$$= \frac{1}{4}\mu_o \int_0^{2\pi} d\phi \int_{-l/2}^{+l/2} dz \int_{\rho_n^o}^{\rho_{n+1}^i} |K_n|^2 \rho d\rho$$

$$= \frac{\pi\mu_o l\delta^2}{2} |K_n|^2 |\tilde{K}_n|^2 \int_{\tilde{\rho}_n^o}^{\tilde{\rho}_{n+1}^i} \tilde{\rho} d\tilde{\rho} = \frac{\pi\mu_o l\delta^2}{4} \tilde{\rho}_n |K_n|^2 \tilde{W}_n^i;$$

$$n = 1,2,\ldots,N, \qquad (6.3.1)$$

where familiar normalized quantities have been introduced so that the results can be conveniently combined with previous

ones. The last step defines the normalized energy stored in the nth insulation layer as

$$\tilde{U}_n^i = \frac{2}{\tilde{\rho}_n}|\tilde{H}_n|^2 \int_{\tilde{\rho}_n^0}^{\tilde{\rho}_{n+1}^i} \tilde{\rho}\,d\tilde{\rho} \; ; \quad n = 1,2,\ldots,N. \qquad (6.3.2)$$

This integration is a simple one which can be rearranged into the following form using equations (4.2.10), (4.2.18), and (6.1.3):

$$\tilde{U}_n^i = \left|\frac{1}{1-\Gamma_n}\right|^2 2\tilde{d}_n\left[1 + \frac{1}{2}\frac{\tilde{\tau}_n+\tilde{d}_n}{\tilde{\rho}_n}\right]. \qquad (6.3.3)$$

Introducing the practical multi-layer assumptions from equations (6.1.1) and (6.1.4) into this expression gives

$$\tilde{U}_n^i = \left|\frac{1}{1-\Gamma_n}\right|^2 2\tilde{d}\left[1 + \frac{1}{2}\frac{\tilde{\tau} + \tilde{d}}{\tilde{\rho}_n}\right]. \qquad (6.3.4)$$

The derivation of the total energy stored in an N-layer winding now proceeds exactly as the derivation of the power dissipation did with the addition of the contributions from the insulation layers just determined. Thus, summing equations (5.2.1) and (6.3.1) gives

$$W = \frac{\pi\mu_o l\delta^2}{4}|K|^2 \sum_{n=1}^{N} \tilde{\rho}_n(\tilde{W}_n^i + \tilde{W}_n) \doteq \frac{\pi\mu_o l\delta^2}{4}|K|^2 N\tilde{\rho}_w \tilde{W} \quad (6.3.5a)$$

where

$$\tilde{W} \doteq \frac{1}{N}\sum_{n=1}^{N} \frac{\tilde{\rho}_n}{\tilde{\rho}_w}(\tilde{W}_n^i + \tilde{W}_n) \quad (6.3.5b)$$

represents the normalized energy storage per layer in an N-layer winding. This definition is analogous to the normalized power definition in equations (6.2.4) except for the addition of the insulation layer terms. The term *per layer* now refers to the combination of both the nth conductor and insulation layers. The results are therefore directly comparable to the single-layer results only if the insulation thickness is taken to be zero, thereby eliminating its contribution. Equation (6.3.5b) can be evaluated for each of the four previously defined levels of solutions by substituting the corresponding single-layer solutions for $\tilde{W}_n$ from equations (5.2.4), (5.2.5), (5.2.6), or (5.4.2), and invoking the practical multi-layer assumptions. Details of these evaluations will not be given since they are the same as those associated with determining the power dissipation. The results are simply stated, and discussion is delayed until the graphical presentation.

Once again, no analytical simplification is possible for the exact solutions; one must simply evaluate equations (5.2.4) and (6.3.4), and sum the results. Considerable simplification is achieved in the large argument asymptotic approximation which is given by

$$\tilde{U} \sim \frac{1}{N}\left\{2\tilde{\alpha}\sum_{n=1}^{N}\frac{\tilde{\rho}_n}{\tilde{\rho}_w}\left|\frac{1}{1-\Gamma_n}\right|^2\left[1+\frac{1}{2}\frac{\tilde{\tau}+\tilde{\alpha}}{\tilde{\rho}_n}\right]\right.$$

$$+\left[\frac{\sinh 2\tilde{\tau}-\sin 2\tilde{\tau}}{\cosh 2\tilde{\tau}-\cos 2\tilde{\tau}}\right]\sum_{n=1}^{N}\frac{\tilde{\rho}_n}{\tilde{\rho}_w}\left[\frac{1+|\Gamma_n|^2}{|1-\Gamma_n|^2}+\frac{1}{2}\frac{\tilde{\tau}}{\tilde{\rho}_n}\frac{1-|\Gamma_n|^2}{|1-\Gamma_n|^2}\right]$$

$$\left.+4\left[\frac{\cosh\tilde{\tau}\sin\tilde{\tau}-\cos\tilde{\tau}\sinh\tilde{\tau}}{\cosh 2\tilde{\tau}-\cos 2\tilde{\tau}}\right]\sum_{n=1}^{N}\frac{\tilde{\rho}_n}{\tilde{\rho}_w}\left[1-\left(\frac{1}{2}\frac{\tilde{\tau}}{\tilde{\rho}_n}\right)^2\right]^{\frac{1}{2}}\frac{\mathrm{Re}(\Gamma_n)}{|1-\Gamma_n|^2}\right\}. \qquad (6.3.6)$$

The usual terms are neglected for the thin-layer approximation, resulting in the expression

$$\tilde{U} \approx \frac{2}{3}\left|\frac{1}{1-\Gamma}\right|^2\left\{\tilde{\alpha}\left[(N^2+\tfrac{1}{2})(1+|\Gamma|^2)+(N^2-1)\mathrm{Re}(\Gamma)+\frac{3}{2}N(1-|\Gamma|^2)\right]\right.$$

$$+\left[\frac{\sinh 2\tilde{\tau}-\sin 2\tilde{\tau}}{\cosh 2\tilde{\tau}-\cos 2\tilde{\tau}}\right]\left[(N^2+\tfrac{1}{2})(1+|\Gamma|^2)+(N^2-1)\mathrm{Re}(\Gamma)\right]$$

$$\left.+2\left[\frac{\cosh\tilde{\tau}\sin\tilde{\tau}-\cos\tilde{\tau}\sinh\tilde{\tau}}{\cosh 2\tilde{\tau}-\cos 2\tilde{\tau}}\right]\left[(N^2-1)(1+|\Gamma|^2)+(N^2+2)\mathrm{Re}(\Gamma)\right]\right\}. \qquad (6.3.7)$$

Finally, the two-term series approximation is given by

$$\tilde{W} \approx \frac{2}{3}\left|\frac{1}{1-\Gamma}\right|^2\left[\tilde{d}\left\{(N^2+\frac{1}{2})(1+|\Gamma|^2) + (N^2-1)\mathrm{Re}(\Gamma) + \frac{3}{2}N(1-|\Gamma|^2)\right\}\right.$$

$$\left.+\tilde{\tau}\left\{N^2\left[1+\mathrm{Re}(\Gamma)+|\Gamma|^2\right] - \frac{\tilde{\tau}^4}{630}\left[(21N^2-5)(1+|\Gamma|^2)+(21N^2+10)\mathrm{Re}(\Gamma)\right]\right\}\right] \tag{6.3.8}$$

All of these results reduce to their single-layer forms derived in the previous chapter when $N = 1$ and $\tilde{d} = 0$. Note that for large N the two-term approximation indicates that the total energy storage per layer will be proportional to N^2. This is in contrast to the result for the power dissipation, where the N^2 proportionality came into play only for larger normalized thicknesses. The low frequency regions of those curves were unchanged. The undesirable effects of increasing the number of layers are therefore expected to be more widespread for the stored energy than the power dissipation. Even so, the resulting increase in leakage inductance may not be as critical as the increase in power dissipation. This tradeoff will depend on the particlar application.

The graphical results are again be restricted to the thin-layer and two-term series approximations. Figures 6.3.1 and 6.3.2 show the energy stored in an N-layer winding for several values of N. The conditions for these curves

are the same as those in Figures 6.2.1 and 6.2.2 for the power dissipation. The behavior of the curves as M increases is again similar to the behavior of the single-layer results as the boundary condition ratio approaches unity (see Figures 5.2.1 and 5.4.2). This follows from the fact that as M increases more individual layers within the winding experience increased boundary condition ratios, thereby influencing the total winding summation. Also note that the two-term approximation is again valid up through the optimization region for minimum power, and that it diverges very rapidly thereafter. The author wishes to reemphasize the extreme care which is required when utilizing the two-term approximation. It is a very attractive solution because of its analytical simplicity, and for that reason it is easy to be overcome and forget to insure that the necessary conditions for its use are met. The primary advantage of the two-term approximation is that it provides an excellent forum for analytically investigating behavior near the minimum power optimum points because it leads to closed form solutions. Any involved design procedures based on the results in this dissertation would benefit greatly from and are well-suited for the use of a computer. It is highly recommended that one of the higher level solutions be used when developing computer software. Finally, the effect of the insulation thickness

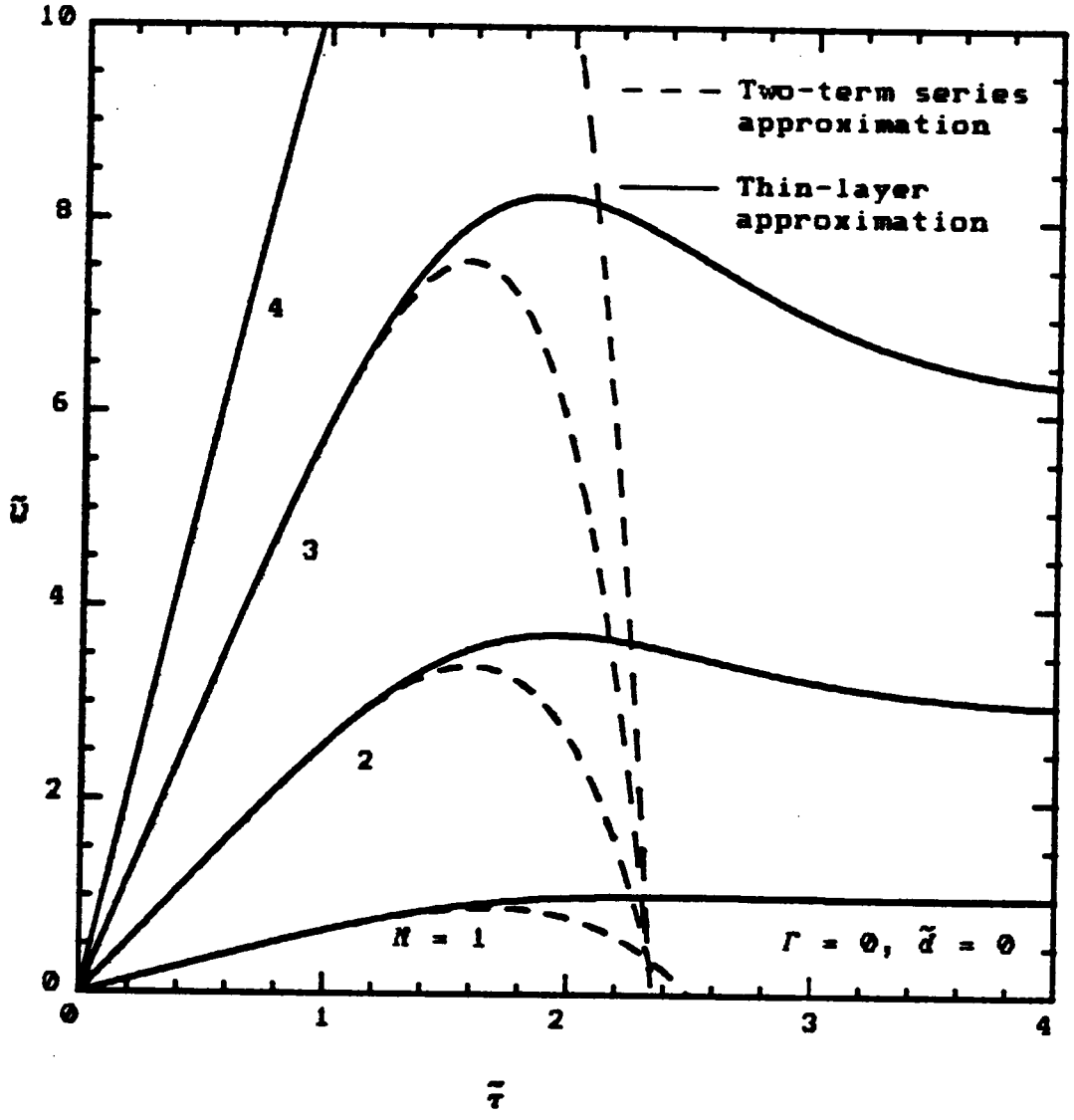

Figure 6.3.1. Normalized energy stored per layer in an N-layer winding vs. normalized conductor thickness with the number of layers varied as a parameter for some low values.

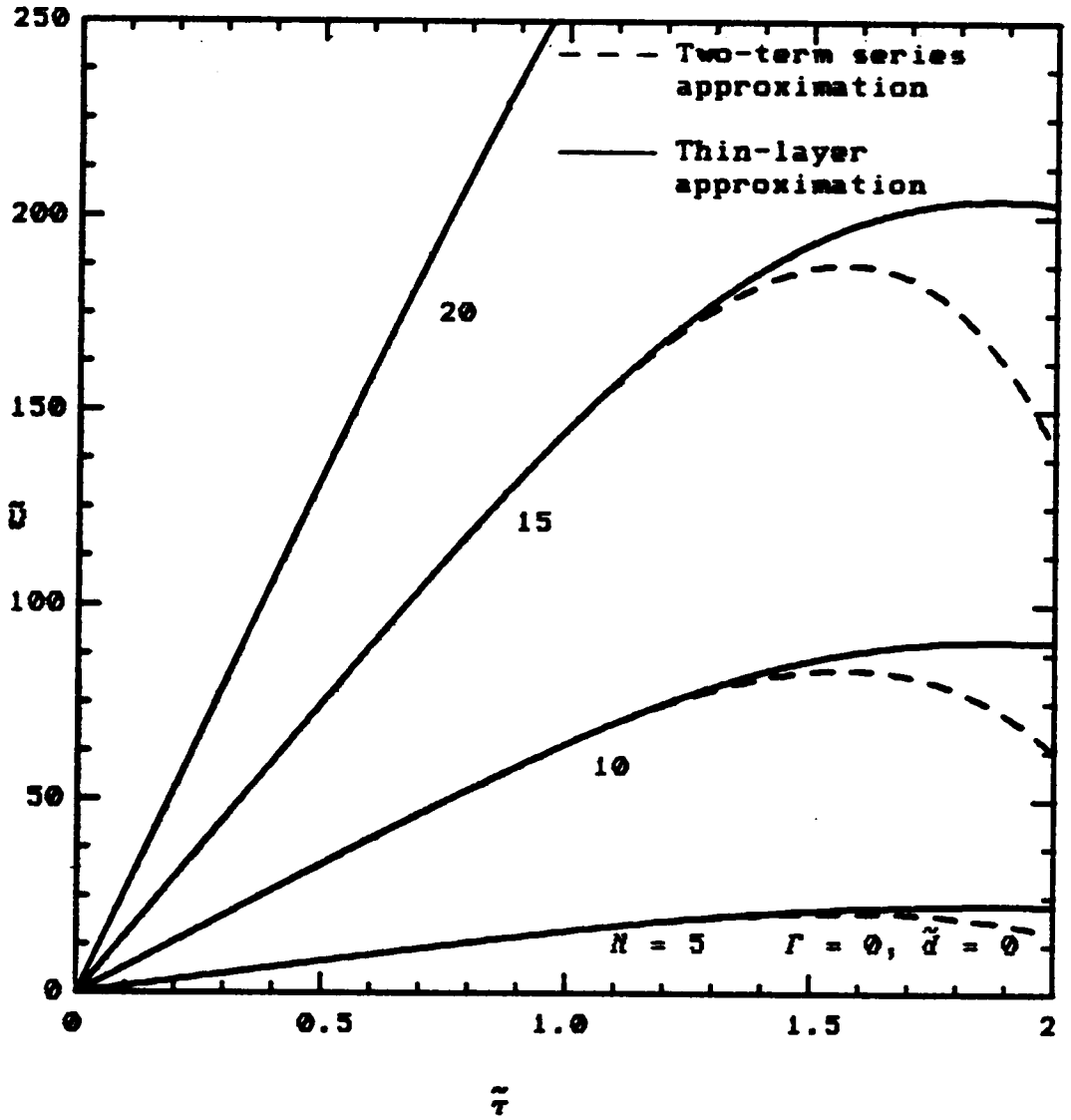

Figure 6.3.2. Normalized energy stored per layer in an N-layer winding vs. normalized conductor thickness with the number of layers varied as a parameter for some higher values.

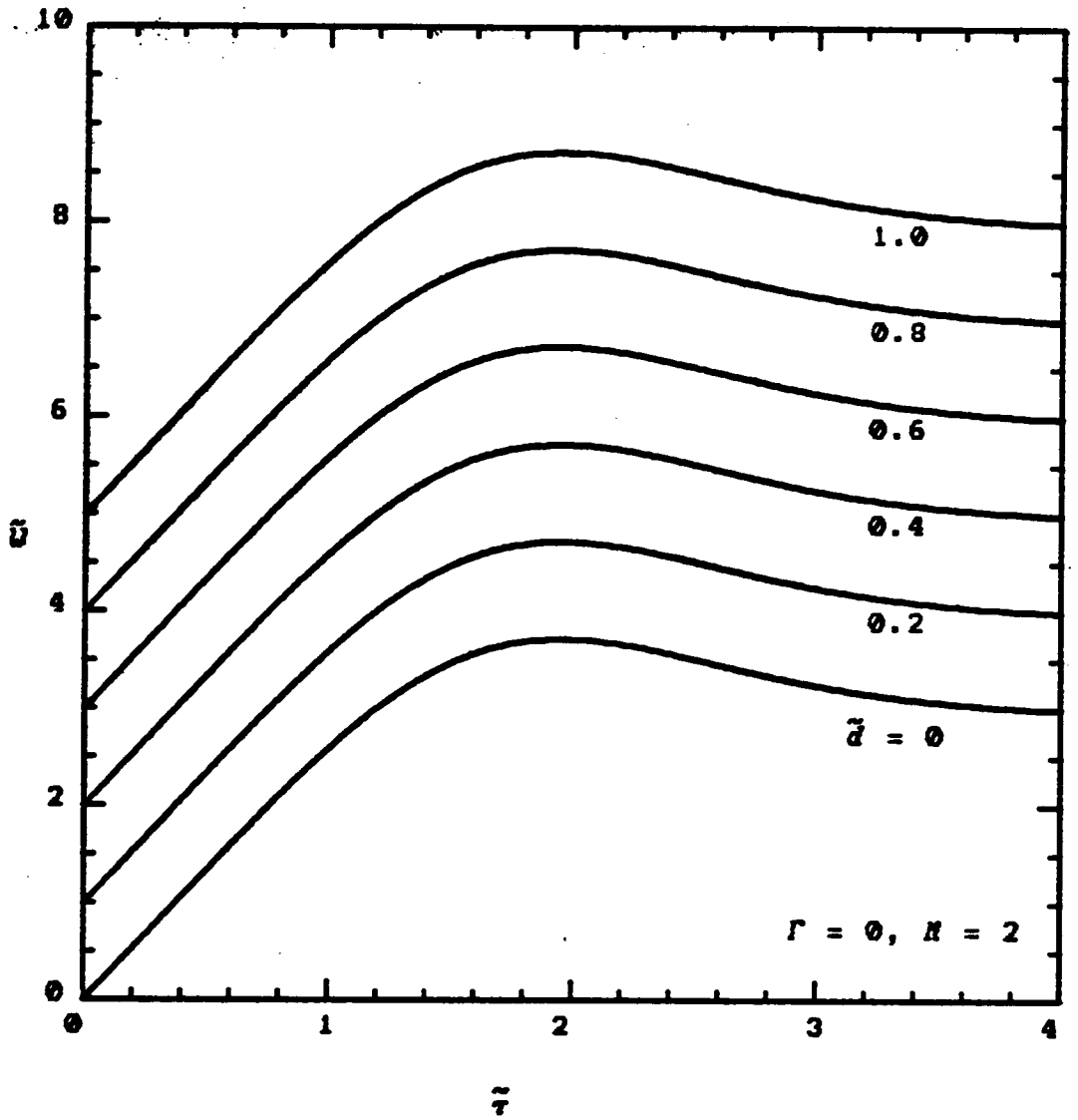

Figure 6.3.3. Normalized energy stored per layer in an N-layer winding vs. normalized conductor thickness with the insulation thickness varied as a parameter. All curves are computed using the thin-layer approximation.

is studied in Figure 6.3.3 for a two-layer winding. Note that the curves simply shift upward, and that this shift is significant even for thicknesses which are a small fraction of a skin depth. This behavoir is also evident in the corresponding term in equations (6.3.7) and (6.3.8). That term is independent of the normalized conductor thickness $\tilde{\tau}$ and directly proportional to the normalized insulation thickness $\tilde{d}$. The frequency is held constant while the thicknesses are varied.

6.4 MINIMUM POWER OPTIMIZATION

The power dissipated in an N-layer winding can be minimized with respect to the conductor thickness in the same manner as it was for the single-layer case. Since the conductor thicknesses are assumed to be equal, the equation that must be solved is

$$\frac{\partial \tilde{P}}{\partial \tilde{\tau}} = 0. \qquad (6.4.1)$$

This corresponds to equation (5.3.1) for the single-layer case and reduces to it for $N = 1$. The optimization procedure for the multi-layer winding is to solve equation (6.4.1) above for the optimum normalized conductor thickness $\tilde{\tau}^{opt}$, and use the result to find the corresponding minimum power dissipation $\tilde{P}^{min}$.

It is impractical to analytically solve equation (6.4.1) using either the exact expression for $\tilde{P}$ or its large argument asymptotic approximation. The same computer algorithm which was developed for the single-layer case can be used here to find the optimum conductor thickness. The main difference is that the number of computations, and therefore the computation time, increases by a factor of N. Software for this multi-layer optimization has been developed and tested by the author. As before, the accuracy of these results is necessary only if the normalized mean radii $\tilde{\rho}_n$ are significantly less than 20. The results under those conditions are similar to those for the single-layer case (see Figures 5.1.3 and 5.2.3) and will therefore not be repeated here. Such low values for the normalized radii are typically impractical anyway since they would leave little space for core material in the center of the windings.

Consider next the thin-layer approximation for $\tilde{P}$ given in equation (6.2.11). Taking the derivative according to equation (6.4.1) leads to the following transcendental equation:

$$\frac{\cosh\tilde{\tau}}{\cos\tilde{\tau}} + \frac{\cos\tilde{\tau}}{\cosh\tilde{\tau}} \approx 2\frac{(N^2+\frac{1}{2})(1+|\Gamma|^2) + (N^2-1)\mathrm{Re}(\Gamma)}{(N^2-1)(1+|\Gamma|^2) + (N^2+2)\mathrm{Re}(\Gamma)}. \quad (6.4.2)$$

This expression is very similar to the corresponding single-layer result in equations (5.3.3). The left-hand side is identical. The right-hand side is slightly more complex because the effect of the number of layers comes into play. Incidently, this equation reduces to the single-layer result in equations (5.3.3) for $N = 1$. The method of solution of equation (6.4.2) is the same as for the single-layer case, since the right-hand side is still just a constant with respect to $\tilde{\tau}$. One simply evaluates this constant for a particular application, and then numerically solves the equation as before.

Consider next the pursuit of a closed form solution via the two-term series approximation. Taking the derivative of equation (6.2.12) with respect to $\tilde{\tau}$ is a trivial exercise, and leads to the simple result

$$\tilde{\tau}^{opt} \approx \left\{15\left[\frac{|1 - \Gamma|^2}{(5N^2-1)(1+|\Gamma|^2) + (5N^2+2)Re(\Gamma)}\right]\right\}^{\frac{1}{4}} \quad (6.4.3)$$

which also reduces to its single-layer counterpart in equation (5.4.3) for $N = 1$. Substituting this optimum conductor thickness back into equation (6.2.12) gives the corresponding minimized power

$$\tilde{P}^{min} \approx \frac{4}{3}\frac{1}{\tilde{\tau}^{opt}} = \frac{4}{3}\left\{\frac{1}{15}\left[\frac{(5N^2-1)(1+|\Gamma|^2) + (5N^2+2)Re(\Gamma)}{|1 - \Gamma|^2}\right]\right\}^{\frac{1}{4}} \quad (6.4.4)$$

Two special cases of the two-term approximation are important enough to warrant further attention. First, consider a zero boundary condition ratio. This case is the most desirable because it results in the lowest power dissipation and energy storage. For this case, equations (6.2.12), (6.3.8), (6.4.3), and (6.4.4) become

$$\tilde{P} \underset{\Gamma=0}{\approx} \frac{1}{\tilde{\tau}} \left[1 + \frac{\tilde{\tau}^4}{45}(5N^2-1)\right] \tag{6.4.5a}$$

$$\tilde{W} \underset{\Gamma=0}{\approx} \frac{2}{3}\left\{\tilde{d}\left[N^2 + \frac{3}{2}N + \frac{1}{2}\right] + \tilde{\tau}\left[N^2 - \frac{\tilde{\tau}^4}{630}(21N^2-5)\right]\right\} \tag{6.4.5b}$$

$$\tilde{\tau}^{\text{opt}} \underset{\Gamma=0}{\approx} \left[\frac{15}{5N^2-1}\right]^{\frac{1}{4}} \tag{6.4.5c}$$

$$\tilde{P}^{\min} \underset{\Gamma=0}{\approx} \frac{4}{3}\left[\frac{5N^2-1}{15}\right]^{\frac{1}{4}}. \tag{6.4.5d}$$

The latter two equations are especially useful and simple formulas for the optimum thickness and minimum power dissipation. For large N the above equations become even simpler:

$$\tilde{P} \underset{\substack{\Gamma=0 \\ N\to\infty}}{\approx} \frac{1}{\tilde{\tau}} \left[1 + \frac{1}{9}N^2\tilde{\tau}^4\right] \tag{6.4.6a}$$

$$\tilde{W} \underset{\substack{\Gamma=0 \\ N\to\infty}}{\approx} \frac{2}{3}N^2\left\{\tilde{d} + \tilde{\tau}\left[1 - \frac{1}{30}\tilde{\tau}^4\right]\right\} \tag{6.4.6b}$$

$$\tilde{\tau}^{opt} \underset{\substack{\Gamma=0 \\ N\to\infty}}{\approx} \frac{3^{1/4}}{N^{1/2}} \qquad (6.4.6c)$$

$$\tilde{P}^{min} \underset{\substack{\Gamma=0 \\ N\to\infty}}{\approx} \frac{4}{3}\frac{N^{1/2}}{3^{1/4}}. \qquad (6.4.6d)$$

Actually, N does not have to be very large for these approximations to be quite good. N = 1 results in only 5.7% error in the optimization equations and at N = 2 the error is practically negligible at 1.3%. Although this degree of simplification is certainly not necessary, it provides a very fundamental result. Namely, the minimum power dissipation is directly proportional to the square root of the number of layers, and the corresponding optimum conductor thickness is inversely proportional to the same. Also, the stored energy is directly proportional to the square of the number of layers. These are more good rules of thumb which come in handy when committed to memory.

Figures 6.4.1 through 6.4.3 show the graphical results of the minimum power optimization for windings with various numbers of layers. The properties discussed above in the special cases can be observed at Γ = 0, and it appears that these properties are preserved as Γ increases. Figure 6.4.1 shows the optimum normalized conductor thickness vs. Γ, and Figures 6.4.2 and 6.4.3 give the corresponding normalized minimum power dissipation and energy storage per layer.

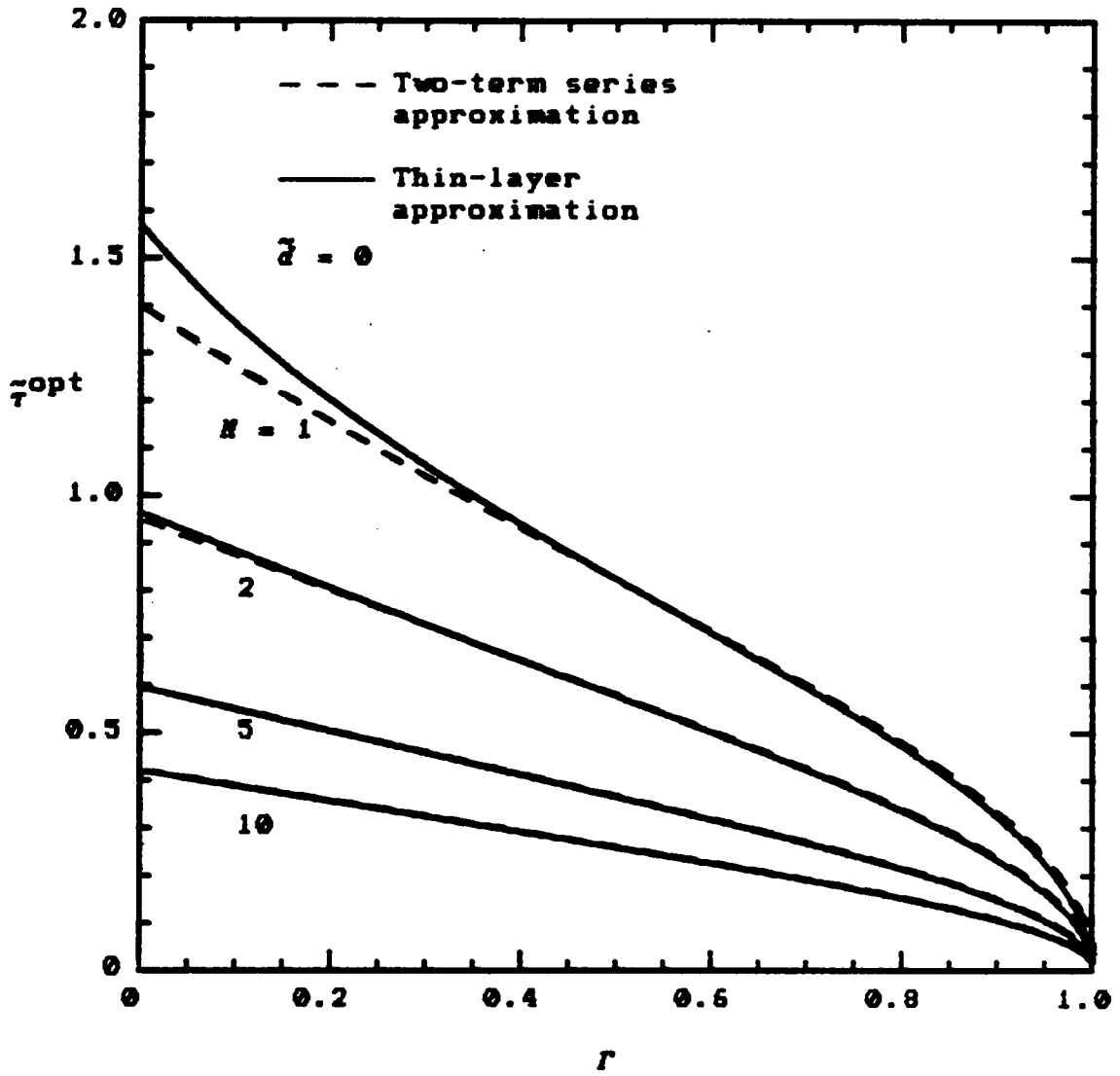

Figure 6.4.1. Optimum normalized conductor thickness for an N-layer winding vs. boundary condition ratio with the number of layers varied as a parameter.

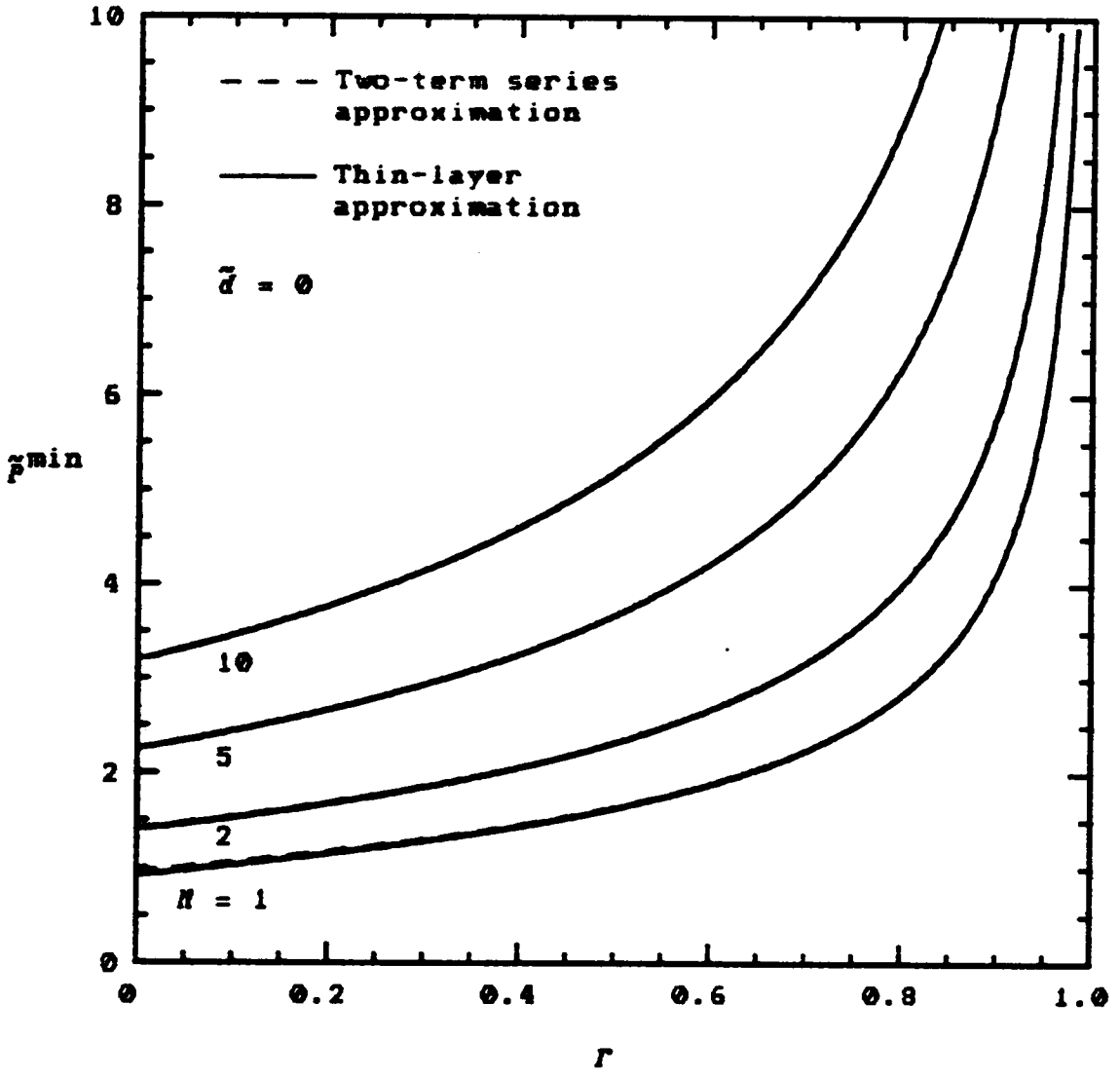

Figure 6.4.2. Minimum normalized power dissipation (at the optimum conductor thickness) in an M-layer winding vs. boundary condition ratio with the number of layers varied as a parameter.

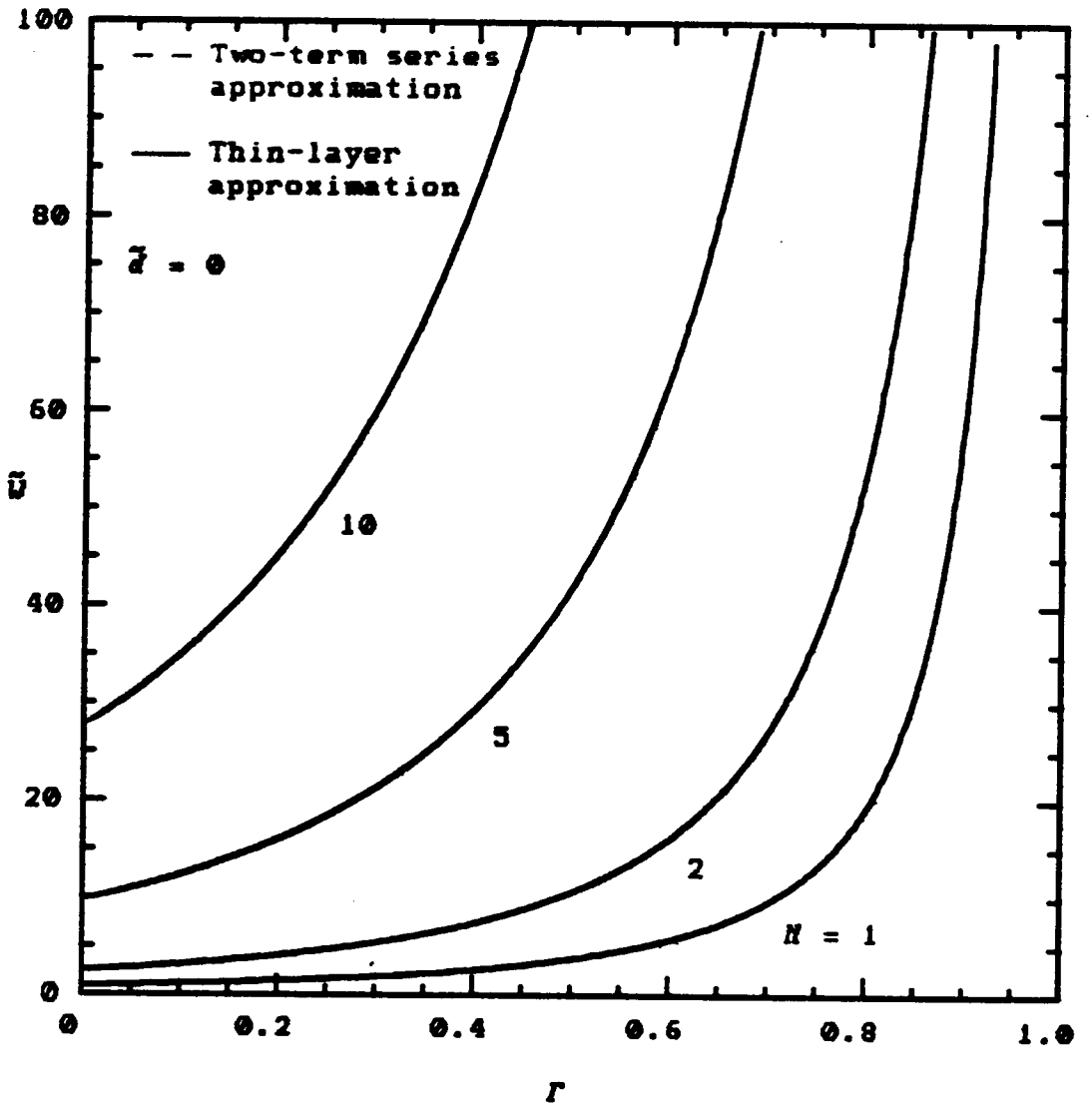

Figure 6.4.3. Normalized energy stored (at the optimum conductor thickness) in an N-layer winding vs. boundary condition ratio with the number of layers varied as a parameter.

Both the thin-layer and the two-term series approximations are presented in these graphs. The accuracy of the two-term approximation is extremely good, verifying its validity in the optimization region. In fact, the curves for these two approximations of the power dissipation and the energy storage are indistinguishable. The accuracy for the optimum thickness is only slightly worse, and it improves as the number of layers increases. The worst case is for a single layer at zero boundary condition ratio. Although this is a very important case, it was found in the single-layer results that the error was still a reasonable 11.4%.

6.5 INDIVIDUAL LAYER OPTIMIZATION

Two techniques for reducing the power dissipation in multi-layer windings are considered in this and the next section. They are both global techniques in the sense that they address the overall strategy of arranging and designing windings on a transformer. Simple and revealing analytical investigations of these techniques are possible because of the accuracy of the two-term series approximations near the optimum conductor thickness, and the fact that they are in closed form. Split windings are discussed in the following section, and individual layer optimization is the topic of this section.

At the beginning of this chapter, certain practical assumptions were made concerning multi-layer windings. The purpose here is to investigate the possibiliy of relaxing one of these assumptions in an attempt to reduce the power dissipation further. The assumption of interest is given by equation (6.1.1). It states that the thicknesses of all of the conductor layers within a winding are equal. While this is usually the case for practical reasons, it is a constraint which ultimately results in increased power dissipation. Since the boundary condition ratio varies from layer to layer, one would expect that optimizing the thickness of each individual layer would result in lower power dissipation. The purpose here is to determine the extent of this reduction, so that it can be compared with the added complexity and cost of construction.

The comparison between the individual layer optimization which allows unequal layer thicknesses and the more practical equal thickness optimization will be made by evaluating the minimum normalized power dissipation per layer $\tilde{P}^{min}$. The result for the equal thickness optimization has already been determined; it is given in equation (6.4.4). It is repeated here with the addition of the subscript e to indicate equal conductor layer thicknesses:

$$\tilde{P}_e^{\min} \approx \frac{4}{3}\left\{\frac{1}{15}\left[\frac{(5N^2-1)(1+|\Gamma|^2) + (5N^2+2)\mathrm{Re}(\Gamma)}{|1-\Gamma|^2}\right]\right\}^{\frac{1}{4}}. \quad (6.5.1)$$

One must return to the results of the single-layer analysis to derive the corresponding expression for individual layer optimization. The minimum normalized power dissipation in the nth layer is given in equation (5.4.4). This result must be summed over the N layers, and then divided by N to get the per-layer dissipation which is directly comparable to the above result:

$$\tilde{P}_u^{\min} \approx \frac{1}{N}\sum_{n=1}^{N}\tilde{P}_n^{\min} \approx \frac{1}{N}\sum_{n=1}^{N}\frac{4}{3}\left\{\frac{1}{15}\left[\frac{4(1+|\Gamma_n|^2) + 7\mathrm{Re}(\Gamma_n)}{|1-\Gamma_n|^2}\right]\right\}^{\frac{1}{4}}. \quad (6.5.2)$$

The subscript u indicates unequal conductor layer thicknesses. The nth layer boundary condition ratio Γ_n was determined in equation (6.1.10) in terms of the overall winding boundary condition ratio Γ. Substituting that relation into equation (6.5.2) and simplifying the summand yields

$$\tilde{P}_u^{\min} \approx \frac{1}{N}\sum_{n=1}^{N}\frac{4}{3}\left\{\frac{1}{15}\left[4 + 15\frac{[\Gamma(N-n+1)+(n-1)][\Gamma(N-n)+n]^*}{|1-\Gamma|^2}\right]\right\}^{\frac{1}{4}}. \quad (6.5.3)$$

This summation cannot be simplified because of the fractional power in the summand. The ratio of the

normalized power dissipations is now formed in order to determine the percentage reduction obtained from individual layer optimization:

$$\frac{\bar{P}_u^{min}}{\bar{P}_e^{min}} \approx \frac{1}{N}\sum_{n=1}^{N}\left[\frac{4|1-\Gamma|^2 + 15[\Gamma(N-n+1)+(n-1)][\Gamma(N-n)+n]^*}{(5N^2-1)(1+|\Gamma|^2) + (5N^2+2)\mathrm{Re}(\Gamma)}\right]^{\frac{1}{4}}. \quad (6.5.4)$$

This expression is rather complex in appearance but it can be easily programmed on a computer or programmable calculater. However, it is instructive to first consider the important case of $\Gamma = 0$, for which the expression simplifies considerably to

$$\frac{\bar{P}_u^{min}}{\bar{P}_e^{min}} \underset{\Gamma=0}{\approx} \frac{1}{N}\sum_{n=1}^{N}\left[\frac{4 + 15n(n-1)}{5N^2-1}\right]^{\frac{1}{4}}. \quad (6.5.5)$$

As $N \to \infty$ the n^2 terms dominate the numerator and consequently the summation, so that

$$\lim_{N\to\infty}\frac{\bar{P}_u^{min}}{\bar{P}_e^{min}} \underset{\Gamma=0}{\approx} \lim_{N\to\infty} 3^{1/4}\,\frac{1}{N}\sum_{n=1}^{N}\left[\frac{n}{N}\right]^{\frac{1}{2}}. \quad (6.5.6a)$$

This expression is recognized as the limiting form of a definite integral, namely,

$$\lim_{N\to\infty}\frac{\tilde{P}_u^{min}}{\tilde{P}_e^{min}} \approx 3^{1/4}\lim_{N\to\infty}\sum_{n=1}^{N}\left[\frac{n}{N}\right]^{\frac{1}{2}}\frac{1}{N} = 3^{1/4}\int_0^1\sqrt{x}dx = 0.877. \quad (6.5.6b)$$

This surprisingly simple result shows that, for a zero winding boundary condition ratio, one can expect to gain at most a 12.3% reduction in power dissipation by individually optimizing the thickness of each conductor layer. For smaller values of N, evaluation of equation (6.5.5) indicates that the reduction is slightly less. A summary of these results is presented in Table 6.5.1a. The ratio is equal to unity for $N = 1$ since there is no difference in the two methods. The percentage reduction spans the narrow range of 8.3% to 12.3% for all other possible values of N from 2 to ∞. This conclusion leads to yet another important and useful rule of thumb: that one can expect roughly a 10% reduction in power dissipation by individually optimizing the thicknesses of the conductor layers. This is certainly not an overwhelming improvement, and in most cases it probably would not be worth the added complexity in the construction.

The results just presented were for a winding boundary condition ratio of zero. It turns out that the reductions in the power dissipation are largest for this case. As the boundary condition ratio increases toward unity, the improvement diminishes. In order to show this, equation

Table 6.5.1a. Ratio of the normalized power dissipation resulting from individual layer optimization to that from equal thickness optimization for an N-layer winding when the winding boundary condition ratio is zero.

N	$\left.\frac{\tilde{P}_u^{min}}{\tilde{P}_e^{min}}\right\|_{\Gamma=0}$
1	1.000
2	0.917
3	0.898
4	0.891
5	0.887
∞	0.877

Table 6.5.1b. Ratio of the normalized power dissipation resulting from individual layer optimization to that from equal thickness optimization for varying values of the boundary condition ratio Γ as $N \to \infty$.

Γ	$\lim_{N\to\infty} \frac{\tilde{P}_u^{min}}{\tilde{P}_e^{min}}$
0.0	0.877
0.2	0.946
0.4	0.977
0.6	0.992
0.8	0.998
1.0	1.000

(6.5.4) must be evaluated for nonzero values of Γ. The trend of the results can be determined by letting $N \to \infty$ in equation (6.5.4), and following the same procedure as equations (6.5.6) to find the corresponding integral representation. The numerical results of this process are listed in Table 6.5.1b.

6.6 SPLIT WINDINGS

Consider the simple case of a transformer with one primary and one secondary, each with N layers. Let the primary and secondary be wound in separate regions as depicted Figure 6.6.1a. Admittedly, this arrangement is somewhat oversimplified, but it is general enough to demonstrate the advantages of split windings. For this arrangement the magnitude of the magnetic field intensity begins at zero at the outer boundary of the primary, increases to the peak value $H_{max} = NK$ at the primary/secondary interface, and then reduces back to zero at the outer boundary of the secondary. This variation is depicted linearly in the figure for convenience, even though it cannot be truly linear unless the current density is uniform. Under optimized conditions, the two-term series approximation of the normalized power dissipated per layer in either the primary or secondary is given by equation (6.4.5d) since the boundary condition ratio is zero:

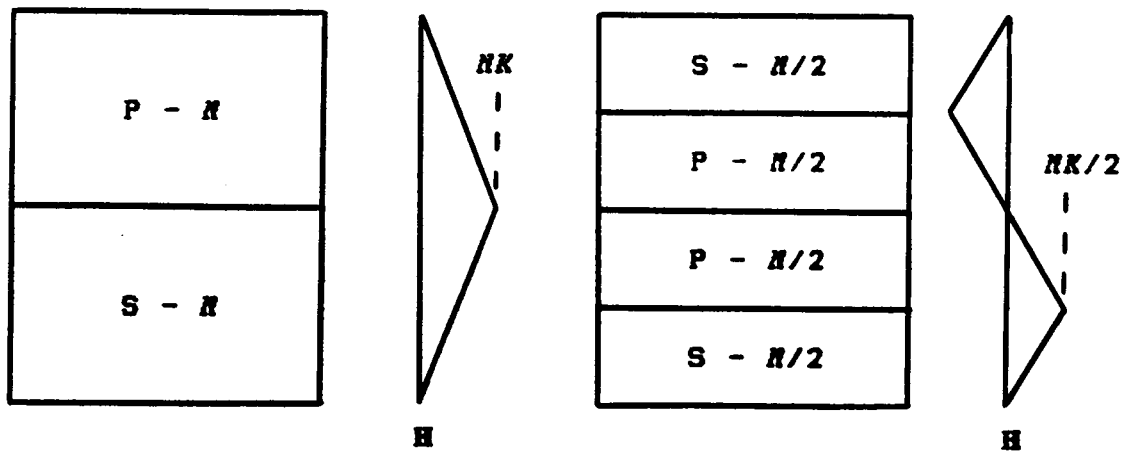

(a) s = 1 section. (b) s = 2 sections.

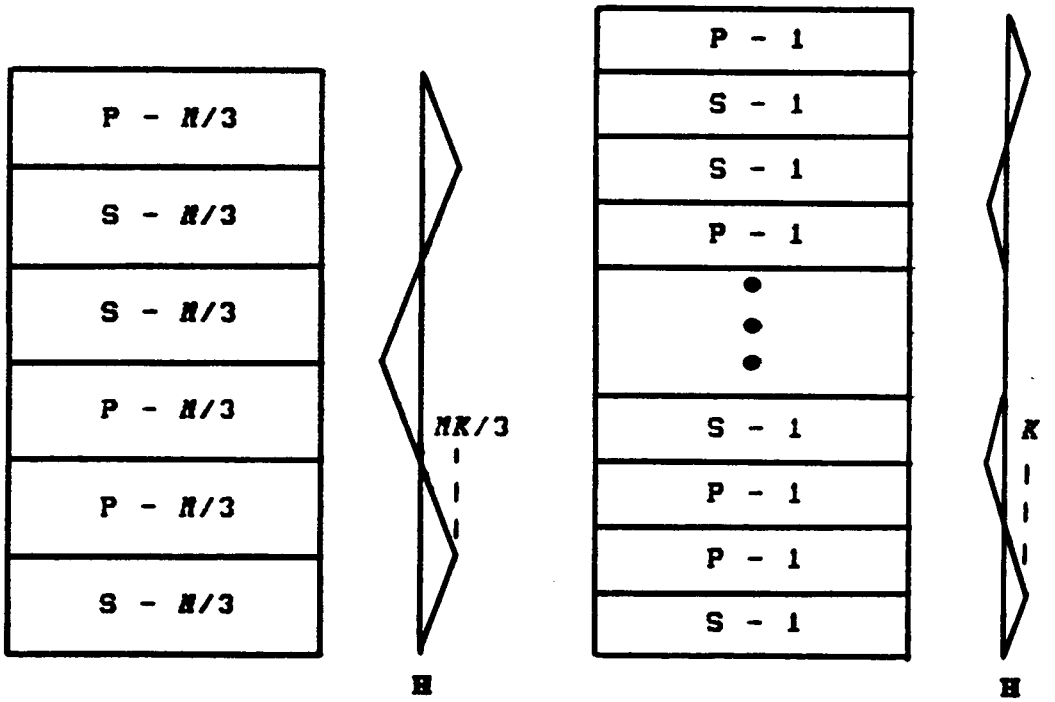

(c) s = 3 sections. (d) s = N sections.

Figure 6.6.1. Sketches of successive stages of sectionalization of a simple transformer with an N-layer primary and secondary. The number of layers in each section is shown, and s denotes the number of sections that each winding is split into.

$$\tilde{P}_1^{\min} \underset{\Gamma=0}{\approx} \frac{4}{3}\left[\frac{5N^2-1}{15}\right]^{\frac{1}{4}}. \qquad (6.6.1)$$

The subscript 1 indicates that each of the windings are in one unsplit section. Now consider the arrangements in Figures 6.6.1b, c, and d; where both primary and secondary are spilt into 2, 3, and N identical sections, respectively. The corresponding number of layers in each section and the peak magnetic field intensity decrease as shown. If s denotes the number of sections that the winding has been split into, then N/s is the number of layers in each section (strictly speaking, values which lead to fractional layers are not covered by this simplified analysis). Each section can therefore be individually optimized. And since they are all identical and have zero boundary condition ratios, then the normalized power dissipation per layer is given by equation (6.6.1) with N replaced by N/s:

$$\tilde{P}_s^{\min} \underset{\Gamma=0}{\approx} \frac{4}{3}\left[\frac{5(N/s)^2-1}{15}\right]^{\frac{1}{4}}. \qquad (6.6.2)$$

The subscript s has been added to represent the number of sections that the winding has been split into. The ratio of equations (6.6.2) and (6.6.1) is now formed in order to determine the percentage reduction in power dissipation that results from splitting the windings:

$$\frac{\tilde{p}_s^{\min}}{\tilde{p}_1^{\min}} \underset{r=0}{\approx} \left[\frac{5(N/s)^2-1}{5N^2-1}\right]^{\frac{1}{4}} \underset{N\to\infty}{\approx} \frac{1}{\sqrt{s}}. \qquad (6.6.3)$$

The last step is a good approximation even for small values of N, and it shows that the power dissipation in a winding is inversely proportional to the square root of the number of sections that it is split into. Several examples of this ratio are computed and listed in Table 6.6.1a. Note that the reductions in power dissipation are very significant. Splitting a winding only once into two sections results in a 30% reduction. Splitting again into three sections gives an additional 13% reduction. The improvements continue, but diminish in magnitude, as the winding is split into more and more sections.

Similar reductions occur for the energy storage when the windings are split and optimized for minimum power dissipation. The ratio of the energy stored per layer in a winding split into s sections to that in an unsplit winding is derived from equations (6.4.5b) and (6.4.5c) as

$$\left.\frac{\tilde{U}_s}{\tilde{U}_1}\right|_{\tilde{\tau}=\tilde{\tau}^{opt}} \quad \underset{r=0}{\approx}$$

$$\frac{\tilde{d}\left[(\frac{N}{s})^2+\frac{3}{2}(\frac{N}{s})+\frac{1}{2}\right] + \left[\frac{15}{5(N/s)^2-1}\right]^{\frac{1}{4}}\left\{(\frac{N}{s})^2-\frac{1}{42}\left[\frac{21(N/s)^2-5}{5(N/s)^2-1}\right]\right\}}{\tilde{d}\left[N^2+\frac{3}{2}N+\frac{1}{2}\right] + \left[\frac{15}{5N^2-1}\right]^{\frac{1}{4}}\left\{N^2-\frac{1}{42}\left[\frac{21N^2-5}{5N^2-1}\right]\right\}} \qquad (6.6.4a)$$

Table 6.6.1a. Ratio of the normalized power dissipation in an optimized N-layer winding which is split into s sections to that in an unsplit winding (see Figure 6.6.1). Results for several combinations of N and s are listed.

$\frac{\tilde{p}_s^{min}}{\tilde{p}_1^{min}}$	$N = 2$	$N = 5$	$N = 10$	$N \to \infty$
$s = 1$	1.000	1.000	1.000	1.000
$s = 2$	0.677	0.703	0.706	0.707
$s = 5$	—	0.424	0.442	0.447
$s = 10$	—	—	0.299	0.316

Table 6.6.1b. Ratio of the normalized energy stored in an optimized N-layer winding which is split into s sections to that in an unsplit winding (see Figure 6.6.1). Results for several combinations of N and s are listed. The insulation thickness is taken to be zero.

$\frac{\tilde{W}_s}{\tilde{W}_1}\Big\vert_{\tilde{\tau}=\tilde{\tau}^{opt}}$	$N = 2$	$N = 5$	$N = 10$	$N \to \infty$
$s = 1$	1.000	1.000	1.000	1.000
$s = 2$	0.342	0.351	0.353	0.354
$s = 5$	—	0.086	0.088	0.089
$s = 10$	—	—	0.030	0.032

which, for large N, becomes

$$\left.\frac{\tilde{U}_s}{\tilde{U}_1}\right|_{\tilde{\tau}=\tilde{\tau}^{opt}} \underset{N\to\infty}{\overset{\tilde{r}=0}{\approx}} \frac{\tilde{d}(N/s)^2 + 3^{1/4}(N/s)^{3/2}}{\tilde{d}N^2 + 3^{1/4}N^{3/2}}. \qquad (6.6.4b)$$

The energy stored in the insulation layers is inversely proportional to s^2, and the energy stored in the conductor layers is inversely proportional to $s^{3/2}$. Thus, the reduction in the stored energy is even more dramatic than the reduction in the power dissipation. Some numerical results are listed in Table 6.6.1b for the same examples in Table 6.6.1a for the power dissipation. For consistency, the insulation thickness is taken to be zero, so that the results reflect the behavior in the conductors.

As a final practical note, it should be pointed out that splitting the winding results in larger optimum conductor thicknesses. In fact, the increase in thickness is in the same proportion as the decrease in the power dissipation, which is immediately evident from equations (6.4.5c) and (6.4.5d). The improvements in the form of reduced power dissipation and energy storage must therefore be weighed against the increased size and complexity of split windings.

Several very simple and useful results have been derived in this section with respect to split windings. They provide more valuable rules of thumb for designing transformers.

CHAPTER 7

GENERALIZATION TO ARBITRARY PERIODIC EXCITATION

Up to this point all of the analysis has been for monochromatic sinusoidal excitation. The waveforms associated with switched-mode power converters vary widely from one topology to another. There are two general characteristics which all of these waveforms share. The first is that they are all periodic in time. And the second is that the majority of the waveforms are far from being pure sinusoids. In fact, many of the waveforms in present designs are very high in harmonic content. For instance, the transition times in square and triangular waves are becoming shorter and shorter as switching devices improve.

The obvious technique for extending the time-harmonic sinusoidal analysis to the case of an arbitrary periodic waveform is Fourier analysis. This technique allows the many existing different types of waveforms and also those encountered in the future to be analyzed uniformly with straightforward and well-known methods. The waveforms are first decomposed into their sinusoidal harmonic components; each may then be handled by the existing time-harmonic analysis. These results may then be appropriately combined to yield the desired solution.

7.1 POWER DISSIPATION

The analysis for the more restricted single-layer case is omitted in this chapter. Instead, it begins with the more general multi-layer case. If desired, the single-layer formulas can be derived by simply letting $N = 1$ and making the appropriate changes in notation to obtain the form for the general nth layer.

The power dissipated in an N-layer winding using the practical multi-layer assumptions in section 6.1 is obtained by generalizing equations (6.2.4) to arbitrary periodic excitation. The current per unit axial length is expanded into a Fourier series, which leads to the following series for the power dissipation since contributions from the cross product terms vanish:

$$P \doteq P_0 + \sum_{k=1}^{\infty} P_k = 2\frac{\pi l}{\sigma} N K_0^2 \frac{\rho_w}{\tau} + \frac{\pi l}{\sigma} N \tilde{\rho}_{w1} \sum_{k=1}^{\infty} K_k^2 \tilde{P}_k \qquad (7.1.1a)$$

$$\tilde{P}_k \doteq \frac{1}{N} \sum_{n=1}^{N} \frac{\tilde{\rho}_{nk}}{\tilde{\rho}_{w1}} \tilde{P}_{nk}, \qquad (7.1.1b)$$

where

$$\tilde{\rho}_{nk} \doteq \frac{\rho_n}{\delta_k} = \tilde{\rho}_{wk} + \left[n - \frac{N+1}{2} \right] (\tilde{\tau}_k + \tilde{d}_k) \qquad (7.1.2a)$$

$$\tilde{\rho}_{wk} \triangleq \frac{\rho_w}{\delta_k} = \tilde{\rho}^{i}_{1k} + \left(\frac{N-1}{2}\right)\tilde{d}_k + \left(\frac{N}{2}\right)\tilde{\tau}_k \qquad (7.1.2b)$$

$$\tilde{\tau}_k \triangleq \frac{\tau}{\delta_k} \qquad (7.1.2c)$$

$$\tilde{d}_k \triangleq \frac{d}{\delta_k} \qquad (7.1.2d)$$

$$\delta_k \triangleq \sqrt{\frac{2}{k\omega_0\mu_0\sigma}}. \qquad (7.1.2e)$$

All of the distances which formerly were normalized with respect to the skin depth are now a function of the kth harmonic frequency. The subscript k is used to denote values at the kth harmonic for which $k = 1$ corresponds to the fundamental frequency

$$\omega_0 \triangleq \frac{2\pi}{T}, \qquad (7.1.3)$$

where T is defined to be the period of the waveform. K_k; $k = 0,1,2,\ldots,\infty$ are the amplitude Fourier coefficients of the current per unit axial length in the conductor layers. Please refer to equations (C.1.5) in Appendix C on Fourier analysis for the definition of these coefficients and how they are related to the standard trigonometric and complex forms of the Fourier coefficients. Appendix C also contains other useful formulas associated with Fourier analysis which

are defined for the purposes of the work here. K_0 is the DC component; it is treated separately since the integration for the power dissipation is trivial and leads to the extra factor of two. The only terms in equations (7.1.1) which have not been identified and discussed are the normalized power dissipations $\tilde{P}_{nk}$ and $\tilde{P}_k$. The former represent the power dissipated in the nth conductor layer at the kth harmonic frequency. They are determined by replacing the normalized distance quantities in the equations for $\tilde{P}_n$ with the new frequency dependent quantities defined in equations (7.2.2). In particular, the equations of interest are (5.1.4), (5.1.6), (5.1.7), and (5.4.1) which give the exact solution, large argument asymptotic approximation, thin-layer approximation, and two-term series approximation for $\tilde{P}_n$, respectively. The latter quantities $\tilde{P}_k$ represent the normalized power dissipation per layer in an N-layer winding at the kth harmonic frequency. These quantities are a weighted average of the corresponding individual layer terms as evidenced by equation (7.1.1b). Except for the exact solution, the summation over the N layers simplifies in varying degrees. The resulting expressions for $\tilde{P}$ have been derived previously for the sinusoidal case; they are given in equations (6.2.5), (6.2.11), and (6.2.12) for the large argument asymptotic approximation, thin-layer approximation, and two-term series approximation,

respectively. Thus, the $\tilde{P}_k$ terms are determined by substituting the frequency dependent quantities defined in equations (7.2.2) into the aforementioned equations for $\tilde{P}$.

The expressions resulting from the preceeding discussion are now summarized for convenience. Since the exact solution does not simplify, it will not be repeated. One must simply make the indicated substitutions and evaluate the expressions. The earlier computer programs are easily modified to accomplish this task. The number of computations, and therefore the computation time, will increase by another factor of k_{max} which denotes the maximum number of harmonics included.

The large argument asymptotic approximation is obtained by substituting the frequency dependent quantities from equations (7.1.2) into equation (6.2.5) which is then substituted into equation (7.1.1a). The result is

$$P \sim 2\frac{\pi l}{\sigma}\tilde{R}\tilde{\rho}_{w1}K_0^2\frac{1}{\tilde{\tau}_1} + \frac{\pi l}{\sigma}\tilde{R}\tilde{\rho}_{w1}\sum_{k=1}^{\infty}K_k^2$$

$$\frac{1}{\tilde{R}}\left\{\left[\frac{\sinh 2\tilde{\tau}_k + \sin 2\tilde{\tau}_k}{\cosh 2\tilde{\tau}_k - \cos 2\tilde{\tau}_k}\right]\sum_{n=1}^{\tilde{R}}\frac{\tilde{\rho}_{nk}}{\tilde{\rho}_{w1}}\left[\frac{1+|\Gamma_n|^2}{|1-\Gamma_n|^2} + \frac{1}{2}\frac{\tilde{\tau}_k}{\tilde{\rho}_{nk}}\frac{1-|\Gamma_n|^2}{|1-\Gamma_n|^2}\right]\right.$$

$$\left. - 4\left[\frac{\cosh\tilde{\tau}_k\sin\tilde{\tau}_k + \cos\tilde{\tau}_k\sinh\tilde{\tau}_k}{\cosh 2\tilde{\tau}_k - \cos 2\tilde{\tau}_k}\right]\sum_{n=1}^{\tilde{R}}\frac{\tilde{\rho}_{nk}}{\tilde{\rho}_{w1}}\left[1-\left(\frac{1}{2}\frac{\tilde{\tau}_k}{\tilde{\rho}_{nk}}\right)^2\right]^{\frac{1}{2}}\frac{\mathrm{Re}(\Gamma_n)}{|1-\Gamma_n|^2}\right\}. \quad (7.1.4)$$

The change to normalized quantities in the DC term is permissible since both the numerator and denominator are changed in such a way that cancellation occurs. For reasons that will become apparent later, this result is now rearranged into the slightly different form

$$P \sim 2\frac{\pi l}{\sigma}K_{rms}^2 N\tilde{\rho}_w\tilde{P}, \qquad (7.1.5)$$

where $\tilde{P}$ represents the normalized power dissipated per layer in an N-layer winding:

$$\tilde{P} \sim \frac{K_0^2}{K_{rms}^2}\frac{1}{\tilde{\tau}} + \frac{1}{2}\frac{1}{N}\sum_{k=1}^{\infty}\sqrt{k}\,\frac{K_k^2}{K_{rms}^2}$$

$$\left\{\left[\frac{\sinh 2\tilde{\tau}_k + \sin 2\tilde{\tau}_k}{\cosh 2\tilde{\tau}_k - \cos 2\tilde{\tau}_k}\right]\sum_{n=1}^{N}\frac{\tilde{\rho}_n}{\tilde{\rho}_w}\left[\frac{1+|\Gamma_n|^2}{|1-\Gamma_n|^2} + \frac{1}{2}\frac{\tilde{\tau}}{\tilde{\rho}_n}\,\frac{1-|\Gamma_n|^2}{|1-\Gamma_n|^2}\right]\right.$$

$$\left. - 4\left[\frac{\cosh\tilde{\tau}_k\sin\tilde{\tau}_k + \cos\tilde{\tau}_k\sinh\tilde{\tau}_k}{\cosh 2\tilde{\tau}_k - \cos 2\tilde{\tau}_k}\right]\sum_{n=1}^{N}\frac{\tilde{\rho}_n}{\tilde{\rho}_w}\left[1-\left(\frac{1}{2}\frac{\tilde{\tau}}{\tilde{\rho}_n}\right)^2\right]^{\frac{1}{2}}\frac{\mathrm{Re}(\Gamma_n)}{|1-\Gamma_n|^2}\right\}. \qquad (7.1.6)$$

Many of the normalized distance quantities (and ratios involving them) have been simplified in this expression by noticing from equations (7.1.2) that

$$\tilde{\rho}_{nk} = \sqrt{k}\tilde{\rho}_n,\ \tilde{\rho}_{wk} = \sqrt{k}\tilde{\rho}_w,\ \tilde{\tau}_k = \sqrt{k}\tilde{\tau},\ \tilde{d}_k = \sqrt{k}\tilde{d}. \qquad (7.1.7)$$

Also, the subscript 1 corresponding to the fundamental frequency has been dropped. It is now understood that normalized distance quantities without a harmonic subscript are normalized to the skin depth at the fundamental frequency. K^2_{rms} denotes the root-mean-squared value of the current per unit axial length. The defining equation (7.1.5) is analogous to equations (6.2.4) for the sinusoidal case. The only difference here is that two times the waveform's rms-squared value is factored out instead of the square of the amplitude of the sinusoid. Consequently, the more general case considered here reduces to the previous results for sinusoid excitation. One final point is important concerning the derivation of equation (7.1.6). The boundary condition ratios have been assumed to be independent of the kth harmonic frequency. This will be true when the windings on a transformer carry currents which have the same shape and are proportional to each other, since the corresponding harmonic components will also be proportional. The boundary condition ratios will also be real if the currents are in phase (see equations (6.1.7) through (6.1.10) and the accompanying discussion). These conditions are usually true in most applications. However, if they are not, then the boundary condition ratio will vary as a function of the kth harmonic and must be computed for each component (under these conditions the subscript k

should be added to the boundary condition ratio in equation (7.1.6)).

The thin-layer approximation may be derived in a similar manner or by simply neglecting the appropriate terms in equation (7.1.6) according to equations (6.2.6) through (6.2.8); both methods lead to the expression

$$\tilde{P} \approx \frac{K_0^2}{K_{rms}^2}\frac{1}{\tilde{\tau}} + \frac{1}{2}\frac{1}{H}\sum_{k=1}^{\infty}\sqrt{k}\frac{K_k^2}{K_{rms}^2}$$

$$\left\{\left[\frac{\sinh 2\tilde{\tau}_k + \sin 2\tilde{\tau}_k}{\cosh 2\tilde{\tau}_k - \cos 2\tilde{\tau}_k}\right]\sum_{n=1}^{N}\left[\frac{1+|\Gamma_n|^2}{|1-\Gamma_n|^2}\right]\right.$$

$$\left. - 4\left[\frac{\cosh\tilde{\tau}_k \sin\tilde{\tau}_k + \cos\tilde{\tau}_k \sinh\tilde{\tau}_k}{\cosh 2\tilde{\tau}_k - \cos 2\tilde{\tau}_k}\right]\sum_{n=1}^{N}\left[\frac{\mathrm{Re}(\Gamma_n)}{|1-\Gamma_n|^2}\right]\right\}. \qquad (7.1.8)$$

The inner summations in equation (7.1.8) have already been evaluated (see equations (6.2.10) and (6.2.11)). Therefore, the final and simplest analytical form for the thin-layer approximation is

$$\tilde{P} \approx \frac{K_0^2}{K_{rms}^2}\frac{1}{\tilde{\tau}} + \frac{1}{3}\left|\frac{1}{1-\Gamma}\right|^2\left\{\left[(N^2+\tfrac{1}{2})(1+|\Gamma|^2) + (N^2-1)\mathrm{Re}(\Gamma)\right]\right.$$

$$\left.\sum_{k=1}^{\infty}\sqrt{k}\frac{K_k^2}{K_{rms}^2}\left[\frac{\sinh 2\tilde{\tau}_k + \sin 2\tilde{\tau}_k}{\cosh 2\tilde{\tau}_k - \cos 2\tilde{\tau}_k}\right] - 2\left[(N^2-1)(1+|\Gamma|^2) + (N^2+2)\mathrm{Re}(\Gamma)\right]\right.$$

$$\sum_{k=1}^{\infty} \sqrt{k} \frac{K_k^2}{K_{rms}^2} \left[\frac{\cosh\tilde{\tau}_k \sin\tilde{\tau}_k + \cos\tilde{\tau}_k \sinh\tilde{\tau}_k}{\cosh 2\tilde{\tau}_k - \cos 2\tilde{\tau}_k} \right] \Bigg\}. \qquad (7.1.9)$$

The last approximation to be considered, the two-term series approximation, requires special attention. Before, in the time-harmonic sinusoidal analysis, the optimum normalized conductor thicknesses were found to be restricted to the range $[0, \pi/2]$. This allowed a series approximation of the terms corresponding to the two summands in equation (7.1.9). The first two terms of the Laurent series were found to provide excellent accuracy throughout the optimization region. Now, however, the normalized thicknesses are frequency dependent, and the preceding argument is valid only for the fundamental component. The normalized conductor thicknesses will increase according to equation (7.1.7) for the higher frequency components. Consequently, the series approximation will become less accurate for the higher harmonics. One might conclude from this reasoning that the two-term series approximation has been rendered useless, but there is some promise. The amplitude Fourier coefficients K_k of practical waveforms decrease as k increases. Therefore, depending on the degree of these reductions, the summations in equation (7.1.9) may be weighted such that the inaccuracy of the higher order terms is de-emphasized. There is no convenient way to

evaluate the overall accuracy of the two-term series approximation other than to test it for several types of waveforms. To this end, the summands in equation (7.1.9) are approximated as before, and equations (7.1.7) are employed to yield the two-term series approximation of the normalized power dissipation per layer:

$$\tilde{P} \approx \frac{1}{\tilde{\tau}} \left\{ \frac{1}{K_{rms}^2} \left[K_0^2 + \frac{1}{2} \sum_{k=1}^{\infty} K_k^2 \right] \right.$$

$$\left. + \frac{\tilde{\tau}^4}{45} \left[\frac{(5N^2-1)(1+|\Gamma|^2) + (5N^2+2)\mathrm{Re}(\Gamma)}{|1-\Gamma|^2} \right] \frac{1}{K_{rms}^2} \left[\frac{1}{2} \sum_{k=1}^{\infty} k^2 K_k^2 \right] \right\}. \tag{7.1.10}$$

This expression can be further simplified using results from Appendix C. The terms in the first set of square brackets are equal to K_{rms}^2 by Parseval's identity. Similarly, the summation in the last set of square brackets is equal to $K_{rms}'^2/\omega_0^2$, where $K_{rms}'^2$ is defined as the rms-squared value of the derivative of K (see eqs. (C.2.2) and (C.2.4)). Hence, the final form of the two-term series approximation is

$$\tilde{P} \approx \frac{1}{\tilde{\tau}} \left\{ 1 + \frac{\tilde{\tau}^4}{45} \beta^2 \left[\frac{(5N^2-1)(1+|\Gamma|^2) + (5N^2+2)\mathrm{Re}(\Gamma)}{|1-\Gamma|^2} \right] \right\}, \tag{7.1.11a}$$

where

$$\beta^2 \triangleq \frac{\frac{1}{2}\sum_{k=1}^{\infty} k^2 K_k^2}{K_0^2 + \frac{1}{2}\sum_{k=1}^{\infty} K_k^2} = \frac{1}{\omega_0^2}\,\frac{K_{rms}'^2}{K_{rms}^2}. \qquad (7.1.11b)$$

The quantity β is given the name *normalized power bandwidth*; it is discussed in detail in Section C.3 of Appendix C. Briefly, it provides measure of the bandwidth of the current waveform and is therefore an indication of the extent of the harmonic content. It is normalized such that it becomes unity for a sinusoid. Comparison of equation (7.1.11a) with its sinusoidal counterpart in equation (6.2.12) reveals that the only difference between the two is the appearance of β^2 in second term of the former. The change in the non-DC portion of the power dissipation is therefore proportional to the square of the power bandwidth. This is an amazingly simple and insightful result which provides a meaningful physical interpretation. It remains to be seen how accurate this approximation is and the extent of its validity.

Figures 7.1.1 through 7.1.4 present the graphical results for both the thin-layer approximation in equation (7.1.9) and the two-term series approximation in equations (7.1.11) for several different types of waveforms. The waveforms chosen for this evaluation are classified and defined in Appendix D. Their names are: I - sinusoid,

II - unidirectional fractional sinusoid, III -unidirectional rectangular wave, and IV - unidirectional triangular wave. Many of the properties of these waveforms are also summarized in Appendix D including the average value, rms value, Fourier coefficients, and the normalized power bandwidth. Curves of the normalized power bandwidth are included in Section C.3 of Appendix C which deals with that quantity. A fifth classification, V - arbitrary periodic waveform, is also defined to conveniently refer to the general treatment of a waveform using a piecewise linear approximation. This treatment is defined and developed in Section C.4 of Appendix C. It is a simple but powerful generalization that provides a means by which the results contained herein can be applied to any switched-mode power transformer, present or future. Its accuracy can be adjusted to a desired level by choosing enough linear segments to model the waveform.

Figure 7.1.1 shows the graphical results for fractional sinusoids with various duty cycles D. The boundary condition ratio is taken to be zero, and the number of layers to be three for this waveform and the remaining ones considered in this section. Notice that the accuracy of the two-term approximation is only slightly worse than for a pure sinusoid (see Figure 6.2.1), corroborating the relatively narrow bandwidth of a fractional sinusoid. Also notice that

the power dissipation increases significantly as the waveform duty cycle decreases, which reflects the corresponding increase in bandwidth. It should be pointed out that the rms value is effectively held constant as the duty cycle is varied for these curves. This is a consequence of the normalization defined by equation (7.1.5). Similar curves are presented in Figures 7.1.2 and 7.1.3 for the unidirectional rectangular and triangular waveforms. A new parameter, the rise-time duty cycle D_r, is introduced to describe these waveforms. It is the ratio of the transition time to the period, and a typical value for present technology is about 0.01 (1%). The characteristics of the curves for these waveform types are similar to the ones for the fractional sinusoid except for the following. The validity of the two-term series approximation is much more restricted. Accuracy is not bad for rise times greater than 10% but becomes much worse for values near or below 1%. Also, the power dissipation itself increases as the rise time is reduced. These effects are once again supported by the related increase in bandwidth.

Finally, the normalized power dissipations caused by each of four waveform types considered thus far are compared in Figure 7.1.4 under typical conditions. Where applicable, the waveform duty cycle is taken as 50%, and the rise-time duty cycle as 1%. The curves cross in several places and

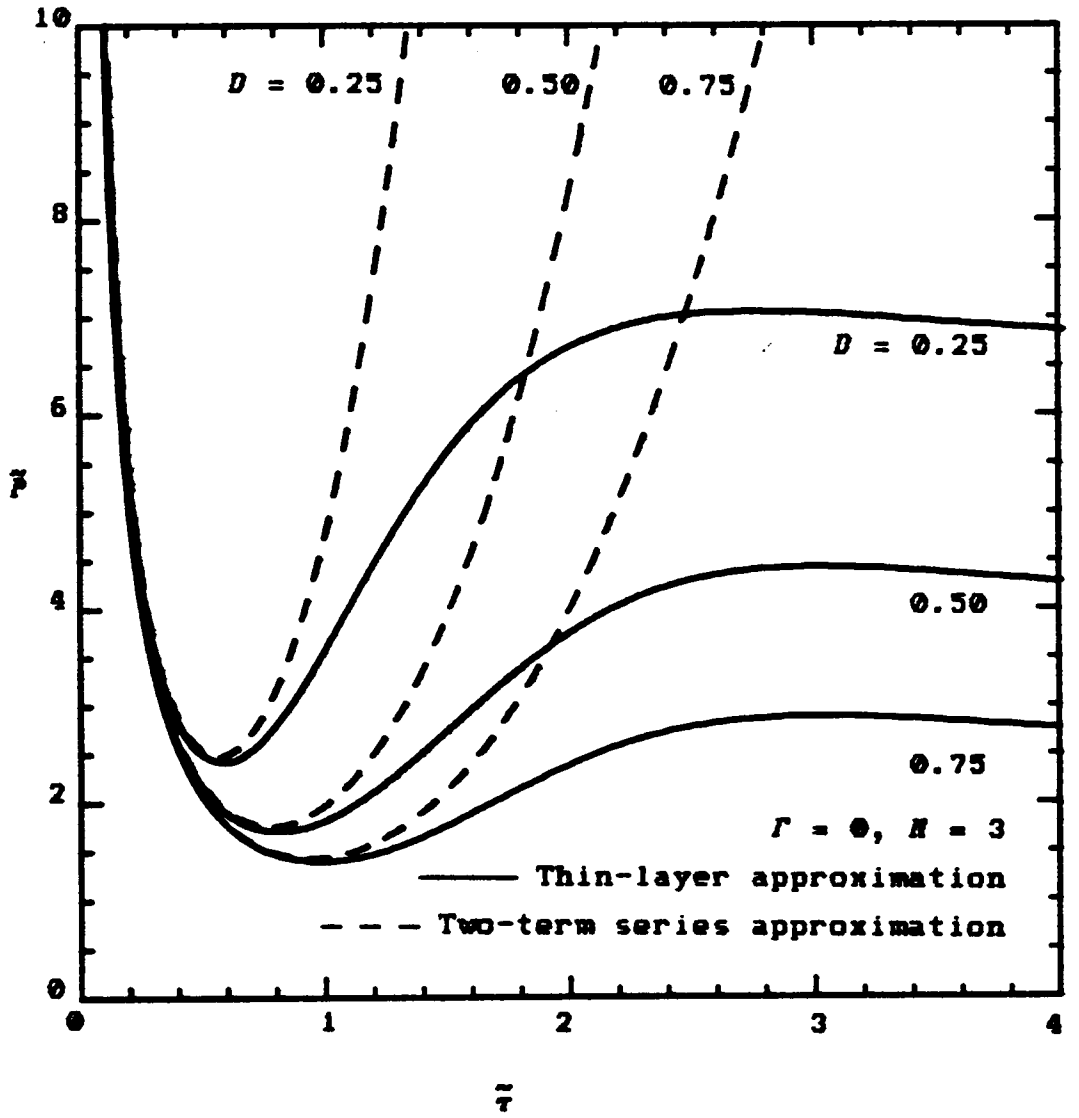

Figure 7.1.1. Normalized power dissipation per layer in an N-layer winding vs. normalized conductor thickness for a unidirectional fractional sinusoid current (Appendix D - Type II). The waveform duty cycle is varied as a parameter.

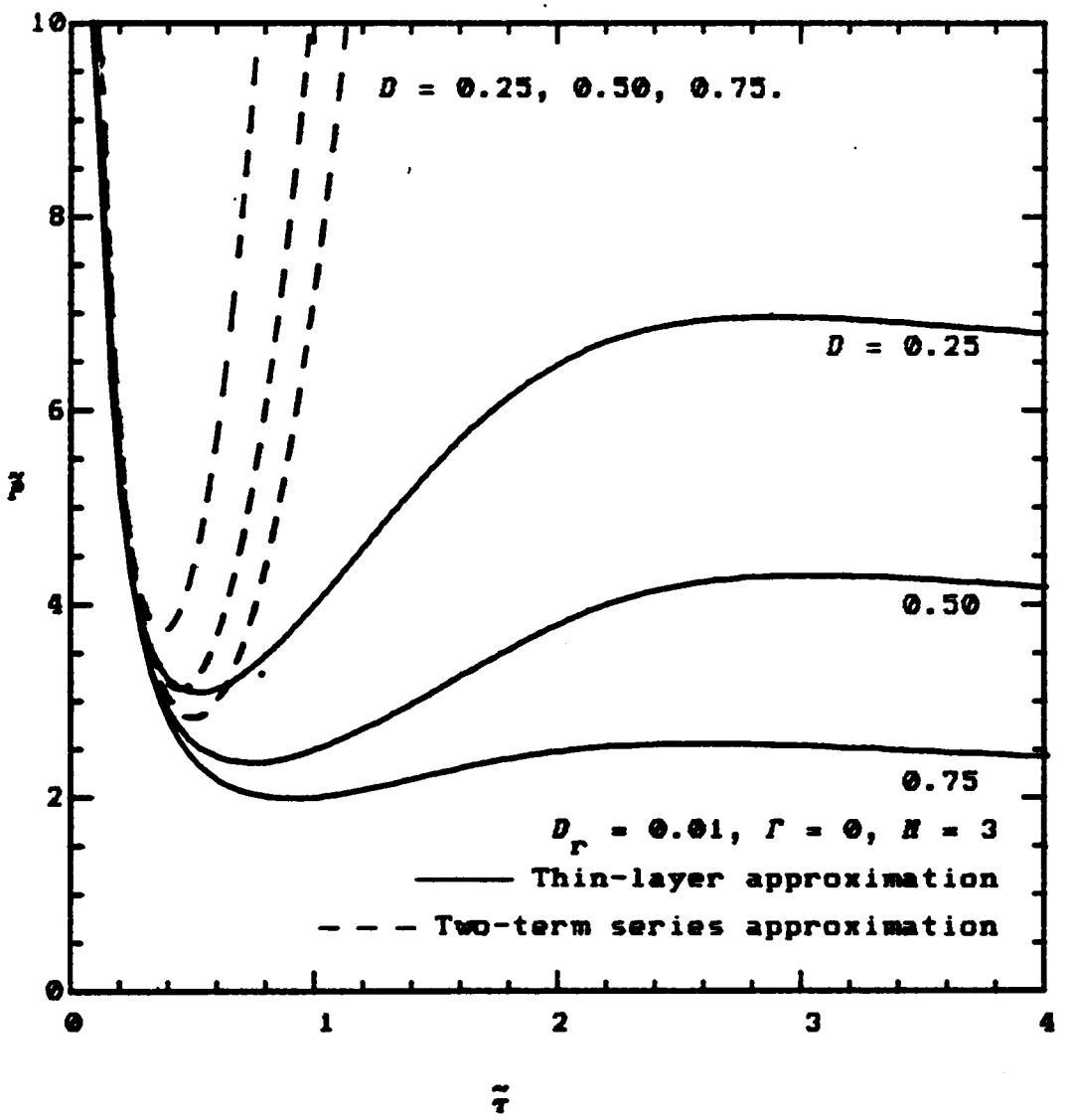

Figure 7.1.2a. Normalized power dissipation per layer in an N-layer winding vs. normalized conductor thickness for a unidirectional rectangular wave current (Appendix D - Type III). The waveform duty cycle is varied as a parameter.

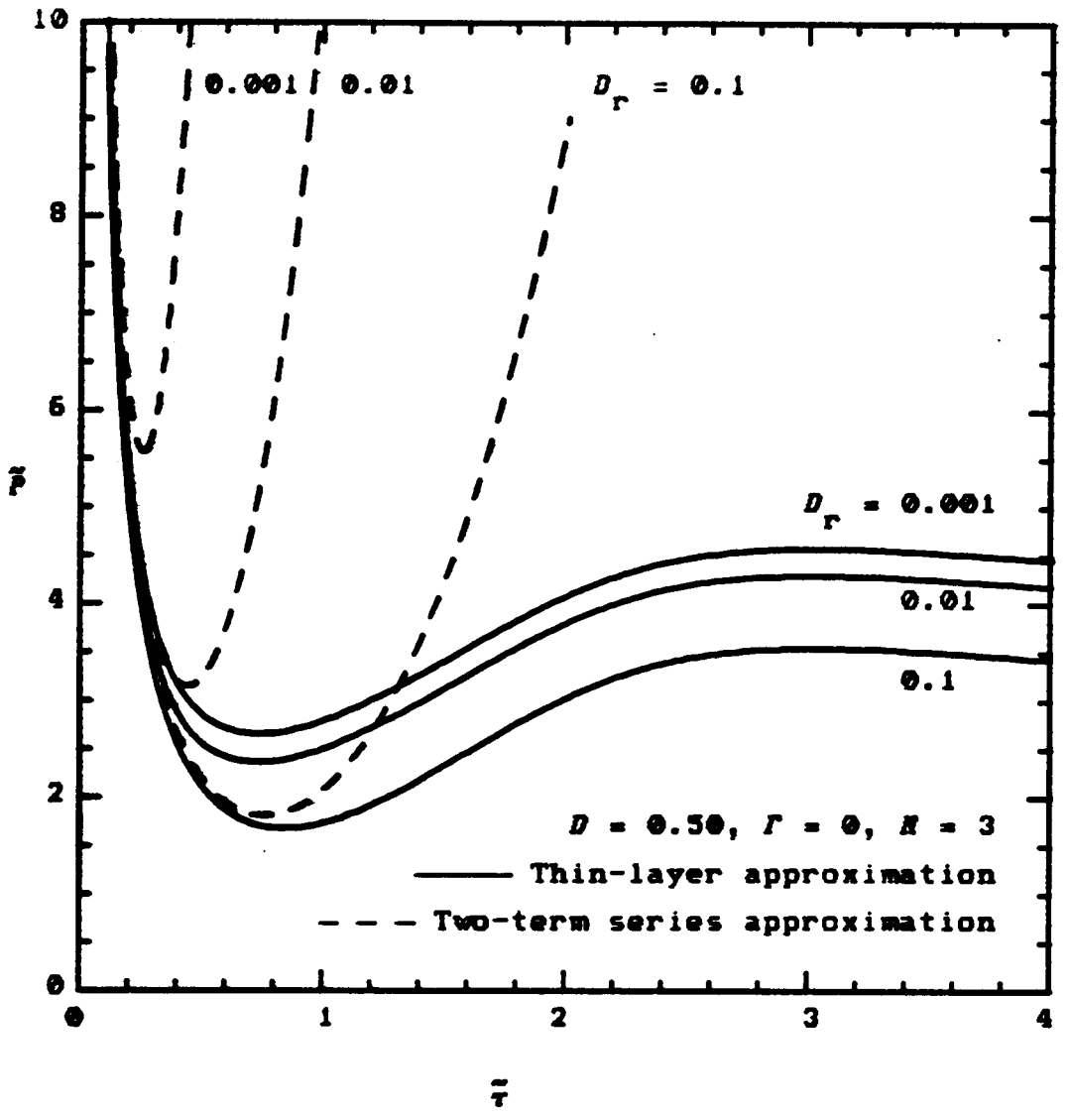

Figure 7.1.2b. Normalized power dissipation per layer in an N-layer winding vs. normalized conductor thickness for a unidirectional rectangular wave current (Appendix D - Type III). The rise-time duty cycle is varied as a parameter.

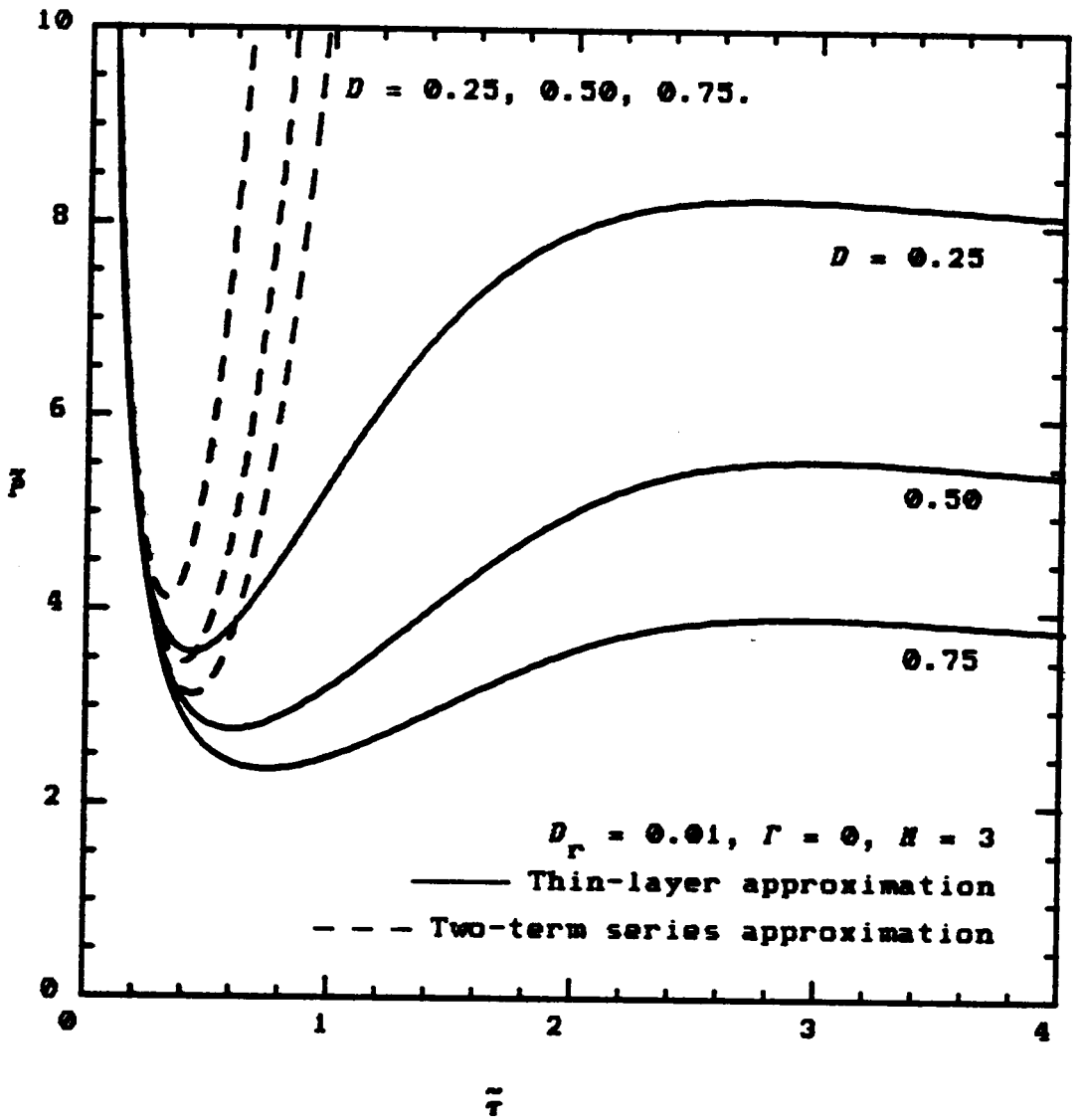

Figure 7.1.3a. Normalized power dissipation per layer in an N-layer winding vs. normalized conductor thickness for a unidirectional triangular wave current (Appendix D - Type IV). The waveform duty cycle is varied as a parameter.

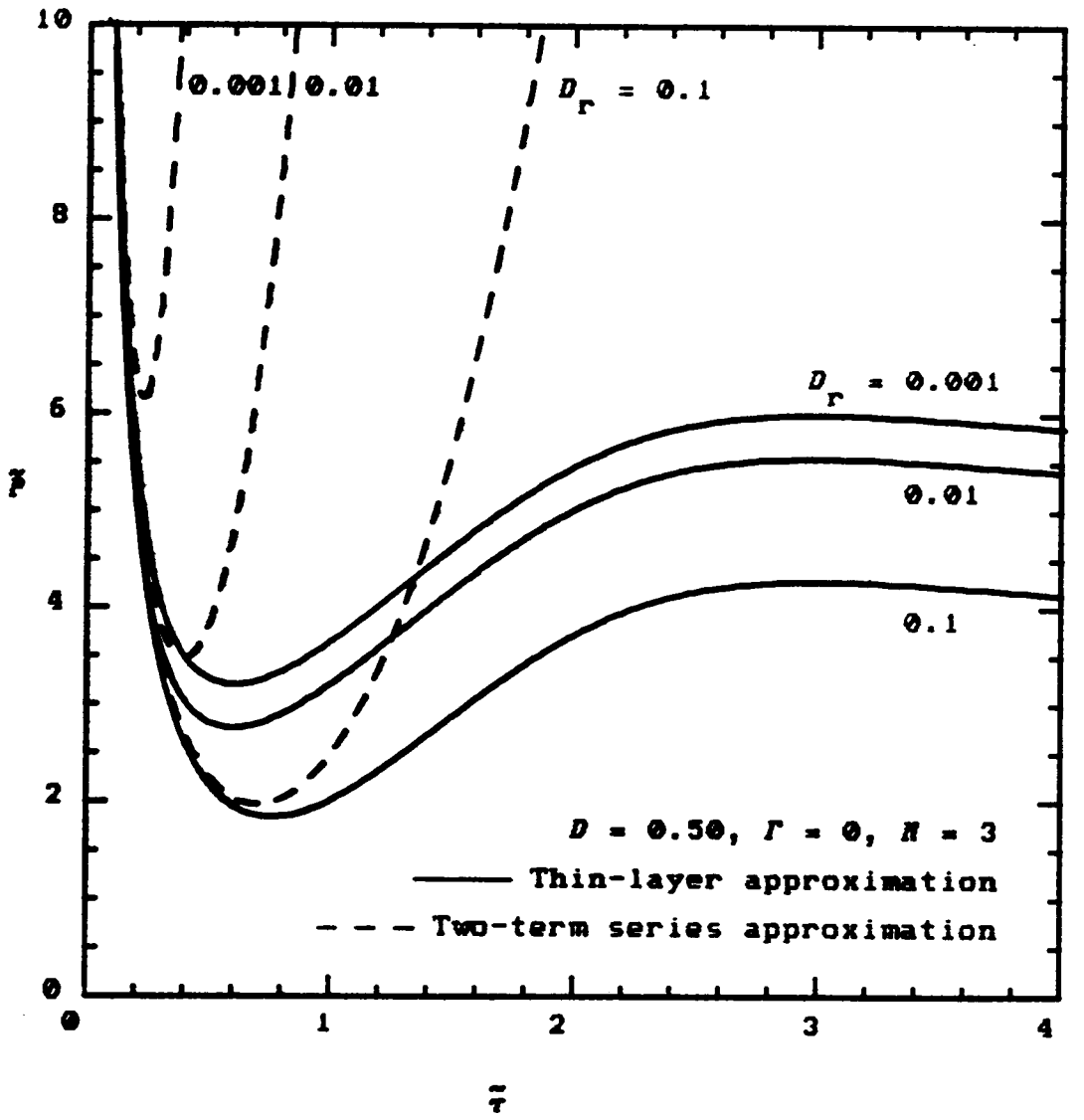

Figure 7.1.3b. Normalized power dissipation per layer in an N-layer winding vs. normalized conductor thickness for a unidirectional triangular wave current (Appendix D - Type IV). The rise-time duty cycle is varied as a parameter.

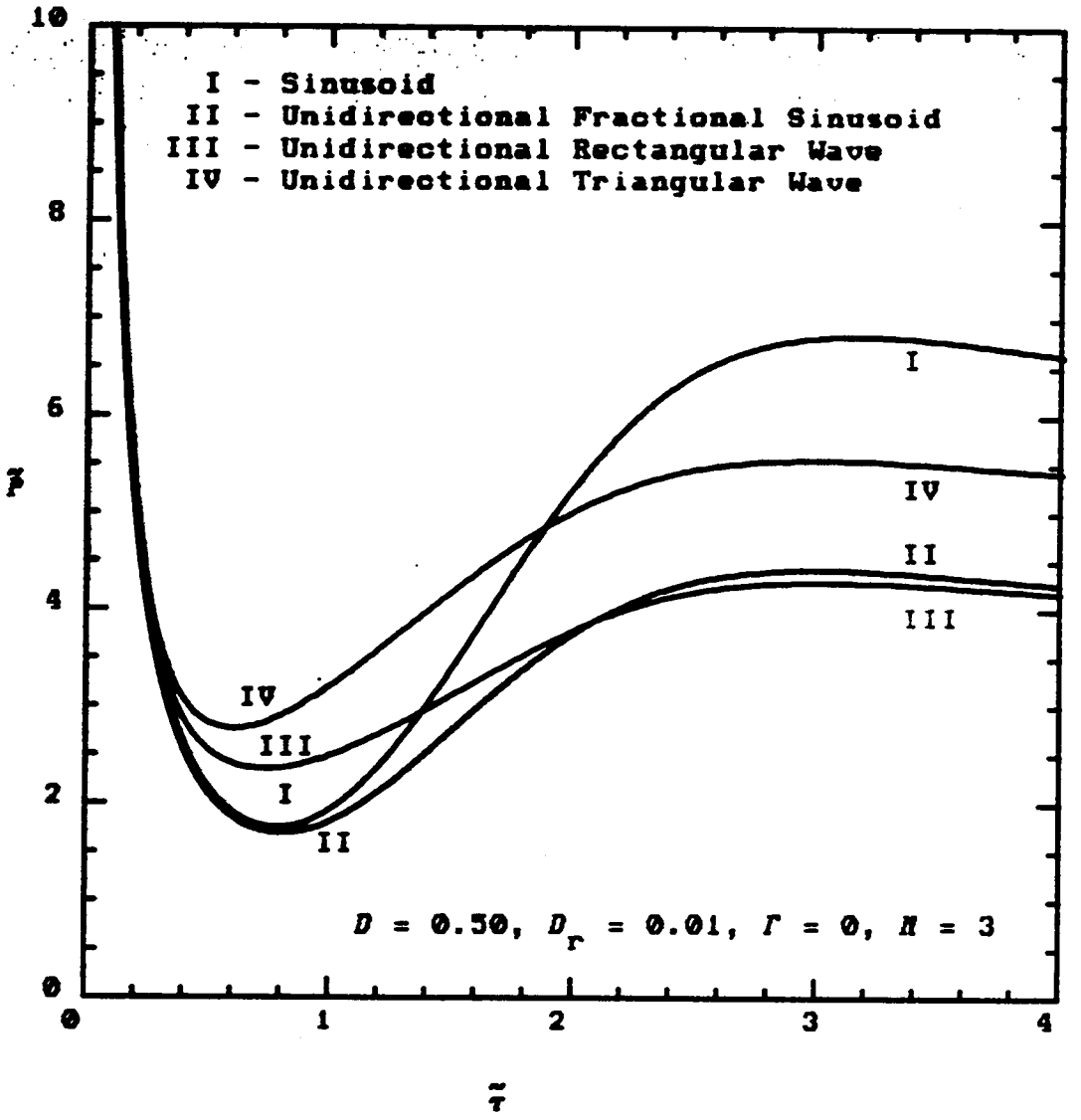

Figure 7.1.4. Normalized power dissipation per layer in an N-layer winding vs. normalized conductor thickness for four different waveform types (see Appendix D). The thin-layer approximation was used for all curves.

the ranking from least to greatest varies as a function of thickness. At the important optimum point of minimum power dissipation, the fractional sinusoid produces the least power. But it is only slightly less than the pure sinusoid. The next highest is for the rectangular wave, and the triangular wave is the worst producing about 60% greater losses than the fractional sinusoid. Notice that the power dissipation for the triangular wave is always greater than for the rectangular wave. Again, remember that the rms value of these waveforms is effectively held constant during these comparisons.

The two-term series approximation has proven to be inadequate for computational purposes for some important waveform types and conditions. In general, the accuracy diminishes as the bandwidth of the waveform increases. Even so, the power and insight gained from its analytical simplicity is tremendously useful. Even when it becomes inaccurate, it is always in the direction of predicting greater than actual power dissipation thereby acting as a worst-case estimate.

7.2 ENERGY STORAGE

The energy stored in an N-layer winding under arbitrary periodic exitation is determined in the same manner as the power dissipation was in the previous section, except for

the addition of the contributions from the insulation layers. The first step is to generalize equations (6.3.5) by expanding the current per unit axial length into a Fourier series; this leads to

$$W = W_0^i + \sum_{k=1}^{\infty} W_k^i + W_0 + \sum_{k=1}^{\infty} W_k$$

$$= W_0^i + \frac{\pi\mu_0 l\delta^2}{4} N\tilde{\rho}_w \sum_{k=1}^{\infty} \frac{1}{k} K_k^2 \tilde{W}_k^i + W_0 + \frac{\pi\mu_0 l\delta^2}{4} N\tilde{\rho}_w \sum_{k=1}^{\infty} \frac{1}{k} K_k^2 \tilde{W}_k, \quad (7.2.1a)$$

where

$$\tilde{W}_k^i = \frac{1}{N} \sum_{n=1}^{N} \frac{\tilde{\rho}_{nk}}{\tilde{\rho}_w} \tilde{W}_{nk}^i \quad (7.2.1b)$$

$$\tilde{W}_k = \frac{1}{N} \sum_{n=1}^{N} \frac{\tilde{\rho}_{nk}}{\tilde{\rho}_w} \tilde{W}_{nk}, \quad (7.2.1c)$$

and the frequency dependent normalized distance quantities are given in equations (7.1.2). Notice the appearance of the extra $1/k$ factor inside the summations in equation (7.2.1a). It is left over from factoring out the square of the skin depth at the fundamental frequency. See equation (7.1.2e) and remember that the absence of the k subscript implies a value of one, i.e. the fundamental frequency.

Consider first the two initial terms in equation (7.2.1a) due to the insulating layers. Under the practical multi-layer assumptions defined by equations (6.1.1), (6.1.2), and (6.1.4), the normalized energy $\tilde{U}_n^i$ stored in the nth insulating layer is given by equation (6.3.4) for sinusoidal excitation. The corresponding kth harmonic terms $\tilde{U}_{nk}^i$ are obtained by replacing the normalized distance quantities with their frequency dependent definitions according to equations (7.1.2). Careful examination of the resulting expression after using the relations in equation (7.1.7) reveals that the terms due to the insulation layers are frequency independent. This is because the $1/k$ factor in equation (7.2.1a) is cancelled by the two $\sqrt{k}$ contributions from $\tilde{\rho}_{nk}$ in equation (7.2.1b) and $\tilde{d}_k$ in equation (6.3.4). This result also follows directly from the assumptions that the magnetic field intensity is uniform and that the conductivity is zero in the insulating layers. The summation over k for the insulation layer terms therefore reduces to a summation of the amplitude squared Fourier coefficients which, when combined with the DC term, yields the rms-squared value of the waveform. Equation (7.2.1a) thus becomes

$$W = 2\frac{\pi\mu_o l\delta^2}{4}K_{rms}^2 H\tilde{\rho}_w \; 2\tilde{d}\frac{1}{H}\sum_{n=1}^{N}\frac{\tilde{\rho}_n}{\tilde{\rho}_w}\left[1 + \frac{1}{2}\frac{\tilde{\tau}+\tilde{d}}{\tilde{\rho}_n}\right]\frac{1}{|1-\Gamma_n|^2}$$

$$+ U_0 + \frac{\pi\mu_0 l\delta^2}{4} N\tilde{\rho}_w \sum_{k=1}^{\infty} \frac{1}{k} K_k^2 \tilde{U}_k, \qquad (7.2.2)$$

where $\tilde{U}_k$ is given by equation (7.2.1c). The evaluation of the DC energy storage term U_0 is not as trivial as the DC power dissipation P_0 was. This is because the DC magnetic field intensity varies linearly within the conductor layers, and also because it has different values at each of the insulation layers. In contrast, the integration for the DC power dissipation was much simpler since the current density is uniform and assumed to be the same for each layer. Details of the integration for U_0 will not be given here; however, the results are included in the following expression which has been rearranged in order to define the normalized energy stored per layer $\tilde{U}$ in an N-layer winding:

$$U = 2\frac{\pi\mu_0 l\delta^2}{4} K_{rms}^2 N\tilde{\rho}_w \tilde{U} \qquad (7.2.3a)$$

$$\tilde{U} = 2\tilde{d}\frac{1}{N}\sum_{n=1}^{N}\frac{\tilde{\rho}_n}{\tilde{\rho}_w}\left[1 + \frac{1}{2}\frac{\tilde{\tau}+\tilde{d}}{\tilde{\rho}_n}\right]\frac{1}{|1-\Gamma_n|^2} + \frac{K_0^2}{K_{rms}^2}\frac{2}{3N}\tilde{\tau}$$

$$\left\{\sum_{n=1}^{N}\frac{\tilde{\rho}_n}{\tilde{\rho}_w}\left[\frac{1+|\Gamma_n|^2}{|1-\Gamma_n|^2} + \frac{1}{2}\frac{\tilde{\tau}}{\tilde{\rho}_n}\frac{1-|\Gamma_n|^2}{|1-\Gamma_n|^2}\right] + \sum_{n=1}^{N}\frac{\tilde{\rho}_n}{\tilde{\rho}_w}\left[1-\left(\frac{1}{2}\frac{\tilde{\tau}}{\tilde{\rho}_n}\right)^2\right]\frac{1}{2}\frac{\mathrm{Re}(\Gamma_n)}{|1-\Gamma_n|^2}\right\}$$

$$+ \frac{1}{2}\sum_{k=1}^{\infty}\frac{1}{k}\frac{K_k^2}{K_{rms}^2}\tilde{U}_k. \qquad (7.2.3b)$$

The exact expression is obtained as usual by substituting previously derived results from the sinusoidal analysis. In particular, equations (5.2.4) must be substituted into equation (7.2.1c) which is in turn substituted into equations (7.2.3). Remember that all frequency dependent quantities must be replaced by their k-subscripted definitions in equations (7.1.2).

The large argument asymptotic approximation once again results in tremendous simplification. The summation analogous to equation (7.2.1c) above was reduced to the form in equation (6.3.6) for the large argument asymptotic approximation in the sinusoidal analysis. Substituting the portion of this result pertaining to the conductor layers directly into equation (7.2.3b) yields the large argument asymptotic approximation

$$\tilde{W} \sim 2\tilde{d}\frac{1}{N}\sum_{n=1}^{N}\frac{\tilde{\rho}_n}{\tilde{\rho}_w}\left[1+\frac{1}{2}\frac{\tilde{\tau}+\tilde{d}}{\tilde{\rho}_n}\right]\frac{1}{|1-\Gamma_n|^2}+\frac{K_0^2}{K_{rms}^2}\frac{2}{3N^2}\tilde{\tau}$$

$$\left\{\sum_{n=1}^{N}\frac{\tilde{\rho}_n}{\tilde{\rho}_w}\left[\frac{1+|\Gamma_n|^2}{|1-\Gamma_n|^2}+\frac{1}{2}\frac{\tilde{\tau}}{\tilde{\rho}_n}\frac{1-|\Gamma_n|^2}{|1-\Gamma_n|^2}\right]+\sum_{n=1}^{N}\frac{\tilde{\rho}_n}{\tilde{\rho}_w}\left[1-\left(\frac{1}{2}\frac{\tilde{\tau}}{\tilde{\rho}_n}\right)^2\right]^{\frac{1}{2}}\frac{\mathrm{Re}(\Gamma_n)}{|1-\Gamma_n|^2}\right\}$$

$$+\frac{1}{2}\frac{1}{N}\sum_{k=1}^{\infty}\frac{1}{\sqrt{k}}\frac{K_k^2}{K_{rms}^2}$$

$$\left\{\left[\frac{\sinh 2\tilde{\tau}_k-\sin 2\tilde{\tau}_k}{\cosh 2\tilde{\tau}_k-\cos 2\tilde{\tau}_k}\right]\sum_{n=1}^{N}\frac{\tilde{\rho}_n}{\tilde{\rho}_w}\left[\frac{1+|\Gamma_n|^2}{|1-\Gamma_n|^2}+\frac{1}{2}\frac{\tilde{\tau}}{\tilde{\rho}_n}\frac{1-|\Gamma_n|^2}{|1-\Gamma_n|^2}\right]\right.$$

$$+ 4\left[\frac{\cosh\tilde{\tau}_k\sin\tilde{\tau}_k - \cos\tilde{\tau}_k\sinh\tilde{\tau}_k}{\cosh 2\tilde{\tau}_k - \cos 2\tilde{\tau}_k}\right]\sum_{n=1}^{N}\frac{\tilde{\rho}_n}{\tilde{\rho}_w}\left[1-\left(\frac{1}{2}\frac{\tilde{\tau}}{\tilde{\rho}_n}\right)^2\right]^{\frac{1}{2}}\frac{\mathrm{Re}(\Gamma_n)}{|1-\Gamma_n|^2}\Bigg\}, \tag{7.2.4}$$

where the relations in equation (7.1.7) have been employed to write the normalized distance quantities as $\sqrt{k}$ times their fundamental component.

The usual terms are neglected according to equations (6.2.6) through (6.2.8) to give the thin-layer approximation

$$\tilde{U} \approx 2\tilde{d}\frac{1}{N}\sum_{n=1}^{N}\frac{1}{|1-\Gamma_n|^2} + \frac{K_0^2}{K_{rms}^2}\frac{2\tilde{\tau}}{3}\frac{1}{N}\left\{\sum_{n=1}^{N}\frac{1+|\Gamma_n|^2}{|1-\Gamma_n|^2} + \sum_{n=1}^{N}\frac{\mathrm{Re}(\Gamma_n)}{|1-\Gamma_n|^2}\right\}$$

$$+ \frac{1}{2}\frac{1}{N}\sum_{k=1}^{\infty}\frac{1}{\sqrt{k}}\frac{K_k^2}{K_{rms}^2}\left\{\left[\frac{\sinh 2\tilde{\tau}_k - \sin 2\tilde{\tau}_k}{\cosh 2\tilde{\tau}_k - \cos 2\tilde{\tau}_k}\right]\sum_{n=1}^{N}\frac{1+|\Gamma_n|^2}{|1-\Gamma_n|^2}\right.$$

$$\left. + 4\left[\frac{\cosh\tilde{\tau}_k\sin\tilde{\tau}_k - \cos\tilde{\tau}_k\sinh\tilde{\tau}_k}{\cosh 2\tilde{\tau}_k - \cos 2\tilde{\tau}_k}\right]\sum_{n=1}^{N}\frac{\mathrm{Re}(\Gamma_n)}{|1-\Gamma_n|^2}\right\}. \tag{7.2.5}$$

All of the summations over n appearing in this expression were also encountered in the sinusoidal analysis. See equations (6.2.10), (6.2.11), (6.3.6), and (6.3.7). These summations are simplified by replacing Γ_n with the relation in equation (6.1.10), and algebraically manipulating them until they can performed analytically. The resulting final form for the thin-layer approximation is

$$\tilde{U} \approx \frac{1}{3}\left|\frac{1}{1-\Gamma}\right|^2\left\{2\tilde{d}\left[(M^2+\tfrac{1}{2})(1+|\Gamma|^2)+(M^2-1)\mathrm{Re}(\Gamma)+\tfrac{3}{2}M(1-|\Gamma|^2)\right]\right.$$

$$+\frac{K_0^2}{K_{rms}^2}2\tilde{\tau}M^2\left[1+|\Gamma|^2+\mathrm{Re}(\Gamma)\right] + \left[(M^2+\tfrac{1}{2})(1+|\Gamma|^2)+(M^2-1)\mathrm{Re}(\Gamma)\right]\sum_{k=1}^{\infty}$$

$$\frac{1}{\sqrt{k}}\frac{K_k^2}{K_{rms}^2}\left[\frac{\sinh 2\tilde{\tau}_k - \sin 2\tilde{\tau}_k}{\cosh 2\tilde{\tau}_k - \cos 2\tilde{\tau}_k}\right] + 2\left[(M^2-1)(1+|\Gamma|^2)+(M^2+2)\mathrm{Re}(\Gamma)\right]$$

$$\left.\sum_{k=1}^{\infty}\frac{1}{\sqrt{k}}\frac{K_k^2}{K_{rms}^2}\left[\frac{\cosh\tilde{\tau}_k\sin\tilde{\tau}_k - \cos\tilde{\tau}_k\sinh\tilde{\tau}_k}{\cosh 2\tilde{\tau}_k - \cos 2\tilde{\tau}_k}\right]\right\}. \qquad (7.2.6)$$

Finally, the two-term series approximation is derived by approximating the remaining summands in equation (7.2.6) with the first two terms of their Laurent expansion, and using equation (7.1.7) to replace $\tilde{\tau}_k$ with $\sqrt{k\tilde{\tau}}$. After some algebraic manipulation, the resulting expression becomes

$$\tilde{U} \approx \frac{1}{3}\left|\frac{1}{1-\Gamma}\right|^2\left\{2\tilde{d}\left[(M^2+\tfrac{1}{2})(1+|\Gamma|^2)+(M^2-1)\mathrm{Re}(\Gamma)+\tfrac{3}{2}M(1-|\Gamma|^2)\right]\right.$$

$$+\frac{K_0^2}{K_{rms}^2}2\tilde{\tau}M^2\left[1+|\Gamma|^2+\mathrm{Re}(\Gamma)\right] + \tilde{\tau}M^2\left[1+|\Gamma|^2+\mathrm{Re}(\Gamma)\right]\sum_{k=1}^{\infty}\frac{K_k^2}{K_{rms}^2}$$

$$\left.-\frac{\tilde{\tau}^5}{630}\left[(21M^2-5)(1+|\Gamma|^2)+(21M^2+10)\mathrm{Re}(\Gamma)\right]\sum_{k=1}^{\infty}k^2\frac{K_k^2}{K_{rms}^2}\right\}. \qquad (7.2.7)$$

The second and third terms may be combined using Parseval's identity from equation (C.2.2). The normalized power bandwidth β defined in equation (7.1.11b) may also be

introduced into the last term, thereby yielding the final form of the two-term series approximation of the normalized energy stored per layer in an M-layer winding:

$$\tilde{W} \approx \frac{2}{3}\left|\frac{1}{1-\Gamma}\right|^2 \left[\tilde{d}\left\{\left(M^2+\frac{1}{2}\right)\left(1+|\Gamma|^2\right)+\left(M^2-1\right)\mathrm{Re}(\Gamma)+\frac{3}{2}M\left(1-|\Gamma|^2\right)\right\}\right.$$

$$+\ \tilde{\tau}\left\{M^2\left[1+|\Gamma|^2+\mathrm{Re}(\Gamma)\right]\right.$$

$$\left.\left.-\ \frac{\tilde{\tau}^4}{630}\beta^2\left[\left(21M^2-5\right)\left(1+|\Gamma|^2\right)+\left(21M^2+10\right)\mathrm{Re}(\Gamma)\right]\right\}\right]. \quad (7.2.8)$$

Note that this result reduces to equation (6.3.8) for the sinusoidal case when $\beta = 1$. The situation here is analogous to that in the previous section for the power dissipation except for the addition of the contribution from the insulation layers. Also, the sign of the last term which contains the normalized power bandwidth is negative. One would therefore expect a reduction in the stored energy for current waveforms with larger bandwidths. The opposite was found to be true for the power dissipation (see equation (7.1.11a) and Figures 7.1.1 through 7.1.4). Because of the similarity of the results here with those in the previous section, the accuracy of the two-term series approximation is expected to be very limited.

Figures 7.2.1 through 7.2.4 present the graphical results for the normalized energy stored per layer in an

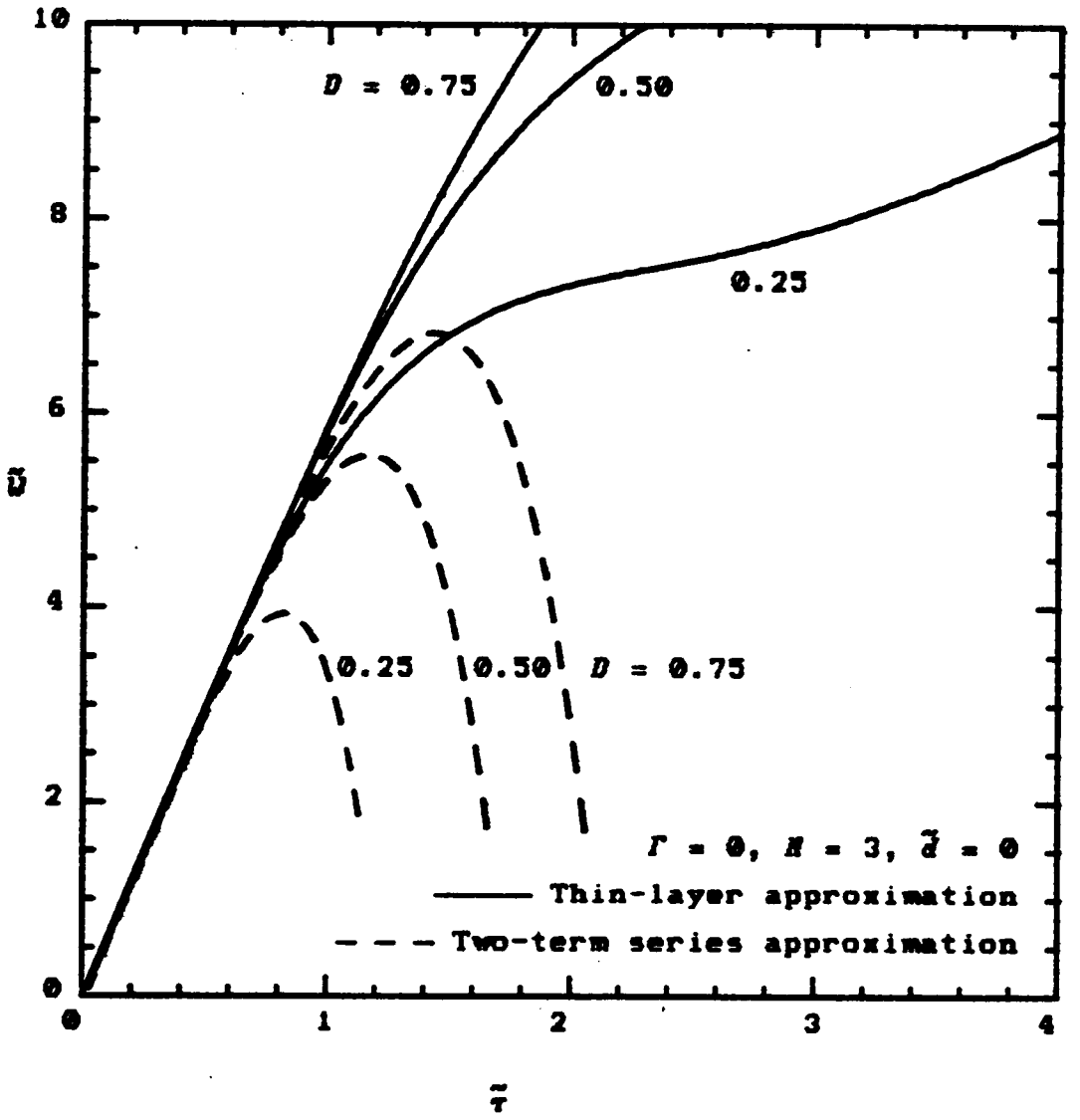

Figure 7.2.1. Normalized energy stored per layer in an N-layer winding vs. normalized conductor thickness for a unidirectional fractional sinusoid current (Appendix D - Type II). The waveform duty cycle is varied as a parameter.

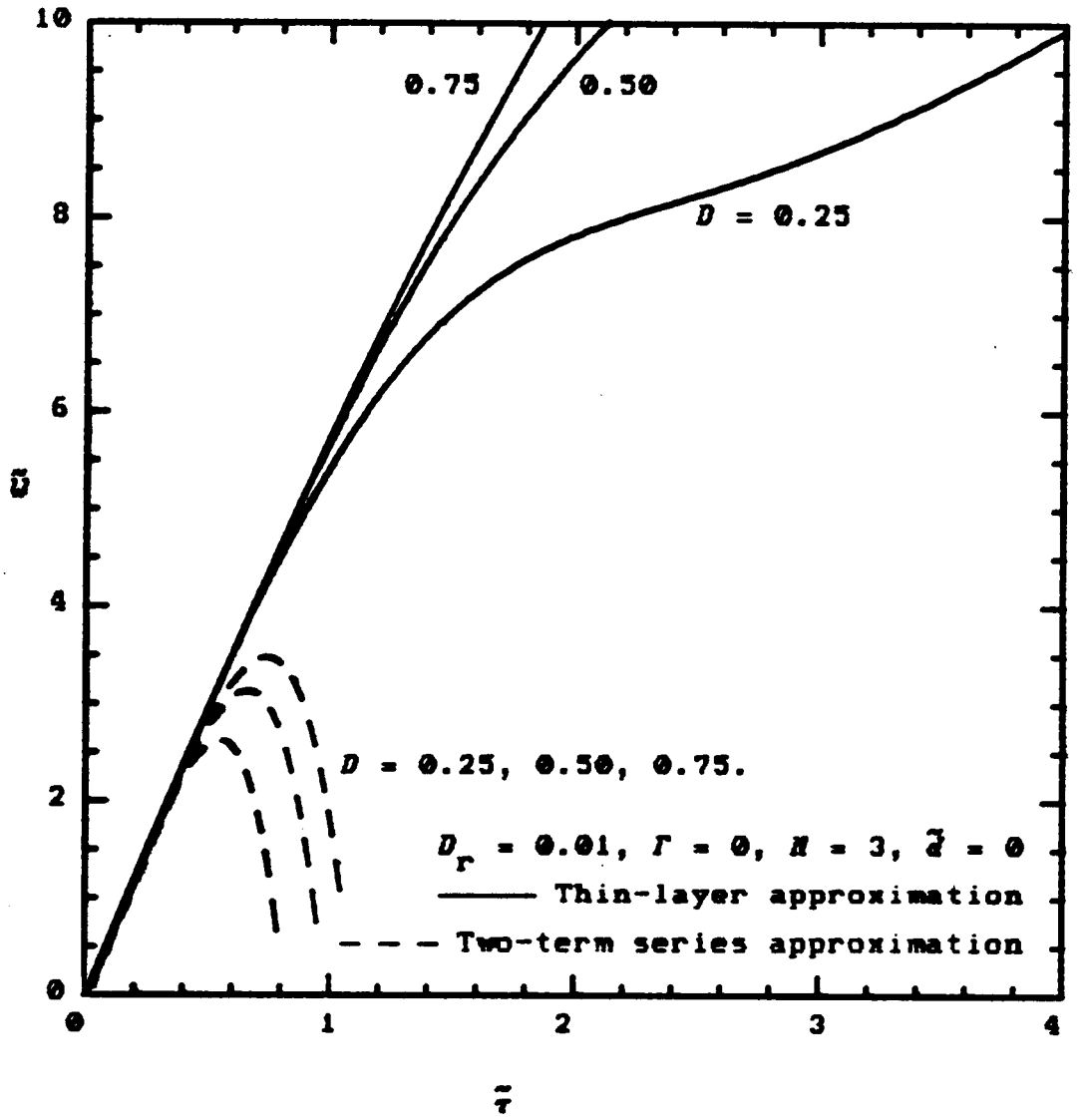

Figure 7.2.2a. Normalized energy stored per layer in an N-layer winding vs. normalized conductor thickness for a unidirectional rectangular wave current (Appendix D - Type III). The waveform duty cycle is varied as a parameter.

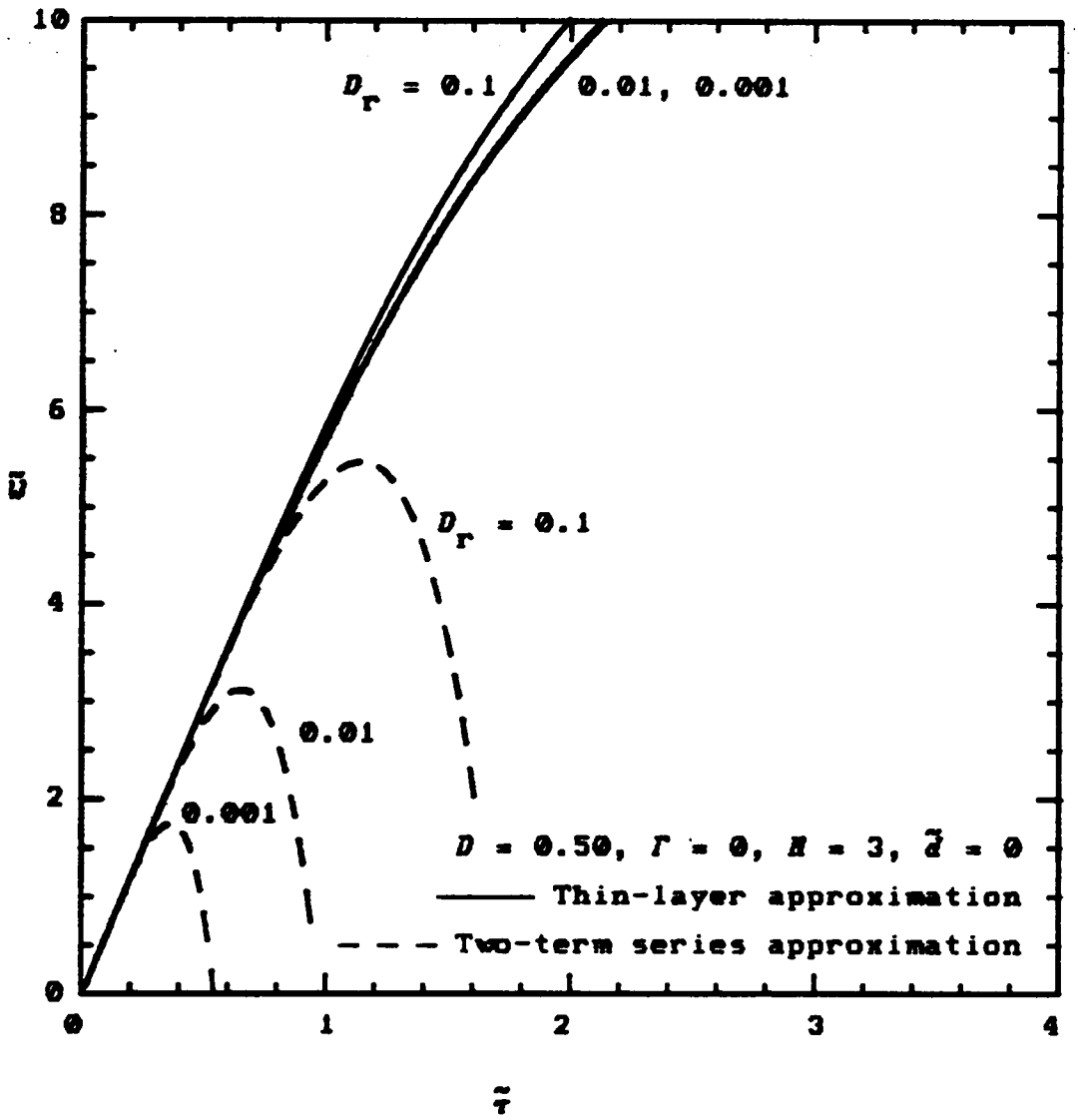

Figure 7.2.2b. Normalized energy stored per layer in an N-layer winding vs. normalized conductor thickness for a unidirectional rectangular wave current (Appendix D - Type III). The rise-time duty cycle is varied as a parameter.

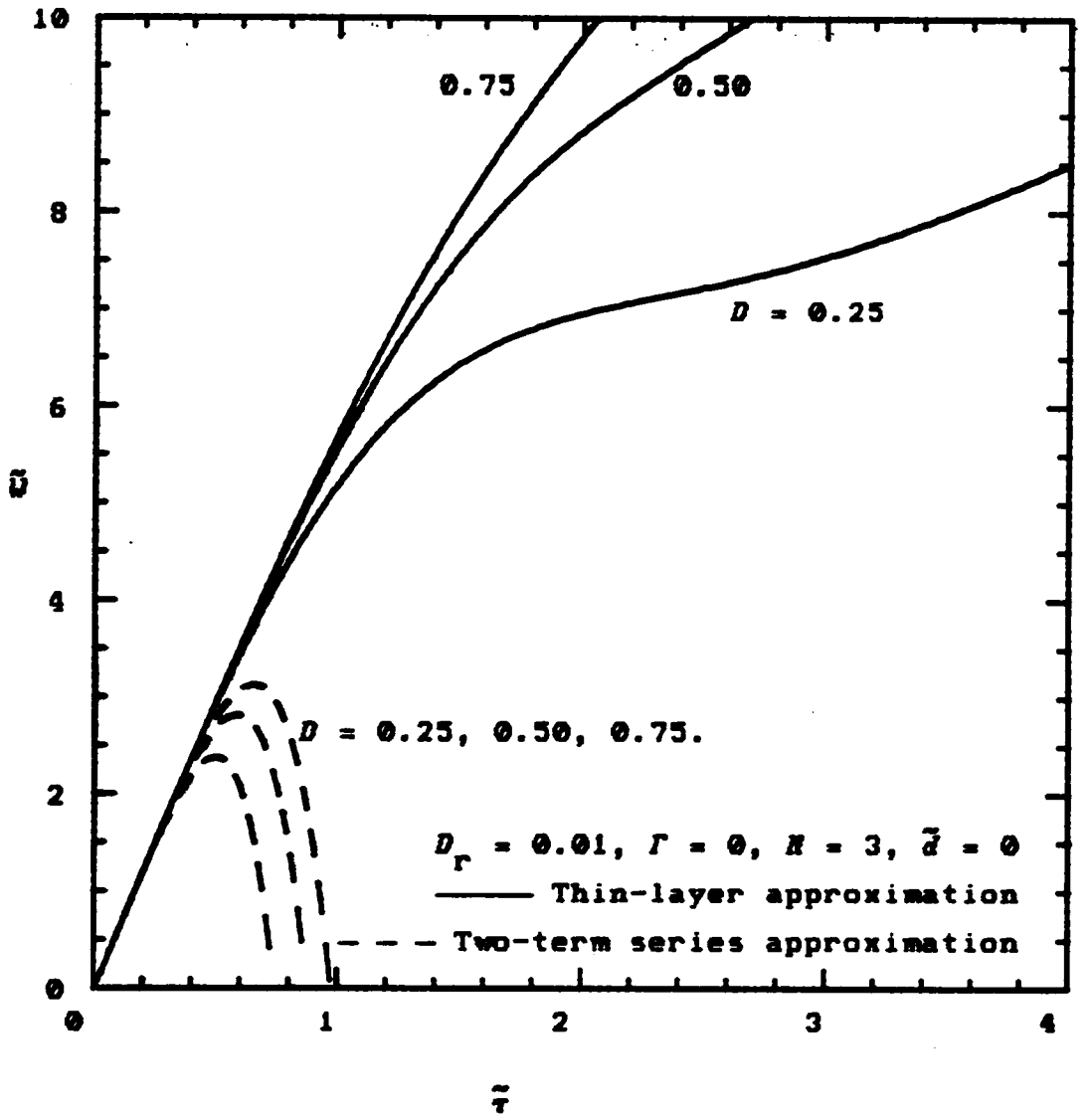

Figure 7.2.3a. Normalized energy stored per layer in an N-layer winding vs. normalized conductor thickness for a unidirectional triangular wave current (Appendix D - Type IV). The waveform duty cycle is varied as a parameter.

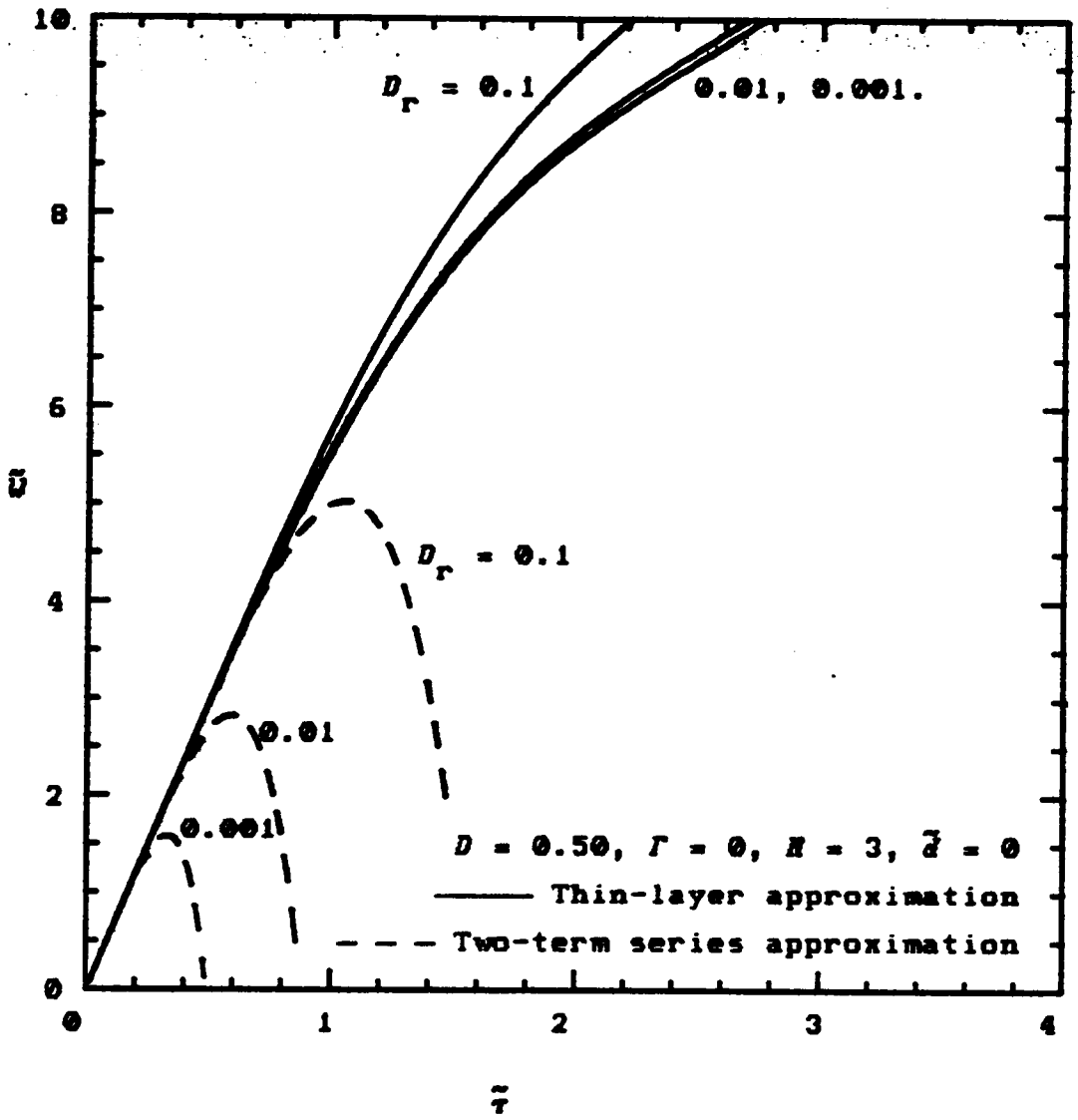

Figure 7.2.3b. Normalized energy stored per layer in an N-layer winding vs. normalized conductor thickness for a unidirectional triangular wave current (Appendix D - Type IV). The rise-time duty cycle is varied as a parameter.

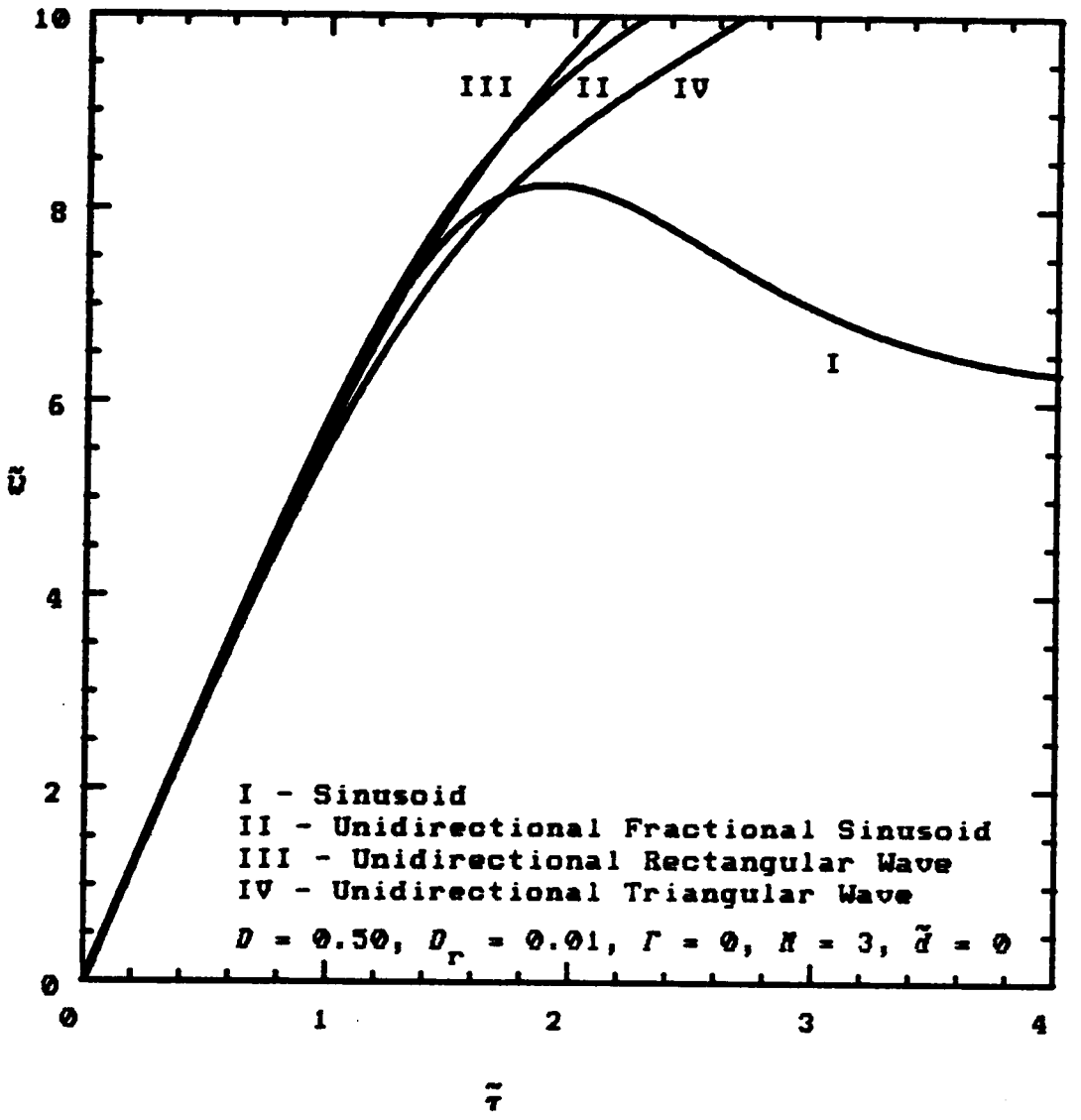

Figure 7.2.4. Normalized energy stored per layer in an N-layer winding vs. normalized conductor thickness for four different waveform types (see Appendix D). The thin-layer approximation is used for all curves.

N-layer winding under the same conditions as Figures 7.1.1 through 7.1.4 for the normalized power dissipation. Notice that the stored energy decreases for both smaller waveform and rise-time duty cycles. Figures C.3.1 through C.3.3 from Appendix C show that these conditions correspond to an increase in the normalized power bandwidth. It is curious to observe that the influence of the rise-time duty cycle is exaggerated by the two-term series approximation much more so than the waveform duty cycle. The influence of the rise time is relatively insignificant as evidenced from the solid curves in Figures 7.2.2b and 7.2.3b. A comparison of the different waveform types under typical conditions is shown in Figure 7.2.4. It is evident from this figure and the other figures in this section that the waveform type and characteristics do not appreciably affect the stored energy in the important optimum regions where the power dissipation is near its minimum. In fact, the stored energy varies almost linearly with the normalized conductor thickness in these regions. This is easily verified by comparing like figures from the previous section with those from this section. Further evidence of this effect is demonstrated in the following section which specifically addresses the optimization problem.

7.3 MINIMUM POWER OPTIMIZATION

The procedure for minimizing the power dissipation in an N-layer winding under arbitrary periodic excitation is identical to the one for sinusoidal excitation. The applicable equation is (6.4.1), where the differentation is now understood to be with respect to the conductor thickness normalized to a skin depth at the fumdamental frequency.

Once again, it is impractical to analytically solve the minimization equation for either the exact solution or the large argument asymptotic approximation given by equation (7.1.6). The previously developed computer algorithms have been generalized for the arbitrary periodic waveform analysis. The number of required computations now increases by another factor of k_{max}, where k_{max} is the number of harmonic components included in the Fourier analysis. The number of components necessary to accurately represent a given waveform varies with the bandwidth and can be quite large for wideband currents. Finding the optimum conductor thickness for a winding carrying rectangular wave currents with 1% transition times may take several minutes on a moderately fast personal computer if the exact solutions are used. Fortunately, the exact solutions and their large argument asymptotic approximations are only needed if the normalized mean radii $\tilde{\rho}_n$ become significantly less than 20.

Because of the added complexity of the generalization to arbitrary periodic waveforms, even the thin-layer approximation in equation (7.1.9) is difficult to minimize with respect to the normalized conductor thickness. The resulting equation contains summations over k which cannot be simplified; consequently, the number of required computations does not reduce. The easiest approach is therefore to simply extend the application of the existing algorithm. As mentioned earlier, this algorithm is based on a numerical implementation of Newton's method and it therefore involves several iterative evaluations of the expressions for $\tilde{P}$.

Finally, consider the two-term series approximation of $\tilde{P}$ in equations (7.1.11). The only difference between this expression and the corresponding one for sinusoidal excitation, equation (6.2.12), is the addition of the factor β^2 which is the square of the normalized power bandwidth. The minimization process is therefore essentially unchanged, and the results may be determined immediately by appropriately adding the β^2 factor to equations (6.4.3) and (6.4.4):

$$\tilde{\tau}^{opt} \approx \left\{ \frac{15}{\beta^2} \left[\frac{|1 - \Gamma|^2}{(5N^2-1)(1+|\Gamma|^2) + (5N^2+2)\mathrm{Re}(\Gamma)} \right] \right\}^{\frac{1}{4}} \quad (7.3.1)$$

$$\tilde{P}^{min} \approx \frac{4}{3}\frac{1}{\tilde{\tau}^{opt}} = \frac{4}{3}\left\{\frac{\beta^2}{15}\left[\frac{(5N^2-1)(1+|\Gamma|^2) + (5N^2+2)Re(\Gamma)}{|1-\Gamma|^2}\right]\right\}^{\frac{1}{4}} \quad (7.3.2)$$

In addition, the two important special cases for zero boundary condition ratio and large N are easily derived from the above equations, or by adding the factor β^2 to the sinusoidal excitation results in equations (6.4.5) and (6.4.6):

$$\tilde{P} \underset{\Gamma=0}{\approx} \frac{1}{\tilde{\tau}}\left[1 + \frac{\tilde{\tau}^4}{45}\beta^2(5N^2-1)\right] \quad (7.3.3a)$$

$$\tilde{U} \underset{\Gamma=0}{\approx} \frac{2}{3}\left\{\tilde{d}\left[N^2 + \frac{3}{2}N + \frac{1}{2}\right] + \tilde{\tau}\left[N^2 - \frac{\tilde{\tau}^4}{630}\beta^2(21N^2-5)\right]\right\} \quad (7.3.3b)$$

$$\tilde{\tau}^{opt} \underset{\Gamma=0}{\approx} \frac{1}{\sqrt{\beta}}\left[\frac{15}{5N^2-1}\right]^{\frac{1}{4}} \quad (7.3.3c)$$

$$\tilde{P}^{min} \underset{\Gamma=0}{\approx} \frac{4}{3}\sqrt{\beta}\left[\frac{5N^2-1}{15}\right]^{\frac{1}{4}} \quad (7.3.3d)$$

and

$$\tilde{P} \underset{\substack{\Gamma=0 \\ N\to\infty}}{\approx} \frac{1}{\tilde{\tau}}\left[1 + \frac{1}{9}N^2\beta^2\tilde{\tau}^4\right] \quad (7.3.4a)$$

$$\tilde{U} \underset{\substack{\Gamma=0 \\ N\to\infty}}{\approx} \frac{2}{3}N^2\left\{\tilde{d} + \tilde{\tau}\left[1 - \frac{1}{30}\beta^2\tilde{\tau}^4\right]\right\} \quad (7.3.4b)$$

$$\tilde{\tau}^{opt} \underset{\substack{\Gamma=0 \\ R\to\infty}}{\approx} \frac{3^{1/4}}{\sqrt{\beta R}} \qquad (7.3.4c)$$

$$\tilde{p}^{min} \underset{\substack{\Gamma=0 \\ R\to\infty}}{\approx} \frac{4}{3}\frac{\sqrt{\beta R}}{3^{1/4}}. \qquad (7.3.4d)$$

The accuracy of the two-term series approximation in determining the optimum conductor thickness, along with the associated minimum power dissipation and energy storage, will now be examined. For brevity, only results for the unidirectional rectangular wave (Type III) will be graphically presented. All of the important characteristics of the solutions can be observed by varying the parameters of this waveform type. The graphical results are presented in Figures 7.3.1 through 7.3.3. The abscissa is taken to be the boundary condition ratio, and the remaining parameters are set equal to the values used previously in this chapter. The points on the ordinate ($\Gamma = 0$) should therefore correspond to the earlier results. There are several interesting characteristics revealed in these figures. First, consider the curves for the optimum conductor thickness in Figures 7.3.1a and 7.3.1b; where the waveform duty cycle and the rise-time duty cycle are varied, respectively. It is also helpful to refer to Figure C.3.2 in Appendix C which shows curves of the normalized power bandwidth for the Type III waveform. Notice that the

optimum thickness decreases for conditions which produce larger bandwidths such as small waveform or rise-time duty cycles. The two-term series approximation is slightly more accurate for small waveform duty cycles and is significantly more accurate for large rise-time duty cycles. In all cases the accuracy improves as the boundary condition ratio approaches unity. Similar trends are evident in Figures 7.3.2a and 7.3.2b for the corresponding minimum power dissipation and in Figures 7.3.3a and 7.3.3b for the energy storage. In general, the accuracy of the two-term series approximation of the power dissipation and energy storage is somewhat better than for the optimum conductor thickness.

Some concluding remarks concerning the two-term series approximation are appropriate. Its accuracy throughout the sinusoidal analysis in Chapters 4, 5, and 6 was found to be excellent in the regions below and near minimum power dissipation. This accuracy deteriorated rapidly, however, as the conductor thickness increased above its optimum value. Extending the application of this approximation to the general case using Fourier analysis was questionable to say the least. But the possibilities for analytical simplification and a closed-form solution which could provide physical insight certainly warranted an investigation. As suspected, considerable simplification did lead to a physically meaningful closed-form solution via

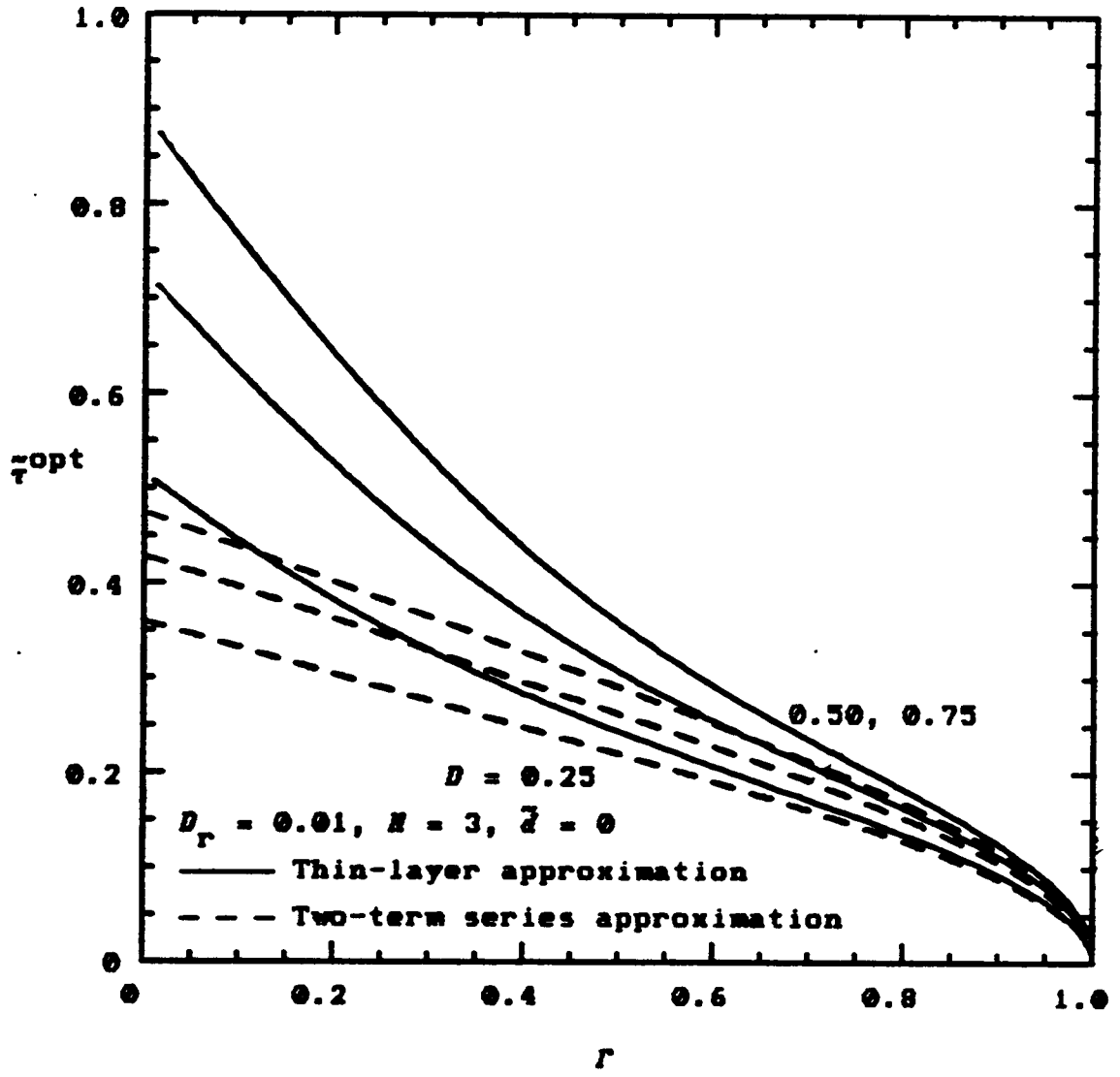

Figure 7.3.1a. Optimum normalized conductor thickness vs. boundary condition ratio for a unidirectional rectangular wave current (Appendix D - Type III). The waveform duty cycle is varied as a parameter.

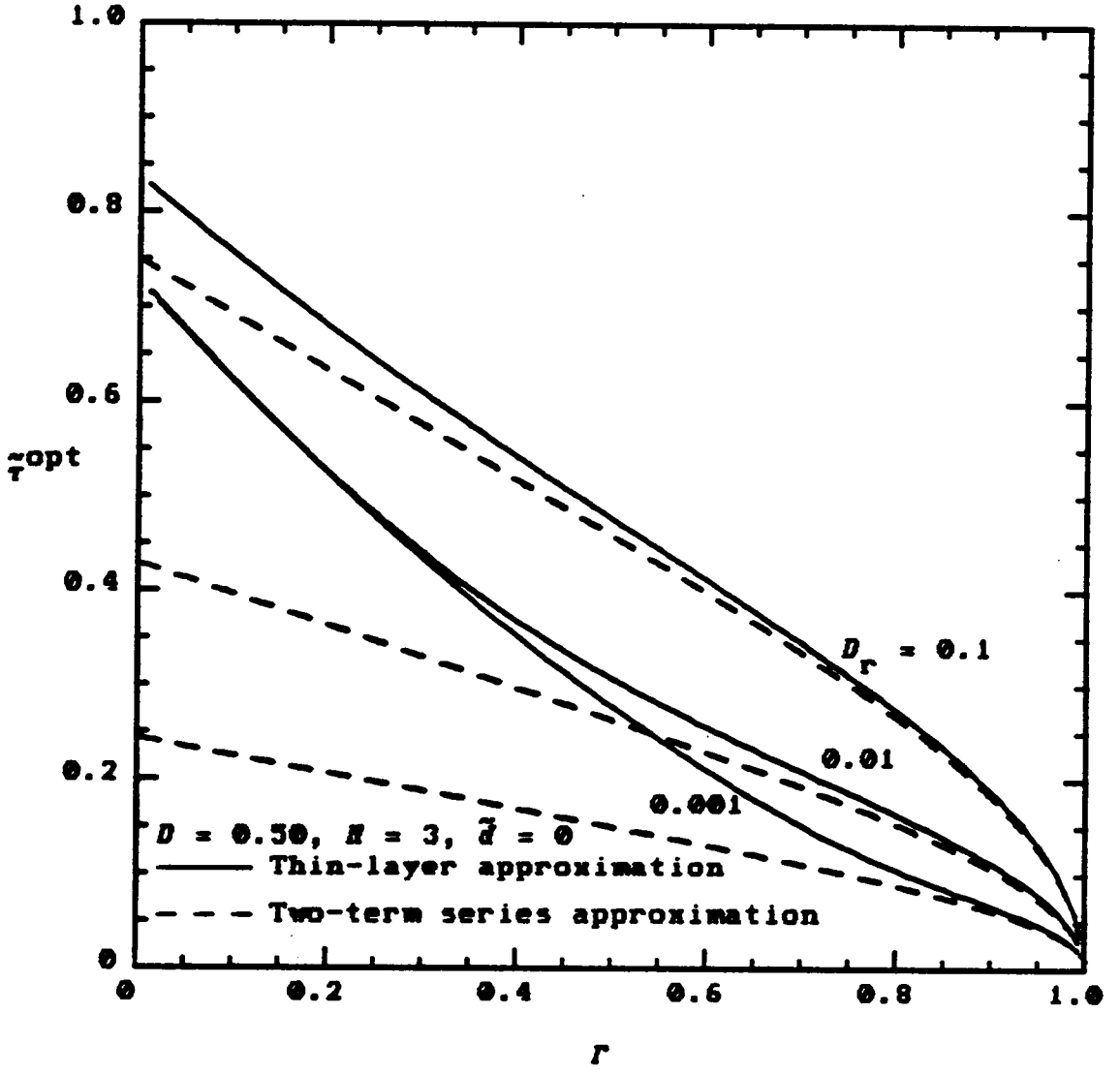

Figure 7.3.1b. Optimum normalized conductor thickness vs. boundary condition ratio for a unidirectional rectangular wave current (Appendix D - Type III). The rise-time duty cycle is varied as a parameter.

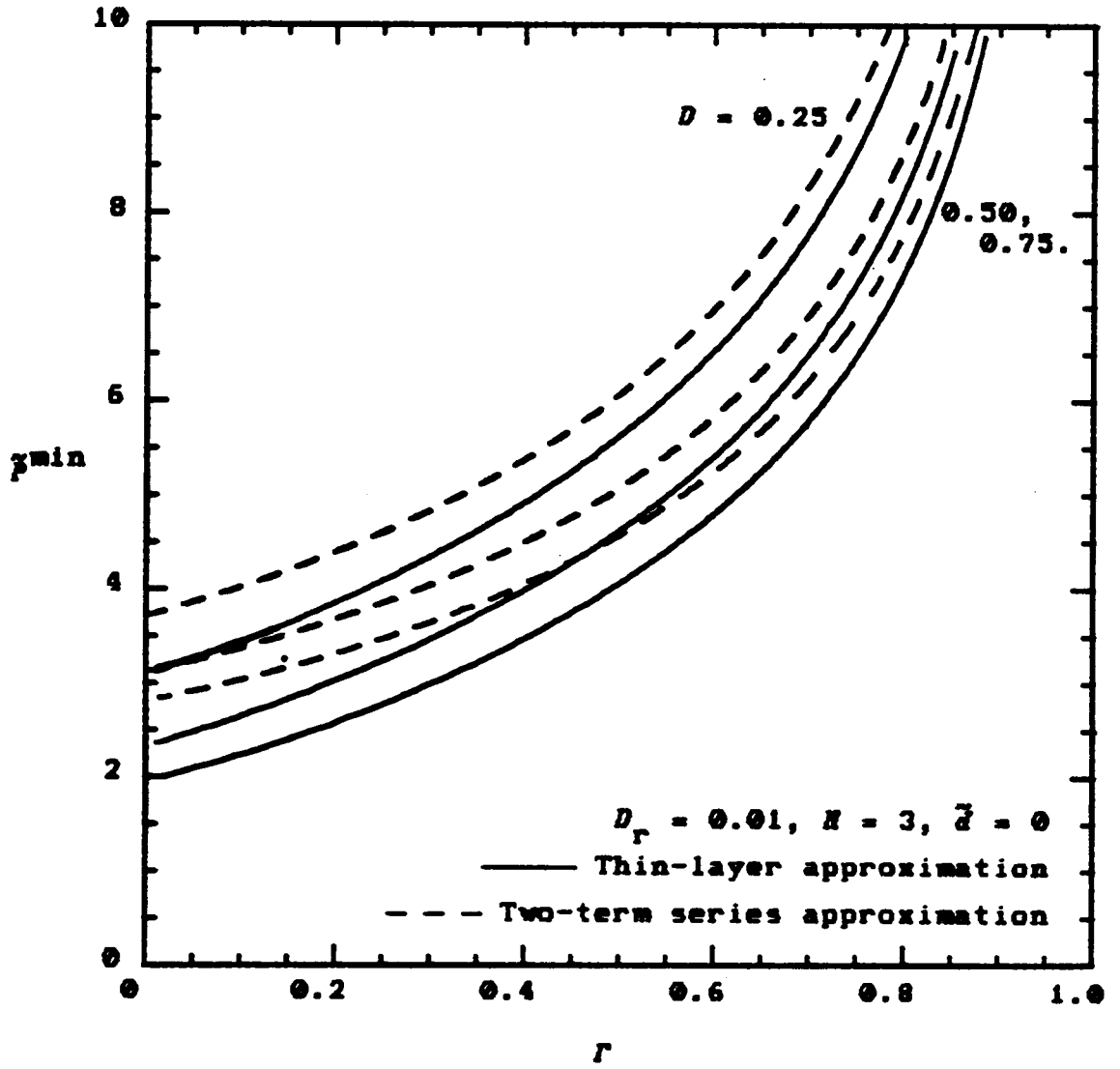

Figure 7.3.2a. Minimum normalized power dissipation (at the optimum conductor thickness) vs. boundary condition ratio for a unidirectional rectangular wave current (Appendix D - Type III). The waveform duty cycle is varied as a parameter.

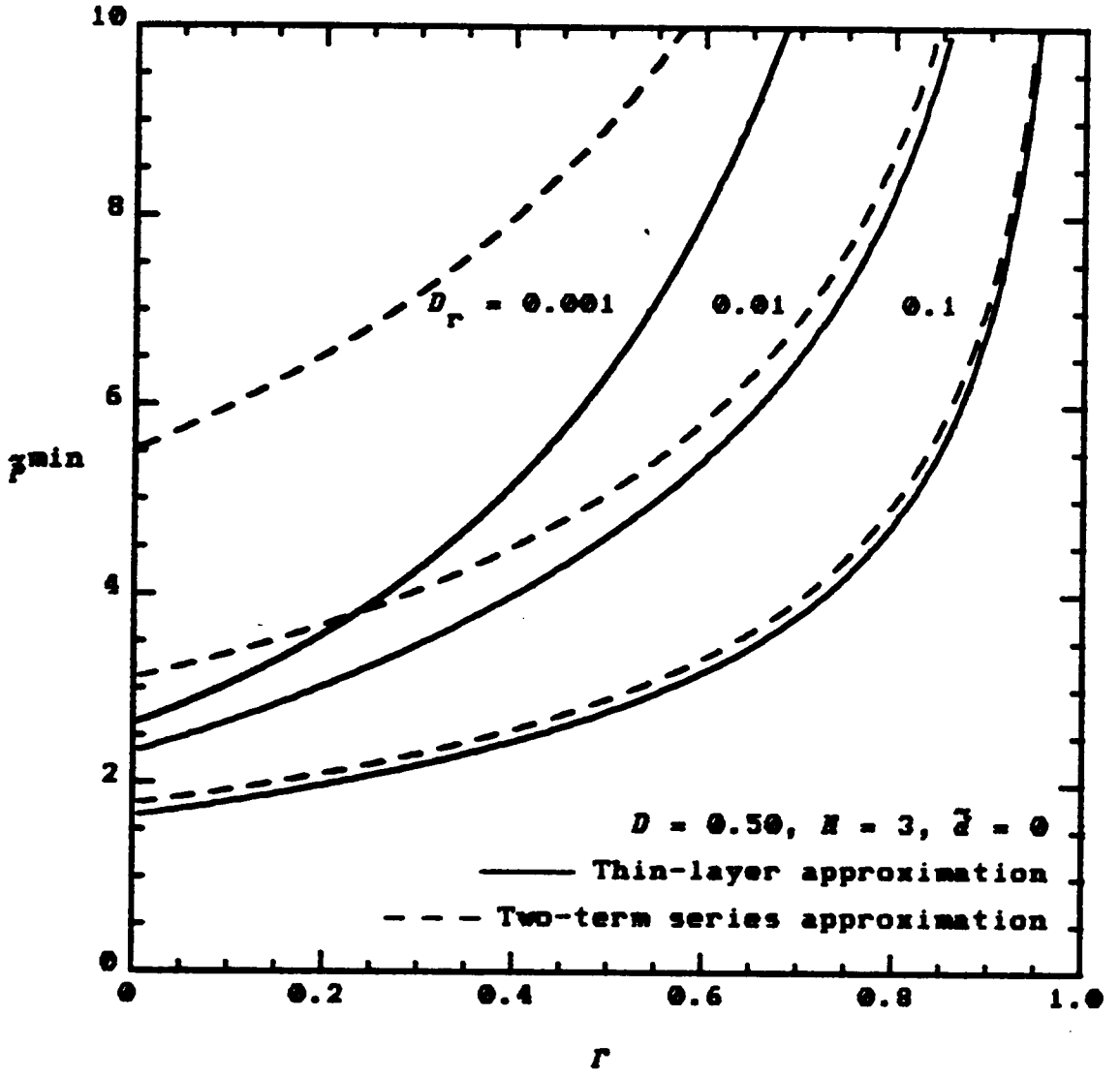

Figure 7.3.2b. Minimum normalized power dissipation (at the optimum conductor thickness) vs. boundary condition ratio for a unidirectional rectangular wave current (Appendix D - Type III). The rise-time duty cycle is varied as a parameter.

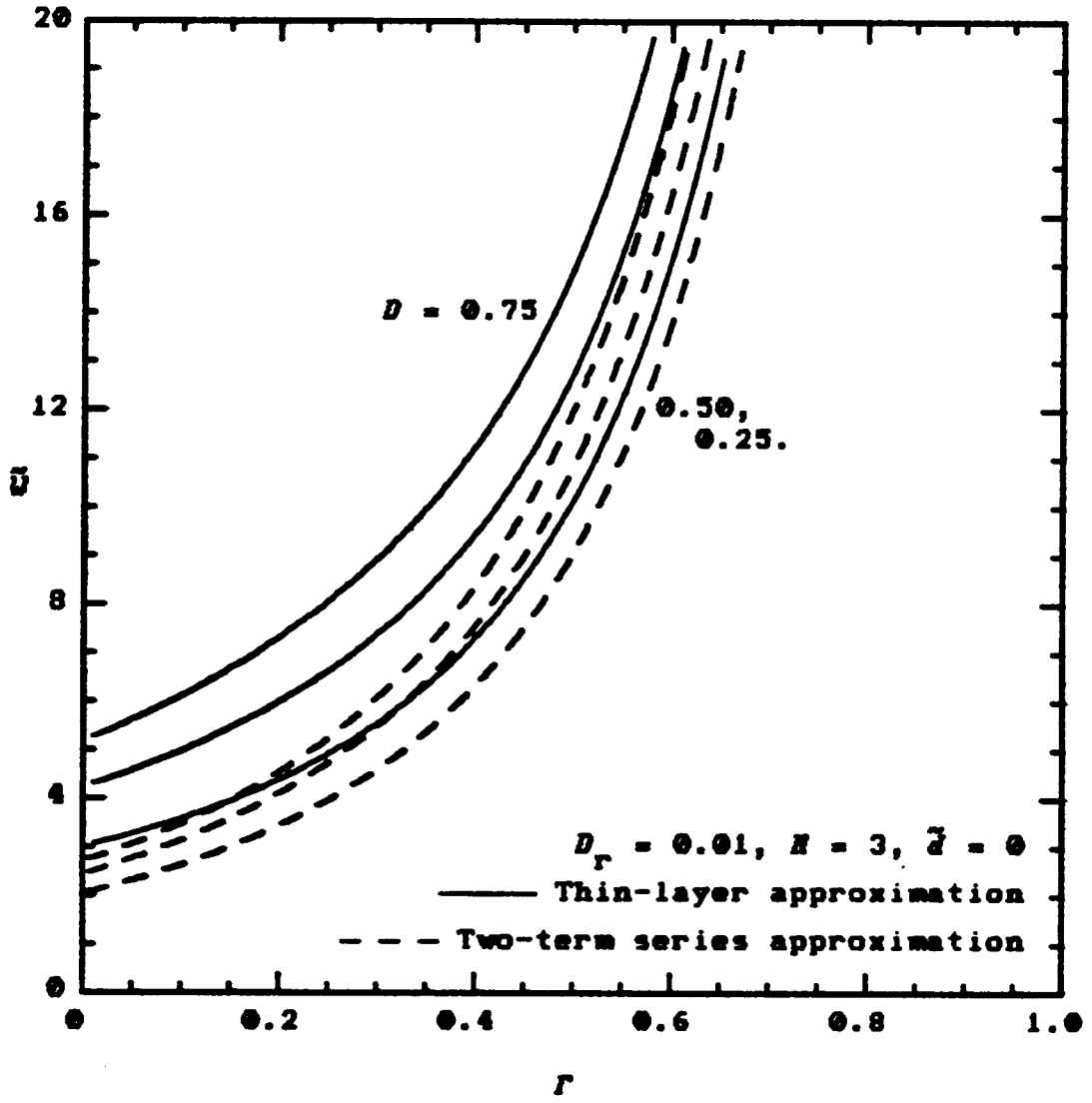

Figure 7.3.3a. Normalized energy stored (at the optimum conductor thickness) vs. boundary condition ratio for a unidirectional rectangular wave current (Appendix D - Type III). The waveform duty cycle is varied as a parameter.

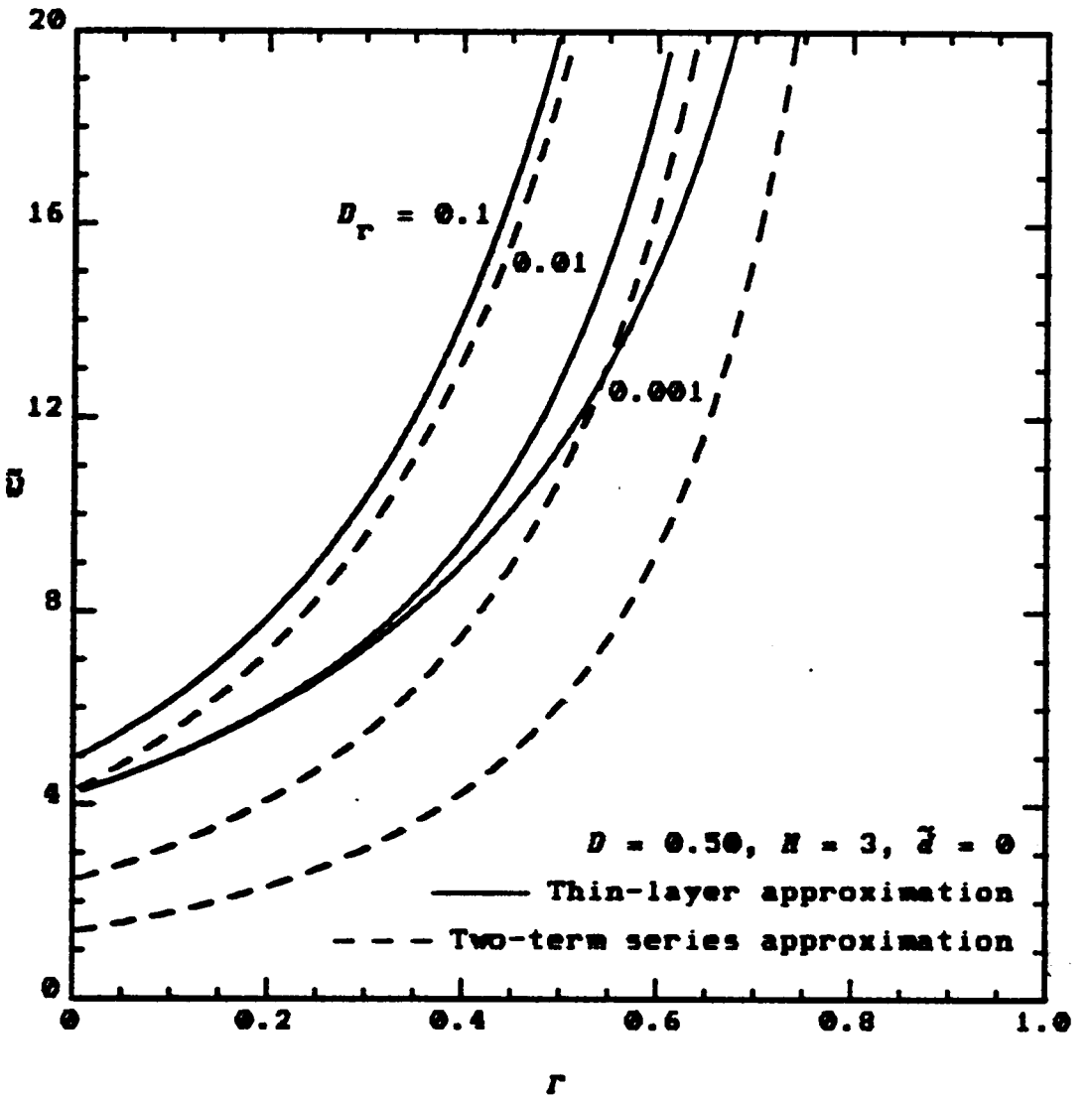

Figure 7.3.3b. Normalized energy stored (at the optimum conductor thickness) vs. boundary condition ratio for a unidirectional rectangular wave current (Appendix D - Type III). The rise-time duty cycle is varied as a parameter.

the normalized power bandwidth β. Although the accuracy of this approximation may certainly be inadequate for many typical conditions and applications, all of the important features and trends of the solutions are evident in it. For that reason, the two-term series approximation is a very important asset in understanding the fundamental nature of the problem and its solution. In addition, it provides very simple formulas which can be easily evaluated on a hand calculator for preliminary design considerations. Another important use is as an initial estimate from which the numerical algorithms using the more accurate solutions can begin. Finally, it is evident from Figures 7.3.1 through 7.3.3 that the two-term series approximation provides either an upper or lower limit, depending on the quantity of interest. In particular, it provides a lower limit of the optimum conductor thickness and energy storage, and an upper limit of the power dissipation. The latter can therefore be interpreted as a worst-case estimate.

CHAPTER 8

PRACTICAL APPLICATIONS AND EXPERIMENTAL RESULTS

The analysis thus far has focused primarily on the determination of the power dissipation and energy storage within transformer windings. The former is the most important in the majority of applications, and it offers excellent opportunities for optimizing the design. The amount of power dissipation in a transformer will determine its operating temperature which in turn affects its performance, reliability, and lifetime. Very often, the amount of power dissipation is the dominating factor upon which a design is ultimately evaluated. Another useful design tool which is of interest to the circuit designer is the equivalent circuit model of the transformer. The first task in this chapter is to relate the power dissipation and energy storage in a transformer winding to elements in its equivalent circuit, namely, the effective winding resistances and leakage inductances. The results of this analysis provide a convenient basis for experimental verification of the theory which is the topic for the remainder of the chapter. Several typical conductor types and arrangements are evaluated. Details on how to apply the theoretical results are given in each case.

8.1 DETERMINATION OF EQUIVALENT CIRCUIT ELEMENTS

A popular equivalent circuit for a single primary/single secondary transformer is shown in Figure 8.1.1. R_p and R_s represent the effective winding resistances of the primary and secondary, respectively. Likewise, L_p and L_s represent the corresponding winding leakage inductances. L_m is the magnetizing inductance, and a is the turns ratio of the ideal transformer which now appears as an element of the overall nonideal transformer.

The effective winding resistances must account for the loss in the conductors of the windings. They may be determined therefore by equating the power dissipation within the winding (see equation (7.1.5)) to the power dissipated in the effective winding resistance:

$$P = 2\frac{\pi l}{\sigma}K_{rms}^2 N\tilde{\rho}_w\tilde{P} = R_{eff}I_{rms}^2, \qquad (8.1.1)$$

where R_{eff} denotes the effective winding resistance of a given winding in general. For instance, in Figure 8.1.1 it may represent either R_p or R_s. The total rms-current flowing through the winding is I_{rms}, so that the current per unit length in a conductor layer can be expressed as

$$K_{rms} = \frac{N_l I_{rms}}{l}, \qquad (8.1.2)$$

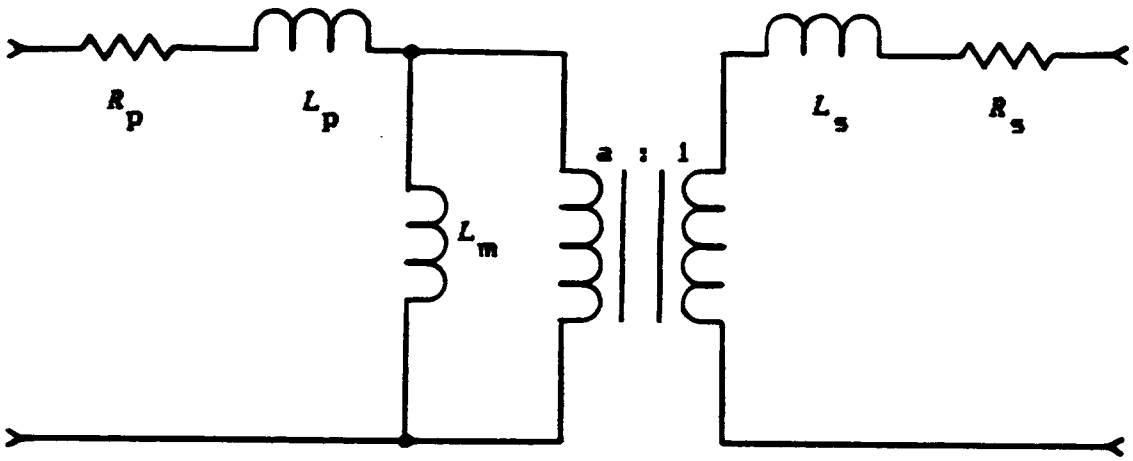

Figure 8.1.1. Equivalent circuit for basic single primary/single secondary transformer.

where N_l is the number of conductor turns per layer. This definition is merely an extension of equations (6.1.2) and (4.1.12), where I represented the total current in the layer. I is now replaced by $N_l I_{rms}$. Replacing K_{rms} in equation (8.1.1) with the relation in equation (8.1.2) and solving for R_{eff} gives

$$R_{eff} = 2\frac{\pi}{l\sigma}N_l^2 K\tilde{P}_w\tilde{P}. \qquad (8.1.3)$$

But the DC resistance is given by

$$R_{dc} = 2\frac{\pi}{l\sigma}N_l^2 K\frac{\tilde{P}_w}{\tilde{\tau}} \qquad (8.1.4)$$

which, upon substitution into equation (8.1.3), leads to

$$\frac{R_{eff}}{R_{dc}} = \tilde{\tau}\tilde{P} \qquad (8.1.5a)$$

or

$$\tilde{P} = \frac{1}{\tilde{\tau}}\frac{R_{eff}}{R_{dc}}. \qquad (8.1.5b)$$

Thus, it is seen that the ratio of the effective resistance to the DC resistance is very simply related to the normalized power dissipation and the normalized conductor

thickness. For pure sinusoidal time-harmonic variation the effective resistance is often referred to as the AC resistance which is usually denoted as R_{ac}. Under these conditions equations (8.1.5) become

$$\frac{R_{ac}}{R_{dc}} = \tilde{\tau}\tilde{P} \tag{8.1.6a}$$

$$\tilde{P} = \frac{1}{\tilde{\tau}} \frac{R_{ac}}{R_{dc}}. \tag{8.1.6b}$$

It is quite easy to measure both the DC resistance and the AC resistance at a given frequency with modern impedance analyzers. This capability provides, in the following sections of this chapter, the basis for experimentally verifying the previously derived expressions for the normalized power dissipation $\tilde{P}$.

A similar relationship can be derived between the normalized energy stored $\tilde{W}$ in the leakage fields and the effective leakage inductance L_{eff} by equating (7.2.3a) to the energy stored in the inductance:

$$W = 2\frac{\pi\mu_o l\delta^2}{4} K_{rms}^2 H \tilde{\rho}_w \tilde{W} = \frac{1}{2} L_{eff} I_{rms}^2. \tag{8.1.7}$$

Incorporating into this result the relationships in equations (3.2.17), (8.1.2), and (8.1.4) leads to

$$\frac{\omega L_{eff}}{R_{dc}} = \tilde{\tau}\tilde{U} \qquad (8.1.8a)$$

$$\tilde{U} = \frac{1}{\tilde{\tau}} \frac{\omega L_{eff}}{R_{dc}} \qquad (8.1.8b)$$

which relates the normalized stored energy to the ratio of the effective leakage reactance to DC resistance. For sinusoidal time-harmonic variation, the effective leakage inductance is generally referred to as the AC leakage inductance, so that the above expressions may be written as

$$\frac{\omega L_{ac}}{R_{dc}} = \tilde{\tau}\tilde{U} \qquad (8.1.9a)$$

$$\tilde{U} = \frac{1}{\tilde{\tau}} \frac{\omega L_{ac}}{R_{dc}}. \qquad (8.1.9b)$$

Once again, the involved quantities are easily measurable, thereby providing a convenient means of experimental verification.

As a final manipulation, it is interesting to relate the complex power dissipation to the quantities defined above through the use of Poynting's theorem in equation (3.2.14). Using equations (8.1.1) and (8.1.7), the result is

$$-\iint_S \mathbf{S} \cdot d\mathbf{s} = I_{rms}^2 (R_{eff} + j\omega L_{eff}) = I_{rms}^2 Z_{eff} \qquad (8.1.10)$$

which simply states that the complex power dissipated in the winding must equal the net complex power flowing into a region s enclosing the winding. An equivalent expression is derived upon substitution from equations (8.1.5) and (8.1.8), namely,

$$-\iint_s \mathbf{S} \cdot d\mathbf{s} = I_{rms}^2 R_{dc} \tilde{\tau}(\tilde{P} + j\omega\tilde{W}). \qquad (8.1.11)$$

Finally, a relationship between the complex impedance ratio and the normalized complex power can be derived by equating equations (8.1.10) and (8.1.11), yielding

$$\frac{Z_{eff}}{R_{dc}} = \tilde{\tau}(\tilde{P} + j\omega\tilde{W}) \qquad (8.1.12a)$$

$$\tilde{P} + j\omega\tilde{W} = \frac{1}{\tilde{\tau}} \frac{Z_{eff}}{R_{dc}}. \qquad (8.1.12b)$$

8.2 SINGLE AND MULTIFILAR ROUND WIRE WINDINGS

Round copper magnet wire is by far the most popular conductor type used in switched-mode power transformers. It is low in cost, easy to use, and widely available in many sizes. See Figure 8.2.1a for a pictorial representation of a layer of round wire along with its associated notation. N_l is the number of turns in the layer, l is the axial

length of the layer, d_w is the diameter of the copper in the wire, and I_{rms} is the rms-current flowing in each turn.

The arrangement of conductors within a conductor layer was left undefined in the geometrical assumptions of Section 3.1. However, the mathematical treatment proceeded as if the layer were a solid conductor. The task now is to model the layer of round wire within the context of that treatment. The model proposed by the author is presented in Figure 8.2.1b. One simply replaces the layer of round wire with a solid conductor of the same cross-sectional area and length l. From these requirements, the following relationship between the solid conductor thickness τ and the copper diameter d_w is easily derived:

$$\tau = \frac{\pi}{4} d_w. \qquad (8.2.1)$$

The only remaining quantity to be determined is the current per unit axial length. Since there is no longitudinal variation allowed, this is simply the total current in the layer $N_l I_{rms}$ divided by the winding length l (see equation (8.1.2)).

A transformer has been constructed to test the validity of this model. The details of its construction are as follows:

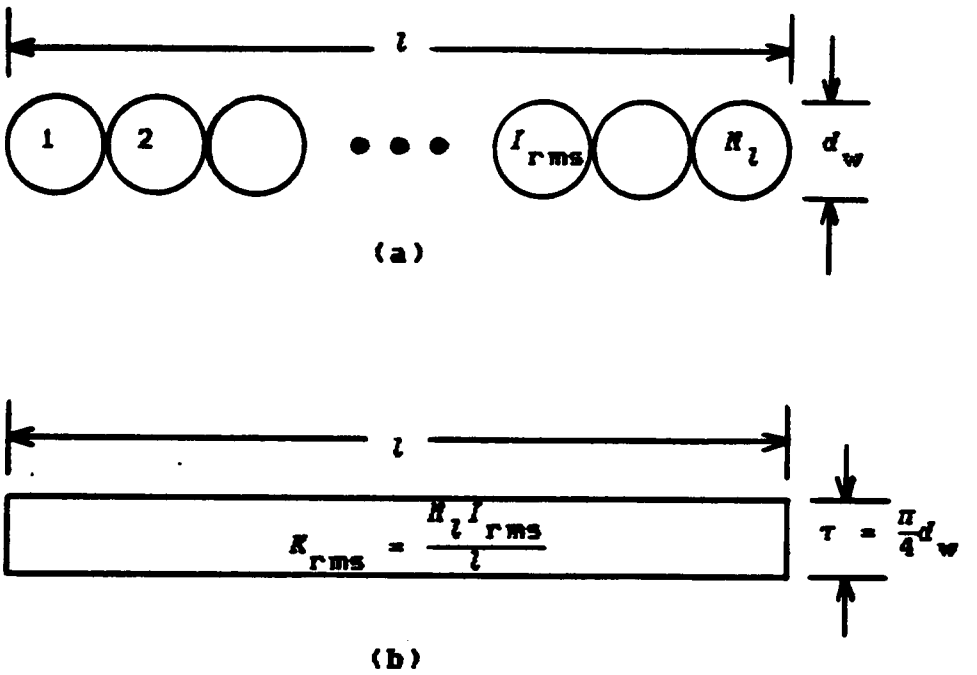

Figure 8.2.1. (a) Pictorial representation of a layer of round wire conductor and (b) its equivalent theoretical model.

- Thompson-CSF ETD-49 core and CAR-4916A bobbin (equivalent to Ferroxcube ETD-49 core and PC1-49H bobbin).
- Ten layers, 57 turns each, of 24 AWG copper magnet wire separated by 0.005 inch mylar insulation.
- Leads were brought out for each layer to allow connections for various configurations of layers and windings.

Results of the experimental measurements are presented in Figures 8.2.2 and 8.2.3. The ratio of the mean winding radius to the conductor layer thickness is approximately 30, so that the thin-layer approximation in equation (6.2.11) was used for the theoretical curves. The individual layers were connected such that both the primary and secondary had the same number of layers, and also such that no conductor layers were present in the space between the primary and secondary (see Figure 6.6.1, for example). The input impedance of the primary with the secondary shorted was measured vs. frequency with an impedance analyzer which was set to read directly the series resistive and inductive components of the impedance. From the equivalent circuit in Figure 8.1.1, this is seen to be a direct measurement of the primary and secondary winding impedances in series if the impedance presented by the magnetizing inductance is

comparatively much larger. This is true because the high permeability of the ferrite core gives rise to a very large magnetizing inductance. The measurements were then converted to the normalized power dissipation and energy storage by using equations (8.1.6b) and (8.1.9b), respectively. Notice that varying the frequency has the effect of changing the normalized conductor thickness without changing the actual thickness itself. This provides a convenient means of evaluating several points on the curves using a single transformer.

Experimental measurements were performed for three different winding configurations: single layer, three layers, and five layers. The agreement of these measurements with the theoretical curves is seen to be very good for the normalized power dissipation in Figure 8.2.2. Good agreement for the normalized energy storage, although not quite to the same degree, is also apparent from Figure 8.2.3. The experimental measurements begin to depart from the theoretical curves as the normalized conductor thickness increases, which here corresponds to increasing the frequency of measurement. The severity of this departure becomes greater as the number of layers increases. There are several possible explanations for this behavior. First of all, the core does not completely surround the winding as the axial symmetry of the model suggests. Consequently,

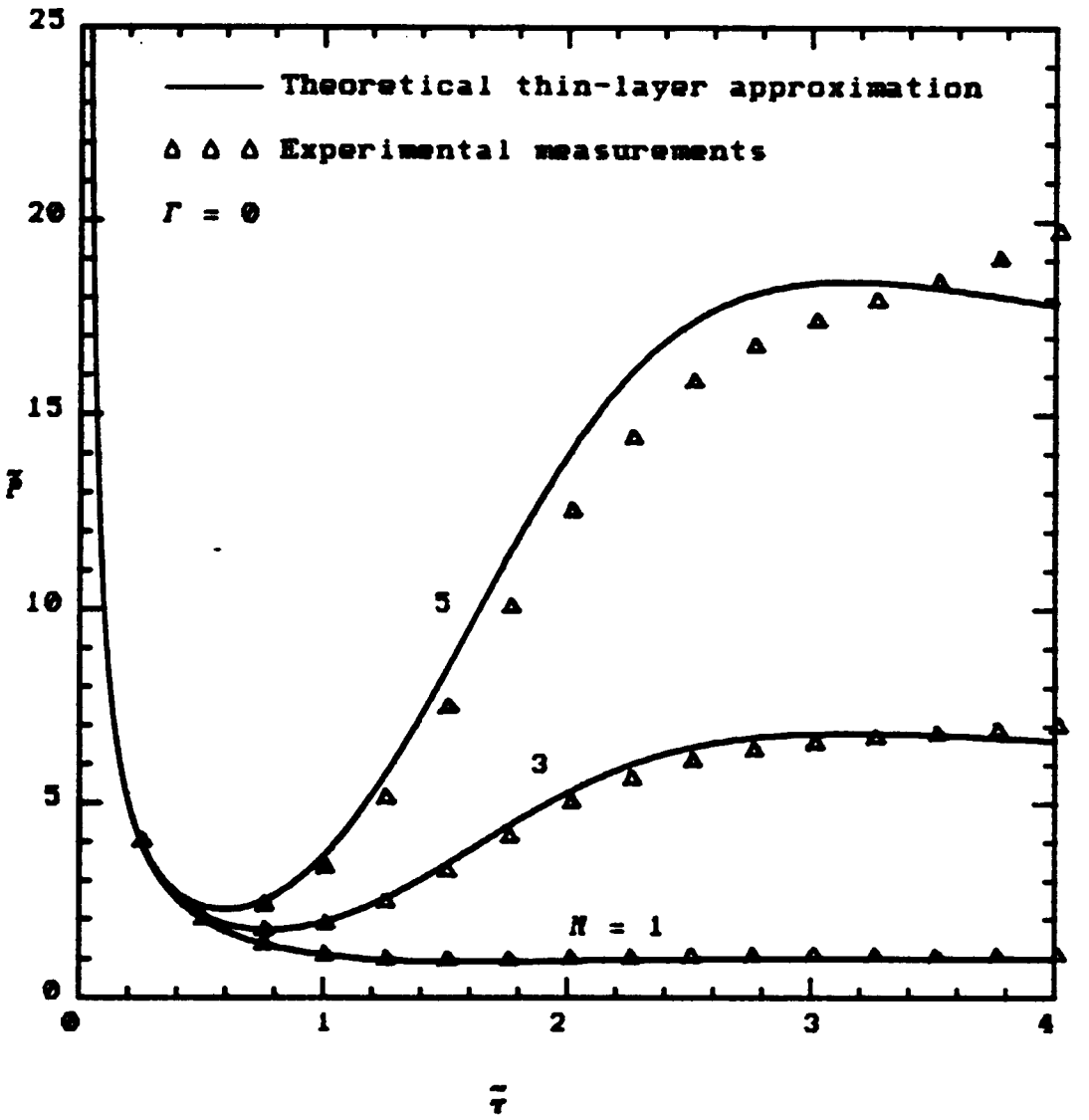

Figure 8.2.2. Normalized power dissipation per layer in an N-layer winding vs. normalized conductor thickness with the number of layers varied as a parameter. The measurements were performed on a transformer with windings of round copper magnet wire.

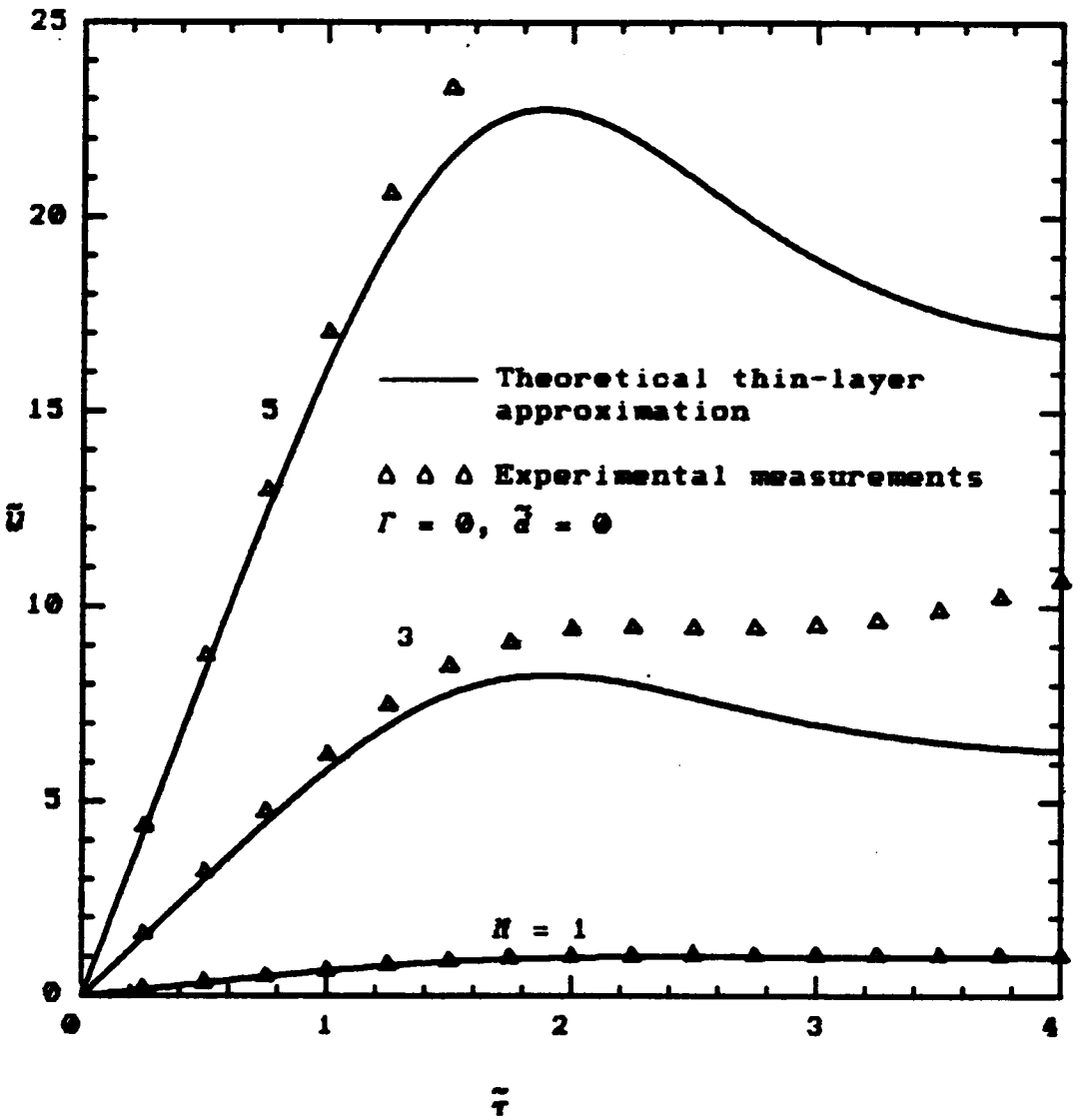

Figure 8.2.3. Normalized energy storage per layer in an N-layer winding vs. normalized conductor thickness with the number of layers varied as a parameter. The measurements were performed on a transformer with windings of round copper magnet wire.

there are certainly present stray leakage fields which are not accounted for by the model. It also seems that this effect would become exaggerated as the frequency increases. Another possible explanation is that impedance contributions from the interwinding or self capacitances of the transformer are beginning to come into play in the measurements at higher frequencies. Despite the noted differences, it is encouraging to point out that the accuracy is extremely good in the important region near the minimum in power dissipation.

One further point concerning the measurements for Figure 8.2.3 should be brought out. For purposes of convenient presentation, the theoretical curves have been computed for zero insulation thickness ($\tilde{d} = 0$). Since there is insulation in the transformer, these contributions have been subtracted out of the leakage inductance measurements according to the thin-layer approximation. This, in effect, causes the error in the normalized stored energy curves to appear greater (as a percentage of the plotted curves) than if these contributions were included.

Suppose that the total rms-current requirement exceeds the capability of the round wire size that corresponds to minimum power dissipation. This is certainly possible since the optimization with respect to the conductor thickness is independent of the magnitude of the total current. In order

to increase the current handling capability without changing the thickness, one can simply parallel the required number of round wire conductors as depicted in Figure 8.2.4a. This technique is often referred to as multifilar winding, and it is becoming increasingly popular in modern switched-mode power transformers. The dotted lines in Figure 8.2.4a indicate the number of wires that are connected in parallel. This particular example shows a trifilar winding which is three wires in parallel.

Multifilar windings provide a practical means of increasing the current handling capability over that of a single round wire. Although it is theoretically possible to parallel as many conductors as needed, the process starts to become impractical from a manufacturability standpoint for more than four conductors.

The theoretical model adopted for multifilar windings is depicted in Figure 8.2.4b; it is essentially the same as that of the single round wire. The only differences are that I_{rms} now represents the total current in the paralleled multifilar conductor (still the winding current) and N_l is the number of turns of the same. With these definitions, equations (8.1.2) and (8.2.1) still apply. The one-dimensional model used throughout this dissertation does not allow any longitudinal variation in the current. Therefore, under the conditions imposed by this model, the

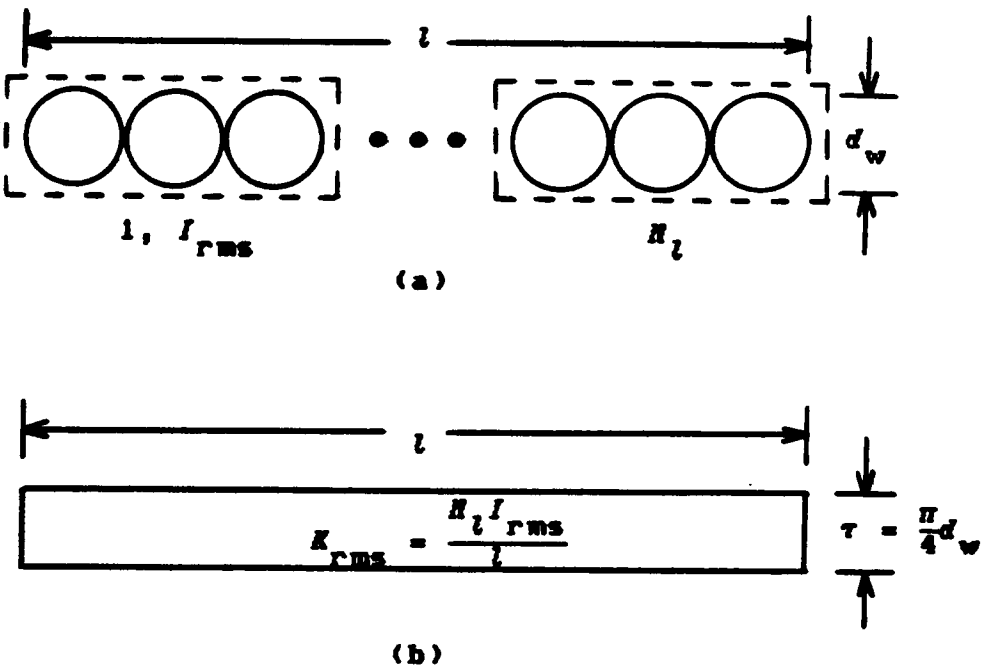

Figure 8.2.4. (a) Pictorial representation of a multifilar wound (trifilar here) layer of round wire conductor and (b) its equivalent theoretical model.

total current must divide evenly among the individual strands that make up the multifilar conductor. The resulting normalized power dissipation and energy storage should then be the same as for the single-wire case if the number of layers M and the boundary condition ratio Γ do not change. The only difference is that now both the DC and effective resistances will decrease by a common factor which, in effect, increases the current handling capability of the winding.

A second transformer has been constructed to test and verify the model for multifilar windings. It is exactly the same as the single round wire transformer previously described except that now three of the individual strands are paralleled to form a trifilar winding. The experimental measurements are presented in Figures 8.2.5 and 8.2.6 along with the predicted results from the thin-layer approximation of the theory. Again, there is good agreement throughout the minimum power region and a gradual divergence as the normalized conductor thickness increases. Comparison of these results with those for the single wire case in Figures 8.2.2 and 8.2.3 reveals that the behavior is indeed similar. An explanation for the slight differences is not immediately apparent to the author other than possible variations in the measurements. The previously discussed effects of parasitic capacitances may also account for some of the differences

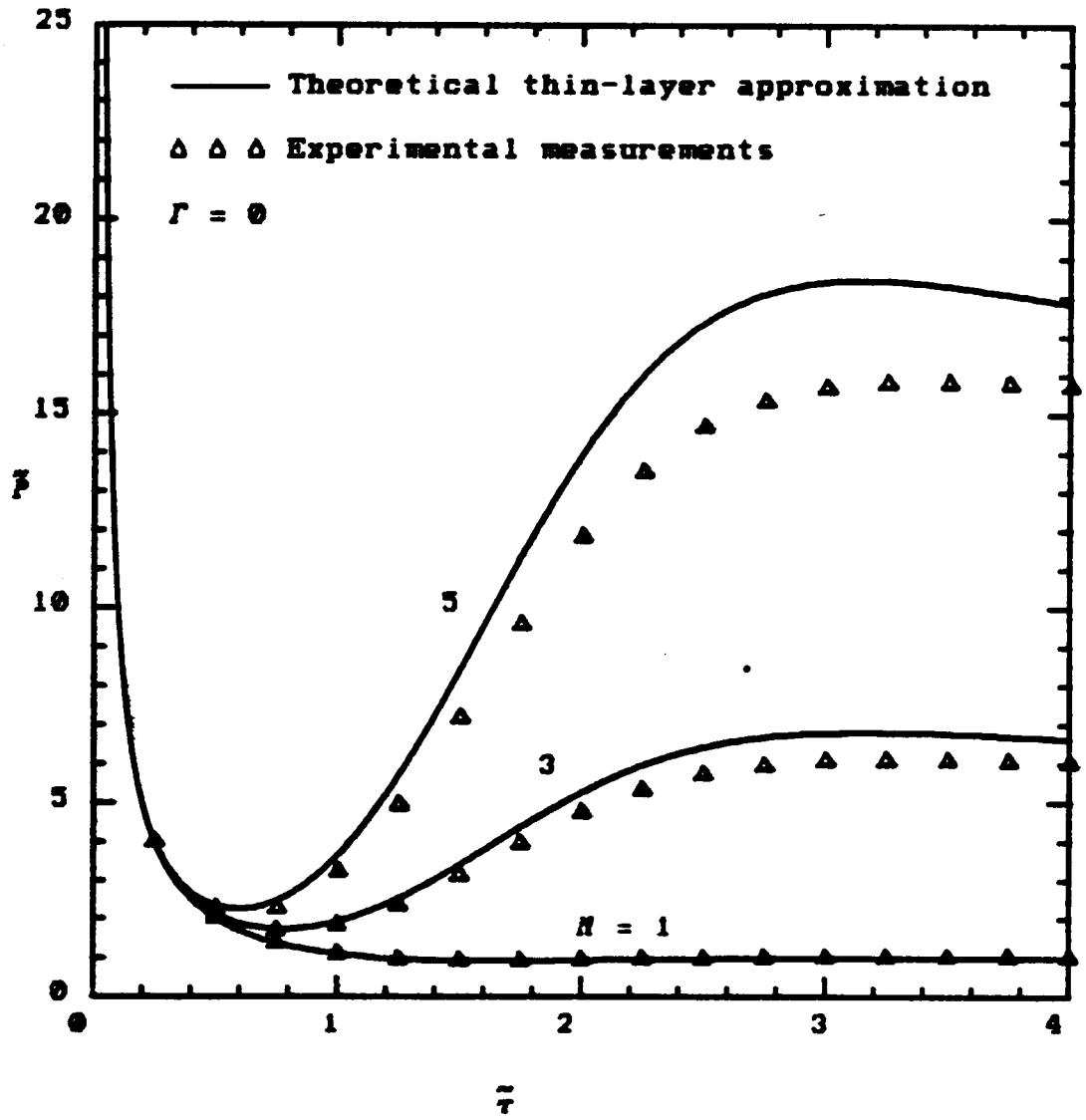

Figure 8.2.5. Normalized power dissipation per layer in an N-layer winding vs. normalized conductor thickness with the number of layers varied as a parameter. The measurements were performed on a transformer with windings of trifilar wound, round copper magnet wire.

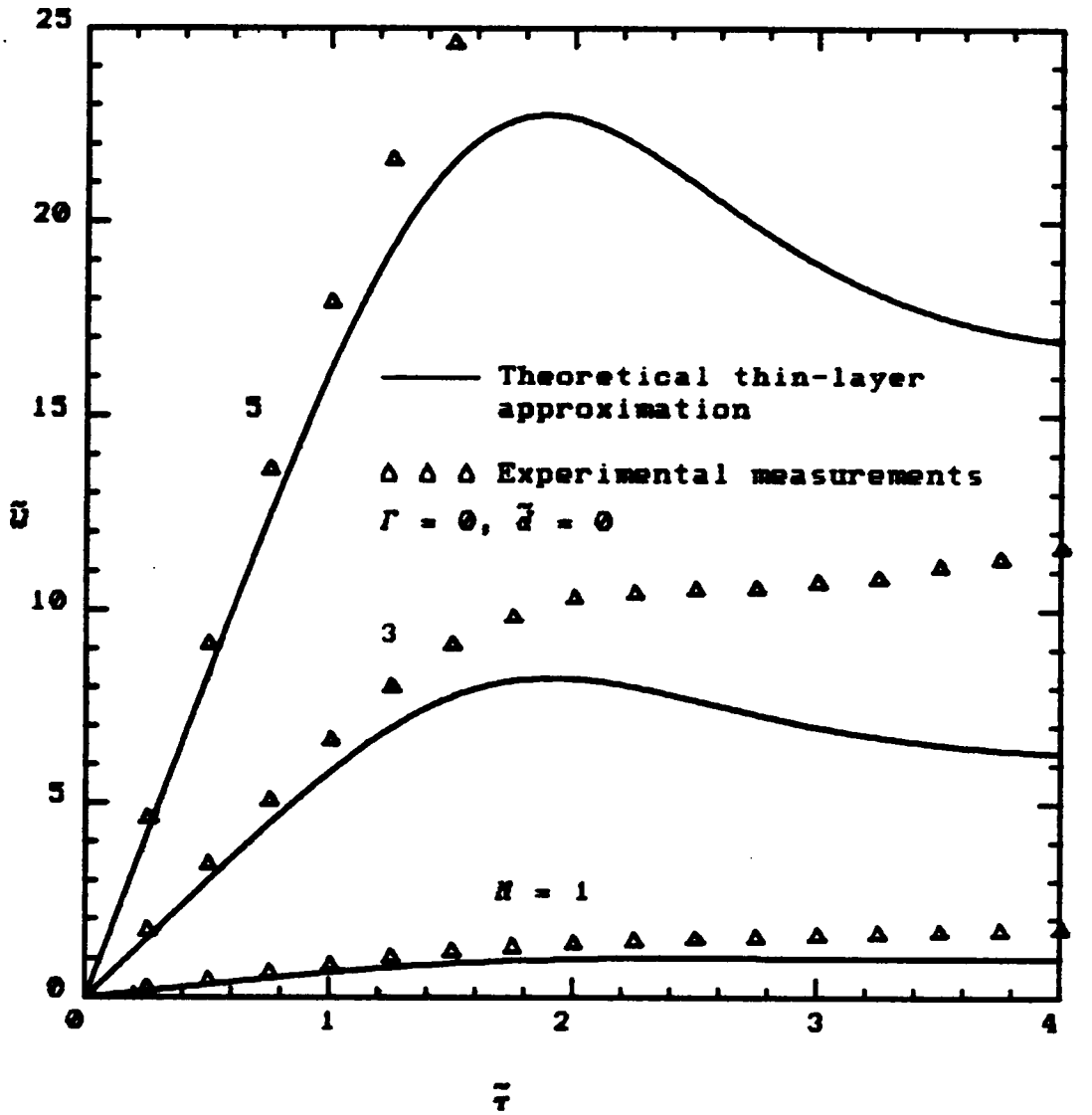

Figure 8.2.6. Normalized energy storage per layer in an N-layer winding vs. normalized conductor thickness with the number of layers varied as a parameter. The measurements were performed on a transformer with windings of trifilar wound, round copper magnet wire.

between the two cases, especially at the higher frequencies. No attempt has been made here to account for these effects which are quite complex and would involve an extensive amount of additional analysis.

8.3 LITZ WIRE WINDINGS

Suppose that multifilar windings still do not yield the necessary current handling capacity. A popular technique for extending the capacity further is to use litz wire as shown in Figure 8.3.1a. Litz wire is a conductor composed of a number of fine, separately insulated strands, usually fabricated in such a way that each strand assumes, to substantially the same extent, the different possible positions in the cross section of the conductor. Ideally, because of this transposition of the individually insulated strands, circulating eddy currents are prevented and the net current in each strand is identical. In Figure 8.3.1a; d_w is the overall diameter of the litz wire, N_t the number of turns per layer of litz wire, I_{rms} the winding current, d_s the diameter of the strands, N_s the number of strands in the litz wire, and l the winding length. The terminology, N_s/strand AWG, is often used to refer to litz wire with N_s strands of a given wire size (AWG). For example, 100/33 litz means 100 strands of 33 AWG round copper wire. The

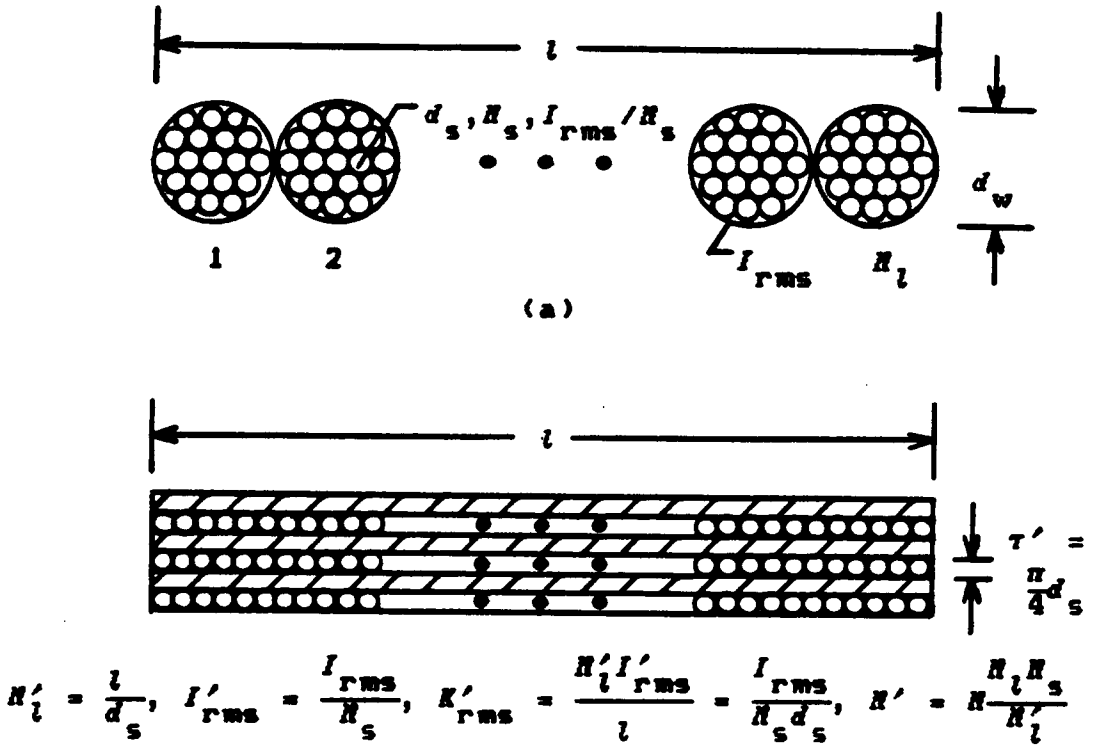

Figure 8.3.1. (a) Pictorial representation of a layer of litz wire conductor and (b) its equivalent theoretical model.

type of litz wire depicted in Figure 8.3.1a is the simplest possible. It represents strands which are bunched together and twisted into a circular shape. There are numerous other techniques for bunching and twisting the strands which yield a more ideal (equal) transposition of the strands. Generally, there is a cost vs. performance tradeoff for the more sophisticated litz types.

The theoretical model proposed by the author for a layer of litz wire is shown in Figure 8.3.1b. This model is based on two basic assumptions. First, the transposition is assumed to be ideal such that the total current is divided evenly among the individual strands:

$$I'_{rms} = \frac{I_{rms}}{N_s}, \tag{8.3.1}$$

where primed quantities will be used in describing the theoretical model of the litz wire. Second, the conductor thickness is based on the strand diameter:

$$\tau' = \frac{\pi}{4} d_s. \tag{8.3.2}$$

The latter assumption is made because one would still expect to see skin and proximity effects within the individual strands if they were large enough. Within the context of these assumptions, the theoretical model is constructed by

arranging the strands into individual layers until they are used up as shown in Figure 8.3.1b. Since litz wire is not 100% space efficient, there will be space left over from the actual overall thickness of the layer d_w. This space is treated as insulation and divided evenly between the conductor layers of the theoretical model as shown. Other quantities associated with the theoretical model are easily derived based on the foregoing assumptions and discussion:

$$N'_l = \frac{l}{d_s} \tag{8.3.3}$$

$$K'_{rms} = \frac{N'_l I'_{rms}}{l} = \frac{I_{rms}}{N_s d_s} \tag{8.3.4}$$

$$N' = N\frac{N_l N_s}{N'_l}. \tag{8.3.5}$$

A third transformer has been constructed to test and verify the model for a litz wire winding. The details of its construction are as follows:

- Thompson-CSF ETD-49 core and CAR-4916A bobbin (equivalent to Ferroxcube ETD-49 core and PC1-49H bobbin).
- Six layers, 25 turns each, of 26/33 litz wire separated by 0.005 inch mylar insulation.

- Leads were brought out from each layer to allow connections for various configurations of layers and windings.

This is the same core and bobbin type as that used in the experimental round wire transformers already considered. The results of the experimental measurements are presented in Figures 8.3.2 and 8.3.3. The individual layers were connected such that both the primary and secondary had the same number of layers. Three cases were measured: N = 1, 2, and 3. Using the definitions of the primed quantities in equations (8.3.1) through (8.3.5), the corresponding numbers of layers in the theoretical model are N' = 4, 8, and 12, respectively. Figure 8.3.2 shows the experimental results for the normalized power dissipation along with the corresponding theoretical curves using the thin-layer approximation. The same measurement techniques were used as for the round wire transformers in the previous section. The experimental measurements are slightly less than the predictions of the theory, but the accuracy is actually quite good considering the assumptions involved. The accuracy is especially good in the important regions near the minima. Therefore, the theory should predict very well the optimum strand size for litz wire and the resulting

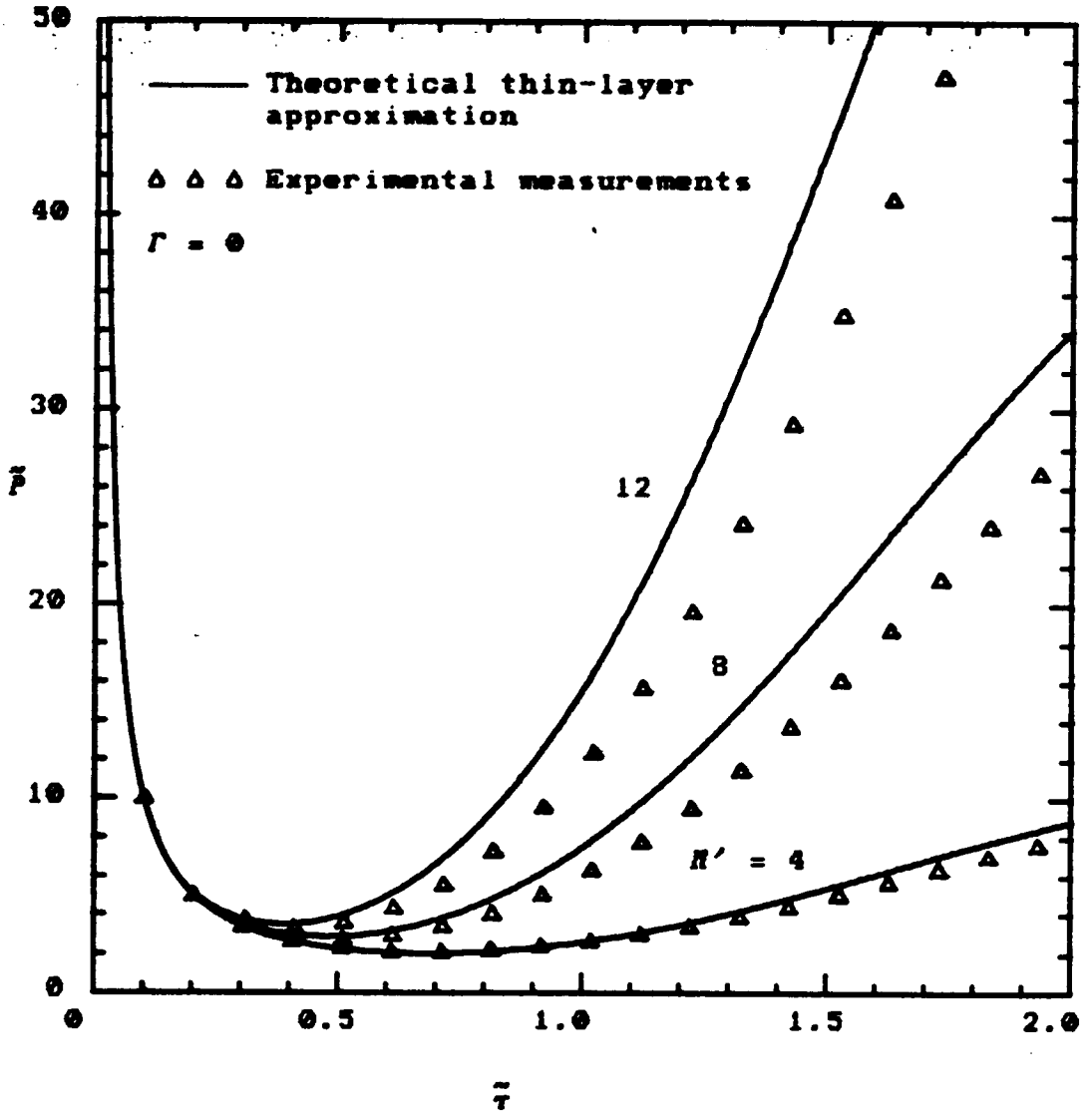

Figure 8.3.2. Normalized power dissipation per layer in an N-layer winding vs. normalized conductor thickness with the number of layers varied as a parameter. The measurements were performed on a transformer with windings of litz wire.

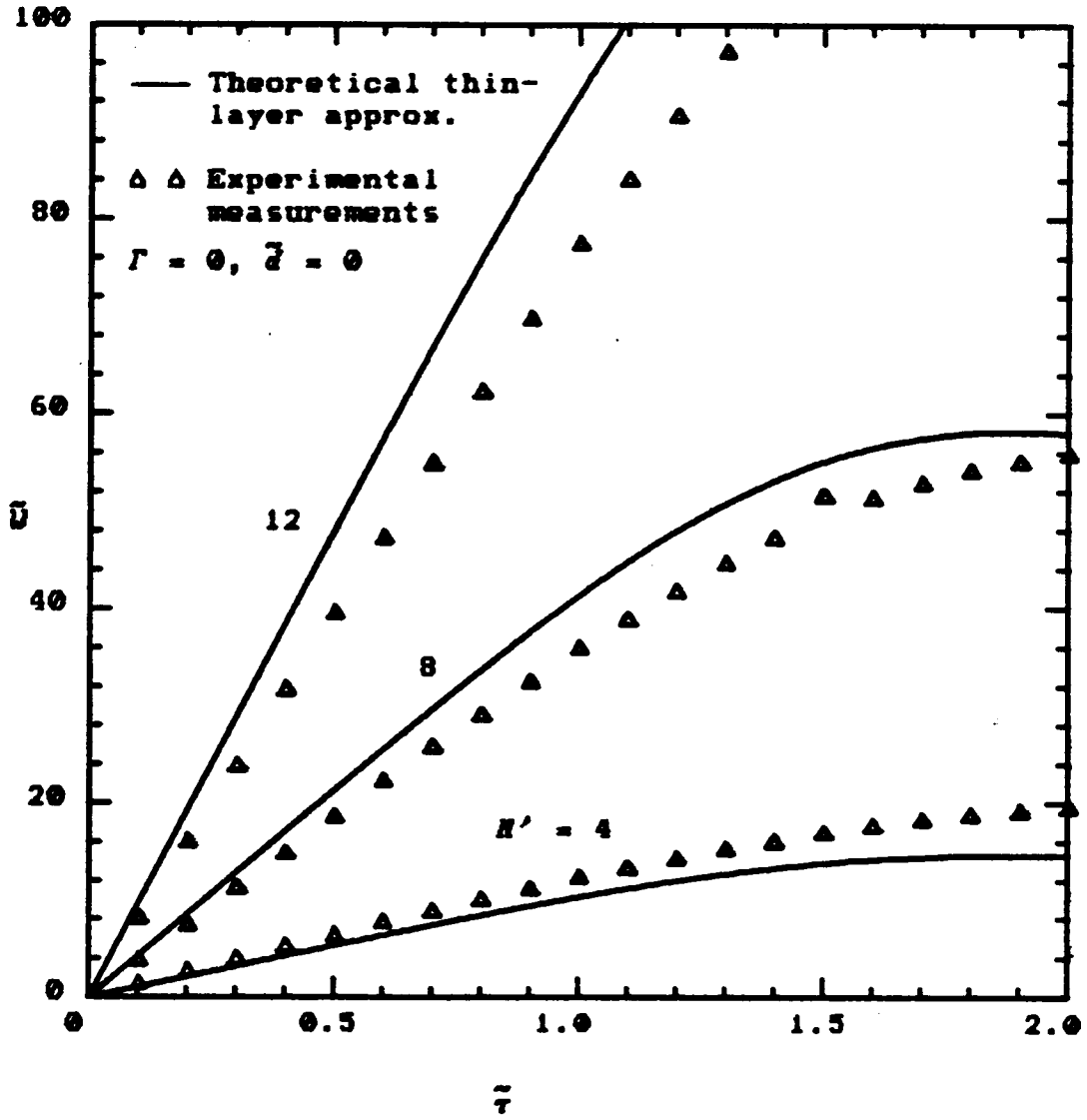

Figure 8.3.3. Normalized energy storage per layer in an N-layer winding vs. normalized conductor thickness with the number of layers varied as a parameter. The measurements were performed on a transformer with windings of litz wire.

power dissipation. Results for the normalized energy stored under the same conditions are presented in Figure 8.3.3. The accuracy is comparable to that obtained for the power dissipation.

The model used here for a litz wire winding is certainly not the only possibility; however, it is the most accurate of the ones thought of by the author. It is perhaps significant that the predictions exceed the measurements. One might expect the opposite of this behavior since the model assumes the ideal condition of equal strand currents. Accuracy would improve if either the layer thickness τ' was taken to be slightly larger or the equivalent number of layers N' slightly smaller. But neither of these alternatives appear to be physically justifiable in light of the earlier results on the round wire windings.

8.4 SHEET CONDUCTOR WINDINGS

Sheet conductor windings, also referred to as foil windings, offer the most efficient utilization of winding space (assuming that there is no longitudinal variation in the current density). They are, however, limited in their application since if one operates at the optimum thickness, then the current handling capability is fixed. Even so, there are many cases of low voltage, high current secondaries (computer power, for instance) where sheet copper windings are the most attractive alternative.

Sheet conductor windings require no adjustments in the original geometrical assumptions and Figure 3.1.2 applies with the conductor layers as solid copper. There can only be one turn per layer, so that the number of layers must equal the number of turns in a winding. Since it is desirable to keep the number of layers low, this is another reason why sheet conductor windings are best suited for low voltage windings with few turns.

A fourth and final experimental transformer has been constructed in order to determine the validity of the theory when applied to sheet conductor windings. The details of the construction follow:

- Thompson-CSF ETD-49 core and CAR-4916A bobbin (equivalent to Ferroxcube ETD-49 core and PC1-49H bobbin).
- A single primary and a single secondary, ten turns each, of 0.005 inch sheet copper separated by 0.003 inch mylar insulation.
- Only one set of leads were connected to each of the two windings.

This is the same core and bobbin type as those used in the other three experimental transformers already considered. Notice that extra sets of leads were not brought out to

investigate different numbers of layers. The reason for this is the very low resistance values of the sheet copper windings. Extra lead length adds a significant amount of resistance to the windings which in turn produces large errors in the measurements. Care was taken when constructing this transformer to keep the lead resistance less than 6% of the total winding resistance.

Figures 8.4.1 and 8.4.2 present the experimental measurements for the normalized power dissipation and energy storage, respectively. Deviation of the theoretical results from measurement in the former is the greatest of the winding types considered thus far. Ironically, one might be led to expect the best agreement for sheet conductor windings since they are modelled exactly by the assumed geometry. This would indeed be the case if the one-dimensional model were truly valid. Unlike the previously considered winding types, the continuous copper permits a gradual longitudinal variation in the current density. For example, the current density in a layer of round wire is forced to be nearly uniform in the longitudinal direction, since each turn must carry the same total current. Only small local variations in each turn would be possible in that case, and their effect appears to be negligble when the wire size is optimized using the one-dimensional model. If there is actually longitudinal

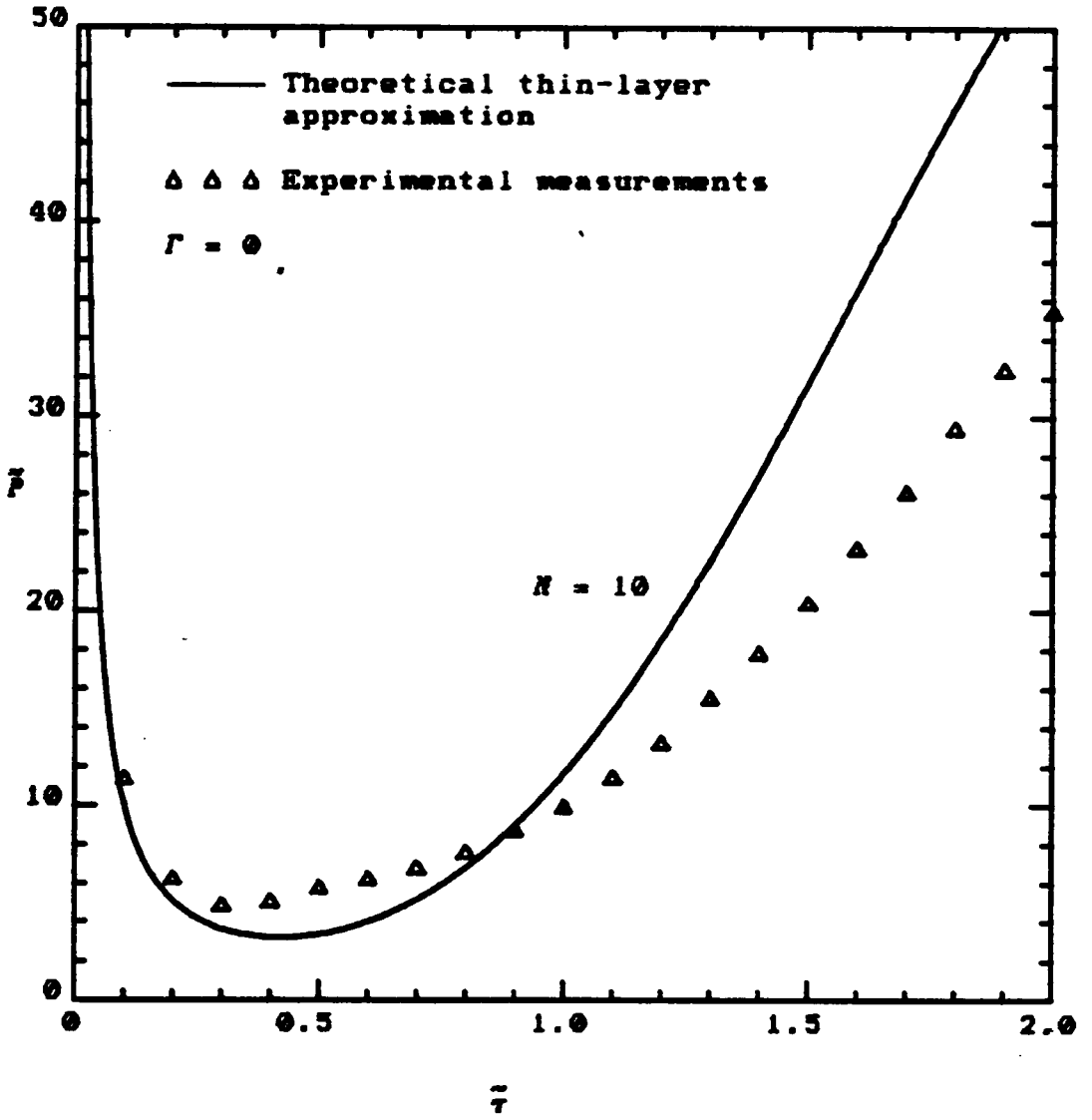

Figure 8.4.1. Normalized power dissipation per layer in a 10-layer winding vs. normalized conductor thickness. The measurements were performed on a transformer with windings of sheet copper.

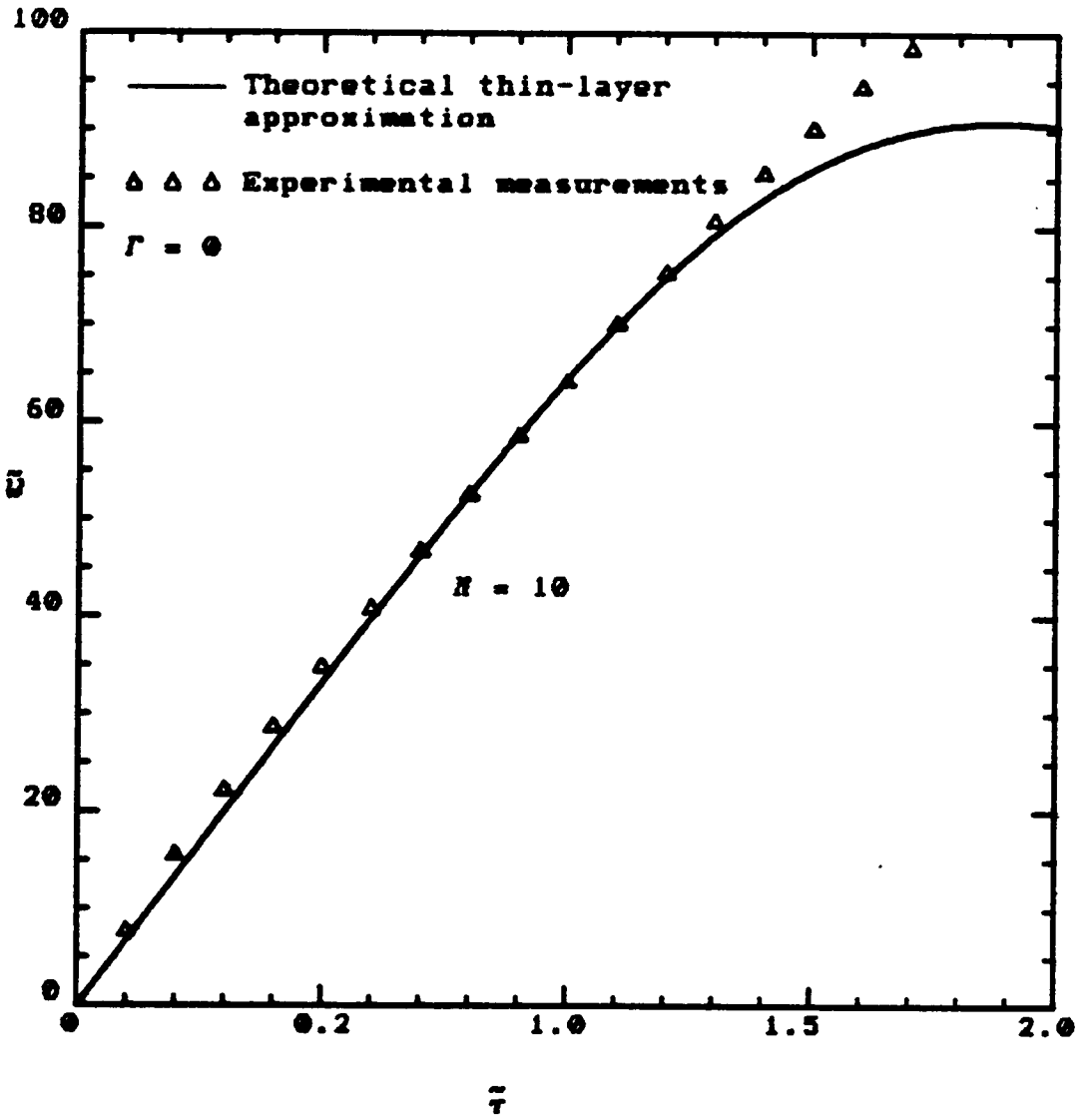

Figure 8.4.2. Normalized energy storage per layer in a 10-layer winding vs. normalized conductor thickness. The measurements were performed on a transformer with windings of sheet copper.

variation of the current density in sheet conductor windings in addition to the assumed radial variation, then the measurements in Figure 8.4.1 would be expected to indicate greater power dissipation than the theoretical results of the one-dimensional model. This is the case, but only up to a certain conductor thickness, above which, the opposite is true. In retrospect, this seemingly contradicting situation may actually be possible if the one-dimensional model is truly inadequate. The only way to confirm this is to solve the two-dimensional problem defined in Section 3.3 and see if the results are in better agreement with the measurements. This topic will not be considered further here; however, the author is presently working on a two-dimensional solution.

In summary, the agreement between the one-dimensional theoretical and the measured normalized power dissipation in sheet conductor windings is marginally acceptable. It does appear to predict a reasonably good optimum thickness, but th corresponding power dissipation is underestimated by a significant percentage. Some of the difference may be attributed to the difficulties associated with low impedance measurements. More likely, though, is the possibility that the one-dimensional model is becoming less valid.

Finally, it is interesting to note from Figure 8.4.2 that the agreement between theory and measurement for the normalized stored energy is very good, much better than for the normalized power dissipation. This situation may still be compatible with the foregoing discussion. It is certainly possible that the energy storage is less susceptible to the inadequacies of the one-dimensional model. Once again, the two-dimensional solution must be derived and studied to find out for sure.

CHAPTER 9

CONCLUSIONS AND FUTURE WORK

A summary of the work in this dissertation is presented in the first section of this chapter, and it follows the developments in the same order. Important conclusions are highlighted in this summary at points where they relate to the subject matter. A design procedure for switched-mode power transformers is outlined at the end of the section.

The second and last section contains a discussion of related topics for future work which the author feels would contribute further to the understanding of phenomena associated with conductor loss in switched-mode power transformers. Most of this work is currently under consideration by the author.

9.1 CONCLUSIONS

It is important to remember that all conclusions are drawn from the analysis of the one-dimensional problem defined in Section 3.4. Some of the more important characteristics of the one-dimensional model are now reviewed.

The cylindrical coordinate system was chosen for the mathematical representation, and axial symmetry assumed for all quantities (no ϕ-dependence). The corresponding geometry and notation for a general transformer winding is given in Figure 3.1.2 and the accompanying discussion. The final assumption, the one which leads directly to the one-dimensional model, is that none of the quantities exhibit longitudinal variation (no z-dependence). This key assumption is based on several possible conditions, each of which contribute to its validity. First, if the length of the winding is long compared to the diameter, then end effects can generally be neglected. To the same end, the presence of high permeability ferrite surrounding the windings also enhances the one-dimensional properties of the fields (see Section 4.1). Finally, most winding types which involve several turns of conductor per layer, all carrying the same total current, inherently support a uniform current distribution in the z-direction. Small local turn-to-turn variations may exist; however, their effect appears

negligible if the conductor size is optimized according to the one-dimensional analysis (see Chapter 8).

The analysis begins with time-harmonic Maxwell's equations in a conducting region (Section 3.2). These equations are simplified immediately by observing that the displacement current is negligible in the applications of interest. Further simplifications occur in Maxwell's equations under the assumptions of the one-dimensional model (Section 3.4). The current density has only a $\hat{\phi}$-component and the magnetic field intensity is $\hat{z}$-directed. Both exhibit variations in the radial coordinate ρ only. As a result, the vector diffusion equations (3.2.18) reduce to the one-dimensional scalar differential equations (3.4.4). The general solutions of these equations are recognized as Kelvin functions, a special class of Bessel functions.

Particular solutions are derived for a single conductor layer in Chapter 4 by applying boundary conditions at the radial boundaries of the conductor layers. These boundary conditions are derived from a simple application of Ampere's law (Section 4.1). The first important conclusions are drawn from the study of these particular solutions. Both the current density and the magnetic field intensity in the nth conductor layer were found to be a function of three parameters: the normalized conductor thickness $\tilde{\tau}_n$, the boundary condition ratio Γ_n, and the normalized mean

radius $\tilde{\rho}_n$. Each of these parameters was studied by observing their effects on the radial distribution of both the current density and the magnetic field intensity (Section 4.2).

For conductor thicknesses which are small compared to a skin depth, the current density increases and approaches a uniform distribution. The corresponding magnetic field intensity varies linearly between its boundary conditions. As the conductor thickness increases, the magnitude of the current concentrates near the radial boundaries, and the phase varies across the layer indicating the presence of circulating currents (the skin effect). Similar behavior is noticed in the magnetic field intensity.

The extent of the concentration at each of the boundaries depends on the boundary condition ratio Γ_n. The current tends to concentrate at the boundary with the highest magnetic field intensity (the proximity effect). For most practical values of the normalized mean radius ($\tilde{\rho}_n \geq 20$), the current and magnetic field distributions displayed no preference to either the inner or outer boundary based on the geometry alone. Consequently, these distributions are approximate mirror images about the center of the conductor for reciprocal values of the boundary condition ratio. In the limit, as the radius of curvature becomes infinite, a flat plate results and the symmetry just

discussed is perfect. On the other hand, if the normalized radius is very small, then the distributions favor slightly the inner boundary. But the mean radius must be reduced to approximately two skin depths to notice this effect, and even then it is not very significant.

The aforementioned studies suggested the possibility of an approximation which would be valid for large values of the normalized mean radius. Indeed, large argument asymptotic approximations exist for Kelvin functions; when substituted into the exact solutions, there results considerable simplification (Section 4.3). A study of these new approximations reveals that they are practically indistinguishable from the exact solutions when the normalized mean radius is greater than 20. Even for the small value of $\tilde{\rho}_m = 2$, the agreement is quite good.

Such encouraging results prompted the developement of a further approximation, the thin-layer approximation (Section 4.4). The essence of this approximation is that the conductor layer thickness is assumed to be much smaller than the mean radius to the center of the layer. This is a good practical assumption for two reasons. First, most practical values for the normalized mean radius are greater than twenty skin depths. Second, effective utilization of the conductor deteriorates for thicknesses significantly greater than one skin depth due to the skin and proximity effects.

Specifically, the thin-layer approximation involves neglecting the ratio $\tilde{\tau}_n/\tilde{\rho}_n$ as compared to unity. Again, there results considerable simplification of the solution. In fact, dependence on the normalized mean radius is completely removed from the solutions just as if the condition $\tilde{\rho}_n \to \infty$ was enforced. A study of the thin-layer approximations reveals very little difference between the two cases $\tilde{\rho}_n \to \infty$ and $\tilde{\rho}_n = 20$.

In an attempt to develop techniques for optimizing the design of transformer windings, the power dissipation and energy storage for a single conductor layer were considered next (Chapter 5). Expressions corresponding to the exact solutions of the current density and magnetic field intensity, along with their large argument asymptotic and thin-layer approximations, were derived and studied.

It was found that, for a given boundary condition ratio and normalized mean radius, the power dissipation experienced a unique minimum value at a particular conductor thickness. This behavior provides the basis for the optimization of the transformer windings for minimum conductor loss. The resulting thickness is referred to as the optimum conductor thickness. The effect of the normalized mean radius on the optimum values was found to be negligible; so that, as before, the thin-layer approximation proved to be adequate under most conditions. The effect of

the boundary condition ratio is quite dramatic, however. As the boundary condition ratio approaches unity, the minimum in the power dissipation becomes much sharper and occurs at a smaller conductor thickness. Also, the magnitude of the minimum power dissipation at the optimum conductor thickness increases significantly.

The behavior of the energy storage was studied in a similar manner, but no further optimization techniques based on it were discovered. The energy stored in the winding portion of a transformer represents flux which is not linked by both the primary and secondary, i.e. leakage flux or energy. This energy increases almost linearly throughout the region of nearly optimum conductor thickness, and then asymptotically approaches a constant value for large thicknesses. Thus, depending on the importance of the leakage energy in the overall design, it may be adjusted either up or down at the expense of an increase in the power dissipation. In most designs the power dissipation is the most important quantity, although it is often helpful to know the leakage energy and its associated inductance.

After discovering that there exists an optimum conductor thickness which yields a minimum power dissipation, an analytical investigation proceeded (Section 5.3). It consisted of taking the derivative of the normalized power

dissipation with respect to the normalized conductor thickness, setting the result equal to zero, and solving for the optimum normalized conductor thickness. This optimum value was then be used to evaluate the corresponding minimum power dissipation. This procedure does not yield practical results for either the exact solution or its large argument asymptotic approximation because of their complexity. Computer implemented algorithms are used to find the optimum solution for these cases. A reasonably simple transcendental equation results from the thin-layer approximation, however. Its solution reveals that the optimum conductor thickness always lies between zero and $\pi/2$ skin depths; this is a very important fundamental result. [1.57]

Because of this rather limited range of optimum conductor thicknesses, another approximation was developed: the two-term series approximation (Section 5.4). Just as the name suggests, this approximation involves the determination of the first two terms of the Laurent expansion (about a conductor thickness of zero) of the power dissipation and the energy storage. The form of this approximation is very simple, and the optimization process yields a closed-form solution. In general, the accuracy of the two-term series approximation is very good up through the near optimum region, but it then diverges rapidly. Consequently, the accuracy of the closed-form expression for

the optimum conductor thickness is very good. The worst-case error occurs for $\Gamma_n = 0$ and is 11.4%. The corresponding error in the minimum power dissipation is only 4.5%. Accuracy improves as the boundary condition ratio increases.

The next step in the analysis was to extend the solution to the case of a multi-layer winding (Chapter 6). Some practical assumptions are introduced at the outset of this analysis. Namely, the layers within a single winding are assumed to be identical in three ways: equal conductor layer thicknesses, equal insulation layer thicknesses, and equal current per unit length in each layer. New expressions were derived (including the exact solutions and all of the previously derived approximations) by summing the results from the individual layers (Sections 6.2 and 6.3). Only the thin-layer and two-term series approximations were studied in detail.

The curves for the normalized power dissipation exhibit the same properties as the single-layer solution. The minima become sharper and increase in magnitude since all but one of the layers in a multi-layer winding has a nonzero boundary condition ratio. A large increase in the energy storage occurs also. Therefore, it is desirable to keep the number of conductor layers in a winding as low as possible. The ideal case is a single layer with zero boundary

condition ratio. The two-term series approximation again yields closed-form solutions to the optimization problem in the multi-layer case (Section 6.4). Most of the foregoing discussion of the behavior of the solutions are directly evident from these solutions. For instance, the optimum conductor thickness is inversely proportional to the square root of the number of layers. The corresponding minimum power dissipation is directly proportional to the same. The energy storage is directly proportional to the square of the number of turns. The accuracy of the two-term series approximation for the multi-layer winding is comparable to the single-layer case. It is perhaps even better in many cases since several of the layers have higher boundary condition ratios.

Two important techniques for reducing further the power dissipation and energy storage are possible. The first technique is to allow the layer thicknesses to be unequal, and then optimize each individual layer separately (Section 6.5). The power dissipation is reduced by approximately 10% for most cases of individual layer optimization. The maximum possible reduction is 12.3% which occurs for a large number of layers and zero boundary condition ratio. The second technique is to split and interleave primary and secondary windings (Section 6.6). This process results in windings with fewer layers and lower magnetic field

intensities at the boundaries, both of which reduce the power dissipation and energy storage. Specifically, the power dissipation is inversely proportional to the square root of the number of equal sections that a winding is split into. Thus, splitting a winding only once into two sections results in a 30% reduction in the power dissipation. The reductions in the energy storage are even more dramatic. The energy storage in the insulation layers is inversely proportional to the square of the number of split sections, and the energy stored in the conducting layers is inversely proportional to the number of split sections to the three-halves power.

The final and most important extension of the theory for switched-mode power transformers is the generalization to arbitrary periodic waveforms (Chapter 7). This generalization is accomplished by incorporating the previously derived results for sinusoidal time-harmonic excitation into a general Fourier analysis. The procedure is straightforward, but the resulting solutions are complicated and unrevealing. Only the two-term series approximation yields a solution whose appearance is physically meaningful. All of the other approximations and the exact solutions must be evaluated on the basis of computed results.

The two-term series approximation yields a very interesting and revealing solution. Through the use of several properties of Fourier analysis (Appendix C), a term is identified in the solution which relates to the bandwidth of the winding current. The power dissipation increases for currents with larger bandwidths. This is not a surprising result, since the higher harmonics would be expected to cause higher losses. Curiously, the energy storage is not affected to the same extent, and it actually decreases slightly as the bandwidth increases.

Unfortunately, the simplicity and insight gained from the two-term series approximation for arbitrary periodic excitation is often overshadowed by its inaccuracy. This approximation becomes less accurate as the bandwidth of the current increases. The reason for this is that the two-term series approximation becomes less valid for the higher harmonic terms, since the resulting normalized conductor thickness increases when evaluated at higher frequencies (skin depth decreases). The overall accuracy depends therefore on the severity of this inaccuracy in relation to the corresponding magnitude of the Fourier coefficients.

Several basic waveform types encountered in switched-mode power converters were studied to determine their influence on winding power dissipation: unidirectional fractional sinusoid, unidirectional

rectangular wave, and unidirectional triangular wave (see Appendix D for definitions of these waveforms). Both the duty cycle and the rise times were varied. The power dissipation caused by a unidirectional fractional sinusoid increases significantly as the duty cycle decreases. The accuracy of the two-term series approximation is reasonably good for this waveform type. Similar behavior is observed for both the unidirectional square and triangular waves; however, the accuracy of the two-term series approximation reduces significantly for practical values of the rise time. In general, the power dissipation increases for shorter rise times, but not to the extent caused by a decrease in the duty cycle. All of these trends are noticed in the stored energy also except that they are much less severe; and where the power dissipation increases, the energy storage decreases slightly.

Finally, when the different waveform types are compared under similar conditions, several interesting conclusions can be drawn. The curves for the power dissipation and energy storage vs. the normalized conductor thickness intersect in several places. Consequently, evaluation is complicated since different waveforms perform better for different ranges of conductor thickness. At the important optimum point, the fractional sinusoid produces the least power dissipation; but it is only slightly less than a pure sinusoid. The next highest power is produced by the

rectangular wave; and the triangular wave is the worst, producing about 60% more loss than the fractional sinusoid. In all cases the power dissipation of a triangular wave is greater than that of a rectangular wave under the same conditions. All of the aforementioned waveform comparisons are made while keeping the rms-value of the waveforms constant.

The optimization problem is also analytically investigated for the case of arbitrary periodic excitation (Section 7.3). Only the two-term series approximation yields a closed-form solution which is physically meaningful. This solution is identical to the corresponding one for sinusoidal excitation except for the addition of the bandwidth factor. The optimum conductor thickness is inversely proportional to the square root of the bandwidth, and the corresponding minimum power dissipation is directly proportional to the same. This is a useful and informative result; however, it should be remembered that it becomes less accurate for large bandwidths. Other more accurate forms of the solution should be used for actual design computations.

Specific applications of the theory to various types of windings are considered in Chapter 8. Several experimental transformers were constructed to evaluate the validity of the theory for each of the winding types considered. First,

the normalized power dissipation and energy storage are related to the effective resistance and leakage inductance of the winding, respectively (Section 8.1). These elements appear in the equivalent circuit of a transformer and are easily measured with modern impedance analyzers.

The model for the most common winding type, layers of round wire conductors, is considered in Section 8.2. The conductor layer thickness for the model is determined by using the actual winding length, and then forcing the cross-sectional areas to be equal. Agreement between the theory and the experimental measurements was very good for this winding type. Some differences occur for large values of the normalized conductor thickness (corresponding to measurements at high frequencies), but it is not advisable to operate there because of the increased loss. Similarly encouraging agreement between theory and experiment was obtained for multifilar round wire windings. Multifilar windings provide a convenient means of increasing the current handling capacity over the case of a single round wire. The same theoretical model is used for multifilar windings as for the single wire case, verifying that the current divides evenly between the paralled strands.

Next, windings of layered litz wire were considered (Section 8.3). Litz wire windings are popular for applications which require a further increase in the current

handling capacity. The theoretical model is based on the ideal assumption that the current divides equally between the individual strands. The strands are then arranged into layers of round wire in order to determine the equivalent number of layers and the conductor layer thickness. Experimental measurements are again in good agreement with the theoretical model, especially in the near optimum regions. The theory, in most cases, seemed to slightly overestimate the actual measurements for both the power dissipation and the energy storage.

The last winding type to be considered, sheet or foil conductors, is the one which is actually modelled the most naturally by the geometry assumed in the theoretical model. Ironically, the agreement between theory and experiment was the worst for this case. The agreement is marginal, in general. In some regions the power dissipation is underestimated, and in others the opposite is true. It has been conjectured by the author that this is due to the inadequacies of the one-dimensional model. In sheet conductors there is nothing physically preventing a gradual longitudinal variation of the current density. In order to determine for sure where the problems lie, the two-dimensional problem defined in Section 3.3 must be solved to see if it yields better accuracy. This is beyond

the scope of this dissertation. However, it is an important topic for future consideration.

Based on the work in this dissertation, a design procedure for switched-mode power transformers has been developed by the author. It is assumed that the number of turns and the current waveforms in each winding have already been determined from external circuit design considerations. Furthermore, it is assumed that a preliminary core and bobbin have been chosen based on the throughput power and other conventional techniques. An outline of the design procedure from this point follows:

(1) Compute the rms-current flowing in each winding.
(2) Compute the skin depth at the fundamental frequency.
(3) Compute the normalized radius of the bobbin. If it is greater than twenty, the thin-layer approximation may be safely used. If it is less than twenty, then either the exact solution or the large argument asymptotic approximation should be considered.
(4) Choose an appropriate winding order based on physical requirements and electrical considerations. It is desirable to keep the magnetic field intensities small, and also to have near zero boundary condition ratios wherever possible.
(5) Determine the boundary condition ratio for each winding.

(6) Based on an initial estimate of one skin depth for the conductor thickness, determine the number of layers required in each winding if using a single round wire.

(7) Use the methods developed in this dissertation to determine the optimum conductor layer thickness for each winding. Use the values determined above for the boundary condition ratio and number of layers.

(8) Check to see if the corresponding optimum wire size results in the same number of layers as predicted in step (6). If not, repeat step (7) using the new value.

(9) Check to see if the optimum wire size is appropriate for the rms-current in the winding. If so, continue to (10). If the wire size is larger than needed, then use simple DC calculations to reduce the size. If the optimum wire size is not large enough to handle the current, then consider multifilar windings. If this is still inadequate, then consider either litz wire or sheet conductor windings. Repeat steps (6) - (8) for these new winding types until an acceptable optimized design is reached for each winding.

(10) Using the results of the optimized designs, compute the power dissipation and energy storage for each winding. If the results are acceptable, then the design is complete. If further reductions are required, then

return to step (4) and try to choose a better winding order. Or consider more sophisticated techniques such as individual layer optimization or split windings.

With a little practice and experience using this design procedure, the iterative procedures can be eliminated. Consequently, an optimized design can be reached very quickly.

The author is hopeful that the efforts of this dissertation will help to provide a thorough understanding of the phenomena associated with conductor loss in switched-mode power transformers. An attempt has been made to keep the treatment general so that it is widely applicable. But at the same time, efforts have been made to derive simple approximations which are physically meaningful and provide insight.

9.2 FUTURE WORK

As is usual the case with research programs, many unexpected topics have emerged. Some have been included in this dissertation. Others have not, either because of the lack of time or because they would logically fit into a new effort with a slightly different emphasis. Those topics which are believed to be important enough for future consideration are now summarized. The author is either

currently involved, or plans to be in the near future, with efforts in all of these areas.

The first group of topics is concerned primarily with improvements on the one-dimensional model used in this dissertation. Although the two-term series approximation yielded a very simple and meaningful solution for the case of arbitrary periodic excitation, its accuracy was disappointing for waveforms with large but typical bandwidths. It would be desirable to find a solution with extended accuracy, but at the same time retaining a level ofsimplicity which would allow physically meaningful interpretations. Another improvement that could be made involves the more complicated solutions which must be evaluated on a computer. For arbitrary periodic excitation, this includes all but the two-term series approximation. The current method for finding the optimum conductor thickness is relatively primitive. More sophisticated numerical techniques could perhaps reduce the computing time significantly.

There are many types of switched-mode converters for which the waveforms in the various windings of the power transformer are either different in shape or shifted in phase. Most of the theory in this dissertation has been kept general enough to handle these situations; however, no studies were made. It would be useful to define and execute

some theoretical and experimental investigations which would demonstrate the effects of these conditions.

Finally, there appears to be room for some improvements in the models for certain types of conductors. The one-dimensional model has proven to be very accurate in describing round wire windings, both single and multifilar. Litz wire has also been successfully modelled under the one-dimensional assumptions. For this case, however, the experimental measurements were consistently slightly below the theoretical predictions. It would be worthwhile to perform another set of experimental measurements designed to confirm these results. If the confirmation is positive, then perhaps further investigation would yield minor modifications in the model which would account for the slight differences. Much more serious differences occurred between the experimental measurements and the theoretical predictions of the one-dimensional model for sheet conductors. Again, it would be wise to construct another transformer and perform another set of experimental measurements designed to either confirm or refute these results. This is particularly important for the case of sheet conductors because of the difficulties experienced in the low impedance measurements. If the results of the previous measurements are confirmed, then a solution of the two-dimensional problem is probably necessary so that

longitudinal variations in the current density can be accounted for. Care should be taken to clearly define when it is necessary to use this more complicated solution.

APPENDIX A

NOMENCLATURE

The nomenclature used in this dissertation is summarized in this appendix. It is provided as a convenience to the reader. Where possible, the applicable ANSI/IEEE standards [51, 52, 53, 54] have been adhered to concerning units and letter symbols. The International System of Units (abbreviated SI) is used. The quantities, along with their SI units and symbols, are listed in Table A.1. They are listed in approximately the same order as their first appearance in this dissertation.

Table A.1. Letter symbols and SI units for quantities used in this dissertation.

Quantity	SI Units	Symbol
cylindrical coordinate system - radial coordinate	m	ρ
cylindrical coordinate system - angular coordinate	rad	ϕ
cylindrical coordinate system - longitudinal coordinate	m	z
length of winding in axial direction	m	l
index indicating the nth layer	–	n
number of layers in a winding	–	N
inner radius of nth conductor layer	m	ρ_n^i
outer radius of nth conductor layer	m	ρ_n^o
magnetic field intensity at outer boundary of the nth conductor layer	A/m	H_n
permeability	H/m	μ
permeability of vacuum	H/m	μ_o
relative permeability	–	μ_r
conductivity	S	σ
permittivity	F/m	ε
permittivity of vacuum	F/m	ε_o
relative permittivity	–	ε_r
angular frequency	rad/s	ω
electric flux density	C/m^2	D

Table A.1. Letter symbols and SI units for quantities used in this dissertation, continued.

Quantity	SI Units	Symbol
electric field intensity	V/m	$\mathbf{E}$
magnetic flux density	T	$\mathbf{B}$
magnetic field intensity	A/m	$\mathbf{H}$
current density	A/m^2	$\mathbf{J}$
frequency	s^{-1}	f
poynting vector	W/m^2	$\mathbf{S}$
magnetic energy density	J/m^3	w_m
dissipated power density	W/m^3	p_d
magnetic energy	J	W_m
dissipated power	W	P_d
skin depth	m	δ
unit vector in the radial direction	–	$\hat{\rho}$
unit vector in the angular direction	–	$\hat{\phi}$
unit vector in the longitudinal direction	–	$\hat{z}$
axial component of two-dimensional current density	A/m^2	$J_\phi(\rho,z)$
radial component of two-dimensional magnetic field intensity	A/m	$H_\rho(\rho,z)$

Table A.1. Letter symbols and SI units for quantities used in this dissertation, continued.

Quantity	SI Units	Symbol
longitudinal component of two-dimensional magnetic field intensity	A/m	$H_z(\rho,z)$
axial component of one-dimensional current density	A/m^2	$J_\phi(\rho)$
longitudinal component of one-dimensional magnetic field intensity	A/m	$H_z(\rho)$
transformation of radial coordinate	–	x
Kelvin function - first kind, order v	–	$ber_v x$
Kelvin function - first kind, order v	–	$bei_v x$
Kelvin function - second kind,order v	–	$ker_v x$
Kelvin function - second kind,order v	–	$kei_v x$
arbitrary constants	–	A_0, B_0 A_1, B_1
magnetic field intensity in ferrite	A/m	H_f
total current in nth conductor layer	A	I_n
current per unit axial length in the nth conductor layer	A/m	K_n
axial component of current density in nth conductor layer	A/m^2	$J_{\phi n}$
longitudinal component of magnetic field in nth conductor layer	A/m	H_{zn}

Table A.1. Letter symbols and SI units for quantities used in this dissertation, continued.

Quantity	SI Units	Symbol
thickness of the nth conductor layer	m	τ_n
mean radius of nth conductor layer	m	ρ_n
arbitrary constants for the nth conductor layer	—	A_{0n}, B_{0n} A_{1n}, B_{1n}
normalized radial coordinate	—	$\tilde{\rho}$
normalized axial component of current density in the nth conductor layer	—	$\tilde{J}_{\phi n}$
normalized longitudinal component of magnetic field in nth conductor layer	—	$\tilde{H}_{zn}$
normalized arbitrary constants for nth conductor layer	—	$\tilde{A}_{0n}, \tilde{B}_{0n}$ $\tilde{A}_{1n}, \tilde{B}_{1n}$
boundary condition ratio for the nth conductor layer	—	Γ_n
normalized inner radius of nth conductor layer	—	$\tilde{\rho}_n^{i}$
normalized outer radius of nth conductor layer	—	$\tilde{\rho}_n^{o}$
normalized mean radius of nth conductor layer	—	$\tilde{\rho}_n$

Table A.1. Letter symbols and SI units for quantities used in this dissertation, continued.

Quantity	SI Units	Symbol
normalized conductor thickness of the nth layer	–	$\tilde{\tau}_n$
power dissipated in the nth conductor layer	W	P_n
normalized power dissipated in the nth conductor layer	–	$\tilde{P}_n$
energy stored in the nth conductor layer	J	W_n
normalized energy stored in the nth conductor layer	–	$\tilde{W}_n$
optimum conductor thickness for the nth layer	m	τ_n^{opt}
optimum normalized conductor thickness for the nth layer	–	$\tilde{\tau}_n^{opt}$
minimum power dissipation in the nth conductor layer	W	P_n^{min}
minimum normalized power dissipation in the nth conductor layer	–	$\tilde{P}_n^{min}$
conductor thickness in a winding with equal layer thicknesses	m	τ
normalized conductor thickness in a winding with equal layer thicknesses	–	$\tilde{\tau}$

Table A.1. Letter symbols and SI units for quantities used in this dissertation, continued.

Quantity	SI Units	Symbol
current per unit axial length in a winding with equal layer thicknesses	A/m	K
insulation thickness in a winding with equal layer thicknesses	m	d
normalized insulation thickness in a winding with equal layer thicknesses	—	$\tilde{d}$
insulation thickness of nth layer	m	d_n
normalized insulation thickness of the nth layer	—	$\tilde{d}_n$
winding boundary condition ratio	—	Γ
power dissipated per layer in an N-layer winding	W	P
normalized power dissipated per layer in an N-layer winding	—	$\tilde{P}$
mean radius of an N-layer winding	—	ρ_w
normalized mean radius of an N-layer winding	—	$\tilde{\rho}_w$
energy stored in the nth insulation layer	J	W_n^i
normalized energy stored in the nth insulation layer	—	$\tilde{W}_n^i$
energy stored in an N-layer winding	J	W

Table A.1. Letter symbols and SI units for quantities used in this dissertation, continued.

Quantity	SI Units	Symbol
normalized energy stored in an N-layer winding	–	$\tilde{W}$
optimum conductor thickness for a winding with equal layer thicknesses	m	τ^{opt}
optimum normalized conductor thickness for a winding with equal layer thicknesses	–	$\tilde{\tau}^{opt}$
minimum power dissipated per layer in an N-layer winding	W	P^{min}
minimum normalized power dissipated per layer in an N-layer winding	–	$\tilde{P}^{min}$
index indicating the kth harmonic	–	k
current per unit axial length at the kth harmonic	A/m	K_k
normalized mean radius of the nth conductor layer at the kth harmonic	–	$\tilde{\rho}_{nk}$
normalized mean radius of an N-layer winding at the kth harmonic	–	$\tilde{\rho}_{wk}$
skin depth at the kth harmonic	m	δ_k
normalized conductor thickness in a winding with equal layer thicknesses at the kth harmonic	–	$\tilde{\tau}_k$
normalized conductor thickness in the nth layer at the kth harmonic	–	$\tilde{\tau}_{nk}$

Table A.1. Letter symbols and SI units for quantities used in this dissertation, continued.

Quantity	SI Units	Symbol
normalized insulation thickness in a winding with equal layer thicknesses at the kth harmonic	–	$\tilde{d}_k$
normalized insulation thickness in the nth layer at the kth harmonic	–	$\tilde{d}_{nk}$
power dissipated in the nth conductor layer at the kth harmonic	W	P_{nk}
power dissipated per layer in an N-layer winding at the kth harmonic	W	P_k
normalized power dissipated in the nth conductor layer at the kth harmonic	–	$\tilde{P}_{nk}$
normalized power dissipated per layer in an N-layer winding at the kth harmonic	–	$\tilde{P}_k$
fundamental frequency	Hz	f_0
fundamental angular frequency	rad/s	ω_0
period	s	T
normalized power bandwidth	–	β
energy stored in the nth conductor layer at the kth harmonic	J	W_{nk}
energy stored per conductor layer in an N-layer winding at kth harmonic	J	W_k

Table A.1. Letter symbols and SI units for quantities used in this dissertation, continued.

Quantity	SI Units	Symbol
normalized energy stored in the nth conductor layer at the kth harmonic	–	$\tilde{W}_{nk}$
normalized energy stored per conductor layer in an N-layer winding at the kth harmonic	–	$\tilde{W}_{k}$
energy stored in the nth insulation layer at the kth harmonic	J	W^{i}_{nk}
energy stored per insulation layer in an N-layer winding at kth harmonic	J	W^{i}_{k}
normalized energy stored in the nth insulation layer at the kth harmonic	–	$\tilde{W}^{i}_{nk}$
normalized energy stored per insulation layer in an N-layer winding at the kth harmonic	–	$\tilde{W}^{i}_{k}$
effective resistance of a winding	Ω	R_{eff}
AC resistance of a winding	Ω	R_{ac}
DC resistance of a winding	Ω	R_{dc}
number of turns per layer	–	N_{l}
effective leakage inductance of a winding	H	L_{eff}

Table A.1. Letter symbols and SI units for quantities used in this dissertation, continued.

Quantity	SI Units	Symbol
AC leakage inductance of a winding	H	L_{ac}
effective impedance of a winding	Ω	Z_{eff}
wire diameter	m	d_w
number of strands in litz wire	–	N_s
diameter of strands in litz wire	m	d_s
time	s	t
Fourier coefficients - complex	–	c_k
Fourier coefficients - cosine	–	a_k
Fourier coefficients - sine	–	b_k
Fourier coefficients - amplitude	–	A_k
Fourier coefficients - phase	–	ϕ_k
$f(t)$ - average value	–	f_{av}
$f(t)$ - root-mean-square value	–	f_{rms}
$f'(t)$ - average value	–	f'_{av}
$f'(t)$ - root-mean-square value	–	f'_{rms}
Fourier transform of $f(t)$	–	$F(\omega)$
$f(t)$ on the interval $[0, T]$	–	$f_T(t)$
$f'(t)$ on the interval $[0, T]$	–	$f'_T(t)$

Table A.1. Letter symbols and SI units for quantities used in this dissertation, continued.

Quantity	SI Units	Symbol
Fourier transform of $f_T(t)$	–	$F_T(\omega)$
Fourier transform of $f'_T(t)$	–	$F'_T(\omega)$
Dirac delta or unit impulse function	–	$\delta(x)$
normalized power bandwidth	–	β
normalized variance of the power spectrum	–	σ_ω^2
duty cycle of waveform pulse	–	D
duty cycle of rise time	–	D_r
time at mth sample point of $f(t)$	s	t_m
value of $f(t)$ at t_m	–	f_m
index indicating mth time interval	–	m
number of time intervals on $[0, T]$	–	M
$f(t)$ on the mth interval $[t_{m-1}, t_m]$	–	$f_m(t)$
unit step function	–	$u(x)$
sampling function	–	$Sa(x)$
duty cycle of mth time interval	–	D_m
time duration of waveform pulse	s	t_d
time duration of rise time	s	t_r
amplitude of waveform	–	A

APPENDIX B

KELVIN FUNCTIONS

Kelvin functions are named in honor of Professor William Thomson (later Lord Kelvin). They are also sometimes referred to as Thomson functions. Several properties of these functions which are used throughout this dissertation are summarized in this appendix for convenience. All of this information has been taken from the readily available references [55] and [56] of which the former is recommended for more detail. Watson's treatise [57] may also be useful, although it is noticeably incomplete with respect to Kelvin functions.

B.1 DEFINITIONS

The logical starting point in defining Kelvin functions is the well-known differential equation due to Bessel,

$$z^2\frac{d^2f}{dz^2} + z\frac{df}{dz} + (z^2 - \nu^2)f = 0, \qquad \text{(B.1.1)}$$

in which the independent variable z and the order ν are both, in general, complex. The most common general solutions of this equation are the Bessel functions of the first and second kind, $J_\nu(z)$ and $Y_\nu(z)$; and the Hankel functions of the first and second kind, $H_\nu^{(1)}(z)$ and $H_\nu^{(2)}(z)$. In many applications the argument is purely imaginary, and for these the modified Bessel functions of the first and second kind, $I_\nu(z)$ and $K_\nu(z)$, have been defined. Similarly, there are many applications in which the phase of the argument turns out to be $\pi/4$ and $\pi/2$ multiples thereof. It is for applications such as these that the special class of Bessel functions known as Kelvin functions have been defined.

The form of Bessel's differential equation leading to solutions of Kelvin functions, Kelvin's differential equation, is given by

$$x^2\frac{d^2f}{dx^2} + x\frac{df}{dx} - (jx^2 + \nu^2)f = 0, \qquad \text{(B.1.2)}$$

where the independent variable x and the order υ are now both real. The general solutions are

$$f_1(x) = \mathrm{ber}_\upsilon x + j\,\mathrm{bei}_\upsilon x \qquad \text{(B.1.3a)}$$

$$f_2(x) = \mathrm{ker}_\upsilon x + j\,\mathrm{kei}_\upsilon x \qquad \text{(B.1.3b)}$$

in which the functions $\mathrm{ber}_\upsilon x$ and $\mathrm{bei}_\upsilon x$ are collectively referred to as Kelvin functions of the first kind, and $\mathrm{ker}_\upsilon x$ and $\mathrm{kei}_\upsilon x$ as Kelvin functions of the second kind. Note that these solutions are divided into their real and imaginary parts so that the Kelvin functions themselves are real. The following relations complete the definition of the Kelvin functions:

$$\begin{aligned}\mathrm{ber}_\upsilon x + j\,\mathrm{bei}_\upsilon x &\doteq J_\upsilon(xe^{j3\pi/4}) \\ &= e^{j\upsilon\pi/2} I_\upsilon(xe^{j\pi/4}) \qquad \text{(B.1.4a)}\end{aligned}$$

$$\begin{aligned}\mathrm{ker}_\upsilon x + j\,\mathrm{kei}_\upsilon x &\doteq j\tfrac{\pi}{2} H_\upsilon^{(1)}(xe^{j3\pi/4}) \\ &= e^{-j\upsilon\pi/2} K_\upsilon(xe^{j\pi/4}). \qquad \text{(B.1.4b)}\end{aligned}$$

The functions $\mathrm{ber}_\upsilon x$ and $\mathrm{bei}_\upsilon x$ are bounded as $x \to 0$ and unbounded as $x \to \infty$. In contrast, the functions $\mathrm{ker}_\upsilon x$ and $\mathrm{kei}_\upsilon x$ are unbounded as $x \to 0$ and bounded as $x \to \infty$. Only Kelvin functions of integer order, namely, the zero and

first orders are encountered in this dissertation. Plots of these functions along with their large argument asymptotic approximations are given in Figures B.4.1 through B.4.4. Further discussion of these plots is delayed until Section B.4 on large argument asymptotic approximations.

B.2 RECURRENCE RELATIONS

For the purposes of this section and the next, let f_ν and g_ν be any of the following pairs of Kelvin functions:

$$f_\nu = \mathrm{ber}_\nu x, \quad g_\nu = \mathrm{bei}_\nu x \tag{B.2.1a}$$

$$f_\nu = \mathrm{ker}_\nu x, \quad g_\nu = \mathrm{kei}_\nu x \tag{B.2.1b}$$

$$f_\nu = \mathrm{bei}_\nu x, \quad g_\nu = -\,\mathrm{ber}_\nu x \tag{B.2.1c}$$

$$f_\nu = \mathrm{kei}_\nu x, \quad g_\nu = -\,\mathrm{ker}_\nu x. \tag{B.2.1d}$$

Each of these four pairs satisfy the recurrence relations

$$f_{\nu+1} + f_{\nu-1} = -\frac{\nu\sqrt{2}}{x}(f_\nu - g_\nu) \tag{B.2.2a}$$

$$f'_\nu = \frac{1}{2\sqrt{2}}(f_{\nu+1} + g_{\nu+1} - f_{\nu-1} - g_{\nu-1}) \tag{B.2.2b}$$

$$f'_\nu - \frac{\nu}{x} f_\nu = \frac{1}{\sqrt{2}}(f_{\nu+1} + g_{\nu+1}) \qquad \text{(B.2.2c)}$$

$$f'_\nu + \frac{\nu}{x} f_\nu = -\frac{1}{\sqrt{2}}(f_{\nu-1} + g_{\nu-1}) \qquad \text{(B.2.2d)}$$

where the prime denotes derivative with respect to x.

Special cases of these recurrence relations involving only Kelvin functions of zero and first order are given by

$$\text{ber}'_0 x = \frac{1}{\sqrt{2}}(\text{ber}_1 x + \text{bei}_1 x) \qquad \text{(B.2.3a)}$$

$$\text{bei}'_0 x = \frac{1}{\sqrt{2}}(\text{bei}_1 x - \text{ber}_1 x) \qquad \text{(B.2.3b)}$$

$$\text{ker}'_0 x = \frac{1}{\sqrt{2}}(\text{ker}_1 x + \text{kei}_1 x) \qquad \text{(B.2.3c)}$$

$$\text{kei}'_0 x = \frac{1}{\sqrt{2}}(\text{kei}_1 x - \text{ker}_1 x) \qquad \text{(B.2.3d)}$$

$$\text{ber}'_1 x = -\frac{1}{x}\text{ber}_1 x - \frac{1}{\sqrt{2}}(\text{ber}_0 x + \text{bei}_0 x) \qquad \text{(B.2.4a)}$$

$$\text{bei}'_1 x = -\frac{1}{x}\text{bei}_1 x - \frac{1}{\sqrt{2}}(\text{bei}_0 x - \text{ber}_0 x) \qquad \text{(B.2.4b)}$$

$$\text{ker}'_1 x = -\frac{1}{x}\text{ker}_1 x - \frac{1}{\sqrt{2}}(\text{ker}_0 x + \text{kei}_0 x) \qquad \text{(B.2.4c)}$$

$$\text{kei}'_1 x = -\frac{1}{x}\text{kei}_1 x - \frac{1}{\sqrt{2}}(\text{kei}_0 x - \text{ker}_0 x). \qquad \text{(B.2.4d)}$$

Finally, for the special case when the order ν is an integer n, the following relations for negative order are satisfied:

$$\mathrm{ber}_{-n}x = (-1)^n \mathrm{ber}_n x \qquad \text{(B.2.5a)}$$

$$\mathrm{bei}_{-n}x = (-1)^n \mathrm{bei}_n x \qquad \text{(B.2.5b)}$$

$$\mathrm{ker}_{-n}x = (-1)^n \mathrm{ker}_n x \qquad \text{(B.2.5c)}$$

$$\mathrm{kei}_{-n}x = (-1)^n \mathrm{kei}_n x. \qquad \text{(B.2.5d)}$$

B.3 INDEFINITE INTEGRALS

Several indefinite integrals of various combinations of Kelvin functions are summarized below. Let f_ν, g_ν be any one of the pairs of Kelvin functions given by equations (B.2.1), and let $\bar{f}_\nu$, $\bar{g}_\nu$ be either the same pair or any other pair. Then

$$\int x^{1+\nu} f_\nu dx = \frac{x^{1+\nu}}{\sqrt{2}}(g_{\nu+1} - f_{\nu+1}) = x^{1+\nu}(g'_\nu - \frac{\nu}{x} g_\nu) \qquad \text{(B.3.1a)}$$

$$\int x^{1-\nu} f_\nu dx = \frac{x^{1-\nu}}{\sqrt{2}}(f_{\nu-1} - g_{\nu-1}) = x^{1-\nu}(g'_\nu + \frac{\nu}{x} g_\nu) \qquad \text{(B.3.1b)}$$

$$\int x f_\nu g_\nu dx = \frac{1}{4}x^2(2 f_\nu g_\nu - f_{\nu-1} g_{\nu+1} - f_{\nu+1} g_{\nu-1}) \qquad \text{(B.3.1c)}$$

$$\int x(f_\nu^2 + g_\nu^2)dx = x(f_\nu g_\nu' - f_\nu' g_\nu)$$

$$= \frac{1}{\sqrt{2}}x(f_\nu g_{\nu+1} - f_\nu f_{\nu+1} - g_\nu f_{\nu+1} - g_\nu g_{\nu+1})$$

$$= \frac{1}{\sqrt{2}}x(-f_\nu g_{\nu-1} + f_\nu f_{\nu-1} + g_\nu f_{\nu-1} + g_\nu g_{\nu-1}) \quad \text{(B.3.1d)}$$

$$\int x(f_\nu^2 - g_\nu^2)dx = \frac{1}{2}x^2(f_\nu^2 - f_{\nu-1}f_{\nu+1} - g_\nu^2 + g_{\nu-1}g_{\nu+1}) \quad \text{(B.3.1e)}$$

$$\int x(f_\nu \bar{g}_\nu + g_\nu \bar{f}_\nu)dx = \frac{1}{4}x^2(2f_\nu \bar{g}_\nu - f_{\nu-1}\bar{g}_{\nu+1}$$

$$- f_{\nu+1}\bar{g}_{\nu-1} + g_\nu \bar{f}_\nu - g_{\nu-1}\bar{f}_{\nu+1} - g_{\nu+1}\bar{f}_{\nu-1}) \quad \text{(B.3.1f)}$$

$$\int x(f_\nu \bar{g}_\nu - g_\nu \bar{f}_\nu)dx = \frac{1}{2}x(f_\nu' \bar{f}_\nu - f_\nu \bar{f}_\nu' + g_\nu' \bar{g}_\nu - g_\nu \bar{g}_\nu')$$

$$= \frac{1}{2\sqrt{2}}x\Big\{\bar{f}_\nu(f_{\nu+1} + g_{\nu+1}) - \bar{g}_\nu(f_{\nu+1} - g_{\nu+1})$$

$$- f_\nu(\bar{f}_{\nu+1} + \bar{g}_{\nu+1}) + g_\nu(\bar{f}_{\nu+1} - \bar{g}_{\nu+1})\Big\}$$

$$= \frac{1}{2\sqrt{2}}x\Big\{f_\nu(\bar{f}_{\nu-1} + \bar{g}_{\nu-1}) - g_\nu(\bar{f}_{\nu-1} - \bar{g}_{\nu-1})$$

$$- \bar{f}_\nu(f_{\nu-1} + g_{\nu-1}) + \bar{g}_\nu(f_{\nu-1} - g_{\nu-1})\Big\}. \quad \text{(B.3.1g)}$$

Two of these integrals, (B.3.1d) and (B.3.1g), are used extensively in this dissertation for the determination of the power dissipated and energy stored in winding conductor layers. Special cases of (B.3.1d) which apply are given by

$$\int x(\mathrm{ber}_0^2 x + \mathrm{bei}_0^2 x)dx = \frac{1}{\sqrt{2}}x(\mathrm{ber}_0 x\,\mathrm{bei}_1 x - \mathrm{ber}_0 x\,\mathrm{ber}_1 x$$

$$- \mathrm{bei}_0 x\,\mathrm{ber}_1 x - \mathrm{bei}_0 x\,\mathrm{bei}_1 x) \quad \text{(B.3.2a)}$$

$$\int x(\mathrm{ker}_0^2 x + \mathrm{kei}_0^2 x)dx = \frac{1}{\sqrt{2}}x(\mathrm{ker}_0 x\mathrm{kei}_1 x - \mathrm{ker}_0 x\mathrm{ker}_1 x - \mathrm{kei}_0 x\mathrm{ker}_1 x - \mathrm{kei}_0 x\mathrm{kei}_1 x) \quad \text{(B.3.2b)}$$

$$\int x(\mathrm{ber}_1^2 x + \mathrm{bei}_1^2 x)dx = \frac{1}{\sqrt{2}}x(-\mathrm{ber}_1 x\mathrm{bei}_0 x + \mathrm{ber}_1 x\mathrm{ber}_0 x + \mathrm{bei}_1 x\mathrm{ber}_0 x + \mathrm{bei}_1 x\mathrm{bei}_0 x) \quad \text{(B.3.2c)}$$

$$\int x(\mathrm{ker}_1^2 x + \mathrm{kei}_1^2 x)dx = \frac{1}{\sqrt{2}}x(-\mathrm{ker}_1 x\mathrm{kei}_0 x + \mathrm{ker}_1 x\mathrm{ker}_0 x + \mathrm{kei}_1 x\mathrm{ker}_0 x + \mathrm{kei}_1 x\mathrm{kei}_0 x), \quad \text{(B.3.2d)}$$

and special cases of (B.3.1g) which apply are given by

$$\int x(\mathrm{bei}_0 x\mathrm{kei}_0 x + \mathrm{ber}_0 x\mathrm{ker}_0 x)dx = \frac{1}{2\sqrt{2}}x\{\mathrm{ker}_0 x(\mathrm{bei}_1 x - \mathrm{ber}_1 x) - \mathrm{kei}_0 x(\mathrm{bei}_1 x + \mathrm{ber}_1 x) - \mathrm{bei}_0 x(\mathrm{ker}_1 x + \mathrm{kei}_1 x) - \mathrm{ber}_0 x(\mathrm{ker}_1 x - \mathrm{kei}_1 x)\} \quad \text{(B.3.3a)}$$

$$\int x(\mathrm{ker}_0 x\mathrm{bei}_0 x - \mathrm{kei}_0 x\mathrm{ber}_0 x)dx = \frac{1}{2\sqrt{2}}x\{\mathrm{ber}_0 x(\mathrm{ker}_1 x + \mathrm{kei}_1 x) - \mathrm{bei}_0 x(\mathrm{ker}_1 x - \mathrm{kei}_1 x) - \mathrm{ker}_0 x(\mathrm{ber}_1 x + \mathrm{bei}_1 x) + \mathrm{kei}_0 x(\mathrm{ber}_1 x - \mathrm{bei}_1 x)\} \quad \text{(B.3.3b)}$$

$$\int x(\mathrm{bei}_1 x\mathrm{kei}_1 x + \mathrm{ber}_1 x\mathrm{ker}_1 x)dx = \frac{1}{2\sqrt{2}}x\{\mathrm{bei}_1 x(\mathrm{ker}_0 x + \mathrm{kei}_0 x) + \mathrm{ber}_1 x(\mathrm{ker}_0 x - \mathrm{kei}_0 x) - \mathrm{ker}_1 x(\mathrm{bei}_0 x - \mathrm{ber}_0 x) + \mathrm{kei}_1 x(\mathrm{bei}_0 x + \mathrm{ber}_0 x)\} \quad \text{(B.3.3c)}$$

$$\int x(\mathrm{ker}_1 x\,\mathrm{bei}_1 x - \mathrm{kei}_1 x\,\mathrm{ber}_1 x)dx$$

$$= \frac{1}{2\sqrt{2}}x\Big\{\mathrm{ker}_1 x(\mathrm{ber}_0 x + \mathrm{bei}_0 x) - \mathrm{kei}_1 x(\mathrm{ber}_0 x - \mathrm{bei}_0 x)$$

$$- \mathrm{ber}_1 x(\mathrm{ker}_0 x + \mathrm{kei}_0 x) + \mathrm{bei}_1 x(\mathrm{ker}_0 x - \mathrm{kei}_0 x)\Big\}. \quad \text{(B.3.3d)}$$

B.4 LARGE ARGUMENT ASYMPTOTIC APPROXIMATIONS

Much more elaborate asymptotic approximations than shown here are given in [55]. If desired, accuracy can be improved by including additional terms given in those expressions. For the purposes of this dissertation, it will be seen that the argument x is sufficiently large so that only the dominant term of the approximation is needed to provide results which are quite accurate. In practice, if accuracy needs to be increased, the author has found that it is practical to use the more accurate polynomial approximations in [55] rather than including additional terms of the asymptotic approximations.

For the general order ν, the dominant term of the large argument asymptotic approximation of each of the Kelvin functions is given by

$$\mathrm{ber}_\nu x \sim \sqrt{\frac{1}{2\pi x}}\, e^{x/\sqrt{2}} \cos\left[\frac{x}{\sqrt{2}} + \frac{\pi}{2}\nu - \frac{\pi}{8}\right] \quad \text{(B.4.1a)}$$

$$\mathrm{bei}_\nu x \sim \sqrt{\frac{1}{2\pi x}}\, e^{x/\sqrt{2}} \sin\left[\frac{x}{\sqrt{2}} + \frac{\pi}{2}\nu - \frac{\pi}{8}\right] \quad \text{(B.4.1b)}$$

$$\ker_\nu x \sim \sqrt{\frac{\pi}{2x}}\, e^{-x/\sqrt{2}} \cos\left[\frac{x}{\sqrt{2}} + \frac{\pi}{2}\nu + \frac{\pi}{8}\right] \qquad \text{(B.4.1c)}$$

$$\mathrm{kei}_\nu x \sim -\sqrt{\frac{\pi}{2x}}\, e^{-x/\sqrt{2}} \sin\left[\frac{x}{\sqrt{2}} + \frac{\pi}{2}\nu + \frac{\pi}{8}\right]. \qquad \text{(B.4.1d)}$$

Examination of these expressions reveals that, asymptotically, Kelvin functions of the first kind are exponentially increasing sinusoids while those of the second kind are exponentially decreasing sinusoids. Also evident is the fact that the real and imaginary parts are in phase quadrature.

Special cases of the large argument asymptotic approximations for orders zero and one are summarized below:

$$\mathrm{ber}_0 x \sim \sqrt{\frac{1}{2\pi x}}\, e^{x/\sqrt{2}} \cos\left[\frac{x}{\sqrt{2}} - \frac{\pi}{8}\right] \qquad \text{(B.4.2a)}$$

$$\mathrm{bei}_0 x \sim \sqrt{\frac{1}{2\pi x}}\, e^{x/\sqrt{2}} \sin\left[\frac{x}{\sqrt{2}} - \frac{\pi}{8}\right] \qquad \text{(B.4.2b)}$$

$$\ker_0 x \sim \sqrt{\frac{\pi}{2x}}\, e^{-x/\sqrt{2}} \cos\left[\frac{x}{\sqrt{2}} + \frac{\pi}{8}\right] \qquad \text{(B.4.2c)}$$

$$\mathrm{kei}_0 x \sim -\sqrt{\frac{\pi}{2x}}\, e^{-x/\sqrt{2}} \sin\left[\frac{x}{\sqrt{2}} + \frac{\pi}{8}\right] \qquad \text{(B.4.2d)}$$

and

$$\mathrm{ber}_1 x \sim \sqrt{\frac{1}{2\pi x}}\, e^{x/\sqrt{2}} \cos\left[\frac{x}{\sqrt{2}} + \frac{3\pi}{8}\right] \qquad \text{(B.4.3a)}$$

$$\mathrm{bei}_1 x \sim \sqrt{\frac{1}{2\pi x}}\, e^{x/\sqrt{2}} \sin\left[\frac{x}{\sqrt{2}} + \frac{3\pi}{8}\right] \qquad \text{(B.4.3b)}$$

$$\mathrm{ker}_1 x \sim \sqrt{\frac{\pi}{2x}}\, e^{-x/\sqrt{2}} \cos\left[\frac{x}{\sqrt{2}} + \frac{5\pi}{8}\right] \qquad \text{(B.4.3c)}$$

$$\mathrm{kei}_1 x \sim -\sqrt{\frac{\pi}{2x}}\, e^{-x/\sqrt{2}} \sin\left[\frac{x}{\sqrt{2}} + \frac{5\pi}{8}\right]. \qquad \text{(B.4.3d)}$$

Plots of the Kelvin functions for orders zero and one are presented in Figures B.4.1 through B.4.4. The solid curves were obtained using the polynomial approximations in [55] whose accuracy is better than 0.0001%. Throughout this dissertation results using these formulas are considered to be exact. The dashed curves represent the corresponding large argument asymptotic approximations in equations (B.4.2) and (B.4.3). It was indicated in Sections 4.2 and 4.3 that a practical lower limit for the argument x in present power conversion technology is about 28. This figure corresponds to a minimum frequency of 20 KHz and a minimum winding radius of 9.4 mm ($\approx$3/8 in). The curves presented here do not extend beyond $x = 8$ mainly because of

the resulting loss of resolution. Even so, the excellent accuracy of the large argument asymptotic approximation is evident in this range, and it improves further as x increases. Table B.4.1 provides some supplemental accuracy figures which are difficult to infer from the curves. They were obtained from numerical data and are based on an examination of the envelopes of the exponentially increasing and decreasing sinusoids which these functions approximate. From these figures it is seen that the worst-case accuracy can be expected to be better than 2%. Present trends in the power conversion industry indicate higher frequencies for the future. As a consequence, sizes will decrease in an offsetting manner leaving the accuracy of the large argument asymptotic approximation at roughly the same level. Finally, note that the accuracy of the zero order approximations is somewhat better than those for the first order functions. Thus, one would expect more accurate results for the magnetic field intensity and stored enery than for the current density and power dissipation.

Table B.4.1. Minimum values of argument x for zero and first order Kelvin functions corresponding to a given accuracy level expressed as a percentage error.

Accuracy Level	Zero Order	First Order
5%	3.5	11.0
2%	8.5	25.0
1%	18.5	50.0

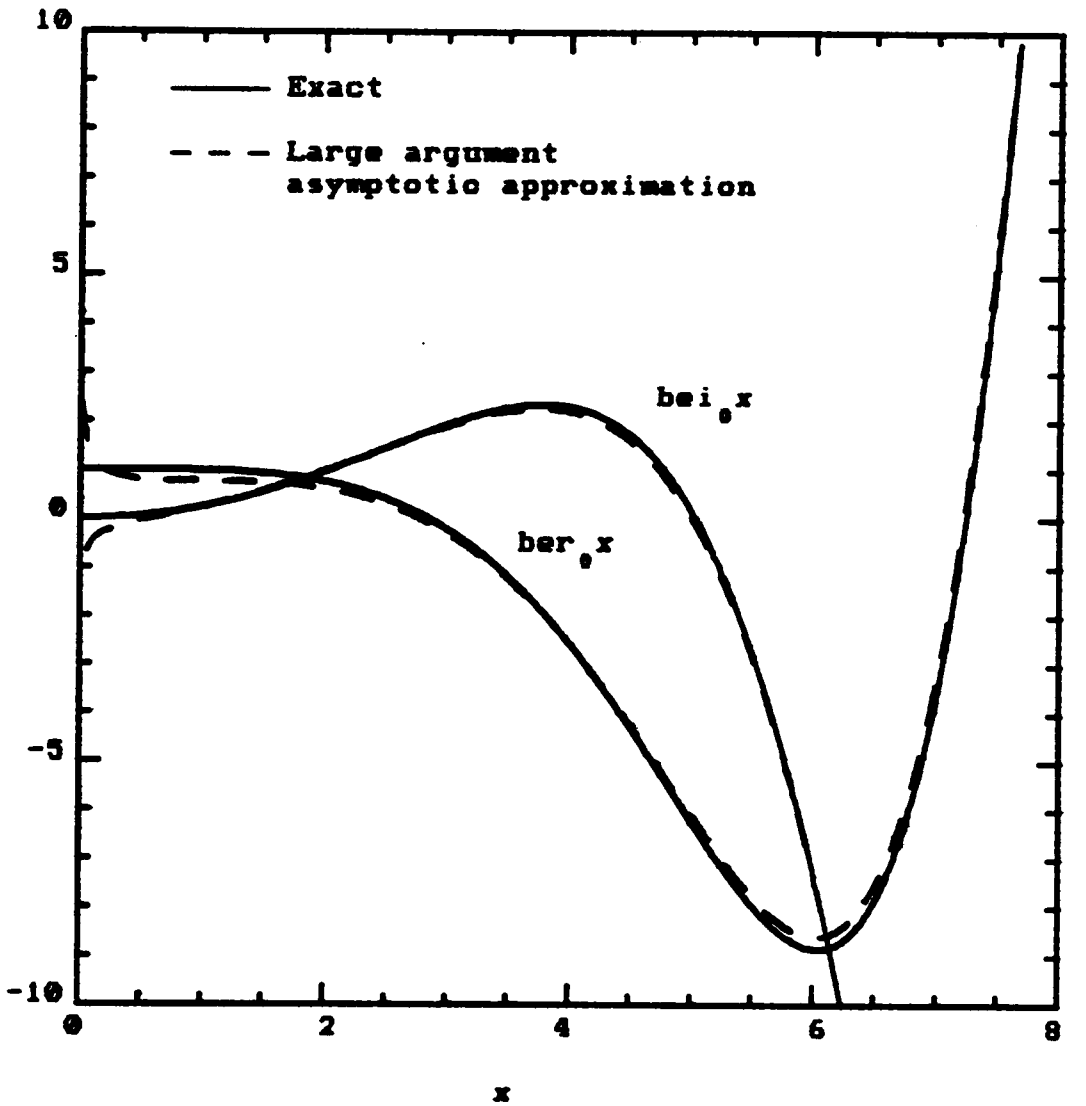

Fig. B.4.1. Zero order Kelvin functions of the first kind and their large argument asymptotic approximations.

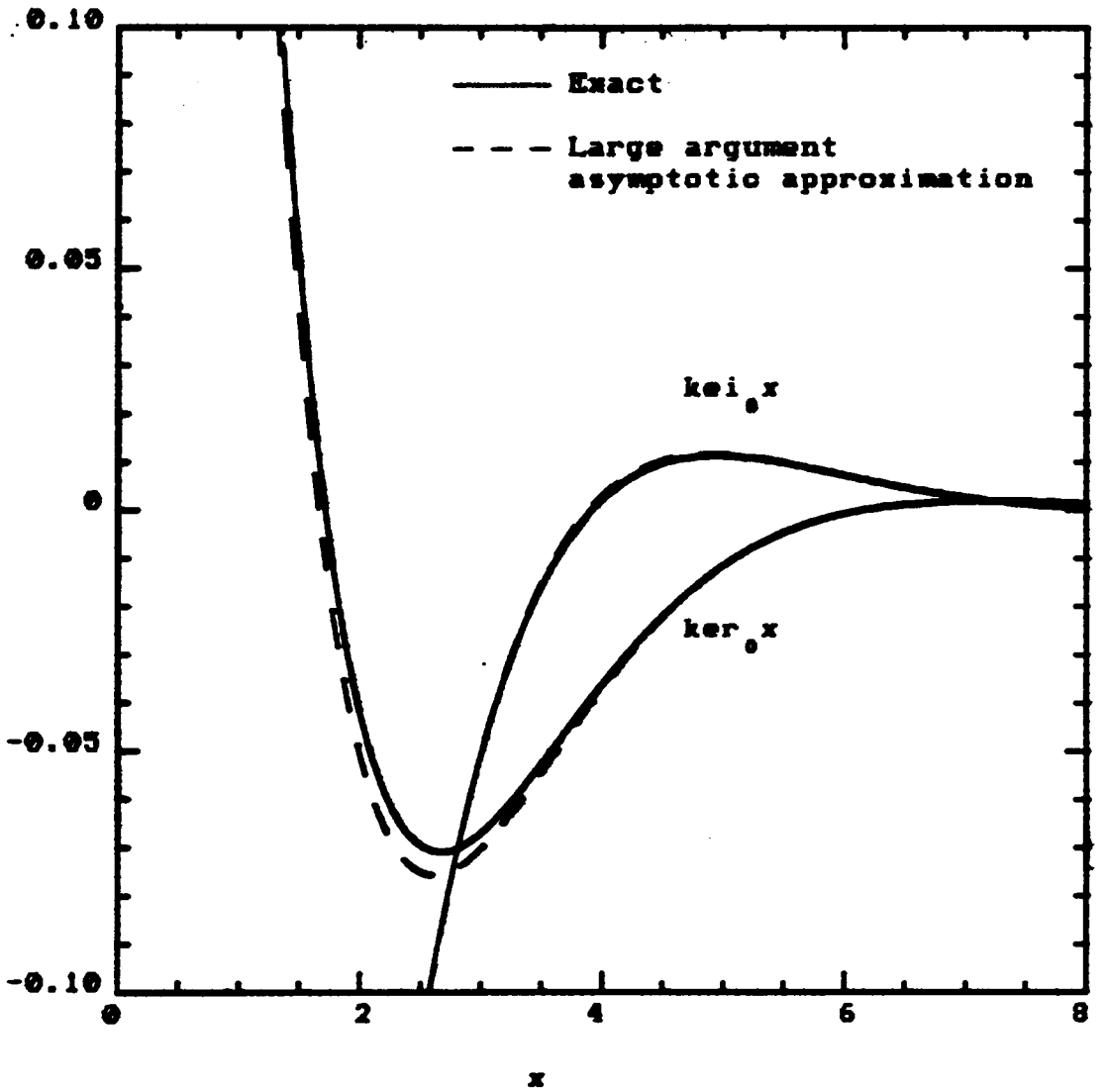

Fig. B.4.2. Zero order Kelvin functions of the second kind and their large argument asymptotic approximations.

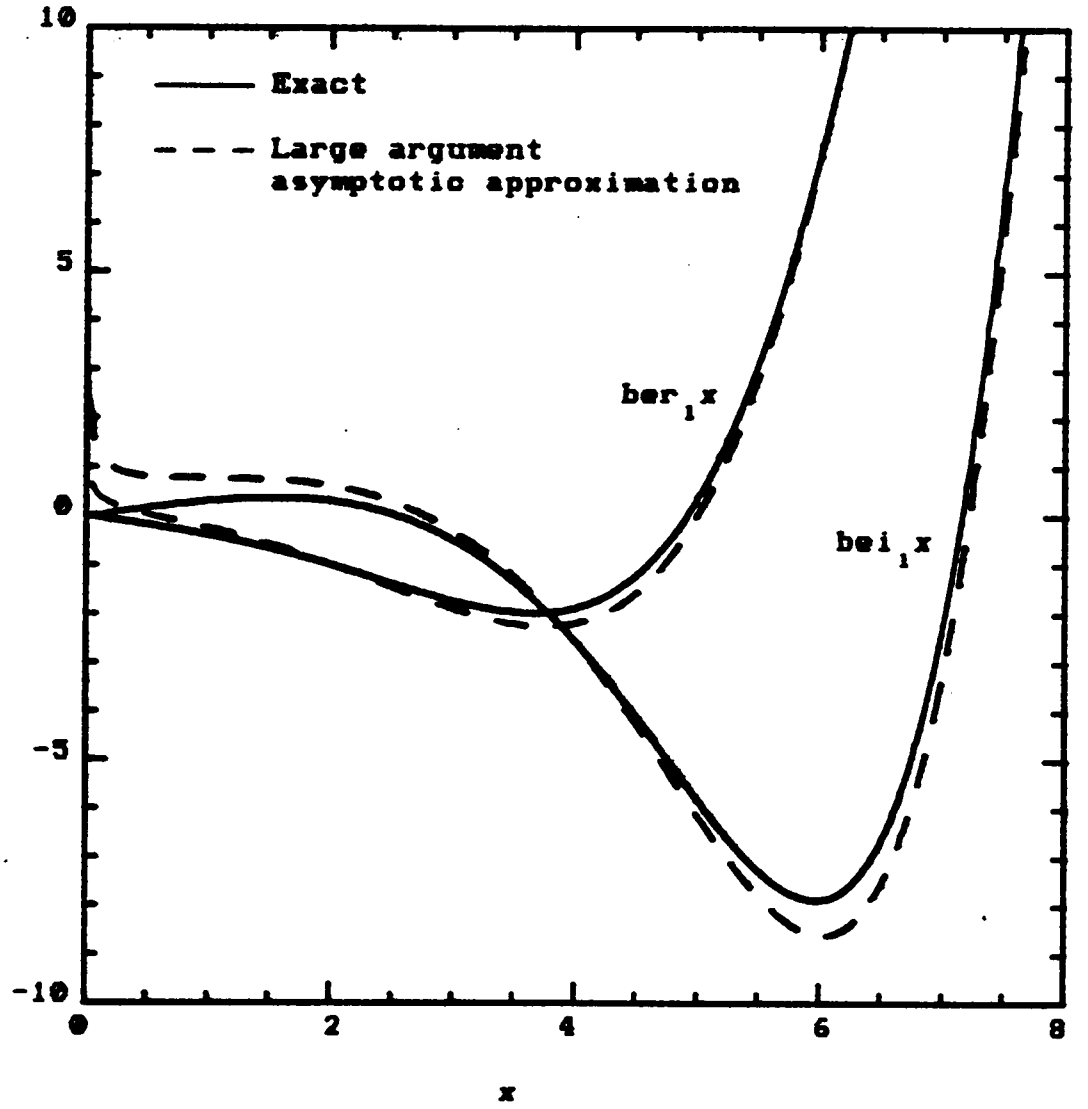

Fig. B.4.3. First order Kelvin functions of the first kind and their large argument asymptotic approximations.

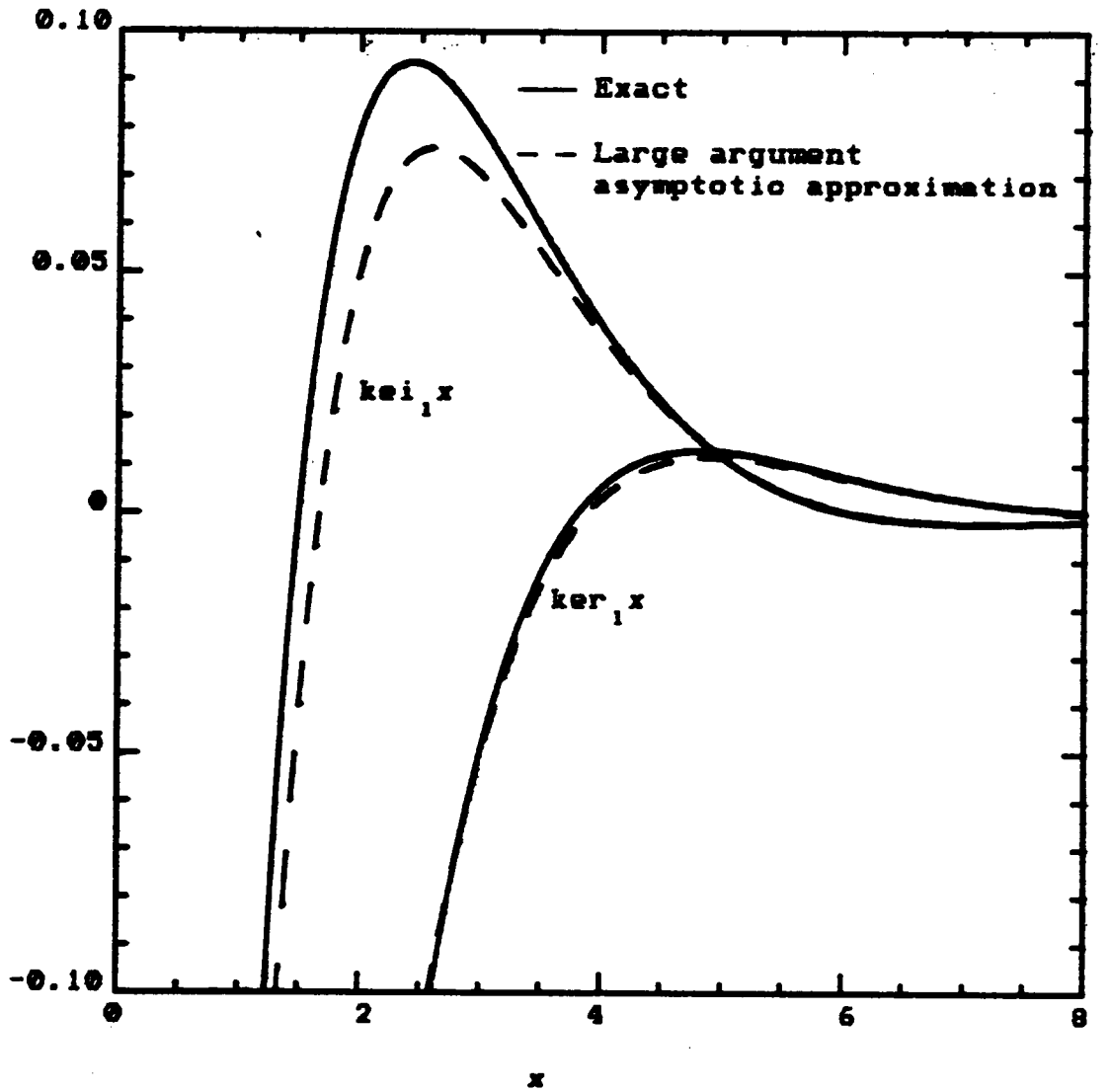

Fig. B.4.4. First order Kelvin functions of the second kind and their large argument asymptotic approximations.

APPENDIX C

FOURIER ANALYSIS

A concise summary of those aspects of Fourier analysis which are used within this dissertation is presented in this appendix. First, the Fourier series is defined in terms of its three most common forms: complex, trigonometric, and phasor. The relations between these forms along with several other useful formulas are then given. Next, an important quantity which has been given the name *normalized power bandwidth* and the symbol β is introduced and defined for the purposes of this dissertation. Several interpretations of this quantity are discussed, and results for the waveform classifications in Appendix D are presented. Also defined for use here is a piecewise linear approximation to the Fourier series. This approximation is appropriate for many of the waveforms encountered in switched-mode power converters.

Many books which contain the basics of Fourier analysis may be used to supplement this material. For example, the author has used Papoulis [58] and Wylie [59], primarily because of his familiarity with them.

C.1 DEFINITIONS

Let the function $f(t)$ satisfy the Dirichlet conditions:

- $f(t)$ is bounded and single-valued everywhere.
- $f(t)$ is periodic with period T.
- $f(t)$ has a finite number of finite discontinuities in any one period.
- $f(t)$ has a finite number of local maxima and minima in any one period.

Then the function $f(t)$ may be represented by a Fourier series which will converge to $f(t)$ at points of continuity and to the average of the right- and left-hand limits at points of discontinuity. The Dirichlet conditions are sufficient but not necessary, i.e. if the conditions are satisfied then convergence is guaranteed. However, if they are not satisfied the series may or may not converge. There are at present no known *necessary and sufficient* conditions for convergence of Fourier series.

All waveforms encountered here satisfy the Dirichlet conditions. Indeed, any voltage or current waveform which can actually be produced must satisfy these conditions. All waveform derivatives are also assumed to satisfy the Dirichlet conditions. Under the above conditions, the Fourier series may be both term-by-term integrated and differentiated.

The most concise form of the Fourier series is the complex Fourier series

$$f(t) = \sum_{k=-\infty}^{\infty} c_k e^{jk\omega_0 t}, \qquad \text{(C.1.1a)}$$

where the complex Fourier coefficients c_k are given by

$$c_k = \frac{1}{T}\int_{\emptyset}^{T} f(t)e^{-jk\omega_0 t}\, dt, \qquad \text{(C.1.1b)}$$

and

$$f_0 = \frac{1}{T}\ \text{s},\ \omega_0 = 2\pi f_0\ \text{rad/s} \qquad \text{(C.1.2)}$$

is the fundamental frequency along with its corresponding radian frequency. The limits of integration in equation (C.1.1b) may, in general, be over any given period. For simplicity, and without loss of generality, all waveforms are referenced to the time $t = \emptyset$.

Another common form of the Fourier series is the trigonometric form

$$f(t) = \frac{a_0}{2} + \sum_{k=1}^{\infty} (a_k \cos k\omega_0 t + b_k \sin k\omega_0 t), \qquad \text{(C.1.3a)}$$

whose coefficients are

$$a_k = \frac{2}{T}\int_0^T f(t)\cos k\omega_0 t \, dt \qquad \text{(C.1.3b)}$$

$$b_k = \frac{2}{T}\int_0^T f(t)\sin k\omega_0 t \, dt. \qquad \text{(C.1.3c)}$$

Simple algebraic manipulation of these definitions yields the following relationships between the coefficients:

$$a_0 = 2c_0 \qquad \text{(C.1.4a)}$$

$$a_k = c_k + c_{-k} \qquad \text{(C.1.4b)}$$

$$b_k = j(c_k - c_{-k}) \qquad \text{(C.1.4c)}$$

$$c_k = \frac{1}{2}(a_k - jb_k) \qquad \text{(C.1.4d)}$$

$$c_{-k} = \frac{1}{2}(a_k + jb_k). \qquad \text{(C.1.4e)}$$

A third and final form of the Fourier series is the amplitude and phase trigonometric form, and it will be referred to as simply the phasor form. Again, simple algebraic manipulation yields

$$f(t) = A_0 + \sum_{k=1}^{\infty} A_k \cos(k\omega_0 t - \phi_k), \qquad \text{(C.1.5a)}$$

where

$$A_0 = c_0 = \frac{a_0}{2} \qquad \text{(C.1.5b)}$$

$$A_k = \sqrt{a_k^2 + b_k^2} = 2\sqrt{c_k c_{-k}} \qquad \text{(C.1.5c)}$$

$$\phi_k = \tan^{-1}\left[\frac{b_k}{a_k}\right] = \tan^{-1}\left[j\frac{c_k - c_{-k}}{c_k + c_{-k}}\right]. \qquad \text{(C.1.5d)}$$

The coefficients A_k will be referred to as the amplitude Fourier coefficients, and ϕ_k the phase Fourier coefficients.

C.2 SOME USEFUL FORMULAS

Several useful formulas are summarized in this section. Each is written in the three forms already defined: complex, trigonometric, and phasor. Remember that all waveform functions and their derivatives are assumed to satisfy the Dirichlet conditions; consequently, their Fourier series representations may be both integrated and differentiated term-by-term. All functions are also assumed to be real.

By substituting the Fourier series representations into the integral definitions of the average value and the rms-squared value of $f(t)$ and performing the integrations, the following formulas may be derived:

$$f_{av} \triangleq \frac{1}{T}\int_{\emptyset}^{T} f(t)\,dt = c_0 = \frac{a_0}{2} = A_0 \qquad \text{(C.2.1)}$$

$$f_{rms}^2 \triangleq \frac{1}{T}\int_{\emptyset}^{T} f^2(t)\,dt = \sum_{k=-\infty}^{\infty} c_k c_{-k} = c_0^2 + 2\sum_{k=1}^{\infty} c_k c_{-k}$$

$$= \frac{1}{4}a_0^2 + \frac{1}{2}\sum_{k=1}^{\infty}(a_k^2 + b_k^2) = A_0^2 + \frac{1}{2}\sum_{k=1}^{\infty} A_k^2. \qquad \text{(C.2.2)}$$

The latter expression is Parseval's identity. It is also referred to as the average power of the function, although a general function itself has no units attached to it. When used in a physical application, however, the function represents quantities with units such as voltage and

current. The term average power attains its significance in such applications. For instance, if $f(t)$ represents the current through a one ohm resistor, then f_{rms}^2 is the power dissipated in that resistor.

Similar formulas can be derived for the derivative of the function $f'(t)$. Term-by-term differentiation is used to determine the Fourier series of $f'(t)$, and after performing the integrations, one obtains

$$f'_{av} \doteq \frac{1}{T}\int_0^T f'(t)\,dt = 0 \qquad \text{(C.2.3)}$$

$$f'^2_{rms} \doteq \frac{1}{T}\int_0^T [f'(t)]^2\,dt = \omega_0^2\sum_{k=-\infty}^{\infty} k^2 c_k c_{-k} = 2\omega_0^2\sum_{k=1}^{\infty} k^2 c_k c_{-k}$$

$$= \frac{1}{2}\omega_0^2\sum_{k=1}^{\infty} k^2(a_k^2 + b_k^2) = \frac{1}{2}\omega_0^2\sum_{k=1}^{\infty} k^2 A_k^2. \qquad \text{(C.2.4)}$$

The Fourier transform is also employed in the next section, hence its definition along with some formulas similar to those above are summarized here. The Fourier integral transform and its inversion formula are defined as

$$F(\omega) \doteq \int_{-\infty}^{\infty} f(t)e^{-j\omega t}\,dt \qquad \text{(C.2.5a)}$$

$$f(t) \doteq \frac{1}{2\pi}\int_{-\infty}^{\infty} F(\omega)e^{j\omega t}\,d\omega, \qquad \text{(C.2.5b)}$$

and will often be represented by the notation

$$f(t) \longleftrightarrow F(\omega). \tag{C.2.6}$$

Now let $f_T(t)$ and $f'_T(t)$ be defined as the truncated function and its derivative, respectively:

$$f_T(t) \doteq \begin{cases} f(t) \ ; \ 0 \le t \le T \\ 0 \ ; \ \text{elsewhere} \end{cases} \tag{C.2.7a}$$

$$f'_T(t) \doteq \begin{cases} f'(t) \ ; \ 0 \le t \le T \\ 0 \ ; \ \text{elsewhere} \end{cases}, \tag{C.2.7b}$$

with corresponding Fourier transforms

$$f_T(t) \longleftrightarrow F_T(\omega) \tag{C.2.8a}$$

$$f'_T(t) \longleftrightarrow F'_T(\omega) = j\omega F_T(\omega). \tag{C.2.8b}$$

Then, using these definitions and Parseval's theorem, the following formulas which correspond to equations (C.2.1) through (C.2.4) can be easily derived:

$$f_{av} = \frac{1}{T}\int_{-\infty}^{\infty} f_T(t)\ dt = \frac{1}{T}F_T(0) \tag{C.2.9}$$

$$f^2_{rms} = \frac{1}{T}\int_{-\infty}^{\infty} f^2_T(t)\ dt = \frac{1}{2\pi T}\int_{-\infty}^{\infty} |F_T(\omega)|^2\ d\omega \tag{C.2.10}$$

$$f'_{av} = \frac{1}{T}\int_{-\infty}^{\infty} f'_T(t)\,dt = \frac{1}{T}F'_T(0) = 0 \qquad \text{(C.2.11)}$$

$$f'^2_{rms} = \frac{1}{T}\int_{-\infty}^{\infty} [f'_T(t)]^2\,dt = \frac{1}{2\pi T}\int_{-\infty}^{\infty} |F'_T(\omega)|^2\,d\omega$$

$$= \frac{1}{2\pi T}\int_{-\infty}^{\infty} \omega^2 |F_T(\omega)|^2\,d\omega. \qquad \text{(C.2.12)}$$

It is sometimes useful to relate the Fourier coefficients of a periodic function $f(t)$ to the Fourier transform of the truncated function $f_T(t)$. This relation is easily obtained by inspection of equation (C.1.1b), yielding

$$c_k = \frac{1}{T}F_T(k\omega_0). \qquad \text{(C.2.13)}$$

In addition, the Fourier transform of the periodic function $f(t)$ may be expressed discretely as

$$F(\omega) = 2\pi\sum_{k=-\infty}^{\infty} c_k\delta(\omega-k\omega_0) = \frac{2\pi}{T}\sum_{k=-\infty}^{\infty} F_T(k\omega_0)\delta(\omega-k\omega_0) \qquad \text{(C.2.14)}$$

which is easily obtained from equation (C.1.1a) and the Fourier transform pair

$$e^{j\omega_0 t} \longleftrightarrow 2\pi\delta(\omega-\omega_0), \qquad \text{(C.2.15)}$$

where δ denotes the Dirac delta function.

C.3 THE NORMALIZED POWER BANDWIDTH

The ratio which has been given the name *normalized power bandwidth* has been identified as an important parameter which relates certain characteristics of a given current waveform to the power it causes to be dissipated in a winding. This ratio is examined in this section in order to provide a more thorough understanding of its properties.

The first occurrence of the normalized power bandwidth appears in the analysis for the two-term series approximation of the power dissipated in a winding with arbitrary periodic exitation (see equations (7.1.11)). There, it originates as an expression involving the Fourier coefficients of the current waveform. It is repeated here in terms of the three alternate forms summarized in the previous section:

$$\beta^2 \doteq \frac{\sum_{k=-\infty}^{\infty} k^2 c_k c_{-k}}{\sum_{k=-\infty}^{\infty} c_k c_{-k}} = \frac{2\sum_{k=1}^{\infty} k^2 c_k c_{-k}}{c_0^2 + 2\sum_{k=1}^{\infty} c_k c_{-k}}$$

$$= \frac{\frac{1}{2}\sum_{k=1}^{\infty} k^2 (a_k^2 + b_k^2)}{\frac{1}{4}a_0^2 + \frac{1}{2}\sum_{k=1}^{\infty} (a_k^2 + b_k^2)} = \frac{\frac{1}{2}\sum_{k=1}^{\infty} k^2 A_k^2}{A_0^2 + \frac{1}{2}\sum_{k=1}^{\infty} A_k^2}. \qquad \text{(C.3.1)}$$

The significance of these expressions is not immediately evident at first glance. If, however, one recognizes these summations as those obtained for the average power of a waveform, then a considerable simplification results. Specifically, using equations (C.2.2) and (C.2.4) yields the simple relationship

$$\beta^2 = \frac{\frac{1}{\omega_0^2}\frac{1}{T}\int_0^T [f'(t)]^2 dt}{\frac{1}{T}\int_0^T f^2(t)\,dt} = \frac{\frac{1}{\omega_0^2} f'^2_{rms}}{f^2_{rms}}. \qquad (C.3.2)$$

This is recognized at once as being proportional to the ratio of the average power of the waveform derivative to that of the waveform itself. In most cases this expression also represents a more efficient method for computing β than the infinite series formulation of equation (C.3.1). The proportionality constant $1/\omega_0^2$ serves to normalize the time derivatives in the numerator. Therefore, the units of the numerator and denominator are identical, so that the ratio β is unitless.

A further interpretation of the ratio β becomes possible if Parseval's theorem is employed. Using equations (C.2.10) and (C.2.12) yields

$$\beta^2 = \frac{\frac{1}{\omega_0^2}\int_{-\infty}^{\infty} \omega^2 |F_T(\omega)|^2 \, d\omega}{\int_{-\infty}^{\infty} |F_T(\omega)|^2 \, d\omega}, \qquad \text{(C.3.3)}$$

where the subscript T denotes the truncated functions defined in equations (C.2.7) and (C.2.8). This is the corresponding frequency domain expression. It may also be written in the more recognizable form

$$\beta^2 = \frac{\sigma_\omega^2}{\omega_0^2}, \qquad \text{(C.3.4a)}$$

where

$$\sigma_\omega^2 = \frac{\int_{-\infty}^{\infty} \omega^2 |F_T(\omega)|^2 \, d\omega}{\int_{-\infty}^{\infty} |F_T(\omega)|^2 \, d\omega} \qquad \text{(C.3.4b)}$$

is the normalized variance of the power spectrum. It is the variance as well as the second moment because the mean is zero as a consequence of the symmetry of the power spectrum about $\omega = 0$. The normalization is with respect to the total energy of the truncated function. The motivation for the term *normalized power bandwidth* should now be evident. The variance is a measure of the bandwidth of the power spectrum

about zero frequency, and the normalization is with respect to the fundamental frequency ω_0.

Before continuing, it would be desirable to compute and examine properties of the normalized power bandwidth for some representative examples. Appendix D provides the basis for the waveform classifications considered here. Most waveforms in power conversion can be represented by one of these fundamental waveform types or a combination of them. First, consider the Type I periodic sinusoidal waveform $A\sin\omega_0 t$, since it is the simplest and provides a very good reference result upon which others can be compared and evaluated. The computation is quite trivial:

$$\beta_I^2 = \frac{\frac{1}{\omega_0^2} f'^2_{rms}}{f^2_{rms}} = \frac{\frac{1}{\omega_0^2}\omega_0^2\frac{A^2}{2}}{\frac{A^2}{2}} = 1, \qquad \text{(C.3.5a)}$$

where the subscript notation is used to identify the waveform types defined in Appendix D. This basic result provides one confirmation of the formulas obtained in the arbitrary periodic waveform analysis, since it reduces them to those derived in the sinusoidal analysis. Results for the next three waveform types (II - unidirectional fractional sinusoid, III - unidirectional rectangular wave, and IV - unidirectional triangular wave) are also easily derived from the application of equation (C.3.2):

$$\beta_{II} = \frac{1}{2D} \qquad \text{(C.3.5b)}$$

$$\beta_{III} = \sqrt{\frac{1}{2\pi^2 D_r (D - \frac{1}{3}D_r)}} \qquad \text{(C.3.5c)}$$

$$\beta_{IV} = \sqrt{\frac{3}{4\pi^2 D D_r}} \, . \qquad \text{(C.3.5d)}$$

In each of these expressions D represents the duty cycle of the waveform pulse, and D_r represents the duty cycle of the rise times in the square and triangular waves. Refer to Appendix D for the complete definition of these waveforms.

Curves for these expressions are presented in Figure C.3.1 as a function of the duty cycle D which may vary from 0% to 100%. A typical value of 1% is used for the rise-time duty cycle of waveform types III and IV. A wide variation of β with respect to both the waveform type and the duty cycle is evident. According to the two-term series approximation given in equation (7.1.11a), this translates into a corresponding variation in the power dissipation in a transformer winding. In addition, from equations (7.3.1) and (7.3.2), it is seen that the optimum conductor layer thickness is inversely proportional to the square root of β. The resulting minimum power dissipation is directly proportional to it. Thus, in general, the power dissipation increases and the optimum conductor layer thickness

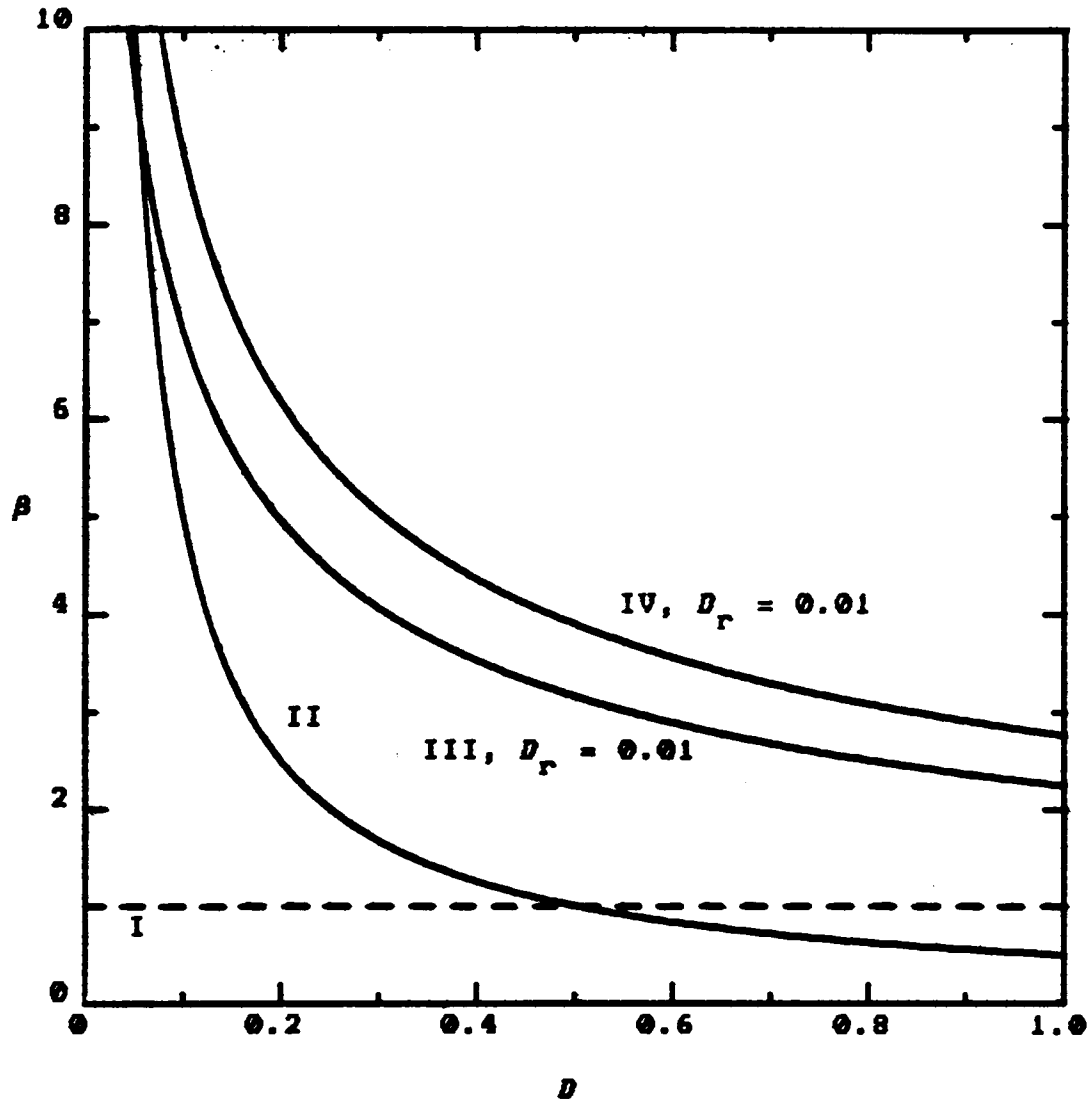

Figure C.3.1. Normalized power bandwidth vs. duty cycle for the following waveform classifications in Appendix D: I - sinusoid, II - unidirectional fractional sinusoid, III - unidirectional rectangular wave, and IV - unidirectional triangular wave.

decreases for smaller duty cycles. Note also the variation with respect to the waveform type. The sinusoidal case is shown by the dashed line; in most cases it results in the least power dissipation. The only exception is a fractional sinusoid whose duty cycle is greater than 50%. Both of the nonsinusoidal waveform types have larger values of β, with the triangular waveform the largest.

The preceeding discussion can be conceptually summarized in a general manner as follows. More rapidly varying periodic waveforms, characterized by larger bandwidths and increased energy levels in the higher harmonics, produce more nonuniform currents which result in greater conductor power dissipation. The normalized power bandwidth β provides the quantitative definition of this rapidness of variation or bandwidth. The nature of these results should not be of great surprise and should be easily remembered since they are in agreement with fundamental concepts such as skin effect and time-bandwidth product. As a further illustration of these concepts, Figures C.3.2 and C.3.3 are provided. These two figures show curves of β for various values of the rise-time duty cycle D_r for the rectangular and triangular waves, respectively. The reference value of unity for a sinusoid is included as the dashed line. Note that in some cases for large values of D and D_r it is possible for β to be less than one. In fact, for a pure DC

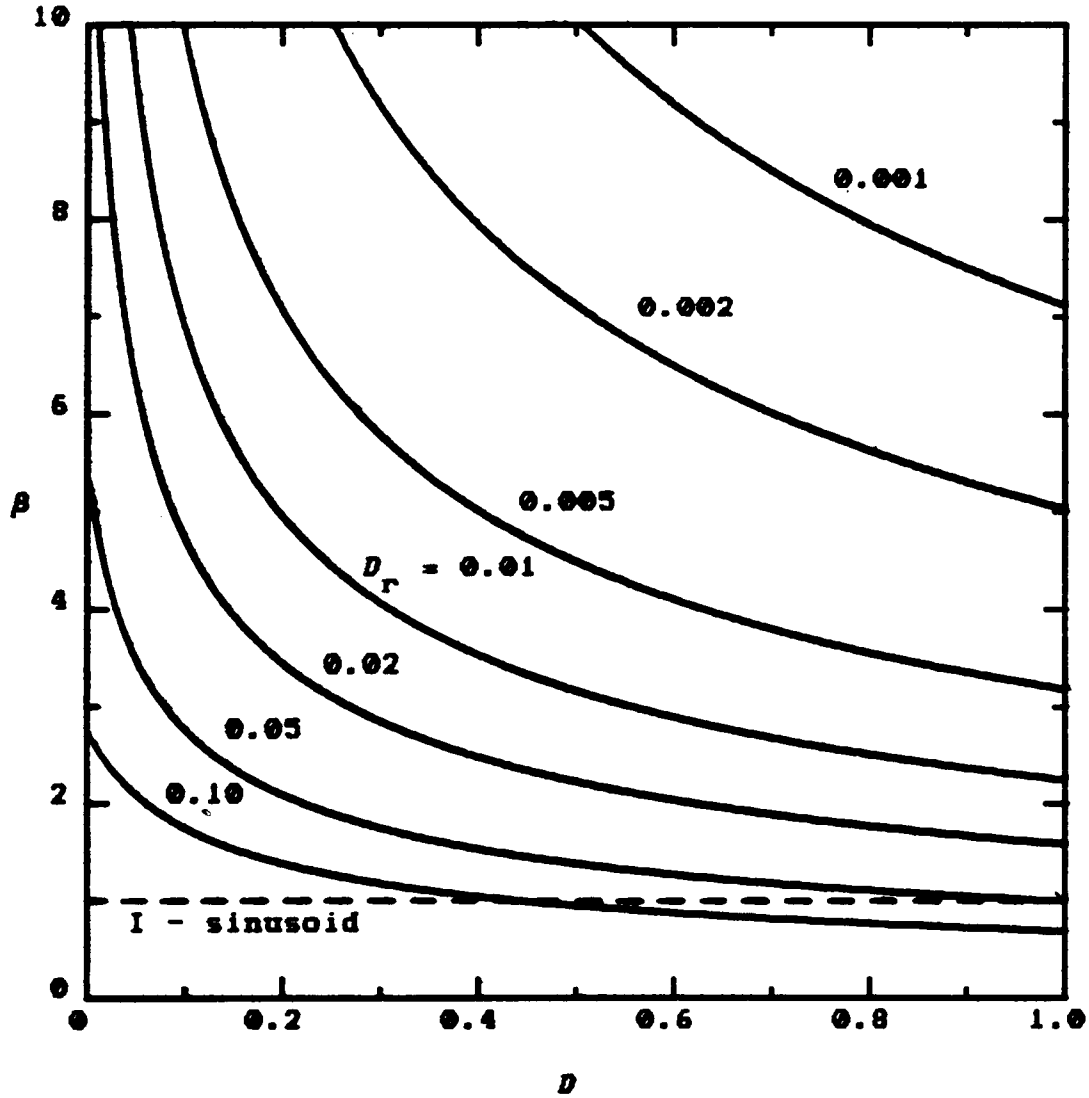

Figure C.3.2. Normalized power bandwidth vs. duty cycle for the unidirectional rectangular wave (Type III) with the duty cycle of the rise time varied as a parameter.

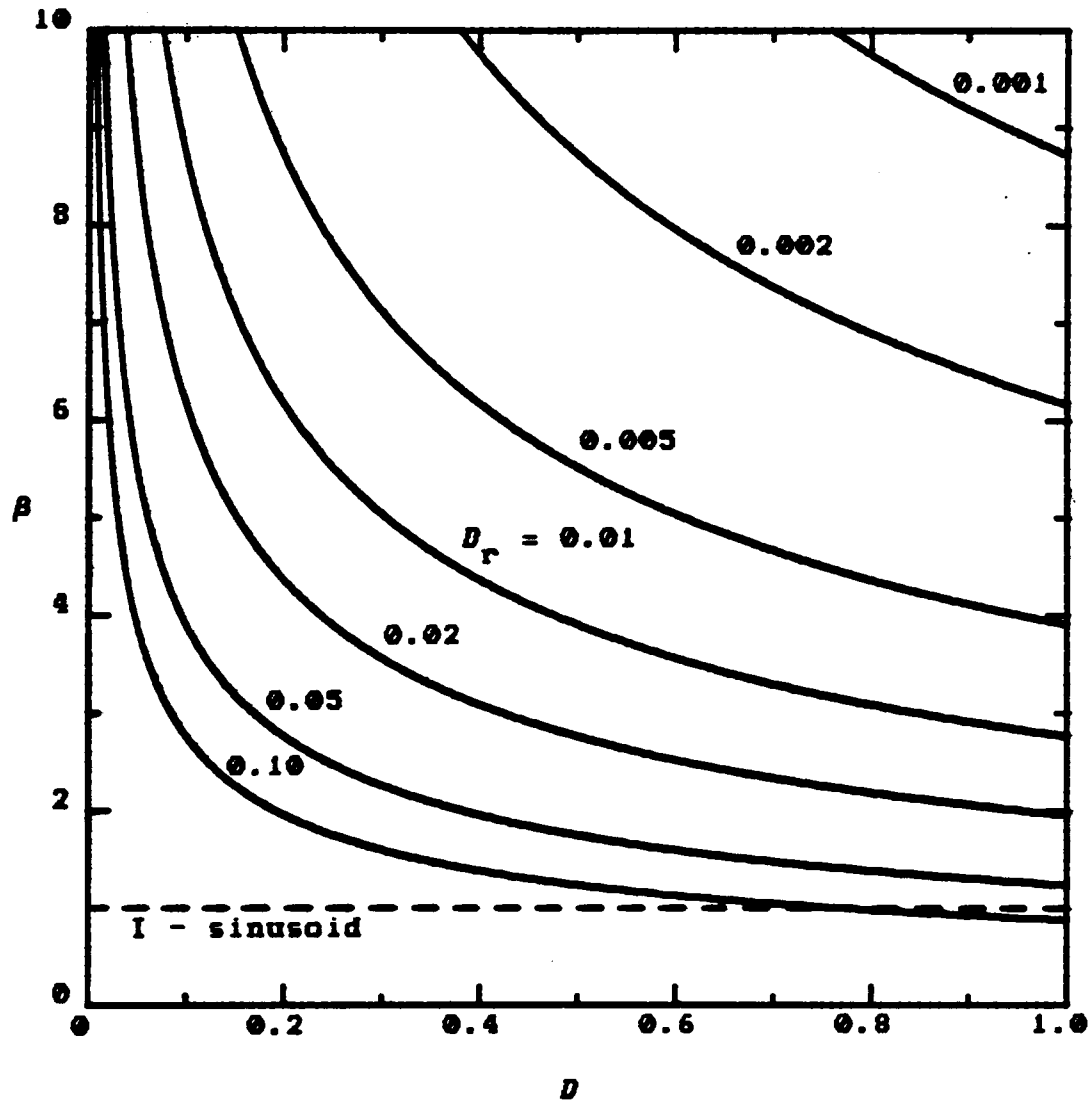

Figure C.3.3. Normalized power bandwidth vs. duty cycle for the unidirectional triangular wave (Type IV) with the duty cycle of the rise time varied as a parameter.

waveform, $\alpha = 0$. In general, however, present trends in power conversion technology are emphasizing shorter rise times in order to reduce switching losses. Ironically, there results a corresponding increase in winding losses. Ultimately, these offsetting effects should be evaluated for each application. Decisions on topics such as operating frequency, circuit topology, and transformer construction should include these evaluations.

No graphical results are presented here for the last waveform classification, Type V, which is for an arbitrary periodic waveform represented by a piecewise linear approximation. This topic is the subject of the next section, and an expression for the normalized power bandwidth will be derived there.

C.4 PIECEWISE LINEAR APPROXIMATION

Many waveforms encountered in switched-mode power conversion are made up of straight line segments. For those cases, the piecewise linear approximation (PLA) given here is actually an exact analysis, making it a natural choice. Other waveforms may be approximated as accurately as desired by choosing a sufficient number of intervals.

Please refer to Figure C.4.1 for the pictorial representation of the following description of the PLA:

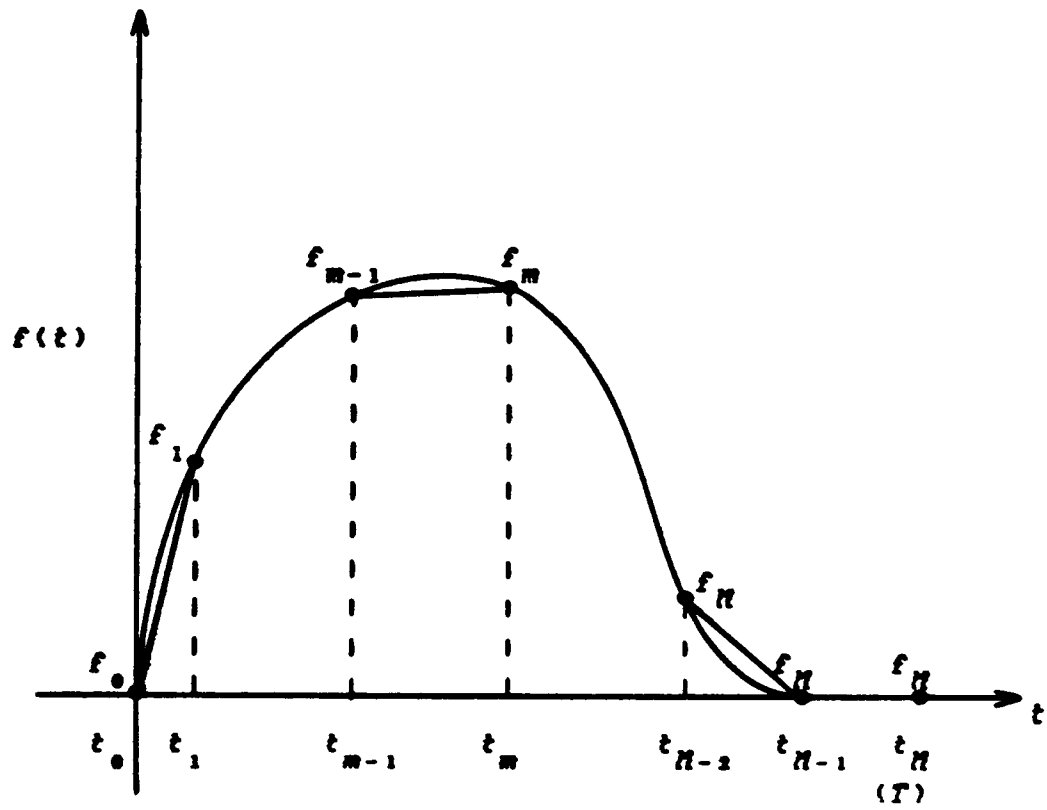

Figure C.4.1. Pictorial representation of the PLA.

- $f(t)$ satisfies the Dirichlet conditions.
- the PLA is defined on the interval $[0, T]$, but it is valid everywhere according to the periodicity of f.
- $M+1$ point pairs $[t_m, f_m]$; $m = 0,1,2,\ldots,M$ are defined on the interval $[0, T]$. f_m represents the function value $f(t_m)$ at time t_m.
- the point pairs are joined in numerical order by straight line segments to form the PLA of $f(t)$.
- there are a total of M time intervals, for which the mth interval is defined to be $[t_{m-1}, t_m]$.

A convenient way to mathematically express the PLA is to define trapezoidal functions $f_m(t)$ which are valid on the mth time interval, namely,

$$f_m(t) = \frac{f_m - f_{m-1}}{t_m - t_{m-1}}(t - t_{m-1}) + f_{m-1}; \quad t_{m-1} \le t \le t_m. \qquad (C.4.1)$$

Thus, the truncated function $f_T(t)$ defined by equation (C.2.7a) may be written as the simple summation

$$f_T(t) = \sum_{m=1}^{M} f_m(t). \qquad (C.4.2)$$

Now these equations can be substituted into the defining integrals for the average value and average power given in

equations (C.2.1) through (C.2.4). Ignoring the Fourier analysis for the time being and performing the time integrations gives

$$f_{av} = \frac{1}{T}\sum_{m=1}^{M} \frac{f_m+f_{m-1}}{2}(t_m-t_{m-1}) \qquad (C.4.3)$$

$$f_{rms}^2 = \frac{1}{T}\sum_{m=1}^{M} \frac{f_m^2+f_m f_{m-1}+f_{m-1}^2}{3}(t_m-t_{m-1}) \qquad (C.4.4)$$

$$f'_{av} = 0 \qquad (C.4.5)$$

$$f'^2_{rms} = \frac{1}{T}\sum_{m=1}^{M} \frac{(f_m-f_{m-1})^2}{(t_m-t_{m-1})}. \qquad (C.4.6)$$

The next task is to determine the Fourier coefficients using the PLA. The obvious approach is to substitute the expressions in equations (C.4.1) and (C.4.2) into the defining integral of equation (C.1.1b). This approach certainly will produce the correct results; however, it is a lengthy and uninteresting endeavor. A more attractive approach which yields quickly the desired results uses both the time differentation property of the Fourier transform and the Dirac delta function. Beginning with equations (C.4.1) and (C.4.2), and taking two time derivatives gives

$$f_T(t) = \sum_{m=1}^{M} \frac{f_m - f_{m-1}}{t_m - t_{m-1}}(t - t_{m-1}) + f_{m-1} \qquad \text{(C.4.7a)}$$

$$f'_T(t) = \sum_{m=1}^{M} \frac{f_m - f_{m-1}}{t_m - t_{m-1}}[u(t - t_{m-1}) - u(t - t_m)] \qquad \text{(C.4.7b)}$$

$$f''_T(t) = \sum_{m=1}^{M} \frac{f_m - f_{m-1}}{t_m - t_{m-1}}[\delta(t - t_{m-1}) - \delta(t - t_m)]. \qquad \text{(C.4.7c)}$$

Using the Fourier transform pair

$$\delta(t - t_0) \longleftrightarrow e^{-j\omega t_0} \qquad \text{(C.4.8)}$$

and the time differentiation property

$$f^{(n)}(t) \longleftrightarrow (j\omega)^n F(\omega) \qquad \text{(C.4.9)}$$

then results in

$$F''_T(\omega) = \sum_{m=1}^{M} \frac{f_m - f_{m-1}}{t_m - t_{m-1}}(e^{-j\omega t_{m-1}} - e^{-j\omega t_m}) \qquad \text{(C.4.10a)}$$

$$F'_T(\omega) = \frac{1}{j\omega}\sum_{m=1}^{M} \frac{f_m - f_{m-1}}{t_m - t_{m-1}}(e^{-j\omega t_{m-1}} - e^{-j\omega t_m}) \qquad \text{(C.4.10b)}$$

$$F_T(\omega) = \frac{1}{(j\omega)^2}\sum_{m=1}^{M}\frac{f_m - f_{m-1}}{t_m - t_{m-1}}\left(e^{-j\omega t_{m-1}} - e^{-j\omega t_m}\right). \quad \text{(C.4.10c)}$$

The complex Fourier coefficients can now be written by inspection by using equation (C.2.13):

$$c_k = \frac{1}{T(jk\omega_0)^2}\sum_{m=1}^{M}\frac{f_m - f_{m-1}}{t_m - t_{m-1}}\left(e^{-jk\omega_0 t_{m-1}} - e^{-jk\omega_0 t_m}\right) \quad \text{(C.4.11a)}$$

which is easily simplified to

$$c_k = \frac{1}{j2\pi k}\sum_{m=1}^{M}(f_m - f_{m-1})\,\mathrm{Sa}\left[\frac{k\omega_0}{2}(t_m - t_{m-1})\right]e^{-j\frac{k\omega_0}{2}(t_m + t_{m-1})}, \quad \text{(C.4.11b)}$$

where

$$\mathrm{Sa}(x) \triangleq \frac{\sin x}{x} \quad \text{(C.4.12)}$$

is the sampling function which arises frequently in communication theory. If desired, the trigonometric and phasor forms of the Fourier coefficients can easily be found via the relationships in equations (C.1.4) and (C.1.5).

In conclusion of this section on the piecewise linear approximation, consider the computation of the normalized power bandwidth. The simplest approach is to substitute equations (C.4.4) and (C.4.6) into (C.3.2), which gives

$$\beta_V^2 = \frac{3}{\omega_0^2} \frac{\sum_{m=1}^{M} \frac{1}{t_m - t_{m-1}} (f_m^2 - 2f_m f_{m-1} + f_{m-1}^2)}{\sum_{m=1}^{M} (t_m - t_{m-1})(f_m^2 + f_m f_{m-1} + f_{m-1}^2)} \qquad \text{(C.4.13a)}$$

or

$$\beta_V^2 = \frac{3}{4\pi^2} \frac{\sum_{m=1}^{M} \frac{1}{D_m} (f_m^2 - 2f_m f_{m-1} + f_{m-1}^2)}{\sum_{m=1}^{M} D_m (f_m^2 + f_m f_{m-1} + f_{m-1}^2)}, \qquad \text{(C.4.13b)}$$

where

$$D_m \doteq \frac{t_m - t_{m-1}}{T} \qquad \text{(C.4.14)}$$

is defined as the duty cycle of the mth time interval. Note also that an alternate expression for the normalized power bandwidth in terms of the Fourier coefficients can be derived by substituting equation (C.4.11b) into (C.3.1). This result, however, has the disadvantages of being both more complicated and also of containing infinite series instead of the finite ones in the above expression.

APPENDIX D

WAVEFORM CLASSIFICATIONS

The waveform types defined in this appendix are used in the examples of Chapter 7 and Appendix C. They are chosen to provide representative examples of how the properties of waveforms affect the power dissipation and energy storage in transformer windings. They are also typical of the waveforms encountered in switched-mode power converters. The waveform types are defined in Figure D.1, where the waveform duty cycle and the rise-time duty cycle are defined as

$$D = \frac{t_d}{T} \tag{D.1}$$

and

$$D_r = \frac{t_r}{T}, \tag{D.2}$$

respectively. For convenience, several properties are also summarized in Table D.1. Note that Type V is used to refer to an arbitrary periodic waveform which is modelled using the piecewise linear approximation in Appendix C.

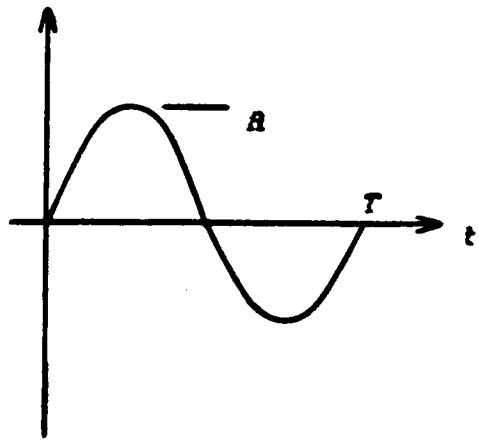

(a) Type I - Sinusoid.

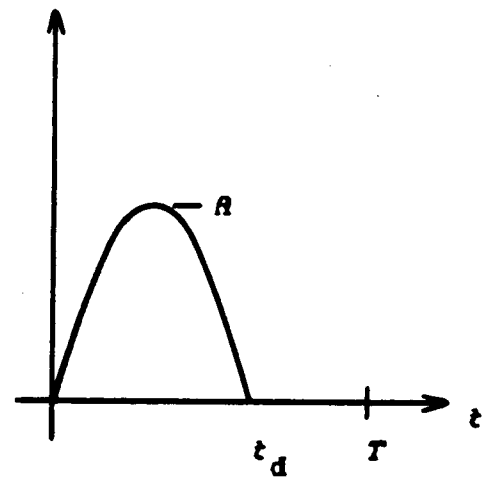

(b) Type II - Unidirectional fractional sinusoid.

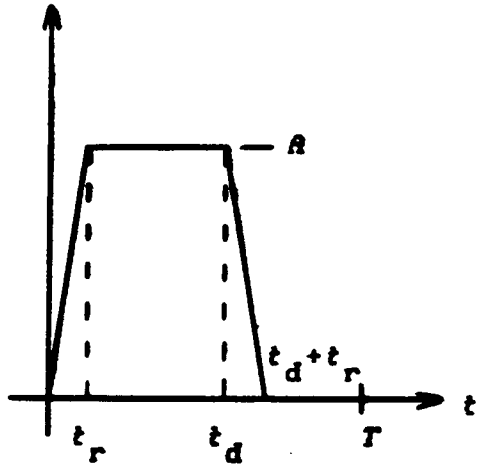

(c) Type III - Unidirectional fractional rectangular wave.

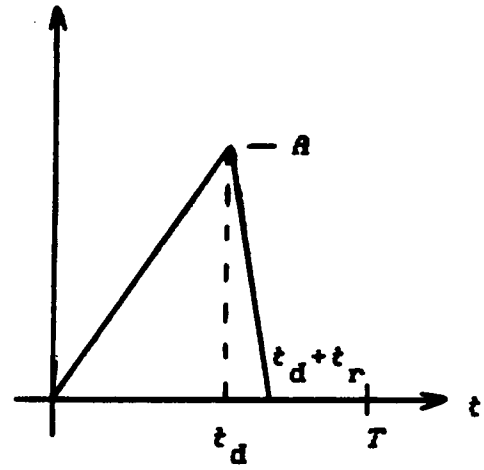

(d) Type IV - Unidirectional fractional triangular wave.

Figure D.1. Waveform classifications.

Table D.1. Properties of Waveform Classifications

Type	f_{av}	f^2_{rms}	f'^2_{rms}	β
I	0	$\frac{1}{2}A^2$	$\frac{1}{2}A^2\omega_0^2$	1
II	$\frac{2}{\pi}AD$	$\frac{1}{2}A^2D$	$\frac{1}{2}A^2D\left[\frac{\pi}{t_d}\right]^2$	$\frac{1}{4D^2}$
III	AD	$A^2(D-\frac{1}{3}D_r)$	$2A^2\frac{D_r}{t_r^2}$	$\frac{1}{2\pi^2D_r(D-\frac{1}{3}D_r)}$
IV	$\frac{1}{2}A(D+D_r)$	$\frac{1}{3}A^2(D+D_r)$	$A^2\frac{D+D_r}{t_r t_d}$	$\frac{3}{4\pi^2DD_r}$
V	(C.4.3)	(C.4.4)	(C.4.6)	(C.4.13)

BIBLIOGRAPHY

[1] J.C. Maxwell, *A Treatise on Electricity and Magnetism*, Vol. 2, Third Edition, New York: Dover, 1954, pp. 320-323.

[2] Lord Rayleigh, "The reaction upon the driving-point of a system exececuting forced harmonic oscillations of various periods, with applications to electricity," *Phil. Mag.*, vol. 21, pp. 369-381, 1886.

[3] Lord Rayleigh, "On the self-induction and resistance of straight conductors," *Phil. Mag.*, vol. 21, pp. 381-394, 1886.

[4] Lord Rayleigh, "Notes on electricity and magnetism: II. The self induction and resistance of compound conductors," *Phil. Mag.*, vol. 22, pp. 469-500, 1886.

[5] D.E. Hughes, "Researches upon the self-induction of an electric current," *Proc. Roy. Soc.* , vol. 40, pp. 450-469, 1886.

[6] Lord Kelvin, "Inaugural address: Ether, electricity, and ponderable matter," *Journ. IEE*, vol. 18, pp. 4-43, 1889.

[7] M. Wien, *Annalen der Physik*, vol. 14, p. 1, 1904.

[8] A. Sommerfeld, *Annalen der Physik*, vol. 15, p. 673, 1904.

[9] A.B. Field, "Eddy currents in large slot-wound conductors," *Trans. AIEE*, vol.24, pp. 761-788, June 1905.

[10] M.B. Field, "Idle currents," *Journ. IEE*, vol. 37, pp. 83-120, Fedruary 1906.

[11] L. Cohen, "The influence of frequency on the resistance and inductance of solenoidal coils," *U.S. Bureau of Standards Bulletins*, vol. 4, No. 1, pp 161-178, 1907.

[12] A. Russell, "The effective resistance and inductance of a concentric main, and methods of computing Ber and Bei and Allied functions," *Phil. Mag.*, vol. 17, pp. 524-552, January 1909.

[13] A.E. Kennelly, F.A. Laws, P.H. Pierce, "Experimental researches on skin effect in conductors," *Trans. AIEE*, vol. 34, pt. 2, pp. 1953-2021, September 1915.

[14] G.W.O. Howe, "The high-frequency resistance of multiply-stranded insulated wire," *Proc. Roy. Soc. A*, vol 93., pp. 468-492, 1917.

[15] H.B. Dwight, "Skin effect in tubular and flat conductors," *Trans. AIEE*, vol. 37, pp. 1379-1403, 1918.

[16] W.V. Lyon, "Current distribution in armature conductors," *Electrical World*, vol. 74, No. 2, pp. 66-68, July 1919.

[17] G.W.O. Howe, "The high frequency resistance of wires and coils," *Journ. IEE*, vol.58, pp. 152-166, December 1919.

[18] H.W. Taylor, "Eddy currents in stator windings," *Journ. IEE*, vol. 58, pp. 279-300, January 1920.

[19] R.E. Gilman, "Eddy current losses in armature conductors," *Trans. AIEE*, vol. 39, pt. 1, pp. 997-1056, June 1920.

[20] H.L. Curtis, "An integration method of deriving the alternating-current resistance and inductance of conductors," *Bureau of Standards Scientific Paper No. 374*, vol.18, pp. 93-124, 1920.

[21] S. Butterworth, "Eddy-current losses in cylindrical conductors, with special applications to the alternating current resistance of short coils," *Phil. Trans. A*, vol. 222, pp. 57-100, September 1921.

[22] W.V. Lyon, "Heat losses in the conductors of alternating-current machines," *Trans. AIEE*, vol. 40, pp. 1361-1395, June 1921.

[23] W.V. Lyon, "Heat losses in stranded armature conductors," *Trans. AIEE*, vol. 41, pp. 199-214, February 1922.

[24] H.B. Dwight, "Skin effect and proximity effect in tubular conductors," *Trans. AIEE*, vol. 41, pp. 189-198, February 1922.

[25] H.B. Dwight, "Proximity effect in wires and thin tubes," *Trans. AIEE*, vol. 42, pp. 850-859, June 1923.

[26] H.B. Dwight, "A precise method of calculation of skin effect in isolated tubes," *Journ. AIEE*, vol. 42, pp. 827-831, August 1923.

[27] R.E. Gilman, "Eddy current losses in armature conductors," *Journ. AIEE*, vol. 43, pp. 194-196, March 1924.

[28] S. Butterworth, "On the alternating current resistance of solenoidal coils," *Proc. Roy. Soc. Lond. A*, vol. 107, pp. 693-715, 1925.

[29] C. Snow, "Alternating current distribution in cylindrical conductors," *U.S. Bureau of Standards Scientific Paper No. 509*, vol. 20, 277-338, 1925.

[30] I.H. Summers, "Reduction of armature copper losses," *Trans. AIEE*, vol. 46, pp. 101-109, February 1927.

[31] J.D. Cockcroft, "Skin effect in rectangular conductors at high frequencies," *Proc. Roy. Soc. Lond.*, vol. 122, pp. 533-542, 1929.

[32] W. Jackson, "Skin effect in rectangular conductors at high frequencies," *Phil. Mag.*, s. 7, vol. 18, pp.433-441, September 1934.

[33] A.H.M. Arnold, "The alternating-current resistance of parallel conductors of circular cross section," *Journ. IEE*, vol.77, pp. 49-58, 1935.

[34] A.H.M. Arnold, "The alternating-current resistance of tubular conductors," *Journ. IEE*, vol. 78, pp. 580-593, 1936.

[35] A.H.M. Arnold, "The alternating-current resistance of hollow, square conductors," *Journ. IEE*, vol. 82, pp. 537-545, 1938.

[36] E. Bennett and S.C. Larson, "Effective resistance to alternating currents of multilayer windings," *Trans. AIEE*, vol. 59, pp. 1010-1017, 1940.

[37] T.H. Long, "Eddy-current resistance of multilayer coils," *Trans. AIEE*, vol. 64, pp. 712-718, October 1945.

[38] J. Lammeraner and M. Stafl, *Eddy Currents*, London: Iliffe Books LTD., 1966, Chapters 8 and 9.

[39] P.L. Dowell, "Effects of eddy currents in transformer windings," *Proc. IEE*, vol. 113, No. 8, pp. 1387-1394, August 1966.

[40] P. Silvester, "Modal network theory of skin effect in flat conductors," *Proc. IEEE*, vol. 54, No. 9, pp. 1147-1151, September 1966.

[41] P. Silvester, "Network analog solution of skin and proximity effect problems," *IEEE Trans. Power App. and Sys.*, vol. PAS-86, No. 2, pp. 241-247, February 1967.

[42] P. Silvester, "AC resistance and reactance of isolated rectangular conductors," *IEEE Trans. Power App. and Sys.*, vol. PAS-86, No. 6, pp. 770-774, June 1967.

[43] P. Silvester, "Dynamic resistance and inductance of slot-imbedded conductors," *IEEE Trans. Power App. and Sys.*, vol. PAS-87, No. 1, pp. 250-256, January 1968.

[44] P. Silvester, "The accurate calculation of skin effect in conductors of complicated shape," *IEEE Trans. Power App. and Sys.*, vol. PAS-87, No. 3, pp. 735-742, March 1968.

[45] P. Silvester, "Skin effect in multiple and polyphase conductors," *IEEE Trans. Power App. and Sys.*, vol. PAS-88, No. 3, pp. 231-238, March 1969.

[46] E.C. Snelling, *Soft Ferrites: Properties and Applications*, London: Iliffe Books LTD., 1969, Chapters 9 and 11.

[47] M.P. Perry, "Multiple layer series connected winding design for minimum losses," *IEEE Trans. Power App. and Sys.*, vol. PAS-98, No. 1, pp.116-123, January 1979.

[48] T.H. Putman, "Eddy-current loss in large electrical reactors," *IEEE Trans. Magn.*, vol. MAG-15, No. 6, pp. 1665-1670, November 1979.

[49] M.P. Perry, "On calculating losses in current carrying conductors in an external magnetic field," *IEEE Trans. Magn.*,vol. MAG-17, No. 5, pp. 2486-2488, September 1981.

[50] P.S. Venkatraman, "Winding eddy current losses in switched mode power transformers due to rectangular wave currents," *Proc. Powercon 11*, A-1, pp. 1-11, 1984.

[51] American National Standard Metric Practice, ANSI/IEEE Std 268-1982.

[52] IEEE Standard Letter Symbols for Units of Measurement (SI Units, Customary Inch-Pound Units, and Certain Other Units), ANSI/IEEE Std 260-1978.

[53] IEEE Standard Letter Symbols for Quantities Used in Electrical Science and Electrical Engineering, ANSI/IEEE Std 280-1985.

[54] IEEE Recommended Practice for Preferred Metric Units for Use in Electrical and Electronics Science and Technology, ANSI/IEEE Std 945-1984.

[55] M. Abramowitz and I.A. Stegun, *Handbook of Mathematical Functions*, Washington, D.C.: U.S Government Printing Office, 1964, pp. 379-385, 430-433.

[56] I.S. Gradshteyn and I.M. Ryzhik, *Table of Integrals, Series, and Products*, Fourth Edition, New York: Academic Press, 1980, pp. 633-634, 983-985.

[57] G.N. Watson, *A Treatise on the Theory of Bessel Functions*, Second Edition, London: Cambridge University Press, 1944, pp. 81-82, 203-204, 658.

[58] A. Papoulis, *The Fourier Integral and its Applications*, New York: McGraw-Hill, 1962.

[59] C.R. Wylie, *Advanced Engineering Mathematics*, Fourth Edition, New York: McGraw-Hill, 1975, Chapter 6.

The vita has been removed from the scanned document